Universitat de les Illes Balears

DOCTORAL THESIS

Sub-dominant modes of the Gravitational Radiation from Compact Binary Coalescences: Construction of hybrid waveforms and Impact on Gravitational Wave searches.

by

Juan Calderón Bustillo

2015

UNIVERSITAT DE LES ILLES BALEARS

**Universitat de les
Illes Balears**

DOCTORAL THESIS

Doctoral programme of physics

Sub-dominant modes of the Gravitational Radiation from Compact Binary Coalescences: Construction of hybrid waveforms and Impact on Gravitational Wave searches.

by

Juan Calderón Bustillo

Doctor por la Universidad de las Islas Baleares

Supervisors:

Alicia M. Sintes Olives & Sascha Husa

April 2015

List of publications derived from this thesis

1. Vijay Varma, Parameswaran Ajith, Sascha Husa, Juan Calderon Bustillo, Mark Hannam, et al. Gravitational-wave observations of binary black holes: Effect of nonquadrupole modes. Phys.Rev., D90(12):124004, 2014. doi: 10.1103/PhysRevD. 90.124004

2. Juan Calderón Bustillo, Alejandro Bohé, Sascha Husa, Alicia M. Sintes, Mark Hannam, et al. Comparison of subdominant gravitational wave harmonics between post-Newtonian and numerical relativity calculations and construction of multi-mode hybrids. 2015. arXiv:1501.00918.

"You can't put a limit on anything. The more you dream, the further you'll get."

Michael F. Phelps

Abstract

Current searches for gravitational waves from compact binaries neglect the higher order modes (HOM) content of the emitted radiation. In this thesis, the consequences of this neglection is evaluated in terms of events loss and parameter bias in the context of several versions of the LIGO detectors. In order to do so, hybrid post-Newtonian/Numerical Relativity waveforms are used as target signals. An algorithm for the construction of such hybrid waveforms is presented along with an analysis of the error content and sources of both post-Newtonian and numerical results. It is found that post-Newtonian waveforms are mainly affected by truncation errors due to unknown PN corrections while numerical error is dominated by the value of the radius at which the wave is extracted. Regarding the effect of higher order modes, it is shown their neglection can cause event losses in a wide range: from negligible for low mass ratio systems to 25% for high mass and mass ratio for the shortcoming version of Advanced LIGO. Parameter estimation is likely to be affected at high mass and mass ratio due to the large higher modes content of the radiation from such systems.

Resumen (en castellano)

Durante las últimas décadas, las colaboraciones científicas LIGO, Virgo y GEO600 entre otras, han dirigido sus esfuerzos hacia la primera detección de las ondas gravitacionales predecidas por la relatividad general de Einstein sin que, de momento, ninguna observación se haya producido . Durante este año y los siguientes, una nueva generación de detectores diez veces más sensibles que los anteriores explorará nuevamente el cosmos en busca de señales de ondas gravitacionales, lo que hace a la comunidad científica confiar en que estamos próximos a detectar dicho fenómeno por primera vez.

De las posibles fuentes de ondas gravitacionales, unas de las más prometedoras son los sistemas compactos binarios (CBC), formados por parejas de agujeros negros y/o estrellas de neutrones. El proceso de detección de dicha radiación se basa en la técnica del filtro adaptado (*matched filter* en inglés) , la cual exige un modelaje preciso de la señal que se espera detectar. Sin embargo, los modelos actuales empleados como filtro de dichas señales ignoran su contenido en armónicos superiores, considerando sólo su armónico dominante. En un símil musical, ésto es equivalente a modelar una orquesta considerando sólo, por ejemplo, los instrumentos de viento. Una CBC se divide en las etapas de inspiral, merger y ringdown. La radiación emitida durante la primera etapa, se puede calcular mediante técnicas analíticas aproximadas, en el marco de la teoría post-Newtoniana. Sin embargo, los fuertes campos gravitatorios y altas velocidades presentes durante la etapa de merger (en la que ambos objetos colisionan) hacen que sea necesario resolver las ecuaciones de Einstein completas, lo que sólo es posible en el marco de la relatividad numérica con la ayuda de superordenadores.

Esta tesis se centra en el estudio de las consecuencias de la no consideración de los armónicos superiores en búsquedas actuales en términos de pérdida de eventos observados y errores en la medición de los parámetros de la correspondiente fuente. Para ello, primero se procederá a la construcción de señales de ondas gravitacionales de sistemas binarios incluyendo armónicos superiores. Ésto se realizará mediante la construcción de formas de onda híbridas, resultado de combinar modelos analíticos y numéricos, incluyendo en el proceso los armónicos superiores. Este proceso nos permitirá asimismo estudiar la precisión de la teoría post-Newtoniana y de las simulaciones numéricas a la hora de calcular dichos armónicos superiores y las correspondientes fuentes de error. Se obtiene que los cálculos post-Newtonianos están dominados por errores debidos a truncamiento mientras que el error dominante en las simulaciones numéricas es el debido a la finitud de la distancia a la fuente a la que la señal es extraída.

En un segundo paso, usaremos las señales construídas como modelos de la señal gravitatoria real de sistemas binarios con espín y comprobaremos la eficiencia de los modelos actuales a la hora de detectar dichas señales y estimar los parámetros del sistema. Los resultados indican que en el marco del diseño final de *Advanced LIGO*, se esperan pérdidas de un 10% de eventos para sistemas con cociente de masas $q \geq 6$, no llegándose nunca a un 20%, y los errores en la estimación de parámetros son dominantes para sistemas de masa total $M > 170 M_\odot$ para un signal-to-noise ratio de ~ 8. Sin embargo, en el caso de *early Advanced LIGO*, que entrará en funcionamiento este año, se esperan pérdidas de hasta un 26% para sistemas de alto cociente de masas y alta masa y los errores en la estimación de parámetros son dominantes para sistemas de masa total $M > 80 M_\odot$.

UNIVERSITAT DE LES ILLES BALEARS

Summary (in English)

During the last decades, a worldwide effort leaded by the LIGO, Virgo and GEO600 have pursued without success the first direct detection of the gravitational waves (GW) predicted by Einstein's general relativity (GR). During this year and the next ones, a new generation of GW detectors up to ten times more sensitive than the previous ones will explore the cosmos searching for GW signals. This makes the scientific community to be confident that we are on the verge of the first direct observation of GW.

Among the possible GW sources, one of the most promising ones are the compact binary coalescences (CBC). These consist of couples of inspiraling black holes and/or neutron stars which eventually merge. The detection process of these systems is based on the matched filter technique. This requires to have at our disposal precise models (or templates) of the signals we expect to detect, which are used as filters of the incoming signal. However, the templates used in current searches neglect the higher order mode content of the signal, considering only the contribution from its dominant harmonic. A CBC can be considered to have three stages: inspiral, merger and ringdown. The GW radiation emitted during the first stage can be analytically modeled in the framework of the post-Newtonian (PN) approximation. However, the strong gravitational fields and high velocities present during the late inspiral and merger makes necessary to solve the full Einstein equations. This is only possible in the framework of numerical relativity, with the help of supercomputers.

This thesis is focused on the study of the consequences of the neglection of higher order modes in current searches in terms of loss of detections and errors in the measurement of the parameters of the corresponding source. To this end, we will first build GW signals including higher order modes, that we will eventually use as our model of the real signal. This will be addressed by constructing hybrid waveforms, combination of the PN and NR result, including in this process the higher harmonics of the signal. This process will motivate a full study of the accuracy of the PN and NR higher order modes and the corresponding sources of error. Results indicate that the dominant error source in PN those due to the truncation of the PN series while NR errors are dominated by those due to the finitude of the radius at which the signal is extracted by NR codes.

In a second step, we will use our hybrid waveforms as model of the real signal emitted by equal spin CBC's and check the ability of current templates for detecting these signals.

Results indicate that for the case of the future *Advanced LIGO* detector, losses of more than 10% of events will happen due to neglection of higher order modes for systems with mass ratio $q \geq 6$ and total mass $M > 100 M_\odot$ and that parameter estimation is likely to be affected by systematic biases due to neglection of higher order modes for systems with total mass $M > 170 M_\odot$ for a signal-to-noise ratio of ~ 8. However, the situation is worse for the upcoming *early Advanced LIGO*, for which losses of 10% happen for $q \geq 4$, reaching values of 26% for the worst cases. Also, systematic parameter biases will affect parameter estimation for systems of total mass $M > 80 M_\odot$.

Acknowledgements

I thank my supervisors Prof. Alicia M. Sintes and Prof. Sascha Husa for introducing me to research and for the unvaluable advice given during these almost three years.

I want to express my most sincere gratitude to Dr. Alejandro Bohé for the infinite amount of hours and patience dedicated to help me in all the aspects of my thesis, for all the hours working together, for your advice and for all the football games I have enjoyed with you during your two years in Palma. This thesis would not have been possible without your help.

I also want to thank Prof. Alan J. Weinstein and Prof. Parameswaran Ajith for inviting me to visit Caltech. I want to thank them and also Profs. Bangalore Sathyaprakash and Stephen Fairhurst (Cardiff University) and Dr. Badri Krishnan for their hospitality and attention when I visited their respective research groups. I also thank Alex Nielsen, Andy Lundgren and Tom Dent for the help given and discussions shared, from which I learnt so many useful lessons.

I want to thank all my friends. I want to give a particular mention to Marcos, David and Rocío for always caring of me, my life and the status of my research, both when being together or via infinite Skype and phone calls. Your support during these three years has been capital for me and part of this thesis belongs to you. I want to thank my office and group mates Gemma, Dani, Alex, and specially Xisco, for all the coffees, football and science discussions, chats and beers (this reminds me to thank Morate) I have had the pleasure to share with. Crec que avui finalment podrem fer un cafetó al nostre banc de ses celebracions.

I would not be writing this lines today if it was not for Miguel. Thanks for your friendship, for your understanding and for your patience. Thanks for having always been there to support me in the worst moments and and for always finding the word that would make me not to give up.

I want to say thanks Seb, Miriam, Vaish, Colin, Avi, Germán, Karo, Marina, Vitor, Lars, Collin, Kate and all the friends I have made during the stays at Cardiff and AEI Hannover, who really managed to make me feel like at home. I was lucky to share office with my friend Tito dal Canton at AEI Hannover, who everyday I learnt so many things from. Grazie Mile!.

I want to specially thank Steve Privitera, for all the support and advices given during these years, both about science and life.

Finally, I want to thank my brother and sister and very especially my parents for all the love and unconditional support I have always enjoyed from you.

Contents

List of Figures

List of Tables

Abbreviations

BBH	Binary Black Hole
BH	Black Hole
BNS	Binary Neutron Star
CBC	Compact Binary Coalescence
CMB	Cosmic Microwave Background
EMRI	Extreme Mass Ratio Inspiral
EOB	Effective One Body
FAR	False Alarm Rate
FF	Fitting Factor
FIM	Fischer Information Matrix
GR	General Relativity
GRB	Gamma Ray Burst
GW	Gravitational Wave
HOM	Higher Order Modes
HW	Hybrid Waveform
IMR	Inspiral Merger Ringdown
LGR	Linearized General Relativity
LIGO	Laser Interferometer Gravitational Wave Observatory
advLIGO	advanced LIGO
eaLIGO	early advanced LIGO
iLIGO	initial LIGO
LSC	LIGO Scientific Collaboration
LISA	Large Interferometer Space Antenna
eLISA	european Large Interferometer Space Antenna
MCMC	Multi Chain Monte Carlo

NR	**N**umerical **R**elativity
NS	**N**eutron **S**tar
PE	**P**arameter **E**stimation
PN	**p**ost-**N**ewtonian Approximation
PTA	**P**ulsar **T**iming **A**rray
PDF	**P**robability **D**ensity **F**unction
PSD	**P**ower **S**pectral **D**ensity
ROM	**R**educed **O**rder **M**odel
SMBBH	**S**uper **M**assive **B**inary **B**lack **H**ole
SNR	**S**ignal-to-**N**oise **R**atio
SPA	**S**tationary **P**hase **A**pproximation
SO	**S**pin-**O**rbit
SS	**S**pin-**S**pin
SVD	**S**ingular **V**alue **D**ecomposition
TT	**T**ransverse **T**raceless

Preface

In the early 20th century, Albert Einstein published his theory of General Relativity (GR), joining the concepts of space and time in an unique entity, the space-time in which matter is hosted. Via the celebrated equation

$$G_{\mu\nu} = 8\pi T_{\mu\nu}$$

GR states that the curvature of space-time determines matter's motion as well as matter determines the curvature of the space-time. Up to now, GR has been extremely successful at describing the behavior of gravity: from the precession of the perihelion of Mercury to the bending of light rays by strong gravitational sources, its predictions have been tested with great accuracy. Among those predictions, there is the one that perturbations of the space-time propagate as waves, the so called gravitational waves (GW). The effect of such waves is to vary the proper distance between particles as the wave passes through, perpendicularly to its direction. However, the amplitude of gravitational waves is so tiny that only those produced in extremely violent events would have a chance for being directly detected. In fact, Einstein himself predicted that gravitational waves would never be directly detected.

In 1974, Hulse and Taylor provided the first indirect evidence of the existence of gravitational waves via measuring the effect of its emission on the period of the binary neutron star PSR B1913+16. However, direct detection remains being a challenge. During the last decade, a worldwide effort lead by the LIGO, Virgo and GEO600 collaborations has pursued the first direct detection of gravitational waves with not yet positive results. Their work, however, has served to place limits on the existence of potential sources and has provided unvaluable knowledge and technology development that makes the scientific community believe that the first detection will be achieved during the next few years. Starting this year, the next generation of gravitational wave detectors composed by Advanced LIGO, Advanced Virgo and KAGRA will come online and eventually reach sensitivities ~ 10 times higher than any of its predecessors, multiplying by ~ 1000 the

corresponding accessible volume. This generates high expectations for a first direct observation of gravitational waves and the opening of a new window to the study of the Universe.

Among the events whose GW emission we hope to detect, the coalescence of two compact objects (CBC) is one of the strongest candidates. These consist of combinations of Neutron Stars (NS) and Black Holes (BH) orbiting around each other as they lose energy in the form of gravitational waves and eventually merge, giving birth to a perturbed Kerr Black Hole. The first stages of this process can be modeled analytically by means of the post-Newtonian (PN) approximation. However, the full Einstein's equations need to be solved for describing the latter ones and eventual merger. Given their high nonlinearity, the equations need to be solved numerically in supercomputing clusters. This is addressed in the context of Numerical Relativity (NR).

Searches for GW from CBC's require having precise models of the signals we aim to detect, otherwise the detection process will degrade and the parameters of the sources can be misidentified. However, up to now, searches have used models that do only consider the dominant part of the gravitational radiation, neglecting the contribution of the so called higher order modes. In this thesis we will deal with the construction of signal models that consider this contribution contribution and evaluate the impact of its current neglection.

Structure of this thesis

The first three Chapters constitute a review of all the material used in the later ones. In particular, Chapter 1 provides an introduction to general relativity and gravitational waves, focusing finally in compact binaries. Chapter 2 is meant to be an overview of most of the formalisms used for computing gravitational wave signals. It will make special emphasis on the role of higher order modes and serve as a catalogue from where current post-Newtonian formulas can be found in a single document. Last, Chapter 3 is an introduction to GW data analysis. I have tried to provide a very direct exposition of the different formulas and methods used for afterwards focusing on their intuitive interpretation, which I think is the key for taking advantage of them. Only the very last part of this chapter contains original results, when sine-Gaussian glitches are discussed.These were obtained in collaboration with the LIGO group at the Albert Einstein Institute for Gravitational Physics, AEI Hannover. As a summary, in these three chapters I have tried to include all I would have liked to find when I was a first year graduate student. They are directed to them.

The remaining chapters constitute original results obtained as a fruit of my research in collaboration with the LIGO groups in UIB, the University of Cardiff. Chapters 4 and 5 are the core of [1], developed in collaboration with Dr. Alejandro Bohe (UIB & AEI Golm), Profs. Sascha Husa and Alicia M. Sintes (UIB) and Prof. Mark Hannam and Dr. Michael Puerrer (U. Cardiff) who kindly provided us with the BAM waveforms employed. These results did also partially contributed to [2], leaded by Mr. Vijay Varma (ICTS Bangalore & Caltech) and Prof. Parameswaran Ajith (ICTS Bangalore). Finally, Chapter 6 constitutes the generalization to aligned spin searches and several detector noise curves of the results in [2]. These two clearly distinguishable studies contain, in Chapters 4 and 6 respectively, their own specific introduction, description of previous studies, goals and methodology that completes and details the global basic notions provided along the introductory chapters. Finally, Chapter 7 provides a summary of final conclusions and possible ways in which the presented work could be extended.

Chapter 1

Introduction to Gravitational Waves

1.1 Brief overview of General Relativity

In the framework of general relativity [3], the space-time consists of a 4-dimensional manifold equipped with a Lorentzian metric g [1] which determines its geometry. In the absence of any gravitational field, the metric g reduces to the Minkowski flat metric, which defines the so called flat space-time. η [2]. In curved spacetime, a curve with tangent vector X is a geodesic if $\nabla_X X = 0$, where ∇ is the covariant derivative given by the Levi-Civita connection. This means that X is parallely transported along a curve with tangent vector X, which is the statement that there is no acceleration along the curve. A vector K is said to be a Killing vector if it satisfies $\mathcal{L}_K g = 0$, $\mathcal{L}$ denoting the Lie derivative. In other words, this means that the metric g is constant along curves with tangent vector K. If there exists a smooth, non vanishing vector field T that satisfies $T_\mu T^\mu < 0$ then we can defined future (past) directed curves as the ones defined by a tangent vector X such that $X^\mu T_\mu < 0 (> 0)$, and time-like (space-like) or null if $X^\mu X_\mu < 0 (> 0)$ or 0. In GR, physical trajectories follow future-directed causal curves, i.e., time-like if it corresponds to massive particles and null in the case of massless ones. Furthermore, free particles follow future-directed causal geodesics.

---

[1]Signature {-,+,+,+}
[2]$\eta = diag\{-1, +1, +1, +1\}$
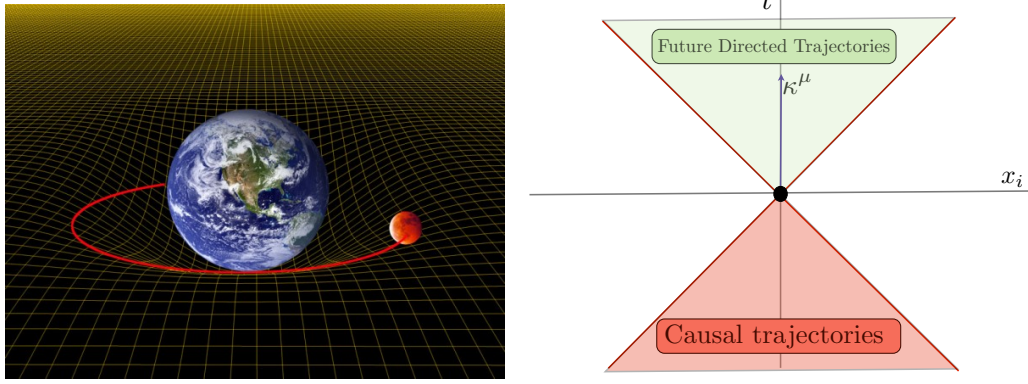
FIGURE 1.1: Left: Representation of Moon's geodesic motion in the grav-
itational field of the Earth due to the curvature of the spacetime (Credit:
*scienceblogs.com/startswithabang/2013/01/09/a-though-experiment-for- the-relativity
skeptics/*. Rigth: 2D summary of trajectories in GR represented in flat spacetime:
the coloured cones represent the set of causal trajectories starting at the origin while
the upper green one represents the future directed (physical) ones.

The Einstein equation, which gives the relation between space-time curvature and matter
motion is given, in natural units [3] by

$$G = 8\pi T, \tag{1.1}$$

where matter is described by means of the T stress-energy tensor and the curvature of
space-time is encoded in the Einstein's tensor G, with components given by

$$G_{\mu\nu} = R_{\mu\nu} - \frac{1}{2} g_{\mu\nu} R. \tag{1.2}$$

Here R and $R_{\mu\nu}$ are the Ricci scalar and the Ricci tensor, respectively defined as

$$R = g^{\mu\nu} R_{\mu\nu} \tag{1.3}$$

$$R_{\mu\nu} = R^{\sigma}_{\mu\sigma\nu}, \tag{1.4}$$

where $R_{\mu\nu\rho\sigma}$ is known as the Riemann curvature tensor. It can be computed as

$$R^{\mu}_{\nu\rho\sigma} = \partial_\rho \Gamma^{\mu}_{\nu\sigma} - \partial_\sigma \Gamma^{\mu}_{\nu\rho} + \Gamma^{\tau}_{\nu\sigma} \Gamma^{\mu}_{\tau\rho} - \Gamma^{\tau}_{\nu\rho} \Gamma^{\mu}_{\tau\sigma}, \tag{1.5}$$

where $\Gamma^{\mu}_{\nu\sigma}$ are the Christoffel symbols of the metric g defined by

$$\Gamma^{\mu}_{\nu\rho} = \frac{1}{2} g^{\mu\sigma} \left(\partial_\nu g_{\sigma\rho} + \partial_\rho g_{\nu\sigma} - \partial_\sigma g_{\nu\rho} \right). \tag{1.6}$$

---

[3]Newton's constant $G = 1$ and speed of light $c = 1$.

1.2 Linearized theory of General Relativity

The Einstein equations consists of a system of coupled non-linear partial differential equations, for which very few exact analytical solutions are known. As an example, the Friedmann-Robertson-Lemaitre-Walker (FRLW) solution, describes an homogenous, isotropic spacetime. Closer to our interests, the Schwarzschild solution describes an spherically symmetric stationary space-time, while the Kerr one describes an axisymmetric one. Furthermore, they describe spacetimes respectively hosting an static and a rotating blach hole.

Despite this lack of exact solutions, for many astrophysically relevant cases the gravitational field is actually weak, which allows to express the metric g as a perturbation to the flat metric η. This gives raise to a linearized theory of general relativity (LGR), in which the equations we have to face are linear and can be explicitly solved in many cases. Gravitational waves appear in the context of LGR and we will thus see how they are obtained.

1.2.1 The linear Einstein's equation

The assumption that the gravitational field is weak implies that for some coordinate system, that we will call *almost inertial* coordinate system, the metric tensor g can be expressed as a small perturbation to the Minkowski metric η as

$$g_{\mu\nu} = \eta_{\mu\nu} + h_{\mu\nu} \tag{1.7}$$

$$|h_{\mu\nu}| << 1. \tag{1.8}$$

The inverse g^{-1} of the metric tensor g has components

$$(g^{-1})^{\mu\nu} = g^{\mu\rho}g^{\nu\sigma}g_{\rho\sigma} = g^{\mu\nu}. \tag{1.9}$$

Then, to first order in h we can express

$$g^{\mu\nu} = \eta^{\mu\nu} - h^{\mu\nu}, \tag{1.10}$$

where

$$h^{\mu\nu} = \eta^{\mu\rho}\eta^{\nu\sigma}h_{\nu\sigma}. \tag{1.11}$$

This means that although index raising and lowering is performed by means of the metric g, in the following derivation we shall do it using the Minkowski metric η. Next, the

Christoffel symbols take the form

$$\Gamma^{\mu}_{\nu\rho} = \frac{1}{2}\eta^{\mu\sigma}\left(h_{\sigma\rho,\nu} + h_{\nu\sigma,\rho} - h_{\nu\rho,\sigma}\right),$$ (1.12)

where $h_{\mu\nu,\sigma} \equiv \partial_\sigma h_{\mu\nu}$. As we only want linear terms in h, we can drop all the $\Gamma\Gamma$ terms in (1.5), so that the Riemann tensor takes the form

$$R_{\mu\nu\rho\sigma} = \eta_{\mu\tau}\left(\Gamma^{\tau}_{\nu\sigma,\rho} - \Gamma^{\tau}_{\nu\rho,\sigma}\right) = \\ \frac{1}{2}\left(h_{\mu\sigma,\nu\rho} + h_{\nu\rho,\mu\sigma} - h_{\nu\sigma,\mu\rho} - h_{\mu\rho,\nu\sigma}\right).$$ (1.13)

The Ricci tensor becomes

$$R_{\mu\nu} = \partial^\rho \partial_{(\mu} h_{\nu)\rho} - \frac{1}{2}\partial^\rho \partial_\rho h_{\mu\nu} - \frac{1}{2}\partial_\mu \partial_\nu h.$$ (1.14)

where $A_{(\mu,\nu)} = \frac{1}{2}(A_{\mu\nu} + A_{\nu\mu})$ is the symmetrization of the tensor A, being $A_{[\mu,\nu]} = \frac{1}{2}(A_{\mu\nu} - A_{\nu\mu})$ the corresponding antisymmetrization and $h \equiv h^\mu_\mu = g^{\mu\sigma}h_{\sigma\mu} = \eta^{\mu\sigma}h_{\sigma\mu}$.

We can now proceed to write down the linearized version of the Einstein's tensor as

$$G_{\mu\nu} = \partial^\rho \partial_{(\mu} h_{\nu)\rho} - \frac{1}{2}\partial^\rho \partial_\rho h_{\mu\nu} - \frac{1}{2}\partial_\mu \partial_\nu h - \frac{1}{2}\eta_{\mu\nu}\left(\partial^\rho \partial^\sigma h_{\rho\sigma} - \partial^\rho \partial_\rho h\right).$$ (1.15)

As in the full theory, the Einstein tensor is related to the matter content by (1.1). Before writing the corresponding linear version of Einstein's equation, it is convenient to define

$$\bar{h}_{\mu\nu} = h_{\mu\nu} - \frac{1}{2}\eta_{\mu\nu}h,$$ (1.16)

with inverse and trace

$$h_{\mu\nu} = \bar{h}_{\mu\nu} - \frac{1}{2}\bar{h}\eta_{\mu\nu} \\ \bar{h} = \bar{h}^\mu_\mu = -h.$$ (1.17)

The linear version of Einstein's equation can now be expressed, after a little bit of algebra as

$$G_{\mu\nu} = -\frac{1}{2}\partial^\rho \partial_\rho \bar{h}_{\mu\nu} + \partial^\rho \partial_{(\mu} \bar{h}_{\nu)\rho} - \frac{1}{2}\eta_{\mu\nu}\partial^\rho \partial^\sigma \bar{h}_{\rho\sigma} = 8\pi T_{\mu\nu}.$$ (1.18)

The gauge symmetry of linearized general relativity & the wave equation

A fundamental principle of GR is the statement that physics is invariant under general changes of coordinates given by general diffeomorphisms $x^\mu \rightarrow \phi(x^\mu)$. In other words, the laws of physics are the same in any reference frame. This means that diffeomorphisms are the gauge symmetry of GR or more mathematically, that in a manifold M with

metric g and energy-momentum tensor T, physical laws take the same form as in the same manifold M with metric $\phi_*(g)$ and energy momentum tensor $\phi_*(T)$. Here $\phi_*(A)$ denotes the pull-back of A by ϕ. However, in linearized theory, we do not consider general metrics but only those that are small perturbations of the Minkowskian metric η . We then have to restrict to diffeomorphisms such that $\phi_*(g)$ can be expressed as (1.8).

Diffeomorphisms can be expressed as a function of a generator vector X and a parameter t. For $t \ll 1$, the pull-back of a tensor T under a diffeomorphism ϕ can be expressed as an expansion around the original tensor T as

$$(\phi_{-t})(T) = T + t\mathcal{L}_X T + \mathcal{O}(t^2), \tag{1.19}$$

so for the metric g we have

$$(\phi_{-t})(g) = g + t\mathcal{L}_X g + ... = \eta + h + \mathcal{L}_\xi \eta + ... \tag{1.20}$$

where $\xi^\mu = tX^\mu \ll 1$, so that we can neglect terms involving ξh. We deduce then that the metrics h and $h + \mathcal{L}_\xi h$ describe physically equivalent metric perturbations. Hence, while GR has the gauge symmetry $g \to \phi_*(g)$, the linearized version has $h \to h + \mathcal{L}_\xi h$ for small ξ^μ. The Lie derivative of a 2-tensor can be expressed as $(\mathcal{L}_\xi \eta)_{\mu\nu} = \partial_\mu \xi_\nu + \partial_\nu \xi_\mu$. Putting all together, we can write the gauge symmetry of LGR as

$$h_{\mu\nu} \to h_{\mu\nu} + \partial_\mu \xi_\nu + \partial_\nu \xi_\mu. \tag{1.21}$$

Note that then, under a gauge transformation we get

$$\partial^\nu \bar{h}_{\mu\nu} \to \partial^\nu \bar{h}_{\mu\nu} + \partial^\nu \partial_\nu \xi_\mu, \tag{1.22}$$

so that we can choose ξ^μ such that $\partial^\nu \partial_\nu \xi_\mu = -\partial^\nu h_{\mu\nu}$, which imposes the gauge condition

$$\partial^\nu \bar{h}_{\mu\nu} = 0. \tag{1.23}$$

This gauge is known as the Lorentz, de Donder or harmonic gauge. In this gauge the Einstein's equation (1.18) becomes simply

$$\partial^\rho \partial_\rho \bar{h}_{\mu\nu} = -16\pi T_{\mu\nu}, \tag{1.24}$$

which is a wave equation for the components of $\bar{h}$ with a source described by the components of the energy-momentum T. The solution can be then obtained as long as appropriate conditions are given by means of the Green function.

1.2.2 Gravitational Waves

Fundamental Properties

Although we will be interested in gravitational waves generated by a source with energy-momentum tensor T, fundamental properties of gravitational waves can be deduced from the study of the vacuum solution. In such a case we have $T_{\mu\nu} = 0$ and (1.24) reduces to

$$\partial^\rho \partial_\rho \bar{h}_{\mu\nu} = 0, \tag{1.25}$$

whose solution can be expressed as a superposition of plane wave solutions as

$$\bar{h}_{\mu\nu} = \mathcal{R}(H_{\mu\nu} e^{i\kappa_\rho x^\rho}). \tag{1.26}$$

From now on we will drop the real part $\mathcal{R}$ symbol. With this solution (1.25) reduces to simply

$$\kappa_\rho \kappa^\rho = 0, \tag{1.27}$$

which implies that the wavevector κ^μ is a null vector and gives the first fundamental property of gravitational waves: they propagate at the speed of light. Substituting the trial solution (1.26) in the gauge equation (1.23) reveals

$$\kappa^\mu H_{\mu\nu} = 0, \tag{1.28}$$

which gives a second fundamental property: the perturbations of the metric $H_{\mu\nu}$ carried by gravitational waves are transverse to their direction of propagation given by κ^μ.

Degrees of freedom of a gravitational wave

In order to find out the number of independent components of $H_{\mu\nu}$ let us take advantage of the eq. (1.23). Note that this equation, although allowing for the election of a gauge does not fully determine ξ^μ. A transformation $h_{\mu\nu} \to h_{\mu\nu} + \partial_\mu \xi_\nu + \partial_\nu \xi_\mu$ will preserve the wave equation provided that

$$\partial_\nu \partial^\nu \xi_\mu = 0. \tag{1.29}$$

This means that there are further degrees of freedom we can take advantage of for further constraining the wave solution $H_{\mu\nu}$. Consider then

$$\xi_\mu = X_\mu e^{i\kappa_\rho x^\rho}. \tag{1.30}$$

This trivially satisfies (1.29) because κ is null. Using that under a diffeomorphism $\bar{h}$ transforms as

$$\bar{h}_{\mu\nu} \to \bar{h}_{\mu\nu} + \partial_\mu \xi_\nu + \partial_\nu \xi_\mu - \eta_{\mu\nu}\partial^\rho \xi_\rho, \tag{1.31}$$

we can deduce that we have the residual gauge freedom

$$H_{\mu\nu} \to H_{\mu\nu} + i(\kappa_\mu X_\nu + \kappa_\nu X_\nu - \eta_{\mu\nu}\kappa^\rho X_\rho), \tag{1.32}$$

that we can now exploit to impose conditions on the 4 components of X. These can be chosen such that the resulting H satisfies

$$H_{0\mu} = 0 \tag{1.33}$$

which imposes the longitudinal gauge condition and determines 3 components of X, and

$$H^\mu_\mu = 0, \tag{1.34}$$

which determines the 4th component and imposes the so called trace-free condition. From (1.17) we see that in this gauge $h_{\mu\nu} = \bar{h}_{\mu\nu}$.

Altogether, we can count the total number of degrees of freedom we are left with. First, the fact that $H_{\mu\nu}$ is symmetric gives 10 initial degrees of freedom. The wave vector equation (1.27) imposes 1 constraint and the transversality condition (1.28) imposes 3 more. Furhter, the 4 degrees of freedom used for imposing the longitudinal and trace-free conditions (1.33) and (1.34) reduce the total degrees of freedom to $10 - 8 = 2$. These correspond to the two gravitational wave polarizations H_+ and $H_\times$. For instance, taking use of all of our constraints, a gravitational wave traveling along the z-direction with propagation vector $\kappa^\mu = (1, 0, 0, 1)$ will be written as

$$H_{\mu\nu} = \begin{pmatrix} 0 & 0 & 0 & 0 \\ 0 & H_+ & H_\times & 0 \\ 0 & H_\times & -H_+ & 0 \\ 0 & 0 & 0 & 0 \end{pmatrix} \tag{1.35}$$

Effect of a gravitational wave

Now we get to the question of how one would measure the effect of a gravitational wave with associated perturbation h of the flat metric η. A natural way of determining this for a given observer at a point p would be to locally distribute a set of test particles and observe any displacements S between the particles and p. These are governed by the

geodesic deviation equation

$$u^a \nabla_b (u^c \nabla_c S_\alpha) = R_{abcd} u^b u^c S^d, \tag{1.36}$$

where S is the geodesic displacement vector and u is the four-velocity of the observer. However, as this deviations are measured in some reference frame ,i.e., in some basis, we need to discriminate whether these correspond to a change of basis or to actual displacements of the particles.

In order to do so, let us consider an observer following some generic worldline with four-velocity u. Now, at some point p in his worldline, consider a local inertial frame whose local spatial coordinates are X, Y, Z. In this frame, the observer is at rest. Now the observer places some measuring rulers along the X, Y, Z directions and some test particles along the same axes at an initial distance of say 1 unit. This defines an orthonormal basis $\{e_\alpha\}$ on the tangent space at p where $e_0^a = u^a$ and e_i^a are space like vectors which satisfy

$$u_a e_i^a = 0 \tag{1.37}$$

$$g_{ab} e_i^a e_j^b = \delta_{ij}, \tag{1.38}$$

we can extend this basis to the entire worldline of the observer by parallely transporting the $\{e_\alpha\}$ basis along the worldline with tangent vector u. Note that the time-like vector e_0 remains trivially constant while the remaining ones will satisfy $u^b \nabla_b e_i^a = 0$, which uniquely determines the basis. Also, since parallel transport preserves inner products, we know that the basis will remain orthonormal. We can then be sure that any changes in the geodesic deviation vector S will be due to real increases in the distance from the observer to a particle. Substituting values one can express (1.36) as

$$\frac{d^2 S_\alpha}{d\tau^2} = R_{abcd} e_\alpha^a u^b u^c e_\beta^d S^\beta. \tag{1.39}$$

Here τ is the proper time of the observer and note that $S_\alpha = e_\alpha^a S_a$ corresponds to one of the components of S_a in our paralelly transported frame. We can further consider our observer to be at rest, i.e., $u^\mu = (1, 0, 0, 0)$ so that

$$\frac{d^2 S_\alpha}{d\tau^2} \simeq R_{\mu 00 \nu} e_\alpha^\mu e_\beta^\mu S^\beta. \tag{1.40}$$

and using (1.13) we get

$$\frac{d^2 S_\alpha}{d\tau^2} \simeq \frac{1}{2} \frac{\partial^2 h_{\mu\nu}}{\partial t^2} e_\alpha^\mu e_\beta^\mu S^\beta. \tag{1.41}$$

Choosing the spatial-like vectors of our orthonormal basis aligned with the x,y,z axis at p then we simply get

$$\frac{d^2 S_0}{d\tau^2} = \frac{d^2 S_3}{d\tau^2} = 0. \tag{1.42}$$

which implies that the observer will not see any acceleration of the test particles in the z directions along which the GW propagates. If the observer sets initial conditions by which the derivative of S_3 is zero initially then it will be constant for all time. The same can be applied to both S_0 and its derivative so that $S_0 = 0$ always. However for the remaining two coordinates this does not hold. Consider that initially $x^\mu = (\tau, 0, 0, 0)^4$. Then for the $+$ polarized component of the GW we get

$$\frac{d^2 S_1}{d\tau^2} = -\frac{1}{2}\omega^2 |H_+| \cos(\omega\tau - \alpha) S_1 \tag{1.43}$$

$$\frac{d^2 S_2}{d\tau^2} = \frac{1}{2}\omega^2 |H_+| \cos(\omega\tau - \alpha) S_2, \tag{1.44}$$

$$\tag{1.45}$$

where $\alpha = \arg H_+$. Since H_+ is small we can solve perturbatively plugging a zero order solution $S_i = \bar{S}_i$ into the RHS of (1.45) and then solve for S_i in order to get

$$\frac{d^2 S_1}{d\tau^2} \simeq \left(1 + \frac{1}{2}\omega^2 |H_+| \cos(\omega\tau - \alpha)\right) \bar{S}_1 \tag{1.46}$$

$$\frac{d^2 S_2}{d\tau^2} \simeq \left(1 - \frac{1}{2}\omega^2 |H_+| \cos(\omega\tau - \alpha)\right) \bar{S}_2, \tag{1.47}$$

$$\tag{1.48}$$

the result being the same for $H_\times$ but rotated $\pi/4$. Thus the effect of a perturbation h to the flat metric η is to change the distance from the test particles to the observer simultaneously in the x and y directions: it enlarges one while stretching the other at the same time and viceversa as depicted in 1.2 for the two possible polarizations.

1.2.3 Gravitational Waves far from a source

The quadrupole formula

The previous discussion considered the case in which a perturbation of the metric η propagates in vacuum, i.e., we considered $T_{\mu\nu} = 0$. In a real case however, there will be a source described by a non-zero energy-momentum tensor T that will generate a gravitational field which far from the source will add a tiny perturbation to the Minkowski metric η. This means that now the equation we need to solve is the original wave

---

[4]This means $t = \tau$ along the worldline described by the observer

$$H_+ \text{ Polarization} \qquad \times \text{ Polarization}$$
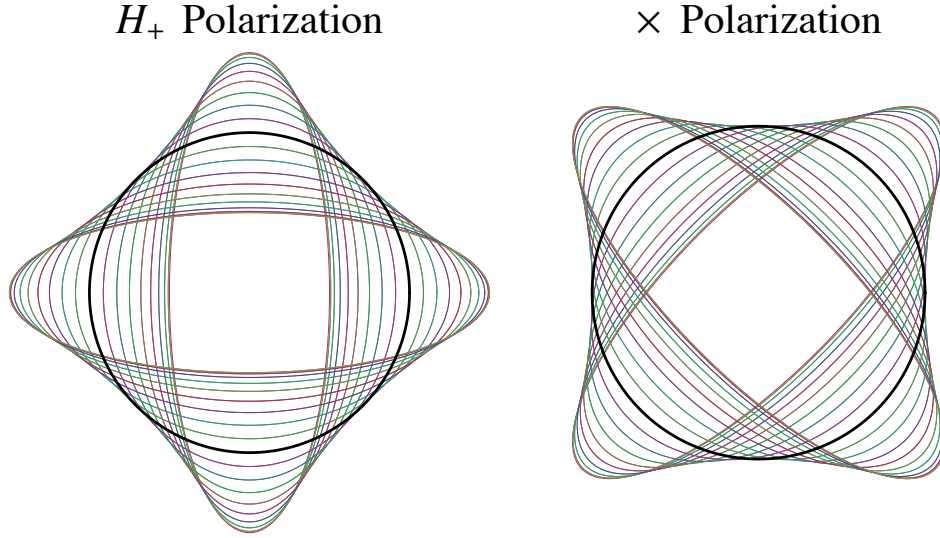
FIGURE 1.2: Effect of the two GW polarizations in a set of test particles set on a circle around a locally inertial observer.

equation

$$\partial^\rho \partial_\rho \bar{h}_{\mu\nu} = -16\pi T_{\mu\nu}, \tag{1.49}$$

which can be analytically solved using the retarded Green function

$$\bar{h}_{\mu\nu}(t,x) = 4 \int d^3x \frac{T_{\mu\nu}(t - |x - x'|, x')}{|x - x'|}, \tag{1.50}$$

$$\tag{1.51}$$

where at x far from the source, described by x', we have $|x| \gg |x'| \sim d$ [5] and we can expand in $r \equiv \sqrt{x - x'}$. Integrating by parts, neglecting surface terms in the integrals and taking into account the conservation of the energy momentum tensor, $\nabla^\mu T_{\mu\nu} = 0$, one gets to the equations for the metric $\bar{h}$

$$\bar{h}_{i,j}(t,x) \simeq \frac{2}{r} \ddot{I}_{i,j}(t - r) \tag{1.52}$$

$$\bar{h}_{00}(t,x) = \frac{4}{r} \int d^3x' T_{00}(t', x') \equiv \frac{4E}{r} \tag{1.53}$$

$$\bar{h}_{0i}(t,x) = \frac{4}{r} \int d^3x' T_{0i}(t', x') \equiv -\frac{4P_i}{r}, \tag{1.54}$$

where $\ddot{I}_{ij} = \int d^3x T_{00}(t,x) x^i x^j$ is the second moment of the energy density. We can choose coordinates such that $P_i = 0$ and then we shall write $E = M$, M being the rest mass (total mass in practice) of the system. Applying conservation of the energy-momentum tensor on the equation for h_{00} shows that the energy of the system E is constant. However, GW do carry energy out of the system. For seeing this, we need to go beyond the linear approximation. As obtaining in detail the formula for the radiated

[5]Note that r is the source-detector distance and d gives the size of the source.

energy would take us some more pages of algebra, we here will just state that the average radiated power is given by the so called quadrupole formula (for details, see for instance [4]).

$$< P >= \frac{1}{5} < \dddot{Q}_{ij} \dddot{Q}_{ij} >, \tag{1.55}$$

where $Q_{ij} = I_{ij} - \frac{1}{3} I_{kk} \delta_{ij}$ is known as the quadrupole tensor. This formula does give us the clue for the kind of system we can expect to radiate GW. For example, for an spherically symmetric body, $Q_{ij} = 0$ and thus such a system will not radiate. Also, a body propagating at constant velocity in straight line will have $\ddot{I}_{ij} = 0$ and will also not radiate.

Last, note that the value of the GW perturbation depends on the location it is evaluated at not only via the distance r. This is, the radiation is not spherically symmetric. In for example, spherical coordinates (r, θ, ϕ) centered on the source, the dependance on (θ, ϕ) can be noted from the $x^i x^j$ term in $\ddot{I}_{ij} = \int d^3 x T_{00}(t, x) x^i x^j$. In the following chapters we will see how of the strain tensor h on the location and the intrinsic parameters of the source can be separated by decomposing h in a basis formed by the so called -2 spin-weighted spherical harmonics.

An example for a source: Compact Binary Systems

In this thesis we focus on the study the GW radiation emitted by the coalescence of compact binary objects. During the first stages of this process both objects inspiral each other describing quasi-circular orbits. Their separation is large enough that the velocity of the objects v is much lower than the speed of light c and the gravitational field that one body generates in the position of the other is low enough to allow for a first description in terms of Newtonian theory. For simplicity, consider that each body has a mass $m = M/2$, and that their separation is given by $d \gg 4M$. Making use of Newton's second law we obtain $Mv^2/d \sim M^2/v^2$ which gives $v \sim \sqrt{M/d}$. The typical magnitude of the quadrupole tensor Q is Md^2 so that $\dddot{Q} \sim Md^2/T^3 \sim (M/d)^{5/2}$ and $P \sim (M/d)^5$. This means that the more compact the radiating system is, the more power it will emit. Note that in GR, an astrophysical body must satisfy that its radius is not smaller than the Schwarzchild radius $2M$ and then (in the non-relativistic regime) $d > 4M$. Furthermore, common stars are such that $d \gg M$ and then the radiated power will be quite low. However, for very compact objects like neutron stars (NS) or black holes the magnitude of d will be comparable to that of M. Introducing the corresponding values in the formula for the amplitude of the GW we get

$$\bar{h}_{ij} \sim \frac{Md^2}{T^2 r} \sim \frac{M^2}{dr}. \tag{1.56}$$

More concretely, in the center-of-mass frame, the non-zero component of the energy momentum tensor T, T_{00} will be given by delta distributions corresponding to two bodies A and B with total mass M

$$x_A^i = \tfrac{M^3\eta}{rd^2}\Big(\cos(\omega_{orb}t), \sin(\omega_{orb}t), 0 \Big) \tag{1.57}$$

$$x_B^i = -\tfrac{m_1}{m_2}x_A^i = -qx_A^i, \tag{1.58}$$

where again $v^2 = M/d$ and $\omega_{orb} = \sqrt{M/d^3} = v/d$. Here we have introduced the assymmetric mass ratio $\eta = m_1 m_2/M^2$ and the mass ratio $q = m_1/m_2$, where m_1 and m_2 denote the individual masses of the compact objects. If we introduce the values in the formula for h (1.54) and choose our observer to be along the z-axis of the system we get

$$h_{i,j} = \frac{4M^3\eta}{rd^2} \begin{pmatrix} -\cos(2\omega_{orb}(t-d)) & \sin(2\omega_{orb}(t-d)) & 0 \\ -\sin(2\omega_{orb}(t-d)) & \cos(2\omega_{orb}(t-d)) & 0 \\ 0 & 0 & 0 \end{pmatrix} \tag{1.59}$$

Looking at (1.59) we can see that the strain h produced by a binary system in a point p at a distance r decays as $1/r$, is proportional to the total mass M and to the compactness of the system given by M/d, and that its frequency is twice the orbital one. The above calculation corresponds to the Newtonian limit of the problem, when $d \to \infty$. In order to obtain realistic estimates of the GW emission during the whole evolution of the system we need to take into account the energy loss via GW, which is responsible for the orbit to shrink. This is the starting point of the so called post-Newtonian (PN) expansion.

In order to get again a feeling of the magnitude of the perturbation that a GW will cause, consider a binary black hole for which the individual masses are $M = 10 M_\odot$ located at 100Mpc with a separation d close enough such that the coalescence will take place in 1 year. Plugging a value of $d = 20M$ gives an estimate of $h \sim 10^{-21}$ for a GW with a frequency of ~ 100Hz. This is the kind of systems that the GW observatory LIGO is more likely to observe.

Of course, these are not the only possible emitting systems. In general, very violent systems with varying quadrupole moment are likely to emit GW radiation detectable by future GW detectors. In particular, radiation from rotating neutron stars, supernovas or remnants from the Big Bang are among the sources whose GW emission will be searched for.

Experimental evidence for gravitational waves: The Hulse & Taylor pulsar.

In 1974, Hulse and Taylor [5, 6] measured the variation of the period of the binary system PSR B1913+16 and compared it to the one predicted by GR due to GW emission. As mentioned before, as the system radiates, the size of its orbit decreases and the period diminishes. One of the neutron stars of this system is what is called a pulsar: a very rapidly rotating NS that emits a beam of radio waves periodically in our direction. This period is extremely stable and can be measured to very high accuracy, which in turn allows for a very accurate measurement of the period of the binary. Concretely GR, predicts for this system a decrease of $10\mu s$ per year. This is measured nowadays with 0.2% accuracy, providing very strong indirect evidence for the existence of GW. Hulse and Taylor were awarded the Nobel prize in 1993. The discovery in 2004, [7] of the first double pulsar (PSR J0737−3039) has provided a new laboratory for the study of the strong gravity regime whose results have so far agreed with GR predictions [8, 9].
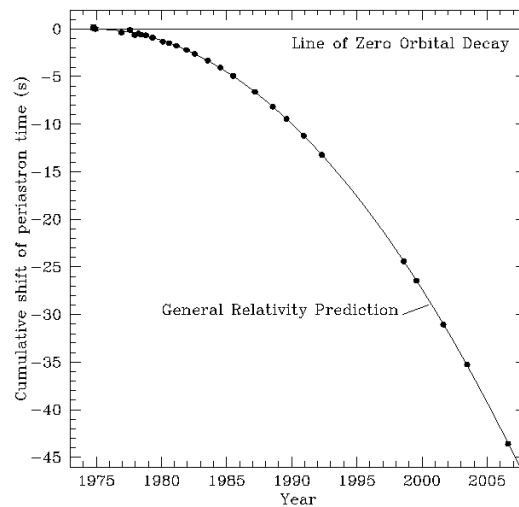
FIGURE 1.3: Results obtained by Hulse and Taylor & for the PSR B1913+16 BNS. Dots represent experimental data while the solid line represents the GR prediction due to GW emission. Credit: [10].

1.3 The quest for the direct observation of gravitational waves

1.3.1 Why gravitational waves?

All the information from the Universe that the human being has access to, comes either in the form of photons in a wide wave-length spectrum or massive particles such

as cosmic rays. These provide fundamental information about the physical processes that happened during the evolution of our Universe such as Galaxy and Star formation, supernovas, Nucleosynthesis or the Big Bang itself. However, there are two clear limitations on the information that these kind of messengers can provide us with.

First, there exist objects in the Universe that due to their nature are invisible in terms of photons or particles such as black holes and the dark matter. In particular, black holes are objects so dense that not even light can scape from their so called event-horizon. However, precisely due to their high density, they constitute an excellent candidate for GW emission, specially when two of them form a binary system. The proximities of a black hole is an excellent example of a region governed by a strong-gravity regime, in which GR can be tested in situations where it has not yet been and thus, where alternative theories of gravity have a chance to be discarded or given some plausibility. All current knowledge about the existence and properties of black holes are due to the effects they generate on their surroundings. As an example, due to the conservation of the angular momentum, gas falling to a black hole usually forms accretion disks that get hotter the closer it is to the black hole. The most inner regions of the disk have temperatures such large that vast emission of X-rays takes place. Also, astrophysical black holes evaporate via radiating the so called Hawking radiation [11]. However, the radiated power is so low that only that emitted during the very last stages would have a chance to be detected. Since the lifetime of a black hole is comparable to that of the Universe, only primordial black holes would be at that stage. Currently, there exist experiments searching for such a radiation. [12].

Secondly, when we look at the Universe we look at its past. The light we detect unveils how the Universe was in the moment it was emitted from the corresponding source and allows us to study its evolution. Naively, this would allow us to receive information from the beginning of the Universe itself. However, in the early stages of the Universe, its high density caused photons to be continuously emitted and re-absorbed, making impossible for them to freely travel. It was not until the Universe density decayed due to its expansion, and became transparent, that photons of a certain energy were able to freely move, during what is known as the last-scattering epoch. Such photons arrive to us nowadays forming what is known as the Cosmic Microwave Background (CMB) [see Fig.1.4]. This constitutes the oldest information from the Universe we currently have access to. It was discovered by Arno Penzias and Robert Wilson [13] in 1964. The CMB was a predicted consequence of the models of a non-stationary Universe which considered the concept of a Big Bang, in contrast with the steady-state Universe model defended by Fred Hoyle. On the other hand, the Universe has always been transparent to gravitational waves, which in principle would allow to obtain information from earlier stages of the Universe.
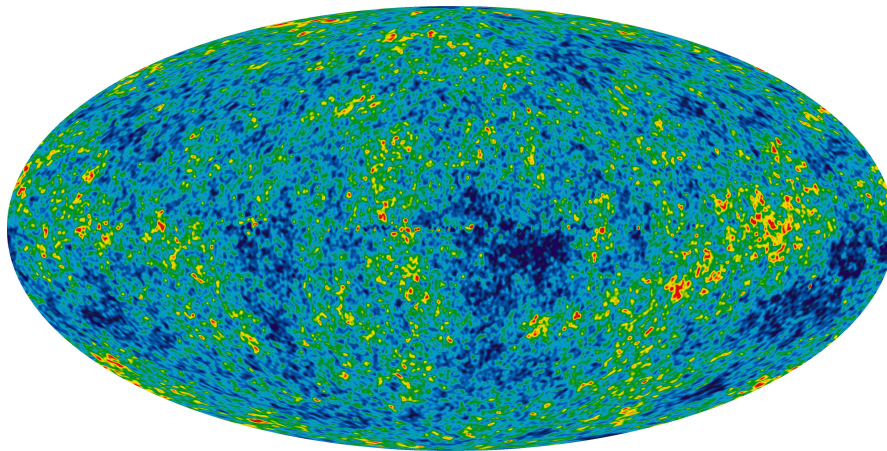
FIGURE 1.4: Temperature map of the Cosmic Microwave Background. The color code denotes the temperature of the CMB radiation as a function of the sky location. The average temperature is 2.725K with fluctuations of $\sim \mu K$.

1.3.2 Brief summary of gravitational wave detectors and sources.

Ground-based Interferometers

The scientific community has pursued during the last decades the first direct detection of GW, which would be the starting point of the GW astronomy. This quest has been led by the LIGO, Virgo, GEO600 and TAMA collaborations. The LIGO Scientific Collaboration (LSC) has operated three interferometric detectors: 2 co-located in Hanford (Washington, USA), with arm-lengths of 4 and 2 km respectively and a third one located in Livingston (Louisiana, USA), with an arm length of 4km. The Virgo collaboration is a joint french-italian project which has operated a 3km interferomenter located at Cascina (Italy). The GEO600 detector, located at Hannover (Germany), although not being comparable in terms of its highest sensitivity to LIGO or Virgo, serves as a test bank for the technology to be implemented in future GW detectors. It is also much more sensitive in the high frequency band ~ 1kHZ than LIGO and Virgo and it is the only operational GW detector until early Advanced LIGO enters its first science run, scheduled for Fall 2015. GEO600 would be sensitive nowadays to nearby supernovae. Finally, the 300m long TAMA-300 detector located in Tokyo (Japan), was for years the most sensitive detector in the world, before LIGO and Virgo entered their operational period in 2002 and 2006 respectively. The several science runs performed by these detectors are summarized in Fig.1.5. Although none of them has provided a detection of GW, the results obtained have allowed for setting upper limits on the number of astrophysical sources emitting GW [14–17] and also for the development of more sensitive detectors that will enter their operation period during the current year: Advanced LIGO [18, 19], Advanced Virgo [20, 21] and also, the japanese observatory KAGRA [22]. It is expected

that this new generation of detectors will increase their sensitivity by a factor of ~ 10, thus incrementing the sensitive volume by a factor of ~ 1000.
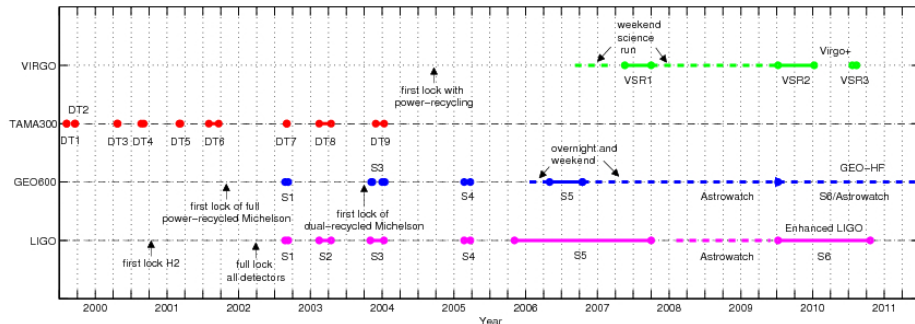
FIGURE 1.5: Summary of the science runs performed by the LIGO, Virgo, GEO600 and TAMA detectors. Credit [23].

Ground-based interferometers are most limited by the seismic noise and by newtonian gravity gradients at low frequencies and shot noise at high ones. The first can be mitigated by isolating the detector via improving the suspensions but the detectors cannot be shielded from gravitational field changes, which is exactly what we intend to measure. This has pushed the lower frequency cutoff of ground based detectors up to 40Hz for the case of initial LIGO (20Hz for the case of Virgo) and is expected to get down to 10Hz for the design version of Advanced LIGO. Terrestrial interferometers such as LIGO are sensitive to the $\sim 10 - 10^3$Hz frequency band, achieving Advanced LIGO $\sim 10^4$Hz. This is the region of the GW spectrum in which mid-mass compact binaries such as binary neutron stars, neutron star-black hole binaries and and low and intermediate mass binary black holes are expected to radiate. Also, rapidly spinning NS and triggered supernovae are expected to radiate in these frequency range together with some components of the so called cosmological stochastic GW background. We will focus on these sources later. Fig.1.6 provides a summary of the different sources and the frequency band they are expected to radiate in.

Space-based Interferometers

Supermassive black hole binaries (SMBBH), extreme mass ratio inspirals (EMRI) or young stellar-mass binaries are expected to radiate in the $\sim 10^{-5} - 1$Hz range. This is the domain of space-based detectors like the old LISA project and the current eLISA mission [24, 25]. These consist of laser interferometers whose arm length is of the order of 10^6km, making them sensitive to signals orders of magnitude weaker than current ground based detectors. The eLISA mission has been recently chosen as a L3 mission by the ESA and is aimed to be launched by 2034. Meanwhile, the upcoming LISA Pathfinder

mission, planned to be launched by the fall of 2015, will demonstrate the technology necessary for eLISA. The extremely high sensitivity of a detector like eLISA adds the extra-difficulty of confusion noise. While for ground based detectors, GW events are expected to be transient events in a terrestrial background noise, space-based detectors will be sensitive to a background GW produced by astrophysical sources among which specially loud ones should be individually identified. For instance, the original LISA mission was very likely to be affected by a background of signals coming from binary systems in our galaxy. The lower sensitivity of eLISA makes it not sensitive to such a background.
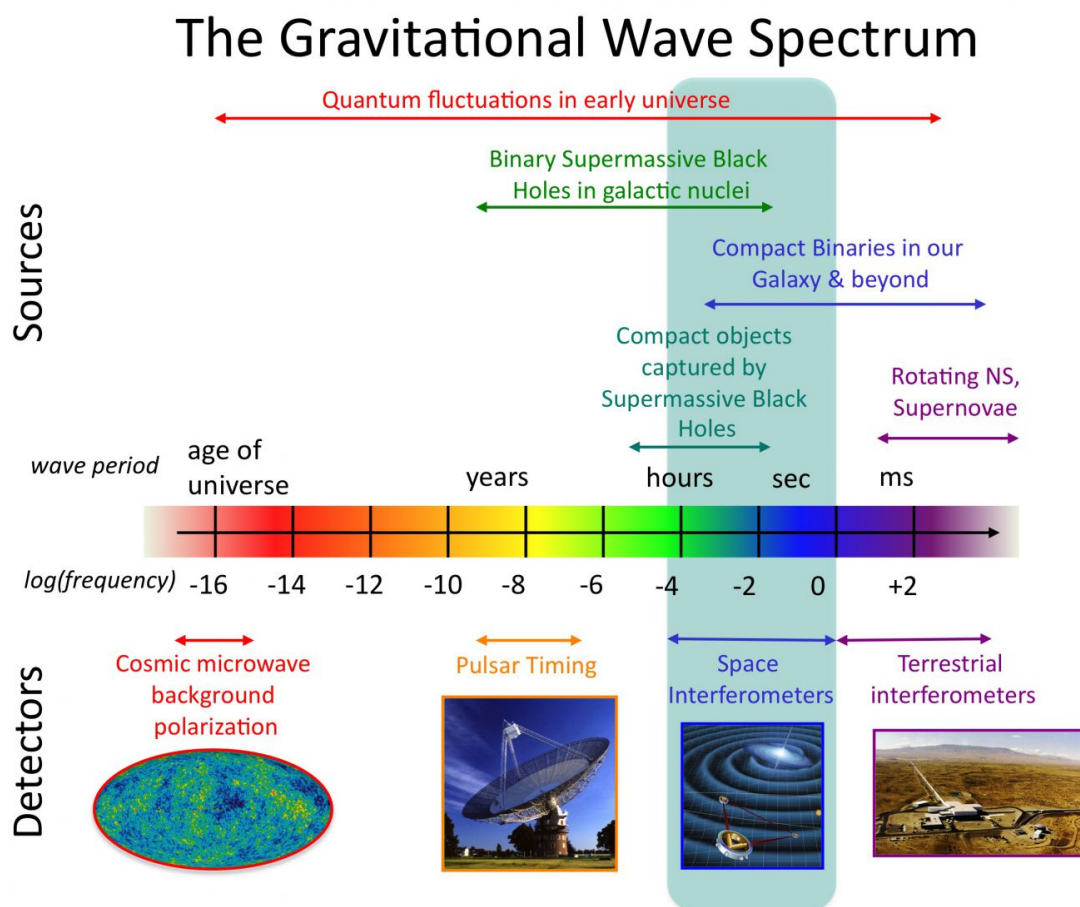
FIGURE 1.6: Summary of the GW spectrum and the detectors expected to be sensitive to it. Credit: NASA.

Pulsar Timing Arrays

Pulsar Timing Arrays (PTA) aim to detect the effect of GW in the $10^{-7} - 10^{-9}$Hz range. Detecting such a signals with interferometry techniques would require detectors larger

than the Solar System itself due to their enormous wave-length. Instead, PTA's measure the periodic variances in the arrival times of pulsar electromagnetic signals. The passage of a gravitational by the Earth distorts the space-time and thus our flow of time with respect to the one in the location of the pulsar. This makes the rate of arrival of signals to change from that expected when the effect of GW's is neglected. The main source PTA's are expected to observe is an astrophysical background of signals coming from SMBBH systems, among which some particularly loud signals might be isolated [26].

The extremely low frequency spectrum: BICEP-2 & Planck

Space based electromagnetic measurements like those performed by the satellite Planck or the BICEP-2 experiment have among their goals to detect the effect of extremely long wavelength GW waves, like those generated during the inflationary era [27, 28] (or cosmological GW background). The expected effect of such a GW is the presence of a particular polarization pattern in the CMB known as B-modes. On the early 2014, the science team involved in the BICEP-2 collaboration claimed to have observed the direct effect of this early GW in the polarization of the photons forming the CMB [29]. This statement was soon put into doubt and further results [30] obtained by the Planck [31] mission pointed that the BICEP-2 measurement is very consistent with the effect expected due to particular models of galactic dust by which the data is likely to be contaminated.

1.4 The LIGO detector: brief overview

1.4.1 Gravitational Wave interferometry

Gravitational wave signals are extremely weak. In particular, the order of magnitude of the expected strain for CBC's is of the order of $h \sim 10^{-21}$. Recall that h is adimensional and represents the fractional displacement $\Delta L/L$ that the proper distance L between two test particles would vary as the GW passes through. If we consider L to be of the order of $L \sim 1km$ (as the LIGO detectors are), then ΔL is of the order of $\Delta L \sim 10^{-18}m$. This means that we want to measure displacements of a length a thousand times shorter than that of a hydrogen nucleus. The way LIGO addresses this challenge is based on large laser interferometers. The spin= 2 nature of the gravitational field, makes that the best approach that can be taken is to consider a Michelson L-shaped set-up as the one depicted in Fig.1.7. With this design, the displacement generated on each arm is $L_y^x = L \pm \Delta L$ and the total relative change on the length of the arms will be
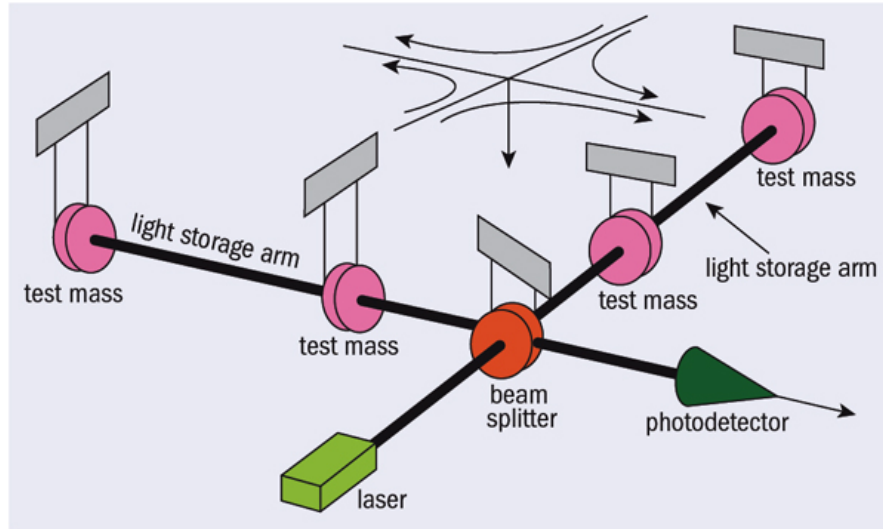
FIGURE 1.7: LIGO interferometer. Credit[CERNcourier]

$\Delta L_{Arms}/L = 2\Delta L/L$. Note that the larger the length L of the arms is, the larger ΔL will be for a given GW strain h, thus the more sensitive the detector will be.

The way a GW interferometer works can be summarized as follows. A single laser beam, which is emitted from "laser" (see, Fig.1.7, light green) is split into two secondary beams at the beam splitter (in red). The resulting beams travel along the two arms and get reflected by mirrors located at test masses (pink) at the end of each arm, returning then to the intersection. The test masses can freely move and will thus vary by ΔL their position if a GW wave signal passes through the detector. This will modify the length of each arm by $\pm\Delta L$, thus changing the original optical path that the beams would have travelled. The set-up of LIGO is such that if no GW affects the detector, the original optical paths are such that the beams arriving-back to B interfere destructively. If however, a GW passes through changing the length of the arms, some light will be detected. A given GW will produce a particular light pattern as a function of time. GW templates describe the expected pattern that a particular source would generate. GW searches consist then on comparing the incoming signal with a "catalog" of waveforms at our disposal. Provided that these waveforms do really represent what they are meant to, and that incoming signals are loud enough, one can then in principle identify the parameters of the source that emitted the GW.

1.4.2   Noise sources

The passing of a GW is not the only reason why the detector might read data. There are lots of different effects that can affect the detector, whose combined effect yields a background noise in which an eventual GW might be buried. Several of these sources

can create signals of a size orders of magnitude larger than the one due to the actual GW. We here give a review of the most important ones.

- Seismic noise: among all the noise sources, seismic noise will have a crucial role in this thesis. This consists of ground vibrations in the surrounding environment. These can be due by either natural sources or to human ones like a train passing near the detector. This causes the mirrors in the detector to need an extremely good isolation. To this end, they are suspended from pendulums that act as mechanical filters above their intrinsic resonance frequency. Furthermore, the mirrors are actively isolated by compensating their spurious movement using magnets that correct their position. The lowest frequency at which the system can be isolated from seismic noise is known as the seismic wall. This was located at 40Hz for initial LIGO [32]. A value of 30Hz is considered for the 2015 version of Advanced LIGO [33, 34] while the design version is expected to lower it down to 10Hz [19]. This will crucially affect the results obtained in Chapter 6.

- Thermal noise: this refers to the thermal vibrations affecting the mirrors and the corresponding suspensions. This is tackled using materials of a high quality factor Q, i.e., by confining vibrations in a small frequency band.

- Shot noise: is given by the statistical nature of the light quanta detection. The uncertainty of this process can be reduced by incrementing the power of the emitted laser. A way to tackle this issue, is the usage of the so called power recycling mirrors which coherently re-inject into the beam light that was previously sent-back to the laser source and that would otherwise be wasted.

- Radiation pressure noise: the quantum nature of lasers makes that the larger the power is the larger uncertainty there is in the momentum transferred to the mirrors. The usage of squeezed light [35] tackles this issue by reducing the uncertainty in the momentum to the cost of increasing the one present in quantities that are irrelevant for GW analysis.

- Gravity gradient noise: this is due to changes in the Newtonian gravitational field. These have not affected measurements up to now but are expected to do so when GW detectors are able to operate at lower frequencies, i.e., once the seismic wall is lowered to 10Hz.

Altogether, Fig.1.8 shows the predicted curves for the three versions of LIGO used in this thesis together with the strain $\tilde{h}_{2,2}(f)$ expected for a non-spinning $q = 1$ source of total mass $M = (15, 50, 100, 200)M_\odot$ for an optimally oriented detector located 1Gpc away from the source. The waveforms belong to the PhenomC family [36]. We consider

the High-Energy-Power-Zero-Detuned noise curve [19], as this corresponds to the design goal of Advanced LIGO whose seismic wall is located at 10Hz. However, the sensitivity given by this noise curve is not expected to be achieved until ~ 2018. For this reason, in this thesis we also consider the so called Early Advanced LIGO noise which is the one predicted for the shortcoming runs starting in 2015 [33, 34]. The sensitivity is a bit lower and more important for our studies, the seismic wall is at 30Hz. Also, since no detections were made in the past science runs performed with initial LIGO [32], we dedicate some effort to elucidate how neglection of higher order modes HOM could have affected these measurements. The noise curve of initial LIGO is quite similar to that of Early Advanced LIGO: it has lower sensitivity and similar seismic wall.
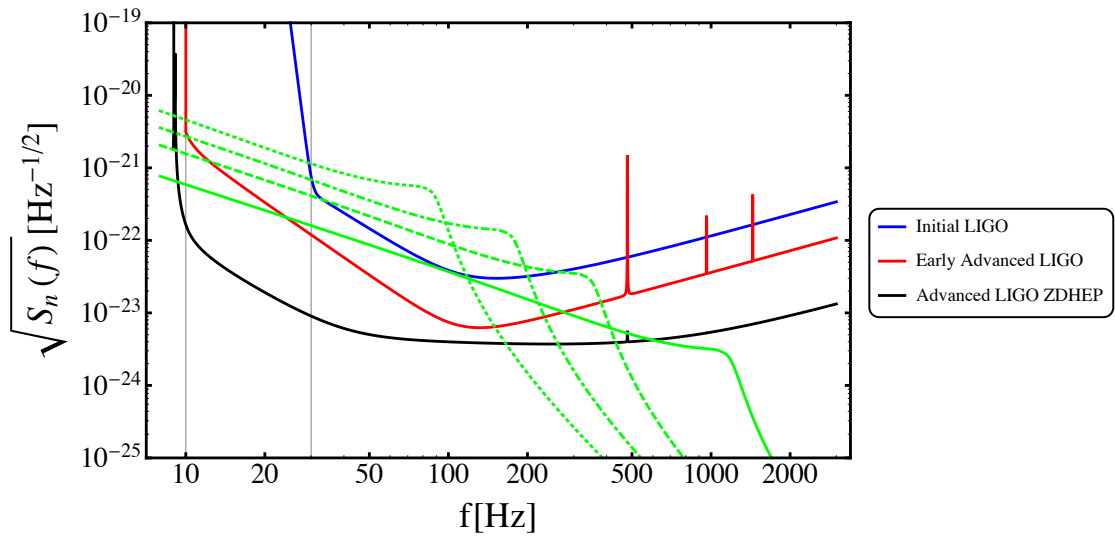
FIGURE 1.8: The three noise curves considered along this thesis together with the amplitude of the Fourier transform $|\tilde{h}_{2,2}(f)|$ (accordingly re-scaled) of a signal from a non-spinning $q = 1$ source of total mass $M = (15, 50, 100, 200)M_\odot$ (from bottom to top) located at 1Gpc and for an optimally oriented detector. The two vertical lines correspond to the 10Hz and 30Hz frequency cutoffs considered for Advanced LIGO and the other two detectors respectively.

1.4.3 Astrophysical sources of Gravitational Waves for ground-based detectors

GW associated to Gamma Ray Bursts

Gamma Ray Bursts (GRB) are the most violent electromagnetic events that take place in the Universe. These can be produced when a NS-NS or NS-BH binary coalesces. In particular, the detection of GW associated to GRB gives strong evidence that the primogenitor of the GRB is a compact binary and helps to distinguish between NS-NS and NS-BH. Another typical scenario is the collapse of rapidly rotating massive stars to

eventually form black holes or neutron stars, which commonly happens after a supernova explosion. A supernova generates GW emission provided it is not spherically symmetric. Given the complexity and numerous physical processes involved in a supernova, there are no templates of such a radiation. Searches for these sort of GW are based on coherent techniques such as the X-Pipeline [37]. Coherent searches combine data from several detectors before analysis, and create a single list of candidate events. In contrast, in incoherent searches like ihope [38] or gstlal [39], candidate events are normally obtained from each detector independently, and one looks for events of similar duration and frequency band that occur that occur in coincidence in all detectors.

Continuous Waves

Compact rapidly rotating non-spherically symmetric bodies continuously emit GW as they rotate [40]. This makes highly rotating neutron stars a perfect candidate for the detection of such a kind of gravitational waves. In particular, defects on its surfaces such as non-symmetric distortions and unstable oscillations of the fluid part of the star are likely to contribute to the emitted radiation. In particular, measurements of GW from NS are a perfect tool for testing the different proposals for the equation their equation of state. Due to the weakness of the emitted radiation, the detection of this sort of GWs requires measurements over long periods of time [41, 42]. Searches for continuous gravitational waves can be classified in 3 categories, depending on our a priori knowledge of the source. In targeted searches [43], the parameters of the source are assumed to be known with great accuracy and the observation time can extend to the order of a year. In directed searches [42], only the sky location of the source is known, while its frequency and its time derivatives are unknown. Finally, all sky searches for unknown pulsars cover the full parameter space of signals [44]. These are computationally limited due to the wide range of parameters one has to look at and the long observation time required to obtain enough signal power.

Compact Binary Coalescences

This thesis is dedicated to the study of Compact Binary Coalescences (CBC). These consist on pairs of NS and BH that inspiral each other describing orbits which shrink as they emit GW. Eventually, both objects coalesce during the merger phase and give birth to a perturbed Kerr black hole that settles to a Kerr black hole during the so called ringdown phase. Although GW are produced during the whole process, these increase their amplitude and frequency as the orbit shrinks, generating a chirping signal that reaches its maximum when the objects merge. The settling of the resulting perturbed

Kerr black hole, during the so called ringdown stage, produces characteristic radiation that can be expressed as a sum of quasinormal modes. Since we know the signal we expect from a CBC, searches for them [17, 45, 46] are based on the matched filter technique [47], which consists on the filtering of the incoming data with the templates of the radiation we expect to observe. This templates can be computed in different frameworks that will be introduced in the next chapter. These range from analytical expressions computed in post-Newtonian (PN) and Effective-One-Body (EOB) [48–51] formalisms for the early emission to numerical results obtained by means of Numerical Relativity [52–55] with the help of computer clusters. The latter allow for the description of the late inspiral, merger and ringdown. There exist also combined waveforms such as hybrid PN/NR waveforms [1, 36] and NR callibrated EOB, called EOBNR models that allow for describing the whole coalescence by means of a single Inspiral-Merger-Ringdown (IMR) waveform. Furthermore, continuous analytical families of IMR waveforms can be obtained by fitting phenomenological models to a given discrete set of hybrid waveforms. These are known as Phenom [36, 56, 57] models. Also, alternative theories of gravity such as scalar-tensor field theories predict the triggering of scalar fields (or matter scalarization) in the presence of strong gravitational fields. This would in particular impact the shape of gravitational waves emitted by NS-NS and NS-BH systems in which the NS would undergo scalarization [58, 59]. Also, burst searches can be sensitive to CBC's, especially for the case of high mass BBH.
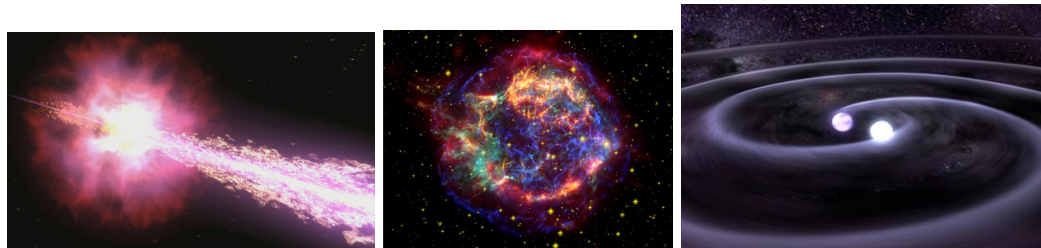
FIGURE 1.9: Examples of the described sources of GW. A GRB, the Supernova Cassiopiea A, and a CBC. GRB Image credit: NASA / Swift / Cruz deWilde.

Chapter 2

Waveforms for Compact Binary Coalescences

In Chapter 1, derived the expression of the GW strain h when the tensor $T_{\mu\nu}$ is computed using Newtonian theory, which is valid in the limit where the distance between both compact objects tends to infinity. The computation of the waveform describing the GW emission during the whole coalescence requires taking into account further effects like the energy loss via GW, the flux of energy through the event horizons of the black holes (if present) or the coupling between the spins of the individual objects with each other and with the total angular momentum of the binary. Also, for the case of neutron stars, the inclusion of effects like the tidal disruption, the presence of local asymmetries (or mountains) and different equations of state (EOS) give a different prediction for the resulting emission. During the last decades several techniques have been developed in order to compute GW waveforms, each of them having different accuracy and different computational cost. These can be roughly classified in the analytical post-Newtonian (PN) expansions [60], perturbation theory [61] and self-force calculations [62–64], the Effective One Body (EOB) formalism [48] and the more recently developed Numerical Relativity (NR) solutions [53, 65, 66]. Together with these, one of the main objects of this thesis, the hybrid waveforms, combine the PN and NR results into a single object. Among other utilities, these serve for the posterior development of the so called phenomenological waveforms. Also, hybrid waveforms can be injected into simulated detector noise in order to test the ability of GW search codes like iHope [38], gstlal [39],[67],[68] or pycbc [69] for detecting GW signals. In the present chapter we will give a review of the PN and NR formalisms and solutions, whose accuracy we will discuss in Chapter 5. For completeness, we will also give a brief overview of the remaining mentioned models except for the hybrid waveforms, which we will describe in detail in Chapter 4.

2.1 Parameters of a CBC

Before discussing several possible approaches to the modeling of GW radiation, let us fix frames of reference and notations. We will normally use a reference frame whose origin is located at the source. The location of a point p in the sky of the source will be then described in spherical coordinates (r, θ, φ). These will be chosen such that the z-axis, defined by $\theta = 0$, is aligned with the orbital angular momentum $\vec{L}$ of the binary. The distance r between the source and a detector located at p will be eventually substituted by the corresponding luminosity distance d_L. With these conventions, a system will be said to be face-on oriented to the detector if the latter is located at $\theta = \{0, \pi\}$ and edge-on when $\theta = \pi/2$. Once we place a detector at a point p, its response to a GW will depend on the orientation of its arms with respect to the propagation vector of the GW. This is encoded in the so called antenna patterns of the detector, that will be introduced later in Chapter 3. In order to describe it, we will use a frame of reference centered on the detector. The location of the source in the sky of the detector will then be described in spherical coordinates $(r, \bar{\theta}, \bar{\varphi})$. The arms of the detector will be aligned with the positive $\bar{x}, \bar{y}$ axis defined by $\bar{\theta} = \pi/2$, $\bar{\varphi} = \{0, \pi/2\}$. Both systems are depicted in Fig. 2.1. Finally, the polarization angle ψ, determines relative rotation of the arms of the detector with respect to the "+" and "×" components of the GW. We will choose our conventions such that when the detector arms are normal to the propagation of the waveform, the polarization angle ψ between the arms of the detectors and the "+" polarization is $\psi = 0$. i.e, the arms coincide with the '+" component of the GW. This uniquely defines the antenna pattern (3.3) of the detector, that we will introduce in Chapter 3.

For completeness, let us now enumerate all the parameters that a GW signal will depend on. We begin by the two component masses m_1 and m_2. These are usually encoded in the total mass $M = m_1 + m_2$ and the mass ratio $q = m_1/m_2$. It is also common, especially in post-Newtonian theory, the usage of the asymmetric mass ratio $\eta = q/(q+1)^2$, which allows to further define the so called chirp mass $\mathcal{M}_c = M\eta^{3/5}$. Apart from their masses, each component of the CBC will in general have a spin $\vec{S}_i$ with three components. This gives us a total of 6 more parameters. In this thesis we will pay attention to systems whose spins are aligned (and anti-aligned) with the orbital angular momentum $\vec{L}$ [1], so that we will only have two $\chi_i \equiv S_i^z/M$ spin components. Let us just recall that in standard GR, the spin S/M of a black hole has to satisfy the Kerr condition $S/M \leq 1$. This is an imposition due to the Cosmic Censorship hypothesis, by which space-time singularities are hidden behind event horizons. The Kerr solution describing a rotating black hole would give raise to a naked singularity if $S/M > 1$. Nevertheless [70], showed

---

[1]That we will align with the $z-$axis of our reference frame centered on the binary.

that the spin of a black hole can be made to exceed the Kerr limit if it is placed in a bath of an scalar field with negative energy. The solution is however not stable and we will thus consider that interesting astrophysical sources do satisfy the Kerr limit.
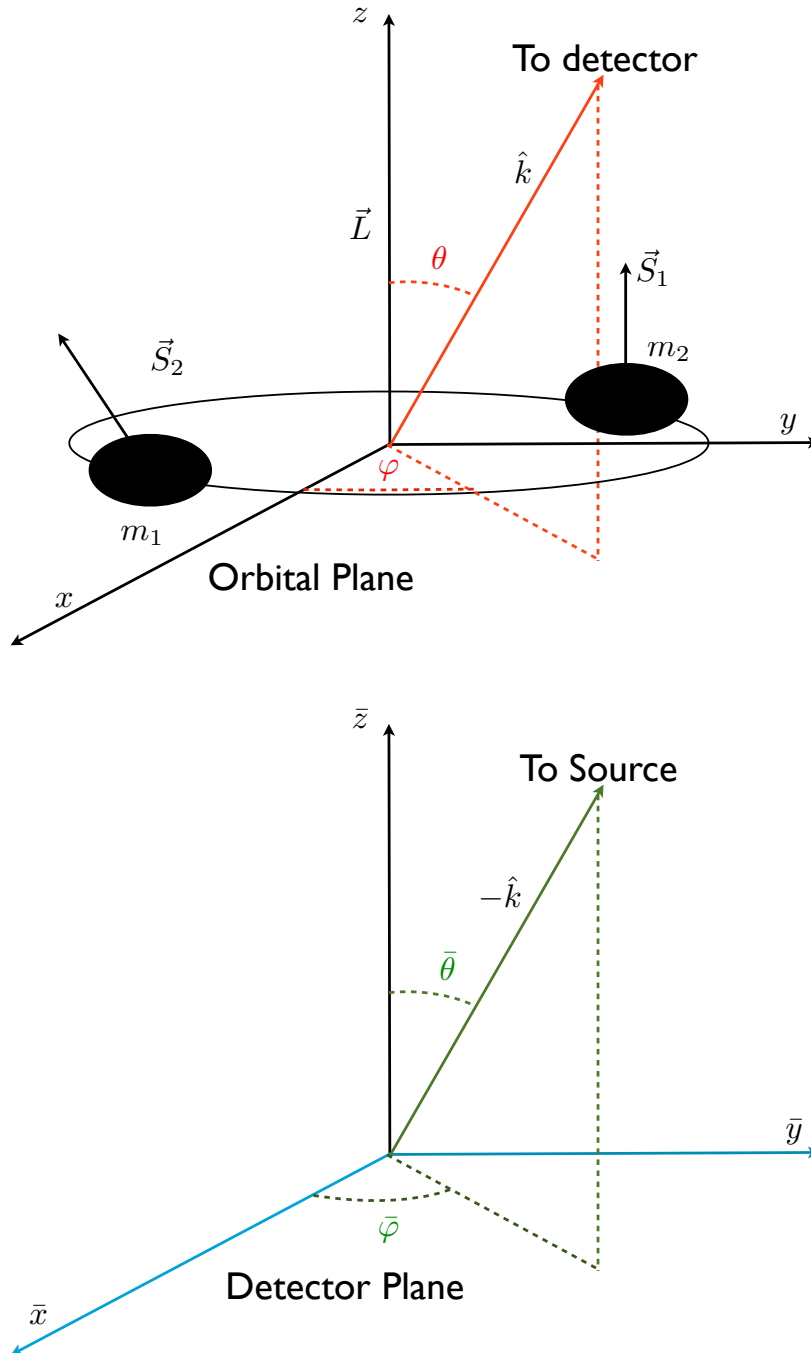
FIGURE 2.1: Top: Source frame used in this thesis. The red solid arrow points to the location (θ, ϕ) of the detector, so that it is parallel to the propagation vector $\vec{k}$ of the GW. Bottom: Detector Frame. The solid green arrow points to the location of the source. In other words, it is antiparallel to the propagation vector $\vec{k}$ of the incoming GW. The two blue positive $\bar{x}$ and $\bar{y}$ axes are aligned with the arms of the detector. d_L denotes the luminosity distance between source and detector.

It will be useful to also define an effective spin as $\chi = \frac{\chi_1 m_1 + \chi_2 m_2}{M}$. The "No Hair Theorem" states that a black hole is specified by its mass, charge and spin [71].However, a charged astrophysical black hole would automatically disperse its charge Q and thus we will always consider $Q = 0$. Although in some moments we will find it convenient to express results as a function of $\mathcal{M}_c$ or η, we will usually refer to the set of variables (q, M, χ) that we will collectively denote as $\Xi \equiv (q, M, \chi)$. We will eventually denote the set of extrinsic angular parameters $(\theta, \varphi, \bar{\theta}, \bar{\varphi}, \psi) \equiv \Lambda$.

2.2 The post-Newtonian Approximation

The post-Newtonian approximation consists of a weak-field, slow-motion approximation to the true GR problem in which relevant quantities are expanded around the zeroth-newtonian order ones as a sum in powers of $(v/c)^{2n}$ or $(M/c^2 d)^n$, where n determines the n-PN order. For example, the well known Kepler law $(\omega d)^2 = GM/d$ is valid at zeroth order. GR corrections add higher powers of the PN-expansion so that in a general form we have

$$(\omega_{orb}^2 d) = \frac{GM}{d} + \sum_n a_n(\theta, \varphi) \left(\frac{GM}{dc^2} \right)^n. \tag{2.1}$$

The modifications to the Kepler formula are required for a description of the orbit that predicts it to shrink. Note that at the zeroth-Kepler orbit regime, the two bodies would orbit forever at a constant distance d, and GW emission would not make them coalesce.

2.2.1 Energy and Flux

Standard PN calculations consider quasi-circular adiabatic orbits. This is, both bodies move in circular orbits whose radius decreases at a very slow rate, so that the radial velocity is negligible compared to the orbital one. Asuuming that all the emitted power is due to GW emission, this is what makes the orbit to shrink. One needs then a formula that relates the energy loss rate of the system with the change of the frequency of the orbit. This is given by the quadrupole formula (1.55),

$$-\mathcal{L} = \frac{dE}{dt} = \frac{1}{5} < \dddot{Q}_{ij} \dddot{Q}_{ij} >, \tag{2.2}$$

where $\mathcal{L}$ is the luminosity or flux of the binary. The zeroth order strain computed in Chapter 1 was of the form

$$h(t) = \frac{4M\eta v^2}{r} e^{-i(2\omega_{orb}t + \phi_0)}, \tag{2.3}$$

This does not describe the entire radiation of the source but rather one of its components: that for which its frequency is twice the orbital one. This is due to the expression we have used for the tensor Q, which has been retained at quadrupolar order. In general, the tensor Q is obtained as a multipolar expansion in which each term gives raise to new components of the GW radiation. As we will see later in this Chapter, the GW emission can be expressed in general as a superposition of several modes $h_{\ell,m}$, with frequencies $\sim m\omega_{orb}$, weighted by the corresponding coefficients. In general, the contributions to the total GW phase ϕ come from the $\sim m\omega_{orb}$ contributions of each mode $h_{\ell,m}$. Also, extra corrections aPDF from complex parts of the amplitude of the $h_{\ell,m}$ modes. This said, (2.3) corresponds to the zero PN order quadrupolar component of the total GW emission.

In order to compute the orbital frequency ω_{orb} one needs expressions for the energy and flux of the system. Once these are obtained, and assuming that the system evolves adiabatically one can obtain $t(v)$ by applying the chain rule

$$\frac{dE}{dt} = \frac{dE}{dv}\frac{dv}{dt} = -\mathcal{L}(v) \Rightarrow \frac{dv}{dt} = -\frac{\mathcal{L}(v)}{dE/dv}, \tag{2.4}$$

for afterwards obtaining an expression for the phase of the binary applying

$$\phi_{orb} = \int \omega_{orb}(t)dt, \qquad M\omega_{orb} = v^3. \tag{2.5}$$

The PN approximation provides an expansion of these and related quantities in powers of the expansion parameter v/c. The expression for the energy $E(v)$ and the flux $\mathcal{L}(v)$ are known up to 3.5PN order [72]. In order to express them, let us adapt the formalism in [72] and define

$$
\begin{aligned}
x &= \left(\frac{GM\omega_{orb}}{c^3}\right)^{2/3} & M &= m_1 + m_2 \\
\delta M &= m_1 - m_2 & \nu &= \mu/M = \frac{m_1 m_2}{M^2} \\
\vec{S} &\equiv \vec{S}_1 + \vec{S}_2 & \vec{\Sigma} &\equiv \left(\frac{\vec{S}_2}{m_2} - \frac{\vec{S}_1}{m_1}\right) \\
S_\ell &= \vec{S}_{\hat{\ell}} & \Sigma_\ell &= \Sigma_{\hat{\ell}}.
\end{aligned}
\tag{2.6}
$$

The up-to-date expression for the energy including 3.5PN non-spinning corrections [72] and 3.5PN spin-orbit [73] corrections reads then

$$
\begin{aligned}
E(x) = -\frac{\mu c^2 x}{2} &\left\{ 1 + x\left(-\frac{3}{4} - \frac{1}{12}\nu \right) + x^2\left(-\frac{27}{8} + \frac{19}{8}\nu - \frac{1}{24}\nu^2 \right) \right. \\
&+ x^3\left(-\frac{675}{64} + \left[\frac{34445}{576} - \frac{205}{96}\pi^2 \right]\nu - \frac{155}{96}\nu^2 - \frac{35}{5184}\nu^3 \right) \\
&+ x^{3/2}\left[\frac{14}{3}S_\ell + 2\frac{\delta M}{M}\Sigma_\ell \right] + x^{5/2}\left[\left(11 - \frac{61}{9}\nu \right)S_\ell + \frac{\delta M}{M}\left(b - \frac{10}{3}\nu \right)\Sigma_\ell \right] \\
&\left. + x^{7/2}\left[\left(\frac{135}{4} - \frac{367}{4}\nu + \frac{29}{12}\nu^2 \right)S_\ell + \frac{\delta M}{M}\left(\frac{27}{4} - 39\nu + \frac{5}{4}\nu^2 \right)\Sigma_\ell \right] \right\}.
\end{aligned}
\tag{2.7}
$$

Corrections to the energy due to spin-spin interaction have been recently computed up to 3PN order [74] and read

$$
\begin{aligned}
E_{SS}(x) = -\frac{1}{2}M\nu c^2 x \frac{1}{G^2 M^4} &\left\{ x^2\left[S_\ell^2(-\kappa_+ - 2) + S_\ell\Sigma_\ell(-\frac{\delta M}{M}\kappa_+ - 2\frac{\delta M}{M} + \kappa_-) \right.\right.\\
&+ \left. \Sigma_\ell^2\left(\left(\frac{\frac{\delta M}{M}\kappa_-}{2} - \frac{\kappa_+}{2} \right) + \nu(\kappa_+ + 2) \right) \right] \\
&+ x^3\left[S_\ell^2\left(\left(-\frac{5\frac{\delta M}{M}\kappa_-}{3} - \frac{25\kappa_+}{6} + \frac{50}{9} \right) + \nu\left(\frac{5\kappa_+}{6} + \frac{5}{3} \right) \right) \right. \\
&+ S_\ell\Sigma_\ell\left(\left(-\frac{5\frac{\delta M}{M}\kappa_+}{2} + \frac{25\frac{\delta M}{M}}{3} + \frac{5\kappa_-}{2} \right) + \nu\left(\frac{5\frac{\delta M}{M}\kappa_+}{6} + \frac{5\frac{\delta M}{M}}{3} + \frac{35\kappa_-}{6} \right) \right) \\
&+ \Sigma_\ell^2\left(\left(-\frac{5\frac{\delta M}{M}\kappa_-}{4} - \frac{5\kappa_+}{4} + 5 \right) + \nu\left(\frac{5\delta\kappa_-}{4} + \frac{5\kappa_+}{4} - 10 \right) \right. \\
&\left.\left.\left. + \nu^2\left(-\frac{5\kappa_+}{6} - \frac{5}{3} \right) \right) \right] \right\}.
\end{aligned}
\tag{2.8}
$$

However, during the development of this thesis, SS corrections where only used up to 2PN [75]. Here we have introduced the variables ($\kappa_+ = \kappa_1 + \kappa_2$ and $\kappa_- = \kappa_1 - \kappa_2$), where κ_i measures the deformation of the corresponding compact object. It is equal to 1 for a black hole while for a neutron star it ranges in $\kappa \in (4 \sim 8)$ depending on the equation of state considered [72]. The corresponding expression for the luminosity (or flux) including 3.5PN non-spinning corrections takes the form

$$
\begin{aligned}
\mathcal{L}_{NS}(x) = \frac{32c^5}{5G}\nu^2 x^5 &\left\{ 1 + \left(-\frac{1247}{336} - \frac{35}{12}\nu \right)x + 4\pi x^{3/2} \right. \\
&+ x^2\left(-\frac{44711}{9072} + \frac{9271}{504}\nu + \frac{65}{18}\nu^2 \right) + \pi x^{5/2}\left(-\frac{8191}{672} - \frac{583}{24}\nu \right) \\
&+ x^3\left[\frac{6643739519}{69854400} + \frac{16}{3}\pi^2 - \frac{1712}{105}\gamma_E - \frac{856}{105}ln(16x) \right. \\
&\left.\left. + \left(-\frac{134543}{7776} + \frac{41}{48}\pi^2 \right)\nu - \frac{94403}{3024}\nu^2 - \frac{775}{324}\nu^3 \right] \right\}.
\end{aligned}
\tag{2.9}
$$

where γ_E denotes the Euler constant. Spin-orbit effect corrections are known up to 3.5PN order [73] and given by

$$
\begin{aligned}
\mathcal{L}_{SO}(x) =& \frac{32c^5}{5G}\nu^2\left(\frac{x^{13/2}}{Gm^2}\right)\Bigg\{ -4S_\ell - \frac{5}{4}\frac{\delta M}{M}\Sigma_\ell \\
&+ x\left[\left(-\frac{9}{2}+\frac{272}{9}\nu\right)S_\ell + \left(-\frac{13}{16}+\frac{43}{4}\nu\right)\frac{\delta M}{M}\Sigma l\right] \\
&+ x^{3/2}\left[-16\pi S_\ell - \frac{31\pi}{6}\frac{\delta M}{M}\Sigma_\ell\right) \\
&+ x^2\left[\left(\frac{476645}{6804}+\frac{6172}{189}\nu - \frac{2810}{27}\nu^2\right)S_\ell + \left(\frac{9535}{336}+\frac{1849}{126}\nu - \frac{1501}{36}\nu^2\right)\frac{\delta M}{M}\Sigma_\ell\right. \\
&+ x^{5/2}\left[\left(-\frac{3485\pi}{96}+\frac{13879\pi}{72}\right)\nu S_\ell + \left(-\frac{7163\pi}{672}+\frac{130583\pi}{2016}\nu\right)\frac{\delta M}{M}\Sigma_\ell\right]\Bigg\}.
\end{aligned}
\tag{2.10}
$$

The corresponding spin-spin corrections have also been recently computed up to 3PN order [74] and read

$$
\begin{aligned}
\mathcal{L}_{SS} =& \frac{32\nu^2}{5}\frac{c^5 x^5}{G}\frac{1}{G^2 M^4}\Bigg\{ x^2\Big]S_\ell^2(2\kappa_+ + 4) + S_\ell\Sigma_\ell(2\frac{\delta M}{M}\kappa_+ + 4\frac{\delta M}{M} - 2\kappa_-) \\
&+ \Sigma_\ell^2\left(\left(-\frac{\delta M}{M}\kappa_- + \kappa_+ + \frac{1}{16}\right) + \nu(-2\kappa_+ - 4)\right)\Big] \\
&+ x^3\Big[S_\ell^2\left(\left(-\frac{41\frac{\delta M}{M}\kappa_-}{16} - \frac{271\kappa_+}{112} - \frac{5239}{504}\right) + \nu\left(-\frac{43\kappa_+}{4} - \frac{43}{2}\right)\right) \\
&+ S_\ell\Sigma_\ell\left(\left(-\frac{279\frac{\delta M}{M}\kappa_+}{56} - \frac{817}{56} + \frac{279\kappa_-}{56}\right) + \nu\left(-\frac{43\frac{\delta M}{M}\kappa_+}{4} - \frac{43\frac{\delta M}{M}}{2} + \frac{\kappa_-}{2}\right)\right) \\
&+ \Sigma_\ell^2\left(\left(\frac{279\frac{\delta M}{M}\kappa_-}{112} - \frac{279\kappa_+}{112} - \frac{25}{8}\right) + \nu\left(\frac{45\frac{\delta M}{M}\kappa_-}{16} + \frac{243\kappa_+}{112} + \frac{344}{21}\right)\right. \\
&+ \nu^2\left(\frac{43\kappa_+}{4} + \frac{43}{2}\right)\Big)\Big]\Bigg\}.
\end{aligned}
\tag{2.11}
$$

2.2.2 The zoo of PN approximants

Different ways of solving (2.4) and (2.5) give raise to different solutions for the GW system phase ϕ_{orb} and thus to the GW phase ϕ. This results in the different PN-approximants. All the possible solutions are physically equivalent but describe slightly different final waveforms. In this thesis we will mostly use the so called Taylor T1 approximant (T1). This is obtained by integrating numerically (2.4) and (2.5). It was first presented at 2PN order [76–79] and is currently known up to 3.5PN order [80–82]. The TaylorT4 (T4) approximant is instead computed by re-expanding $\mathcal{L}$ in terms of v and truncating $\mathcal{L}/(dE/dv)$ at the appropriate PN order for numerically integrating afterwards. This was introduced by [83]. The Taylor T2 (T2) approximant is obtained

via inverting (2.4) and re-expanding $(dE/dv)/\mathcal{L}$, from which $t(v)$ can be then analytically integrated. The phase ϕ_{orb} is then obtained by integrating $\frac{d\phi_{orb}}{dv} = \frac{v^3}{M}\frac{dt}{dv}$.

In the framework of the Stationary Phase Approximation (SPA) [4, 60], the Fourier transform of a chirping signal can be approximately computed. This is the starting point of an interesting kind of PN approximants known as the TaylorF models. The TaylorF1 model is built by substituting the energy and flux functions by their PN expressions without doing any re-summation. Instead, the TaylorF2 [60] model re-expands the ratio $\frac{\mathcal{F}}{E'}$. This allows for the corresponding integral to have an explicit solution, providing an explicit analytical waveform and allowing for a very fast waveform generation.

2.2.3 Spherical harmonics decomposition

Once $\phi_{orb}(t)$ and $v(t)$ have been computed with a chosen PN approximant, it is convenient to decompose the GW strain $h = h_+ - ih_\times$ onto a -2 spherical harmonics basis [84] as

$$h(\theta, \varphi; t) = h_+ - ih_\times = \sum_{\ell \geq 2} \sum_{m=-\ell}^{m=\ell} Y_{\ell,m}^{-2}(\theta, \varphi) h_{\ell,m}(t). \tag{2.12}$$

The harmonics $Y_{\ell,m}^{-2}(\theta, \varphi)$ form a basis for functions defined on a sphere and due to their transformation properties under rotations are particularly suitable for the description of spin-2 fields as the gravitational field. Note that all the information depending on the parameters of the source is now encoded into the $h_{\ell,m}(\Xi; t)$ modes, while sky-location dependencies are described by the harmonics $Y_{\ell,m}^{-2}(\theta, \varphi)$. These are given by the formula

$$Y_{\ell,m}^{-2}(\theta, \varphi) = \sqrt{\frac{2\ell+1}{4\pi}} d_{\ell,m}(\theta) e^{im\phi}, \tag{2.13}$$

with

$$\begin{aligned} d_{\ell,m} &= \sum_{j=\max(0,m-2)}^{min(\ell+m,\ell-2)} \frac{(-1)^j}{j!} \frac{\sqrt{(\ell+m)!(\ell-m)!(\ell+2)!(\ell-2!)}}{(j-m+2)!(\ell+m-j)!(\ell-j-2)!} \\ &\times (\cos\frac{\theta}{2})^{2\ell+m-2j-2} \times (\sin\frac{\theta}{2})^{2j-m+2}. \end{aligned} \tag{2.14}$$

This allows to express the harmonics as $Y_{\ell,m}^{-2}(\theta, \varphi) = \mathcal{A}_{\ell,m}(\theta) e^{im\varphi}$, $\mathcal{A}_{\ell,m}(\theta)$ being real. Using the orthogonality of the harmonics given by,

$$\int Y_{\ell,m}^{-2}(\theta, \phi) Y_{\ell'm'}^{-2*}(\theta, \phi) \sin\theta d\theta d\phi = \delta^{\ell\ell'}\delta^{mm'}, \tag{2.15}$$

the expression (6.1) can be inverted to yield

$$h^{\ell,m} = \int [h_+ - ih_\times] Y_{\ell,m}^{-2*}(\theta,\phi) \sin\theta d\theta d\phi. \tag{2.16}$$

The resulting $h_{\ell,m}$ modes are usually expressed in two different ways. The one we will mainly use in this thesis separates them into a real amplitude $A_{\ell,m}$ and a phase $\phi_{\ell,m}$ as

$$h_{\ell,m} = A_{\ell,m} e^{i\phi_{\ell,m}}. \tag{2.17}$$

Normally, the total strain h is dominated by the $(\ell,|m|) = (2,2)$ modes and further
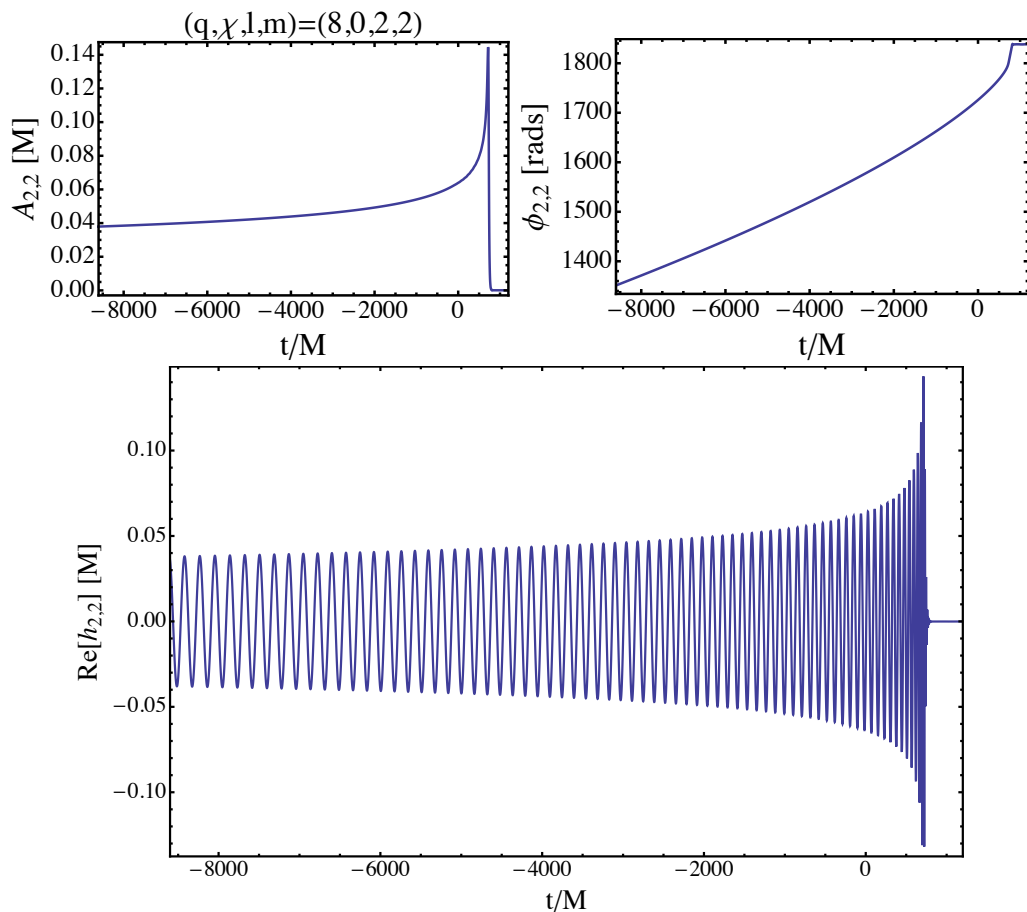
FIGURE 2.2: Amplitude, phase and real part of the $(2,2)$ mode of a $(q,\chi) = (8,0)$ system during the last orbits of the coalescence. The waveform represented is a hybrid T1-SXS waveform.

ones, known as higher order modes (HOM), are small corrections which are nowadays neglected for practical purposes. Evaluating the consequences of this neglection in GW searches will be the topic of Chapter 6. Fig. 2.2 shows the amplitude, phase and real part of the $(2,2)$ mode of the GW radiation emitted by a CBC with mass ratio and spin $(q,\chi) = (8,0)$. As we will see in detail in Chapter 5, if one expresses the phase of each

mode as

$$\phi_{\ell,m} = m\phi_{orb} + \Lambda_{\ell,m}, \tag{2.18}$$

the latter term is much small than the first one during the most part of the evolution of the binary, which yields the approximate rule $\phi_{\ell,m} \simeq m\phi_{orb}$. Consequently, some authors prefer to express $h_{\ell,m}$ as

$$h_{\ell,m} = A^c_{\ell,m} e^{im\phi_{orb}}, \tag{2.19}$$

where $A^c_{\ell,m}$ is now complex. Expressing the PN strain h in terms of its modes $h_{\ell,m}$ is of particular interest in the context of this thesis. In Chapters 4 and 5 we will accomplish the task of glueing the PN results with those obtained by NR and eventually compare their accuracy. The result of NR simulations is precisely given in terms of modes. Note that the sum in (2.16) does not consider the $\ell = 0, 1$ values. This is because here we are only interested in the radiative components of h. The $\ell = 0$ monopole components are due to changes in the total mass M of the binary while the $\ell = 1$ dipolar components can always be gauged away by a suitable election of the reference frame. Note also that although h is a complex quantity, the actual perturbation arriving at the detector is a real quantity combination of the two polarizations h_+ and $h_\times$. However h is suitable for obtaining a compact expression that encompasses all the radiation arriving at a given point. When restricting to the non-precessing case, the geometry is symmetric with respect to the orbital plane, which is preserved in time. This equatorial symmetry implies

$$h(t, \theta, \varphi; \Xi) = h^*(t, \pi - \theta, \varphi; \Xi). \tag{2.20}$$

Provided that the polarizations are defined using some appropriate choice of triad/tetrad where h is projected (which is usually the case in the literature), the individual modes satisfy

$$h_{\ell,m}(t, \Xi) = (-1)^\ell h^*_{\ell,-m}(t, \Xi). \tag{2.21}$$

2.2.4 Brief summary of possible corrections to a waveform

In (2.19), it is a common practice to retain only the $(l, |m|) = (2, 2)$ modes, or quadrupolar modes. This is because (in the non precessing case) they carry the vast majority of the power emitted by the source. In fact, up to now, searches for GW do only consider these modes. We will call this the quadrupolar approximation and refer to waveforms that do not include HOM as quadrupolar waveforms. Furthermore, it is also usual to retain as high as possible PN corrections to the phase of the $(2, 2)$ mode while leaving the

amplitude at zeroth PN-order. This is known as the restricted waveform approximation. The reason for this is that the search algorithms are extremely sensitive to the phase of the GW, having the amplitude a very secondary effect.

As depicted in 2.2.1 the inclusion of effects like spin-spin and spin-orbit interactions gives raise to new contributions to a given PN order. These are known as spinning-corrections, which are classified in spin-orbit (SO) corrections and spin-spin (SS) corrections. These are respectively, the result of taking into account the interactions between the spin of the individual objects and the angular momentum of the binary and between the individual spins themselves.

In order to compute the contribution to h of the higher modes $h_{\ell,m}$ one needs to compute corrections not to the energy and flux expressions but rather add new terms to the $Q_{i,j}$ to the quadrupolar tensor. The phase (i.e., energy and flux formulas) of all modes is known with 3.5PN order non-spinning corrections [72] with 3.5PN order spin-orbit corrections [73] and 2PN spin-spin [75] ones while for the amplitudes non-spinning corrections are known up to 3PN order [85] with 2PN spinning corrections [86]. The exception is the $(3,3)$ mode, for which 3.5PN order non-spinning corrections have been

FIGURE 2.3: Summary of PN corrections divided into addition of modes, nPN corrections and physical effects. The PN order n up to which corrections are known are specified in general. Exceptions are denoted in red ($(3,3)$ mode) and orange (modes other than $(2,2)$ and $(3,3)$).

recently computed [87][2]. All the corrections we will use are summarized in Fig. 2.3. Also, in this figure, we do not include recent computed 3PN spin-spin corrections to the energy and flux [74]. For a detailed expression of the mode amplitudes as a function of the intrinsic parameters Ξ, see [72].

2.2.5 Visualizing the higher order modes

The dominancy of the $(2,2)$ mode during the coalescence of two compact objects can be noted in Fig.2.4, where the amplitude $A_{\ell,m}$ of several modes $h_{\ell,m}$ is shown as a
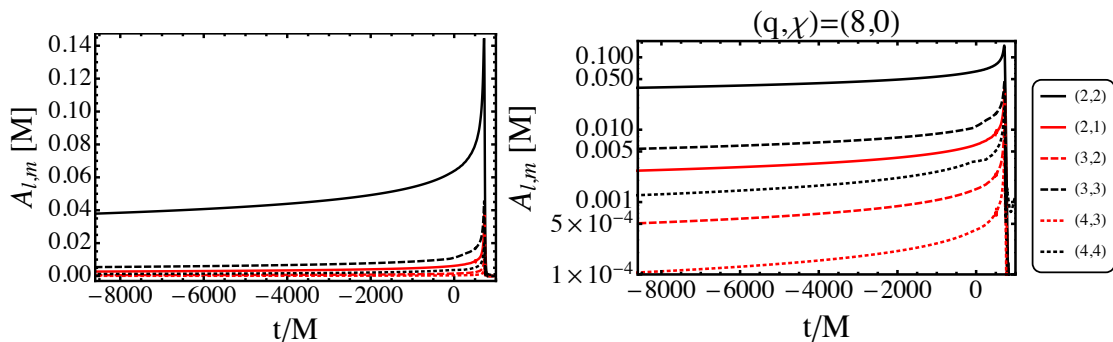
FIGURE 2.4: Amplitude of the (ℓ, m) modes of a $(q, \chi) = (8, 0)$ system during the last orbits of the coalescence in lineal (left) and logarithmic (right) scale. The waveform represented is a hybrid T1-SXS waveform.

function of the time in the coalescence. Note $t/M = 0$ does not represent any special time. The left plot is shown in linear scale in order to clearly show how dominant the $(2,2)$ mode is: during the inspiral it is ~ 2 orders of magnitude larger than the next strongest mode. However, during the very late inspiral and eventual merger (located at the peak) the ratio $A_{\ell,m}/A_{2,2}$ can get to the order of ~ 0.3 for the strongest HOMs. The more the binary tightens, the more the geometry of the system deviates from the original quadrupolar symmetry, radiating a larger fraction of the power in the form of higher modes, until these reach their maximum at the merger. This is best seen in the logarithmic version of the plot in the right panel. Note also that since each mode has an approximate phase $\phi_{\ell,m} \simeq m\phi_{orb}$, their frequencies are roughly $\omega_{\ell,m} \simeq m\omega_{orb}$. Recall that the GW frequency scales with the mass M of the system as $1/M$. This implies that for massive systems for which the $(2,2)$ mode has a frequency lower than lower frequency cutoff of the detector, higher order modes will be in band dominating the GW signal arriving at the detector. As we will see in Chapter 6, this is a key point regarding the effect that higher order modes can have in a GW search.

The ratio $A_{\ell,m}/A_{2,2}$, depends in particular on the intrinsic parameters (q, χ) of the binary. Instead of giving the explicit expressions of the modes, in which evaluating the

---

[2]Unless specified, we will however use 3PN corrections for the $(3,3)$ mode.

dependencies on the intrinsic parameters of the source might be cumbersome, and in order to get a direct visualization of their dependencies, it is preferable to see the actual modes plotted. To this end, the left panel of Fig.2.5 shows the ratio $A_{3,3}/A_{2,2}$ during the evolution of the binary for several non-spinning systems. The right panel shows the corresponding $A_{4,4}/A_{2,2}$ ratio. As a general trend, PN predicts a more important contribution from HOM the higher the mass ratio is. Regarding the spin, in general, contributions from higher modes are larger the more positive the spin is. The exception is the $(3, 3)$ mode, whose relative amplitude grows as the spin gets more negative. Note this mode is also the strongest of the HOMs [see Fig.2.4]. This behavior is shown in Fig 2.6.

Finally, let us note that when constructing waveforms including HOM, we will include
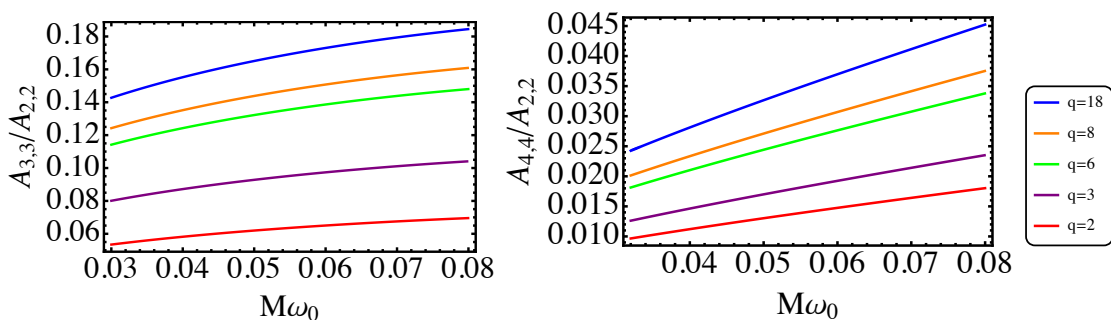
FIGURE 2.5: Relative T1 amplitude of the higher modes $(3, 3)$ and $(4, 4)$ relative to the dominant $(2, 2)$ mode as a function of the frequency for several non-spinning systems. Note how the higher the mass ratio q, the larger the contribution from higher order modes.

the most dominant ones, namely the $(2, 1)$, $(3, 2)$, $(3, 3)$, $(4, 3)$ and $(4, 4)$. For these, let us give the explicit expressions of the corresponding harmonics and their profiles as a function of θ, shown in Fig. 2.7. The various plots represent in dashed red the absolute value of the corresponding (ℓ, m) harmonic as a function of θ, while the corresponding negative m harmonic is represented in dashed-blue. In order to give an idea of how the contribution of each "doublet" of modes to the full signal depends on θ, the black curve shows the absolute value of the quantity $D_{\ell,m} = a_{\ell,m}Y_{\ell,m}^{-2} + a_{\ell,-m}Y_{l,-m}^{-2}$, where $a_{\ell,m} = 1 + i$ and $a_{\ell,-m} = (-1)^{\ell}a_{\ell,m}^{*} = (-1)^{\ell}(1 - i)$. The a functions have been defined such that they behave as a sort of "fake modes". Note that the $(2, 2)$ doublet has its minimum contribution at $\theta = \pi/2$ (when the source is edge-on to the detector) while $m \neq 2$ are relatively close to their maximums, conversely to what happens at $\theta = 0$ (when the source is face-on). We can then give a first estimation that HOM will be more important for data analysis purposes at edge-on orientations of the source, i.e., as $\theta \to \pi/2$, particularly for large q, large M and large positive spin χ. A detailed review of all factors regarding the effect of HOM will be given in Section 6, when this effect will be quantified.
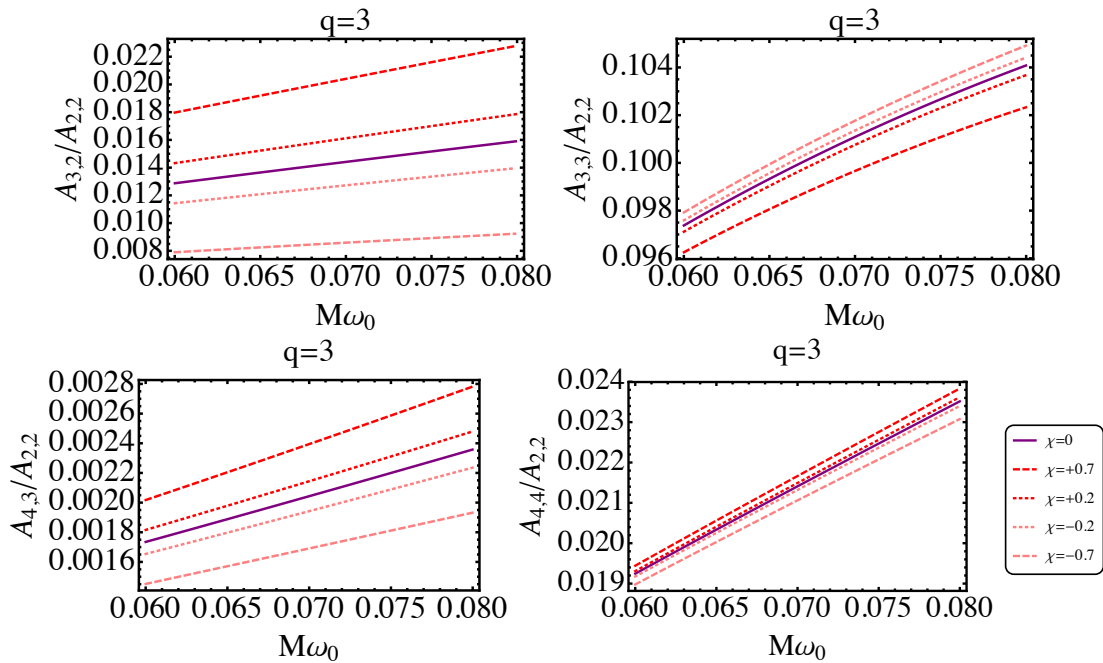
FIGURE 2.6: Relative T1 amplitude of several higher modes relative to the dominant $(2, 2)$ mode as a function of the frequency for several $q = 3$ spinning systems. Except for the $(3, 3)$ mode, the contribution from higher modes is larger the more positive the spin is. The $(3, 3)$ mode is, however, the one having the larger contribution.

Reaching the limits of PN

Although being extremely useful for its analytical condition, the PN approximation loses its accuracy as the binary evolves. When the binary tightens, velocities become comparable to c and strong gravitational regime effects appear. The expansion parameter $x = (\frac{GM\omega_{orb}}{c^2})^{2/3}$ is no longer much smaller than 1. Thus for a system such that only the late radiation gets in the band of the detector, PN does not provide suitable waveforms. Consider for example $f = 130$Hz, where advanced detectors are close to their maximum sensitivity. For a $5M_\odot$ system this corresponds to $x = 0.215$ and for $100M_\odot$ we get $x = 0.58$, which is inconsistent with the assumption that $x \ll 1$. In order to describe the last few orbits of the coalescence, the resolution of the highly non-linear Einstein equations is required, which can only be done via Numerical Relativity and with the help of supercomputing clusters.

Also, it has been recently shown that PN approximants significantly disagree between them when for low mass cases such as NS-BH systems where the BH has a moderate spin $\chi_{BH} \sim 0.4$ and the binary has a mass ratio $q \sim 4$, starting this disagreement at $v/c \sim 0.2$ [88] in the evolution of the system. This suggests that PN spin corrections further than those currently known will be needed for searches and parameter estimation of NS-BH.
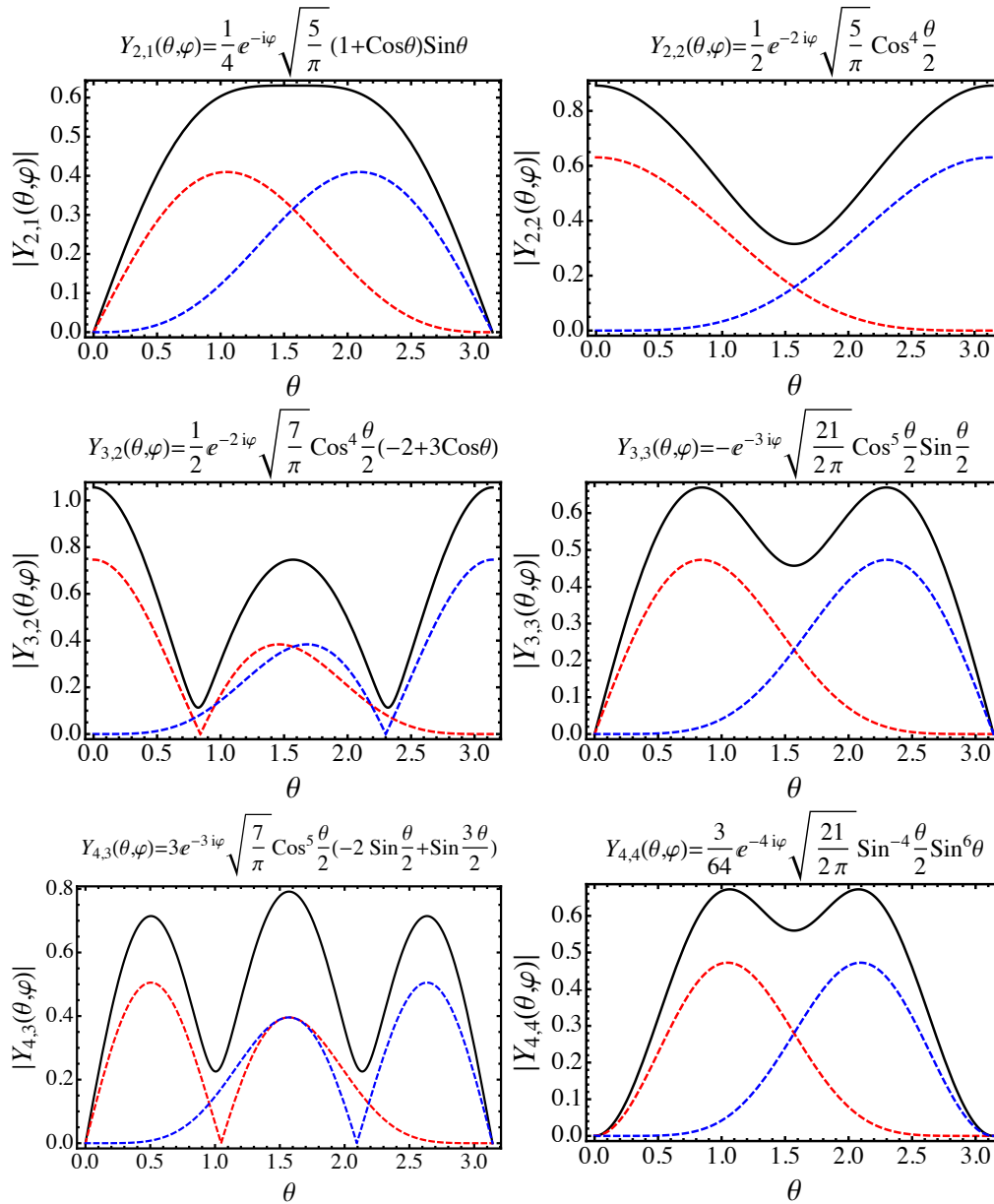
FIGURE 2.7: Absolute value, as a function of θ, of $Y_{\ell,m}^{-2}$ (red), $Y_{\ell,-m}^{-2}$ (blue) and the doublet $D_{\ell,m} = a_{\ell,m}Y_{\ell,m}^{-2} + a_{\ell,-m}Y_{l,-m}^{-2}$, in black with $a_{\ell,m} = 1 + i$ and $a_{\ell,-m} = (-1)^{\ell}a_{\ell,m}^*$. Note how the quadrupolar (2,2) mode has its minimum and maximum at $\theta = (0, \pi/2)$ respectively while $m \neq 2$ modes behave in the opposite way.

2.3 Numerical Relativity solutions

We will give here a brief review of the basic concepts of Numerical Relativity and describe the main error sources of NR simulations, whose influence in the final waveform we will study in Sec. 5.

In NR one aims to write Einstein's equations in as a time evolution problem, in order to iteratively integrate them. A natural way to to this is to distinguish between the time

coordinate and the spatial ones. In NR, the 4-dimensional spacetime manifold $\mathcal{M}$ with metric g is foliated in 3-dimensional sub-manifolds Σ_t with induced metric γ and normal vector n. The foliations Σ_t are commonly chosen to be spacelike, i.e., with timelike normal vector. The lapse function α determines how time changes from one hypersurface to the next one while the shift vector β determines the coordinates on Σ_t. Tensor fields can be then expressed as a function of their time-like and space-like components. These procedure is known as the 3+1 decomposition [52]. The remaining problem now does consist in specifying the initial metric γ on an initial surface and the value of its extrinsic curvature K[3] (which can be interpreted as the time-derivative of the metric γ) and solving then for all time. The resulting set of equations (known as the ADM equations due to by Arnowitt, Deser and Misner [89]), consists of two evolution equations and two constraint equations. The ADM equations form however a non-hyperbolic set of equations which is numerically unstable. This makes them not suitable for their implementation in simulations. However, several alternative formulations of GR provide an equivalent numerically stable set of equations that can be implemented for numerical simulations, as for example, the BSSN and GBSSN [90–92] or the Z4 [93–95] formulations. Instead of directly measuring the GW as a perturbation of a flat background, normally NR codes compute instead the outgoing transversal gravitational radiation by means of the so-called Newmann-Penrose scalar ψ_4 [96]. Once ψ_4 is computed on a sphere of constant radius R (or extrapolated to infinity [97–99]), it can be decomposed on a spherical harmonics basis applying (2.16) for obtaining the corresponding $\psi_4^{\ell,m}$ modes. This quantity is very convenient because ψ_4 is directly related to the GW strain by $\psi_4 = \frac{\partial^2 h}{\partial t^2}$. The strain h is thus obtained from Ψ_4 by applying a double time integration (see [100] for a discussion of the issues arising in this procedure). NR codes can be roughly classified by the choice of the formulation of the Einstein equations, the treatment of the singularity and the numerical methods employed.

- The SpEC code, used by the joint collaboration of the NR groups at Caltech, Cornell, CITA (Toronto), Washington State, UC Fullerton, and others, [97, 99, 101–103] employs the so called generalized harmonic formulation of the Einstein equations [104] and applies an *excision* treatment of the singularity [105]. This basically consists in eliminating the interior of the BHs from the simulated spacetime. In order to obtain the full solution, the Einstein equations are solved in finite spatial regions called subdomains and it is expressed in a basis of spectral functions which depends on the particular shape of the subdomain [101, 106]. This technique provides exponential convergence to smooth problems.

---

[3]$K_{\mu\nu} = \frac{1}{2}\mathcal{L}_n\gamma_{\mu\nu}$, n being the vector normal to Σ_t.

- In contrast, the BAM code [107, 108] opts instead for a BSSN formulation of the Einstein equations which are solved in cartesian coordinates via finite difference numerical methods. The treatment of the BH singularities is based on the *moving puncture* technique [107]. The puncture method consists on factoring the solution into an analytical part (the puncture), which contains the BH singularity and a numerical part, which is free from singularities. Originally, this method required the puncture to be static. However, in BBH simulations one needs BH that orbit, and thus the puncture must move. In 2005 [65, 109] the ability to simulate moving punctures was demonstrated.

- The Llama code, originally developed at AEI Potsdam [98], combines the generalized harmonic and excision techniques with finite difference methods. A particularity of this code, that we will mention afterwards, is the usage of the "Cauchy characteristic", which allows to analytically express the GW signal at null infinity. This is achieved by the SpEC code via extrapolating results at finite radii r by fitting them to a polynomial while the BAM code directly uses the finite radius results. Also, recent work by [110], has used a treatment similar to that of SpEC, the extrapolation being done in terms of an $1/r^n$ expansion.

There will be some error in the result obtained for h not only due to the integration process (which can lead to unphysical drifts) but also due to numerical errors in the calculation of ψ_4. Some of the main sources being:

- NR simulations do usually assume that the metric is flat at null infinity (conformal flatness) which introduces an artificial initial radiation in the simulation known as junk radiation (see bottom left plot in Fig.2.8) that quickly leaves the system once it has started to evolve.

- GW signals as observed by GW detectors are to be extracted at null infinity. However, NR simulations need to extract the data (ψ_4) at some sphere with finite extraction radius R. It is on this sphere that ψ_4 is then decomposed on a spherical harmonics basis and that the $h_{\ell,m}$ modes are then computed. As we will see (and noted by for example [1, 111]) the finitude of R is a source of error for the resulting modes. When simulations extracted at several R are available, the result can be extrapolated to infinity via a polynomial expansion of order N, as done by the SpEC [97] code. Recently, [110] has computed the wave at infinity as an expansion in terms of $1/R$. Also, a very elegant way of obtaining such a result is by means of the so called Cauchy-Characteristic, used by the Llama code [98]. Finally, recent work by Vañó-Viñuales et. al., is opening the gate for direct extraction at null infinity using a compactified hyperboloidal foliation of the spacetime [112, 113].

- NR simulations have a finite resolution determined by the grid in which ψ_4 is computed. The resolution needed is related to the wavelength λ of the GW extracted and thus to its frequency ω. The lower λ (the larger ω), the less resolution will be needed. We shall see how some of the finite radius errors are lower important in the high frequency regime. In Chapter 5, we will pay special attention to the analysis of the effect of the finitude of the extraction radius R of NR simulations as well as to the effect of the resolution and the extrapolation order N and the NR resolution.

- NR simulations are usually affected by residual eccentricity that generates periodical oscillations of the GW strain. The reason behind this is that initial data for the simulation is computed via PN. Since the PN solution differs from the true GR one, the conditions that PN predicts for circular non-eccentric orbits differ from the true ones, yielding as a result an eccentric motion. The effect of residual eccentricity for data analysis purposes has been studied in [111, 114] and we will review it in the context of hybrid PN/NR waveforms in Chapter 4.

When available, NR waveforms can provide the closest description to the real GW emission. However, they are by far the most computationally expensive ones. Furthermore, until the breakthrough in 2005 by Pretorius [65, 66], NR simulations could not evolve more than a couple of orbits before the code would breakdown due to the instability of the equations. Since then, NR simulations have become a common tool in GW science and there has been a tremendous progress in the generation of longer NR simulations (i.e., obtaining a larger number of GW cycles before merger) and in sampling larger portions of the CBC parameter space. NR simulations are extremely computationally expensive ($\sim$ one month on $\sim$ 100 CPU's) which is $\sim$ 8 orders of magnitude above the cost of any of the other waveform models. Due to this, simulations would hardly cover a few cycles before merger, being more challenging the larger the mass ratio q of the simulated system is. The longest simulations available nowadays are due to the SXS collaboration [115], formed by the groups in Caltech, Cornell, CITA and others. These, publicly available, cover non-spinning systems ranging from $q = 1$ to $q = 8$ and spinning ones up to $\chi = \pm 0.99$ for the equal mass case. These longest of them covers up to $\sim$ 80 GW cycles. Remarkably, the work done in the context of the BAM code [105, 116] has made possible to complete challenging simulations such as those corresponding to $q = 18$ non-spinning and spinning systems. The corresponding waveform is shown in Fig.2.8 together with some taken from the SXS catalogue. In this thesis we will show results obtained using NR simulations from both the SXS and BAM codes. It is worth to note that recently, a new waveform for a $q = 7$ non-spinning system covering 350 GW cycles was presented by Szyagli et. al., [117] being the first time that a NR waveform

covers the full sensitivity band of a GW detector. This will in principle allow to test the accuracy of PN results in the low frequency regime, where PN is supposed to be accurate enough.
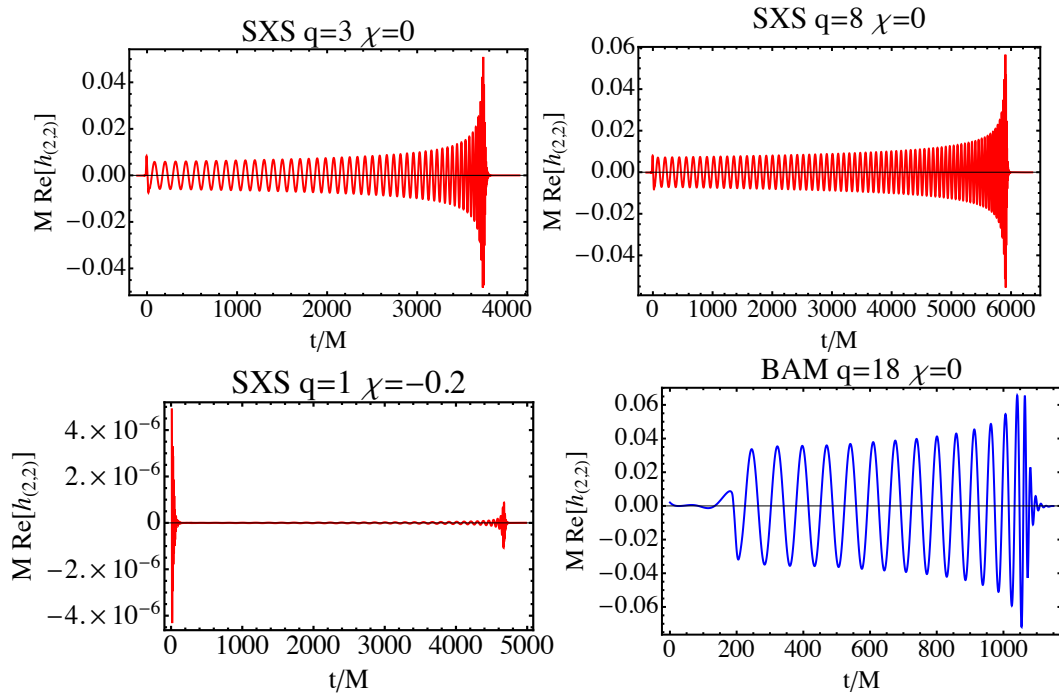
FIGURE 2.8: Examples of NR simulations. The red ones have been produced by the SXS collaboration. The spinning case has been plotted so that the initial junk radiation burst is clearly noticeable. The blue $q = 18$ waveform has been produced by the BAM code.

2.4   The Effective One Body formalism

The Effective One Body (EOB) formalism provides an analytical framework in which the calculation of the emitted radiation can be carried out up to the merger. It was initially proposed in [48, 49] for solving comparable mass systems. In this formalism, the problem of two objects orbiting each other is described in terms of the equivalent problem of a single body moving in a background spacetime. Unlike in the PN formalism, the assumption of the system being adiabatic is never done. The EOB calculation can be carried out up to the merger and the eventual ringdown radiation is computed by means of perturbation theory and then attached to the EOB solution. EOB facilitates the definition of a minimal set of adjustable parameters of the waveform that can be calibrated by comparison with NR results. This is the basis of the so called EOBNR models. EOB and PN calculations agree up to the known PN terms. However, calibration of EOB using NR somehow helps to compute the higher unknown PN terms and gives results in very good agreement with the actual NR ones. Once the calibration to a

finite number of NR simulations has been done, one can interpolate over the parameter space in order to obtain a continuous family. As an example, the so called SEOBNRv2 [50, 51](S-for spinning) model is calibrated up to $q = 8$ but it gives very good results even for $q = 18$, as we will see in Chapter 4.

SEOBNR waveforms are much faster to generate than NR ones ($\sim$ CPU seconds) but still slow for being used in a search or parameter estimation studies, for which thousands of waveforms need to be generated. However, recent work [118] has provided Reduced Order Models (ROM) that allow for a very fast generation of SEOBNR waveforms. In this framework, the original SEOBNR model is decomposed on a certain set of basis waveforms. The original ones can be then obtained with very high accuracy performing linear combinations of the basis waveforms, which is computationally much cheaper than generating every single SEOBNR waveform. This is also the bases of the Singular Value Decomposition (SVD) methods [68]. We will employ this kind of waveforms in Chapter 6.

2.5 Phenomenological Waveforms

Phenomenological waveform models [36, 56, 57] provide Fourier domain expressions describing the radiation emitted during the whole coalescence. Since these provide analytical expressions for the actual waveforms and not sets of equations that need to be solved, the waveform generation is much faster than that of SEOBNR models. The first step in the production of such models is the generation of hybrid PN/NR waveforms. These are the result of gluing PN waveforms to the tail of NR ones, in order to cover the early stages of the coalescence that NR simulations do not reach. After this, analytical models depending on several adjustable parameters that are calibrated to a finite set of hybrid waveforms. Pieces describing the amplitude and phase during the inspiral, merger and ringdown stages are normally calibrated separatedly for afterwards constructing IMR waveforms that are then interpolated along the parameter space, yielding a continuous family of IMR Phenom waveforms. There exist several Phenom models that use different calibration strategies. The inspiral stage is commonly described by a polynomial in powers of the frequency f. For instance, the PhenomC model [36] uses:

$$\phi_{2,2}^{SPA}(f) = 2\pi f t_0 - \phi_{2,2}^0 - \frac{\pi}{4} + \frac{3}{128\eta}(\pi f)^{-5/3} \sum_{k=0}^{7} \alpha_k (\pi f)^{k/3}, \qquad (2.22)$$

where t_0 and $\phi_{2,2}^0$ are arbitrary constants. This is inspired by the SPA result for the TaylorF2 approximant. Also, the corresponding expression for the amplitude is motivated by the SPA behavior $|\tilde{h}(f)| \sim f^{-7/6}$. The late inspiral and merger phase are then

modeled similarly including further powers of f as

$$\phi_{2,2}^{PM}(f) = \frac{1}{\eta}\left(\alpha_1 f^{-5/3} + \alpha_2 f^{-1} + \alpha_3 f^{-1/3} + \alpha_4 + \alpha_5 f^{2/3}\alpha_6 f\right). \qquad (2.23)$$

Finally, the ringdown stage is described using by the ansatz

$$\phi_{2,2}^{RD}(f) = \beta_1 + \beta_2 f, \qquad (2.24)$$

and the total phase is built as $\phi_{phen} = \phi_{2,2}^{SPA}(f)\omega_{f_1}^- + \phi_{2,2}^{PM}(f)\omega_{f_1}^+\omega_{f_2}^- + \phi_{2,2}^{RD}(f)\omega_{f_2}^+$ with $\omega_{f_0}^{\pm} = \frac{1}{2}\left[1 \pm \tanh\left(\frac{4(f-f_0)}{d}\right)\right]$ while the amplitude is built in a similar manner. Different ansatzs give raise to different Phenom models. The Phenom C model describes non precessing systems using an effective spin parameter $\chi \equiv \frac{1+\delta M/M}{2}\chi_1 + \frac{1-\delta M/M}{2}\chi_2$. While the PhenomC model considers corrections up to 3.5PN non-spinning and 3PN spinning corrections, the previous PhenomB model [56] was also produced to describe non-spinning and spinning including systems but including up to 2PN corrections. It has been implemented in GW searches template banks as well as for testing the performance of detection pipelines for the future detectors as in the NINJA-2 project [34] together with SEOBNRv2. Finally, the recently developed PhenomP model [57] has opened the gate for the phenomenological description of precessing binaries.

Further improvement of Phenom models could be performed via the inclusion of HOM. If so, the discussion of them given in , suggests that one should focus on including the $(3,3)$ mode due to its magnitude and its importance for edge-on systems and the $(3,2)$. The latter, although not being as dominating as the $(3,3)$, can have important contributions to the optimum SNR (mainly when the source is face-on) when the mass of the source is such that the radiation emitted in form of the $(2,2)$ and $(3,2)$ modes is close to the sweet-spot of the detector. Note that at that point, the amplitude of both modes is comparable. Also, although the $(2,1)$ mode dominates the GW emission more than the $(3,2)$, its low frequency content makes it to be largely dominated by the $(2,2)$ when it is in band.

Chapter 3

Elements of gravitational waves data analysis for CBCs

In this chapter we will see how the output of a GW detector is to be analyzed in order to find whether or not there is a GW signal buried in the data. We will first give explicit expressions for the signals expected for afterwards introduce to the reader the matched filter formalism. We will in particular define and the concepts of signal-to-noise ratio (SNR), overlap, match, horizon distance and fitting factor, which will be essential in this thesis. Last, once mathematical concepts have been introduced, we will give explicit expressions for the matched filter operation for general filter waveforms expressed as a sum of spherical harmonics. This will allow us to show explcitly how the match filter is to be optimized over different parameters of the incoming signal. Although this material has already been widely studied in existing literature, expressions are mostly given for the usual case in which only the quadrupolar $(\ell, |m|) = (2, 2)$ modes are considered. This the makes inclusion of HOM in this kind of analysis cumbersome and diffcults the understanding of how maximization over several parameters of the GW signal is to be carried out.

3.1 General expressions for the strain h: from signal to template

In order to perform searches for CBCs, we need models of the potential GW signals h we expect to be buried in the output of the detector. An outline of how these are computed was given in the previous chapter. We also learnt how the GW strain h can be expressed as either a couple of polarizations h_+ and $h\times$ or as a function of modes $h_{\ell,m}$.

However, in this process we have not yet considered the influence of the orientation of the detector with respect to the GW propagation vector $\vec{k}$. We have only considered its location $p = (\theta, \varphi)$. Adding this ingredient will be the final step in order to give the final expression of the signal arriving to our detector. We will afterwards see how this expression can be simplified and expressed as a simple sum of cosine functions, give explicit expressions for the matched filter and show how analytical optimizations over extrinsic parameters can be carried out when only quadrupolar templates are considered in our search.

3.1.1 From the source to the detector

The GW signal at a given sky location

The GW radiation arriving at a point p on the sky of the source will depend on its location, as shown in Chapter 2, as

$$h_p(\Xi; r, \theta, \varphi; t) = h_+ - ih_\times = \frac{1}{d_L} \sum_{\ell \geq 2} \sum_{m=-\ell}^{m=\ell} Y_{\ell,m}^{-2}(\theta, \varphi) h_{\ell,m}(\Xi; t), \qquad (3.1)$$

where the dependence on the source-detector distance r is encoded in the luminosity distance d_L, the spherical harmonic modes $h_{\ell,m}$ and the $Y_{\ell,m}^{-2}$ factors, known as -2 spin weighted spherical harmonics. Let us recall the property of the GW modes in the absence of precession

$$h_{\ell,-m} = (-1)^\ell h_{\ell,m}^*, \qquad (3.2)$$

that we will use in the following calculation in order to simplify the final expression for the GW strain.

The GW signal as observed by the detector

The effect of the GW signal on a detector will depend on the location $(d_L, \bar{\theta}, \bar{\varphi})$ of the source in its sky and on the polarization ψ of the GW. The exact response of an interferometric detector to a weak, plane GW in the long wavelength approximation (i.e., when the size of the detector is much smaller than the wavelength of the wave) is well known [119]. This response its encoded by the so called antenna patterns $(F_+, F_\times)$

of the detector

$$
\begin{aligned}
F_+ &= \frac{1+\cos^2\bar\theta}{2}\cos 2\bar\varphi \cos 2\psi - \cos\bar\theta \sin 2\bar\varphi \sin 2\psi \\
F_\times &= \frac{1+\cos^2\bar\theta}{2}\cos 2\bar\varphi \sin 2\psi + \cos\bar\theta \sin 2\bar\varphi \cos 2\psi.
\end{aligned}
$$

and the observed real GW signal is simply

$$
h^D(\Xi;\theta,\varphi;\bar\theta,\bar\varphi,\psi;d_L,t) = \frac{1}{d_L}\left[F_+(\bar\theta,\bar\varphi,\psi)h_+(\Xi;\theta,\phi;t) + F_\times(\bar\theta,\bar\varphi,\psi)h_\times(\Xi;\theta,\phi;t) \right].
$$
(3.3)

At this point, it is worth to note that there are situations in which a GW detector can be blind to a GW signal. Consider for example the particular situation in which our detector located on the equatorial plane of the source $\theta = \pi/2$ and that $\psi = \pi/2$. It would then be sensitive to only the $h_\times$ polarization of the GW. However, Eq. (4.4) reveals that $h_\times = 0$ at $\theta = 0$ and no signal would be detected.

We will now obtain an expression for (3.3) where as many things as possible appear as multiplicative factors. Although the reason for this will be clear at the end of the chapter, we can anticipate some of it. In principle, one needs to filter the incoming signal with templates corresponding to all the possible combinations of the parameters of the incoming signal. This would give raise to an enormous template bank and it would take too long. However, the result of this comparison [1] is not sensitive to the "norm" of the template (i.e, to global amplitude factors). We will thus identify which parameters can be factored out. In fact we will see how in the case that templates are quadrupolar, one does only need to include templates for all the possible values of the intrinsic parameters of the source $\Xi = (q, M, \chi)$. Let us show how.

With a little bit of algebra (3.3) can be reduced to

$$
h^D(\Xi;\theta,\varphi;\bar\theta,\bar\varphi,\psi;d_L,t) = \frac{F(\bar\theta,\bar\varphi,\psi)}{d_L}\left[\cos(\kappa)h_+(\Xi;\theta,\phi;t) + sin(\kappa)h_\times(\Xi;\theta,\phi;t) \right],
$$
(3.4)

where

$$
F = \sqrt{F_+^2 + F_\times^2}
$$
(3.5)

$$
\tan\kappa = \frac{F_\times}{F_+}.
$$
(3.6)

---

[1] We really mean the amount of Signal-to-noise ratio, which we will define later.

Then F is simply a global amplitude factor and κ acts as an effective polarization angle. Using (3.1) we get

$$
h^D(\Xi; \theta, \varphi; \bar{\theta}, \bar{\varphi}, \psi; d_L, t) =
$$
$$
\frac{F(\bar{\theta}, \bar{\varphi}, \psi)}{d_L} \left[\cos(\kappa) \mathcal{R} \sum_{\ell \geq 2} \sum_{m=-\ell}^{m=\ell} Y_{\ell,m}^{-2}(\theta, \varphi) h_{\ell,m}(\Xi; t) + \sin(\kappa) \mathcal{I} \sum_{\ell \geq 2} \sum_{m=-\ell}^{m=\ell} Y_{\ell,m}^{-2}(\theta, \varphi) h_{\ell,m}(\Xi; t) \right],
$$
$$(3.7)$$

where $\mathcal{R}$ and $\mathcal{I}$ denote respectively the real and imaginary part. Making use of (3.2) and expressing the harmonics as $Y_{\ell,m}^{-2}(\theta, \varphi) = \mathcal{A}_{\ell,m}(\theta) e^{im\varphi}$ we can express the sums as sums over positive m modes as

$$
\sum_{\ell \geq 2} \sum_{m=-\ell}^{m=\ell} Y_{\ell,m}^{-2}(\theta, \varphi) h_{\ell,m}(\Xi; t) =
$$
$$
\sum_{\ell \geq 2} \sum_{m=0}^{m=\ell} (\mathcal{A}_{\ell,m}(\theta) e^{im\varphi} h_{\ell,m}(\Xi; t) + (-1)^\ell \mathcal{A}_{\ell,-m}(\theta) e^{-im\varphi}(\theta, \varphi) h_{\ell,m}^*(\Xi; t)),
$$
$$(3.8)$$

Where we need to redefine $h_{\ell,0} \to \frac{1}{2} h_{\ell,0}$. From now on we will drop all the dependencies in order to alleviate the notation. Also we will express $\sum_{\ell \geq 2} \sum_{m=0}^{m=\ell} \equiv \sum_{\ell,m}$. Considering now

$$
h_{\ell,m} = A_{\ell,m} e^{i\phi_{\ell,m}}
$$
$$
\mathcal{H}_{\ell,m} = \sqrt{A_{\ell,m}(\mathcal{A}_{\ell,m} + (-1)^\ell \mathcal{A}_{\ell,-m})}
$$
$$
\tan \beta = \frac{(-1)^\ell \mathcal{A}_{\ell,-m}}{\mathcal{A}_{\ell,m}},
$$
$$(3.9)$$

we get

$$
h = \frac{1}{d_L} \sum_{\ell,m} \mathcal{H}_{\ell,m} \left[\cos \beta e^{i(m\varphi + \phi_{\ell,m})} h_{\ell,m} + \sin \beta e^{i(-m\varphi - \phi_{\ell,m})} h_{\ell,m}^* \right].
$$
$$(3.10)$$

Finally using (3.10), expanding $e^{i\alpha} = \cos \alpha + i \sin \alpha$ and defining

$$
\gamma_{\ell,m} = \beta + m\varphi + \kappa,
$$
$$(3.11)$$

we reduce the observed strain h^D to the simple expression

$$
h^D = \frac{F}{d_L} \sum_{\ell,m} \mathcal{H}_{\ell,m} A_{\ell,m} \left[\cos \gamma_{\ell,m} \cos \phi_{\ell,m} + \sin \gamma_{\ell,m} \sin \phi_{\ell,m} \right],
$$
$$(3.12)$$

which if we consider only the $(2,2)$ mode and define $\bar{\mathcal{H}}_{2,2} \equiv \frac{F}{d_L}\mathcal{H}_((2,2)$ we can express as

$$h^D = \bar{\mathcal{H}}_{2,2}A_{2,2}\left[\cos\gamma_{\ell,m}\cos\phi_{2,2} + \sin\gamma_{\ell,m}\sin\phi_{2,2}\right], \tag{3.13}$$

which coincides with the waveform expression given in [38]. This expression is very convenient for data analysis because all the information about the polarization angle κ and the azimuthal angle φ, also known as the coalescence phase is contained in a unique effective angle $\gamma_{\ell,m} = \beta + m\varphi + \kappa$ and all the dependance on the rest of extrinsic parameters is contained in a common amplitude factor $\bar{\mathcal{H}}_{2,2}$. As we will see later, this allows to perform an analytical optimization of the basic quantities used in data analysis over all the extrinsic parameters of the source represented by the template. Although we will not take much advantage of it, let us express h^D in the simplest possible form as

$$h^D = \frac{F}{d_L}\sum_{\ell,m}\mathcal{H}_{\ell,m}A_{\ell,m}\cos\bar{\phi}_{\ell,m}. \tag{3.14}$$

Hence, any GW signal can be expressed as a sum of real amplitudes $A_{\ell,m}(\Xi;t)$, which depend on the intrinsic parameters of the source multiplied by factors $\mathcal{H}_{\ell,m}$ and cosine functions whose argument $\bar{\phi}_{\ell,m}$ depends on the orbital phase of the binary $\phi(\Xi;t)$, the polarization κ and the polar angle θ.

3.2 The detection problem: extracting signals from background noise

The ability of a GW detector for detecting GW signals is mostly dominated by the presence of noise in the data streams. The corresponding main sources of noise were outlined in 1.4.2. In general, GW signals, if present, will be buried in a background noise orders of magnitude larger than the one of the GW, from which we will have to extract them. In this section we will define the power spectral density of the noise, for later defining the concept of singal-to-noise ratio.

3.2.1 The background noise

The output $s(t)$ of a detector will in general consist of a superposition of background noise $n(t)$ and a gravitational wave signal $g(t)$. Then we have

$$s(t) = n(t) + g(t). \tag{3.15}$$

The noise n consists in general on a stationary component over certain periods plus transients. The stationary Gaussian component of the noise can be modeled via the noise power spectral density (PSD) function. This gives us a picture of the average noise present in the detector and give an idea of its sensitivity. Let us denote the background noise of the detector as by $n(t)$ and take its Fourier transform

$$\tilde{n}(f) = \int_{-\infty}^{\infty} n(t)e^{-2\pi i f t}dt, \tag{3.16}$$

If $n(t)$ is defined for all t, its total power is defined as

$$Pow = \lim_{T\to\infty} \frac{1}{T} \int_{-T/2}^{T/2} |n(t)|^2 dt. \tag{3.17}$$

The above can be expressed, by virtue of the Parseval theorem as

$$Pow = \lim_{T\to\infty} \frac{1}{T} \int_{-\infty}^{\infty} df \left| \int_{-T/2}^{T/2} n(t)e^{-2\pi i f t}dt \right|^2 \equiv \int_{\infty}^{\infty} P_n(f)df, \tag{3.18}$$

where $P_n(f)$ is known as the power spectral density (PSD) of n. One can then identify

$$P_n(f) = \lim_{T\to\infty} \frac{1}{T} \left| \int_{-T/2}^{T/2} n(t)e^{-2\pi i f t}dt \right|^2 \equiv \lim_{T\to\infty} \frac{1}{T}\tilde{n}(f)\tilde{n}^*(f). \tag{3.19}$$

It is common in data analysis to define quantities such that the power corresponds to the integral of $P_n(f)$ defined only over positive frequencies. This motivates the definition of the one sided PSD, $S_n(f)$ as

$$\frac{1}{2}S_n(f) = P_n(f) \tag{3.20}$$

Of course we cannot measure $n(t)$ during infinite time. However, in the case of stationary noise, the PSD can be estimated via finite time measurements. For this case, the PSD is the Fourier transform of the so called auto-correlation function $\mathcal{A}$ of n. In the particular case that the detector output has zero-mean, as we will suppose in this case, $\mathcal{A}$ is defined as

$$\mathcal{A}(t,\tau) = \langle n(t)|n(t+\tau)\rangle = \lim_{T\to\infty} \frac{1}{T} \int_{t-T/2}^{t+T/2} n(t')n(t'+\tau)dt'. \tag{3.21}$$

If the noise is stationary then the auto-correlation function does only depend on the relative time τ and can be expressed as

$$\mathcal{A}(\tau) = \lim_{T\to\infty} \frac{1}{T} \int_{-T/2}^{T/2} n(t')n(t'+\tau)dt'. \tag{3.22}$$

Taking $T \to \infty$ for the integration limits, the Wiener-Khinchin theorem allows for expressing (3.22) by means of Fourier transforms as

$$\mathcal{A}(\tau) = \lim_{T \to \infty} \frac{1}{T} \int_{-\infty}^{\infty} \tilde{n}(f)\tilde{n}^*(f)e^{+2\pi i f \tau} df, \qquad (3.23)$$

and then we can express the one sided PSD as a function of $\mathcal{A}$ as

$$\frac{1}{2}S_n(f) = \lim_{T \to \infty} \frac{\tilde{n}(f)\tilde{n}^*(f)}{T} = \frac{1}{T} \int_{-\infty}^{\infty} \mathcal{A}(\tau)e^{-2\pi i f \tau} d\tau. \qquad (3.24)$$

This will be the model we will use for estimating the stationary component of the noise. Neglecting low frequency periodicity allows for the PSD to be estimated via truncation of the auto-correlation function to a finite time. This yields a discrete number of frequencies that can be measured. However, the incoming data is to be digitized, which implies it is already discrete in time steps which depend on the frequency sampling. The allowed frequencies are determined by the sampling rate but the resolution is limited by the duration τ of the sample. Under the assumption that noise is stationary, this quantity to be computed for any start time. The PSD will thus be time independent for stationary noise. Of course, in real searches it is impossible to isolate the background noise n from GW signals and terrestrial transients known as glitches. For this reason, the PSD is really estimated by substituting the noise n by the detector data stream s in all the above calculation. In this process, the presence of low frequency transients and real GW signals in the data may corrupt the estimation of the PSD. Also, simulated signals are commonly injected in the data in order to asses the sensitivity of the search [38] which can further affect the estimation of the PSD if they are too numerous. A technique for alleviating these effects consists in estimating the PSD as the average (or rather median) of different instances of the discrete PSD. This is known as the Welch method [120] and has been commonly applied in GW searches like [38].

3.2.2 Basic waveform operations.

Given two complex functions $h(t)$ and $g(t)$, their inner product $\langle | \rangle$ is defined as

$$\langle h(t)|g(t)\rangle = \int_{-\infty}^{\infty} \frac{\tilde{h}(f)\tilde{g}^*(f) + \tilde{h}^*(f)\tilde{g}(f)}{S_n(f)} df, \qquad (3.25)$$

where $\tilde{a}$ denotes the Fourier transform of $a(t)$ with respect to t and $S_n(f)$ is the one-sided power spectral density of the noise. In the particular case that both h and g are real, the relation $\tilde{g}^*(f) = \tilde{g}(-f)$ allows to rewrite

$$\langle h(t)|g(t)\rangle = 4\mathcal{R} \int_0^{\infty} \frac{\tilde{h}(f)\tilde{g}^*(f)}{S_n(f)} df. \qquad (3.26)$$

The overlap $\mathcal{O}$ of h and g is then defined as their normalized inner product

$$\mathcal{O}[h, g] = \frac{\langle h|g \rangle}{\sqrt{\langle h|h \rangle \langle g|g \rangle}}. \tag{3.27}$$

Where $\sqrt{\langle h|h \rangle} \equiv ||h||$ is the norm of h. In our particular case h and g will represent gravitational waveforms and the variable t will denote time. However, in general both h and g will be functions of several parameters $\{x_i\}$ like the total mass of the source M, its mass ratio q or the polar angle θ. There could be also a time-shift t_0 between h and g. The overlap of two functions maximized over the parameters $\{y_i\} \in \{x_i\}$ will be called match and denoted by

$$\mathcal{M}[h, g]_{\{y_i\}} = \max_{\{y_i\}} \mathcal{O}[h, g]. \tag{3.28}$$

3.2.3 Detecting signals: The matched filter and statistics in Gaussian noise.

The output $s(t)$ of a GW detector consists in general of a superposition of a gravitational wave signal $g(t)$ and background noise $n(t)$, so in general we have

$$s(t) = g(t) + n(t). \tag{3.29}$$

The background noise $n(t)$ can be assumed to consist of a superposition of stationary zero-mean Gaussian noise represented by $S_n(f)$ and transients of terrestrial origin known as glitches. When the latter is neglected, the best possible filter in order to decide if a signal $h(t)$ is buried in $s(t)$ is the well known matched filter. Its output, the signal-to-noise ratio (SNR), can be expressed as

$$\rho[s, h] = \frac{\langle s|h \rangle}{\sqrt{\langle h, h \rangle}}. \tag{3.30}$$

In Gaussian noise with zero mean, ρ is Gaussian distributed with zero mean and standard deviation one, which means

$$f(\rho) = \frac{1}{\sqrt{2\pi}} e^{-\rho^2/2}, \tag{3.31}$$

where f is the probability density function for the pure Gaussian noise to generate a value of the SNR equal or larger than ρ when filtered with the template h. Given this, if the SNR crosses some threshold ρ_0, it can be assumed that something else than Gaussian noise is present in the data, in which case we will claim to have a trigger. Assuming that data consists only of Gaussian noise and a GW signal, one can assume that the signal h (or some GW signal with a large match) is buried in the detector data. In other

words, the presence of a GW signal g in the data stream modifies the statistical Gaussian distribution that the SNR has in pure Gaussian noise. In particular, the expected value of $\rho[n+g|h]$ is given by

$$< \rho[s|h] >=< \rho[n+g|h] >=< \rho[n|h] > + < \rho[g|h] >= 0 + \rho[g|h], \qquad (3.32)$$

where $<>$ indicates averaging over realizations of n. One can check that $\rho[g|h]$ will be maximal when g is filtered with g itself, i.e, when $h = g$. We will thus define the optimal SNR of a signal g as $\rho_{opt} = \rho[g,g]$. If however g is filtered with a template that has an overlap of $\mathcal{O}$ with it then we have

$$\rho[h|g] = \frac{\langle h|g \rangle}{\sqrt{\langle h|h \rangle}} = \frac{\langle g|g \rangle \langle h|g \rangle}{\langle g|g \rangle \sqrt{\langle h|h \rangle}} = \frac{\langle g|g \rangle}{\sqrt{g|g}} \frac{\langle g|h \rangle}{\sqrt{\langle g|g \rangle \langle h|h \rangle}} = \mathcal{O} \times \rho_{opt}. \qquad (3.33)$$

Thus the SNR will drop by a factor $\mathcal{O}$ and the probability that h of having a trigger will decay consequently.

3.2.4 Optimized SNR, Fitting Factor and Horizon Distance

Since the parameters of an incoming GW are not known a priori, GW searches are carried out filtering the incoming data $s = g + n$ with a set of templates $h_{\mathcal{B}}$ from a given template bank $\mathcal{B}$. The templates, $h_{\mathcal{B}}(\Xi, \Lambda; t)$ aim to represent the signals emitted by the sources we aim to detect. The *fitting factor* $\mathcal{F}$ of $\mathcal{B}$ towards a waveform g is defined as the maximum of the overlaps $\mathcal{O}$ of g among all the templates forming $\mathcal{B}$. Thus we define

$$\mathcal{F}_{\mathcal{B}}(g) = \max_{\Xi, \Lambda, t_0} \mathcal{O}[g, (h_{\mathcal{B}}(\Xi, \Lambda, t_0)]. \qquad (3.34)$$

This gives the maximum fraction of the optimal SNR $\mathcal{F}_{\mathcal{B}}(g) \times \rho[g,g]$ that the template bank $\mathcal{B}$ can recover from g when averaged over realizations of the Gaussian noise. The fitting factor is also known as the effectualness of the bank towards g. It is worth to recall that g depends on both the intrinsic parameters of the source Ξ and on the extrinsic parameters Λ. Thus for the same Ξ, different values of Λ will give different fitting factors. Looking at (3.14) it is clear that the SNR produced by a source will be inversely proportional to the luminosity distance d_L. If a given threshold SNR ρ_0 is set in order to claim a trigger, the horizon distance d_H is equal to the maximum distance d_L at which a given source can produce an SNR $\rho \geq \rho_0$. If a signal g emitted from a distance d_L produces an SNR ρ when it is filtered with g itself we then have

$$\frac{\rho_0}{d_H} = \frac{\rho}{d_L} \Rightarrow d_H = d_L \frac{\rho}{\rho_0}. \qquad (3.35)$$

If however g is filtered with a template bank with fitting factor $\mathcal{F}_\mathcal{B}(g)$ to g we have instead

$$d_H^\mathcal{B} = d_L \frac{\mathcal{F}_\mathcal{B}(g)\rho}{\rho_0} = d_H \mathcal{F}_\mathcal{B}(g). \tag{3.36}$$

Thus the maximum distance at which the source can be detected will decay to a fraction of $\mathcal{F}_\mathcal{B}(g)$ and consequently the accessible volume in which g can be detected will decay to a fraction of $\mathcal{F}_\mathcal{B}(g)^3$. In Chapter 6, we will see how averaging the *fitting factor* over all the possible extrinsic parameters Λ of g allows for the definition of an *effective fitting factor* and to its interpretation in terms of sensitive volume loss.

3.2.5 Causes of imperfect filtering

In an ideal situation, for any given signal g, a template bank would be such that $\mathcal{F}_\mathcal{B}(g) = 1$ and then $\rho = \rho_{opt}$. However, there are various reasons why an incoming signal g may not be optimally filtered. Let us summarize the main ones:

- Presence of noise: First of all, let $\mathcal{B}$ be a bank that contains all the perfect representations of all the possible GW signals. In the absence of noise n, we have $s = g$ and we could always filter g optimally, i.e, we would always find $\mathcal{F}_\mathcal{B}(s) = \mathcal{F}_\mathcal{B}(g) = 1$. However, the presence of noise in our detector will make that in general $\mathcal{F}_\mathcal{B}(s) \neq 1$ and $\rho \neq \rho_{opt}$. This can give raise to two situations:

  1. The SNR just drops, and the probability of a detection decays.
  2. The combination $n + g$ is detected by a waveform other than g, with $\rho \neq \rho_{opt}$ and so the parameters are wrongly estimated.
  3. The glitches: Suppose there is no GW in the data. It is common that noise transients g_n present in the data produce an SNR large enough to claim a trigger. These features, known as glitches, commonly consist on very strong bursts that have a very large intrinsic SNR $\rho[g_n|g_n]$ such that $\rho = \rho[g_n|g_n] \times \mathcal{F}_\mathcal{B}(g_n)$ is larger than the required trigger threshold. If glitches are not identified they may lead to false detections. When a trigger is found in a search, several tests are applied to the data in order to discriminate between GW and glitches. The most common are the various χ^2 and bank veotes and the r-test [38] [121].

- Wrong modeling of the GW signals: suppose now that the data cosists only on a GW g. It is possible however that the templates in the template bank are not accurate descriptions of the incoming signal. This will lead to $\mathcal{F}_\mathcal{B}(g) < 1$. In Chapter 6, we will study this effect for the case that signals contain HOM and templates are quadrupolar.

- Discreteness of the template bank: Template banks used in real searches are discrete. Template banks are usually constructed such that no more than 10% of signals will be missed due to the its discreteness. This means that the minimum match of the template bank to any of the signals of the corresponding continuous version has to be $\mathcal{M} \geq \sqrt[3]{0.9} \simeq 0.97$.

3.2.6 Analytical optimization of SNR and overlap

The match of two waveforms and the maximization of the SNR over the parameters of the template involves a maximization over the extrinsic parameters Λ of either one or both of the waveforms and over relative time-shifts t_0. The maximization over the t_0 or "time of arrival" is commonly performed analytically by means of the inverse Fourier transform as

$$\mathcal{M}_t(h, g) \equiv \max_t \mathcal{O}(h, g) = \max_t 4\mathcal{R} \frac{\int_0^\infty \frac{\tilde{h}(f)\tilde{g}^*(f)}{S_n(f)} e^{-2\pi i t f} df}{\sqrt{\langle g|g \rangle \langle h|h \rangle}}. \tag{3.37}$$

The maximization over the extrinsic parameters Λ is however more involved and needs to be carried out numerically, except in the special case that at least one of the two waveforms is quadrupolar. Previously we showed that any quadrupolar waveform can be expressed as

$$h^D = \bar{\mathcal{H}}_{2,2} A_{2,2} \left[\cos\gamma_{2,2} \cos\phi_{2,2} + \sin\gamma_{2,2} \sin\phi_{2,2} \right], \tag{3.38}$$

where $A_{2,2}$ and $\phi_{2,2}$ depend on the intrinsic parameters Ξ of the source and the time, and the dependencies on extrinsic parameters is encoded in $\mathcal{H}_{2,2}$ and $\gamma_{2,2}$. The Fourier transform of signals whose phase varies much faster than their amplitude (i.e., highly oscillating signals), such as the chirping signals we deal with, can be approximately computed by means of the stationary phase approximation (SPA) [122]. In this context, the Fourier transforms of two signals $a^+(t) = A(t)\cos(\phi(t))$ and $a^\times(t) = A(t)\sin(\phi(t))$ are related by

$$\tilde{a^+}(f) = -i\tilde{a^\times}(f), \tag{3.39}$$

In the context of GW searches, this relation is noted and utilized in for instance [38]. In order to derive (3.39) we recommend to look at [123], pag. 65 and simply change the factor $(e^{i\phi(t)} + e^{-i\phi(t)})$ in (3.30) by $\frac{(e^{i\phi(t)} - e^{-i\phi(t)})}{i}$.

Given this, denoting $h_{2,2}^+ \equiv A_{2,2} \cos \phi_{2,2}$[2], the Fourier transform of h can then be expressed as

$$\tilde{h} = \bar{\mathcal{H}}_{2,2} \tilde{h}_{2,2}^+(\Xi;t) \left[\cos \gamma_{2,2} - i \sin \gamma_{2,2} \right] = \bar{\mathcal{H}}_{2,2} \tilde{h}_{2,2}^+ e^{-i\gamma_{2,2}}. \tag{3.40}$$

The overlap of two quadrupolar waveforms can be expressed as

$$\mathcal{O}[h_1, h_2] = 4\mathcal{R} \frac{\int \bar{\mathcal{H}}_1 \tilde{h}_1^+ e^{-i\gamma_1} \bar{\mathcal{H}}_2 \tilde{h}_2^{+,*} e^{+i\gamma_2} df}{\bar{\mathcal{H}}_1 \bar{\mathcal{H}}_2 ||h_1^+|| ||h_2^+||} = 4\mathcal{R} \frac{\int \tilde{h}_1^+ \tilde{h}_2^{+,*} e^{-i(\gamma_1-\gamma_2)} df}{||h_1^+|| ||h_2^+||}, \tag{3.41}$$

where maximization over the phase $\gamma_1 - \gamma_2$ can be done by taking the absolute value of the integral instead of the real part, thus

$$\max_{\gamma_1,\gamma_2} \mathcal{O}[h_1, h_2] = 4 \frac{|\int \tilde{h}_1^+ \tilde{h}_2^{+,*} e^{-i(\gamma_1-\gamma_2)} df|}{||h_1^+|| ||h_2^+||} = 4 \frac{|\int \tilde{h}_1^+ \tilde{h}_2^{+,*} df|}{||h_1^+|| ||h_2^+||}. \tag{3.42}$$

Optimizing also over time gives

$$\max_{\gamma,t_0} \mathcal{O}[h_1, h_2] = \max_{t_0} 4 \frac{|\int \tilde{h}_1^+ \tilde{h}_2^{+,*} e^{-i2\pi f t_0} df|}{||h_1^+|| ||h_2^{+,*}||}. \tag{3.43}$$

So the match of two quadrupolar waveforms optimized over time and phase is just the normalized inner product or overlap their "+" components. Similarly, for the SNR, for any incoming signal s we get

$$\max_{\gamma,t_0} \rho[s, h] = \max_{t_0} 4 \frac{|\int \tilde{s} \tilde{h}^{+,*} e^{-i2\pi f t_0} df|}{||h^+||}. \tag{3.44}$$

The latter equation implies that in order to maximize the SNR $\rho[s|h(\Xi)]$ over all the possible templates $h(\Xi, \Lambda; t)$ with common intrinsic parameters Ξ, it suffices to compute (3.44) with $h^+ = h(\Xi, \Lambda_0; t_0)$. Once again, this holds if h is a quadrupolar waveform. In a hypothetic search where HOM are included in templates, one would need to filter the incoming signal with templates constructed for all the possible Λ and numerically optimize over them.

Modification of SNR statistics in Gaussian-noise due to maximization over phase and the False Alarm Rate.

The SNR of a single template, in Gaussian noise, is Gaussian distributed with probability density function (PDF)

$$f(\rho) = \frac{1}{\sqrt{2\pi}} e^{-\rho^2/2}. \tag{3.45}$$

---

[2]One can write in general $h_{\ell,m} = h_{\ell,m}^+ - i h_{\ell,m}^\times$. Although this is a very common notation, it can lead to a misunderstanding of what the GW polarization is and we will try to avoid it as much as possible. For completeness, note that $\langle h_{\ell,m}^+ | h_{\ell,m}^\times \rangle = 0$.

However, when we maximize the SNR over the extrinsic parameters of a template, we really are looking for the maximum SNR among a family of templates, thus the statistical distribution of the SNR must change. It is easy to obtain the distribution of the maximized SNR taking advantage of the analytical formula we use to maximize it [see (3.44)]. We just take the absolute value of

$$\frac{\int_0^\infty \frac{\tilde{s}(f)\tilde{h}^*(f)}{S_n(f)}df}{\sqrt{\langle h|h \rangle}} = x + iy \tag{3.46}$$

Thus the maximized SNR ρ is just equal to $\sqrt{x^2 + y^2}$. Since x and y are Gaussian distributed in Gaussian noise we have

$$\begin{aligned}
P(\rho > \rho_0) &= P(x > \rho_1)P(y > \sqrt{\rho_0^2 - \rho_1^2}) \\
&= \frac{1}{\sqrt{2\pi}}\frac{1}{\sqrt{2\pi}}\int_{\rho_1}^\infty \int_{\sqrt{\rho_0^2-\rho_1^2}}^\infty e^{-x^2/2}e^{-y^2/2}dxdy.
\end{aligned} \tag{3.47}$$

Choosing polar coordinates $x = \rho\cos\phi$, $y = \rho\sin\phi$ we can rewrite (3.47) as

$$\frac{1}{2\pi}\int_0^{2\pi} d\phi \int_{\rho_0}^\infty \rho e^{-\rho^2/2}d\rho = 2\pi\frac{1}{2\pi}\int_{\rho_0}^\infty \rho e^{-\rho^2/2}d\rho \tag{3.48}$$

so that the PDF for the maximized SNR is the so called Rayleigh distribution

$$f(\rho) = \rho e^{-\rho^2/2}, \tag{3.49}$$

and the probability that we measure a certain SNR ρ_0 or larger is,

$$P(SNR > \rho_0) = e^{-\rho_0^2/2}. \tag{3.50}$$

Searches for GW are performed filtering the data with the N templates of the template bank. If we assume them to be statistically independent, then the probability that n templates produce an SNR larger than ρ_0 out of N attempts is [124]

$$P(n; SNR > \rho_0, N) = \frac{N!}{n!(N-n)!}e^{-n\rho_0^2/2}(1 - e^{-\rho_0^2/2})^{N-n}. \tag{3.51}$$

We can then compute the probability that at least one attempt out of N produces an SNR larger than ρ_0 by first evaluating the probability that no attempt does. We then obtain that

$$P(SNR_N > \rho_0) = 1 - P(0, SNR > \rho_0, N) = (1 - e^{-\rho_0^2/2})^N \simeq Ne^{-\rho_0^2/2}, \tag{3.52}$$

where the last equality holds as long as $e^{-\rho_0^2/2} \ll 1$ and for large N. This defines the false alarm rate (FAR) of a search when the noise is assumed to be Gaussian with zero-mean. The FAR is then directly related to the number of templates one filters with. A search including only non-spinning templates will have less chances to detect a generic GW but will in turn have a lower FAR than a template bank including aligned-spin templates. As an example, the non-spinning template bank used in [69] contained ~ 28000 templates while the spinning version needed ~ 150000 which in principle increments the FAR by a factor of ~ 6. A very naive first analysis shows that if we wanted to keep the same FAR for the second search we would require a new SNR threshold ρ_S such that

$$FAR_{NS} = FAR_S \Rightarrow N_{NS}e^{-\rho_{NS}^2/2} = N_S e^{-\rho_S^2/2}, \tag{3.53}$$

where the subscripts NS and S denote non-spinning and aligned-spin search respectively. Since $\rho_{NS} = 8$ and $N_S = 6N_{NS}$, one obtains $\rho_S \sim 8.22$. A more detailed calculation [69] [125], yields a value of 8.3. This means that we would need signals a $\sim 3\%$ louder in order to claim a trigger, reducing by a factor of $\sim 10\%$ the sensitive volume achieved if one could keep a threshold value of 8. Roughly, this means that a search including spinning template banks would be more sensitive that a non-spinning one for the region of the parameter space where the non-spinning template bank has a fitting factor < 0.97. For instance, a spinning search will be less sensitive to non-spinning sources than a non-spinning search but will be more sensitive to spinning sources for which the non-spinning bank has a fitting factor < 0.97. In fact, [69] showed that for NS-BH targets with spins uniformly distributed in $(-1, 1)$, the sensitive volume of a search with aligned-spin templates increases by $\sim 50\%$ compared to the non-spinning search, while for signals with aligned spins uniformly distributed in the range $(0.7, 1)$, the increment is of a factor of ~ 10.

3.3 Gravitational Wave Searches: Real noise and identification of glitches

The SNR has a clear statistical meaning when the background noise is assumed to be Gaussian and with zero mean: it is directly related to the probability that a GW is buried in the noise if one assumes that data consists on a combination of GW and Gaussian noise. In real searches however, there are two main non-Gaussian sources of triggers: gravitational waves and glitches. The presence of glitches makes background distributions differ from those predicted in Gaussian noise at high SNR. The SNR is then not enough to evaluate the probability of an event being a real GW and a more detailed description is needed. In other words, an event is not univocally described by its

SNR. To this end, searches use two approaches. Together with the SNR, GW searches test the consistency of the signal with a GW via consistency test such as the χ^2 or bank vetoes [126] [121]. These aim to measure properties of the signal further than the simple SNR. Their output are quantities whose statistical distribution can be computed both under the supposition that the signal contains Gaussian noise or Gaussian noise plus a GW signal. The χ^2 can be then combined with the SNR to give a new definition of the measured event and provide an event ranking statistic. If this is suitably chosen, the larger it is, the larger the probability of having a GW will be. In particular, the pycbc and ihope pipelines combine the ρ and χ^2 numbers into the so called new SNR (ρ_{new}) [38]. The significance of the event is then evaluated by looking at the background distribution of such ρ_{new}. This is, one measures with which frequency the background is able to produce events with a certain ρ_{new}. Note that this probability would raise if one looked at only ρ, since less information about the true GW signal would be used, and less accurate reproduction of the searched signal by the background would be required. Thus, the more detail one can describe events in, the less probable that the background reproduces them, and the better GW's and glitches will be discriminated.

3.3.1 Signal Based Vetoes

Signal based vetoes aim to measure whether the incoming signal is consistent with a gravitational wave or not by looking at further properties than the plain SNR. A GW signal can be thought of as a vector belonging to some a vector space $\mathcal{W}$ whose inner product is just (3.26). With this description, the SNR is simply the projection of the signal s along the direction defined by the template h. We are missing the angle they form. A glitch is thus a signal that has a large projection over h but is not h, so the angle between s and h is not 0. The χ^2 tests provide effective attempts to measure this angle or overlap.

The classic χ^2 veto.

The classical χ^2 veto [126] expresses h as a combination of p sub-waveforms h_i such that $\rho[h_i|h_i]^2 = \rho[h_j|h_j]^2 = \rho[h|h]^2/p = \rho^2/p \ \forall \ i,j$. Thus if s is really a GW represented by h, in the absence of noise one should have $\rho_i = \rho[s|h_i] = \rho_j \forall \ i,j$. In the presence of Gaussian noise, the ρ_i values follow instead statistical distributions. We recall that the SNR is the real part of a complex number, i.e., $\rho[s|h] = \mathcal{R}z/\sigma$, where sigma is the norm

of the template, i.e.,

$$\rho_{complex} = 2\frac{z}{\sigma}$$
$$z = \int_{f_0}^{\infty} \frac{\tilde{s}(f)\tilde{h}(f)^*}{S_n(f)} df \tag{3.54}$$
$$\sigma^2 = \int_{f_0}^{\infty} \frac{\tilde{h}(f)\tilde{h}(f)^*}{S_n(f)} df.$$

Assuming that the template h does only contain quadrupolar modes, one can consider the real part of $\rho_{complex}$ as the SNR obtained when s is filtered with a template h_0 and the imaginary part as the SNR obtained when filtering s with h_0 phase-shifted by $\pi/2$, i.e., $h_{\pi/2}$. Due to this, it is usually written

$$\rho_{complex} = 2\frac{(\rho[s|h_0] + i\rho[s|h_{\pi/2}])}{\sigma}. \tag{3.55}$$

The classic chi-square χ_c^2 is defined then as

$$\chi_c^2 = \sum_i^p |z_i - z/p|^2, \tag{3.56}$$

where $z_i = \rho_{complex}[s|h_i]$. In Gaussian noise χ^2 is chi-squared distributed with $2p - 2$ degrees of freedom and has an expectation value of [121]

$$\langle\chi_c^2\rangle = \min\{2\delta\rho^2, 2p\delta^2\rho^2\}, \tag{3.57}$$

where δ is a measure of the possible mismatch between signal and template due to, for example, the discreteness of the template bank. Recall that in current GW searches from CBC's, $\delta = 0.03$. In practice, the N subtemplates that h is decomposed into, are the result of chopping the Fourier domain expression of h into N pieces that have equal optimal SNR. What we are measuring is if the amount of SNR produced by each piece is consistent with what is expected from the true waveform. Real GW signals that are really similar to h will give low χ^2 values while glitches should produce significantly larger ones. This veto has been used in GW search pipelines like ihope [38] and is currently employed by the pyCBC toolkit [69].

The template bank veto

A more geometrical approach to the identification of glitches is the so called bank veto [121], implemented in the gstlal pipeline. The templates h_i that form a template bank are correlated by their overlap $\mathcal{O}_{ij} \equiv \mathcal{O}[h_i|h_j]$. Suppose that h_i is triggered by a signal s with an SNR $\rho_i = \rho[s|h_i]$. In the absence of noise one should expect $\rho_j = \rho[s|h_j] = \mathcal{O}_{ij} \times \rho_i$.

The bank χ^2 veto is then defined as

$$\chi_B^2 = \sum_{j=1}^{N} \frac{|z_j - \mathcal{O}_{ij}\rho_i|^2}{1 - |\mathcal{O}_{ij}|}, \tag{3.58}$$

Its expected value is given by

$$\langle \chi_B^2 \rangle \le N\rho_i^2 \left[\frac{1}{1-\delta} - 1 \right]^2 \simeq N\rho_i\delta^2, \tag{3.59}$$

where the last equality stands for low δ.

Accounting for the χ^2: the newSNR

The two described methods attempt to identify glitches by finding excesses/lacks of power in determined regions of the waveform manifold that are inconsistent with s containing h. Note that this does not necessarily mean that g does not contain a GW: if such a GW is wrongly modeled by the template bank or is just not included [3] it will have a large χ^2 value and will be interpreted as a glitch. Also, a low value of the χ^2 does not guarantee that the data contains a GW. The χ^2 vetoes explore a finite number of the signal-vector-space dimensions and thus can only find excesses of power in a limited number of them. In more geometric terms, χ^2 tests are an attempt to measure the the overlap between the incoming signal and the triggered template. The SNR and χ^2 are usually recombined in what is known as the newSNR (ρ_{new}). The exact expression for $\rho_{new}(\rho, \chi^2)$ is obtained after tunning. Such a tunning is done by injecting simulated signals (injections) into data and looking for the expression of ρ_{new} that best discriminates triggers due to injections from those due to glitches. As an example [38] used,

$$\rho_{new} = \begin{cases} \rho & \text{if } \chi^2 \le 2p - 2 \\ \rho \left[\frac{1}{2} \left(1 + (\frac{\chi^2}{2p-2})^3 \right) \right]^{-1/6} & \text{if } \chi^2 > 2p - 2. \end{cases} \tag{3.60}$$

Fig. 3.1 shows SNR vs. χ^2 results for both injections (red) and glitches (blue) and the corresponding constant ρ_{new} lines. Note how for this particular case, the green line gives a reasonably good separation of injections and signals for $\rho > 8$.

The high mass problem with glitches.

The newSNR has been proven to be particularly efficient separating low mass-high SNR signals from the background noise. However, high mass signals, which are shorter than

---

[3]For instance consider that the data contains a GW spinning signal and that the bank is non-spinning.
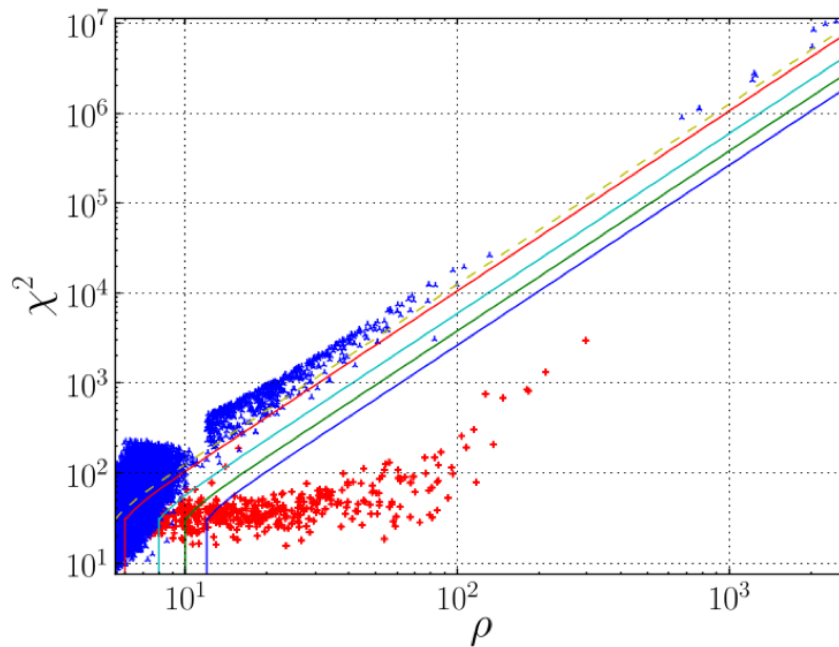
FIGURE 3.1: SNR-χ^2 plane for several triggers due to both injections (red) and glitches (blue). Colored lines represent constant ρ_{new} lines. Credit [38].

low mass ones, can be such that both signals and glitches give similar results when the χ^2 test is performed, making them indistinguishable. In particular, for high mass signals, the late part of the Fourier domain waveform, which corresponds to the merger-ringdown stage, is particularly well imitated (see Fig. 3.2) by a concrete class of glitches known as sine-Gaussian glitches [127]. In the Fourier domain these take the form

$$S_g(f) = \frac{\sqrt{\pi}}{2}\tau e^{-\pi^2\tau^2(f-f_0)+i\phi_0}\left[1 + e^{-Q^2\frac{f}{f_0}-2i\phi_0}\right], \tag{3.61}$$

where Q is the quality factor and f_0 the central frequency. The initial phase ϕ_0 can be neglected for practical purposes as long as $Q > 1$. Fig.3.2 shows the Fourier transform of a $q = 1$ non-spinning waveform together with a sine-Gaussian glitch with $(Q, f_0) = (5, 108)$. The waveform has been re-scaled so that it compares in amplitude with the glitch. In order to estimate by eye how large the overlap is, the plot shows also the early Advanced LIGO noise PSD multiplied by a factor of 10^{40}. Note that in the region where the PSD has its minumum (known as sweet-spot), both waveform and glitch almost overlap each other. In fact their actual overlap is 0.886. Further, and in order to get an estimation of how indistinguishable sine-Gaussian glitches and GW signals can become as the total mass of the system grows, Fig.3.3 shows the Fitting Factor of a set of SEOBNRv1 waveforms to a bank of sine-Gaussian glitches. Note that in general, the larger the mass of the system is, the larger the overlap between sine-Gaussians and signal is. This justifies that the performance of χ^2 tests decays as the total mass of the
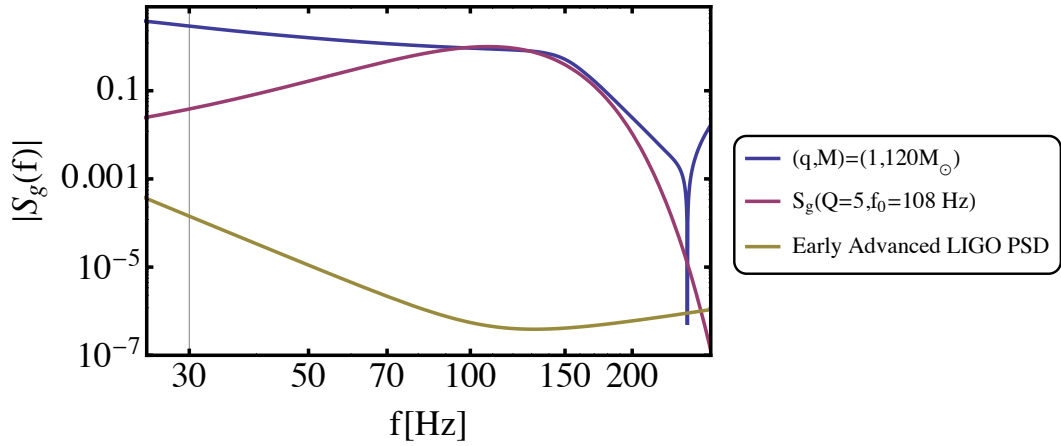
FIGURE 3.2: The plot shows an SEOBNRv1 ROM waveform and a sine-Gaussian glitch with the parameters specified in the legend. The waveform has been re-scaled such that it has the same amplitude as the glitch. Since global amplitude factors do not affect the match between waveform and glitch, this facilitates the by-eye estimation of their overlap. Their actual match is 0.886.

triggered template grows. Note also how the lower frequency cutoff of Advanced LIGO allows for a better distinction of GW's and glitches, getting the largest match down to ~ 0.6, in contrast with the ~ 0.90 obtained for early Advanced LIGO. This suggest that sine-Gaussian glitches should be much less relevant once the detector has reached its design sensitivity.
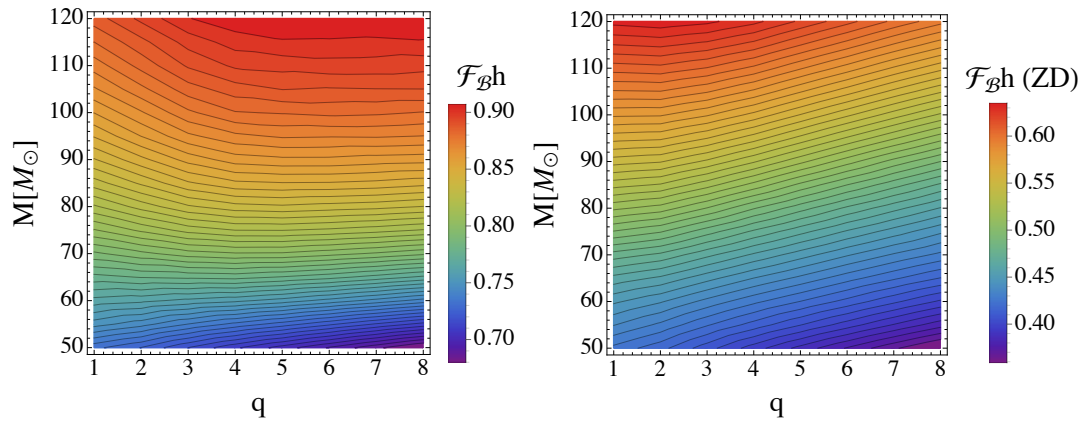
FIGURE 3.3: Fitting factor of a of bank sine-Gaussian glitches ranging in $Q \in [1, 10]$, $f_0 \in (20, 500)$ to SEOBNRv1 waveforms. We consider the noise curves for Early advanced LIGO with a 30 Hz cutoff (left), and the Zero Detuned High Energy Power curve with a 10 Hz cutoff (Right). The axes correspond to the mass ratio q and total mass M of the target waveform. Results show that for a given mass ratio, the larger the total mass the more similar sine-Gaussian glitches are to the GW signal. This makes them more difficult to identify via χ^2-tests (and in general).

3.4 Parameter Estimation of signals from CBC

3.4.1 Systematic biases

Let $h(\Xi)$ be a waveform with intrinsic parameters Ξ and let $\mathcal{B}$ be a template bank built of waveforms $h_i^{\mathcal{B}}(\Xi_i^{\mathcal{B}})$. The maximum fraction of SNR that $\mathcal{B}$ can recover from h is given by the fitting factor of $\mathcal{B}$ towards h, $\mathcal{F}_{\mathcal{B}}h$ and the corresponding recovered parameters $\Xi_{max}^{\mathcal{B}}$ are the ones of the template $h_{max}^{\mathcal{B}}$ for which $\mathcal{M}_h h_{max}^{\mathcal{B}}(\Xi_{max}^{\mathcal{B}}) = \mathcal{F}_{\mathcal{B}}h$. In general one has

$$\Xi_{max}^{\mathcal{B}} = \Xi_h + \delta\Xi_{sys}, \tag{3.62}$$

and we call $\delta\Xi_{sys}$ the systematic parameter bias of $\mathcal{B}$ towards h. A systematic parameter bias has its origin on the models describing both waveforms being different, i.e., the two models give slightly different waveforms for the same parameters Ξ. These kind of biases make in principle that model A cannot correctly estimate the parameters of a waveform of the model B. However, if the error $\delta\Xi_{sys}$ is small enough, it is possible that it gets dominated by statistical uncertainties due to the presence of noise in the data in which h may be buried.

3.4.2 Statistical uncertainty

Consider that we now compute the fitting factor $\mathcal{F}_{\mathcal{B}}h$ of a bank made up of waveforms of the same family as h. In the absence of noise, it is trivial that the template that will have the best match with h will be h itself and that then $\mathcal{F}_{\mathcal{B}}h = \mathcal{M}_h h = 1$, so that $\Xi_{max}^{\mathcal{B}} = \Xi_h$, and the parameter bias will be $\delta\Xi = 0$. However, in a real search the presence of noise n makes the incoming data be $s = h + n$. This makes $\mathcal{F}_{\mathcal{B}}(h + n) \neq 1$ and $\delta\Xi \neq 0$. The size of $\delta\Xi$ depends on the particular realization of the noise n and its standard deviation σ will be an indicative of the resolution of our detector. If σ is such that $\delta\Xi_{sys} < \sigma$, then our systematic biases will not influence significantly the accuracy of the measurements and we shall assume that our waveform model is suitable for parameter estimation.

Currently, there are several criterions for estimating σ. One of the most common ones is the usage of the so called Fisher Information Matrix (FIM). In this formalism, a template is first expressed as an expansion around some Ξ_0 parameters up to first order as

$$h(\Xi) = h(\Xi_0) + \delta\Xi_i h_i + \cdots \tag{3.63}$$

Given a signal s, the likelihood p for given set of parameters $\Xi_r = \Xi + \delta\Xi$ being the recovered ones is given by [128] [129]

$$
\begin{aligned}
p(s|\Xi_r) &\sim \exp\left[-\frac{1}{2}\langle s - h(\Xi_r)|s - h(\Xi_r)\rangle \right] \\
&\sim \exp\left[-\frac{1}{2}\langle n|n\rangle + \delta\Xi_i\langle n|d_i\rangle - \frac{1}{2}\delta\Xi_i\delta\Xi_j\langle d_i|d_j\rangle \right],
\end{aligned}
\tag{3.64}
$$

where $d_i \equiv \frac{\partial h}{\partial \Xi_i}$. Note that p is a probability distribution over parameters Ξ that depends on the detector output s. In [130] it is shown that this linear approximation is equivalent to the leading term of p expanded as a series in $1/\rho$. It is for this reason that this calculation will be applicable in the high-SNR regime. The Fisher Information Matrix is then given by

$$
F_{ij} = \langle d_i|d_j\rangle. \tag{3.65}
$$

When we consider that $\delta\Xi_i$ are the displacements of the waveform parameters from the best-fitting values Ξ_0, (3.64) can be treated as a multidimensional Gaussian with variance-covariance matrix $\Sigma_{ij} = (F^{-1})_{ij}$. This formalism thus assumes that for sufficiently loud waveforms, p becomes a true Gaussian, and that Σ_{ii} describes the uncertainties in the measurement of the several parameters Ξ_i. In this limit, we thus expect that the uncertainties returned by parameter estimation will coincide with those predicted by the FIM. The standard deviations of the parameters are then given by

$$
\sigma_i = \sqrt{\Sigma_{ii}}. \tag{3.66}
$$

Computing the FIM of a family of waveforms can be cumbersome, especially if such a family is non-analytical and derivatives need to be computed using limits. Also, the number of dimensions/parameters one includes in the analysis will modify its value. Based on the same formalism [131] provide criteria for indistinguishability of two waveforms based on the SNR of $h(\Xi_0)$ and the distance (overlap) between it and any other template $h(\Xi_0 + \delta\Xi)$. Further, [111] re-wrote this criterion as a function of their mismatch $\epsilon = 1 - \mathcal{O}$ as

$$
\epsilon < \frac{1}{2\rho^2}, \tag{3.67}
$$

which provides a very simple test for deciding when two waveforms are indistinguishable. The threshold depends on the loudness of the signal (say h_1): the louder it is, the less likely it will be that the background Gaussian noise "makes it look" like something else.

Coming back to the problem of the separation between high mass signals and glitches (in particular sine-Gaussians), the results shown in Fig.3.3 suggest that although matches between signals and glitches are large, they are not that large that both waveforms are

really indistinguishable. As an example, using , for an SNR of 8, one would need a fitting factor of ~ 0.992 between glitch and waveform for them being indistinguishable. If this is true, then the results shown in Fig. 3.3, suggest that if sine-Gaussian glitches were incorporated to waveform template banks, bayesian parameter estimation should be able to distinguish between high mass signals and sine-Gaussian glitches.

Chapter 4

Modeling the full gravitational radiation from Compact Binary Coalescences: Construction of multi-modal hybrid waveforms

4.1 Introduction

In Chapter 2 we mentioned the concept of "hybrid waveform". A hybrid waveform is the result of joining two different waveforms in a single one. The goal of this construction is, in general, to obtain a waveform that can cover a lager period of the coalescence than each its components. For example, in a PN/NR hybrid waveform, the early inspiral is described by means of the PN approximation, which becomes inaccurate at late stages. In order to describe the late inspiral and eventual merger and ringdown one usually attaches the corresponding NR waveform (if available) which in turn is not long enough to cover the stages described by PN. The result is a waveform that covers all the stages of the coalescence described by the PN and NR waveforms. The very basic process of hybridizing two waveforms that aim to describe the same system is composed by two stages. First, one must correct for any different conventions that they might present [1]. Last, a piecewise function is constructed in which residual differences between PN and NR are smoothed in the so called hybridization region. Of course, in order to be able to perform such a construction, it is required that both waveforms describe some common period of the coalescence. This was a caveat only a decade ago, when NR simulations would cover so few cycles of the coalescence that in order to overlap them with the PN

---

[1] As for instance, different time domains or a different choice of the origin for φ.

result, one needed to hybridize at frequencies at which PN was not reasonably accurate anymore. A detailed study regarding the length of NR simulations needed for such a construction is given by [111]. The recent developments of NR simulations, particularly in the context of the SpEC code, have provided several simulations that can cover up to 80 GW cycles. Furthermore, in early 2015, a $q = 7$ non-spinning simulation covering 350 GW cycles was presented in [117].

PN/NR hybrid waveforms are not suitable for being used in searches or PE studies since one would need an enormous number of NR simulations that covers the searched parameter space. However, hybrid waveforms are the basis of phenomenological models [56] [36] and can be used as target signals (injections) to be injected in real detection pipelines in order to test their sensitivity, such as in [34]. The study of the construction of such objets when only the quadrupolar mode is considered, and the influence of the different parameters that go into the construction has been extensively performed for both constructions in time domain [111] and frequency domain [36] [132]. We note that hybrid waveforms containing HM have been already produced (although not publicly released) in the context of the NINJA-2 project [34] by the SpEC, Gatech, Llama and RIT groups and also in [2] for the purpose of testing the effect of higher order modes (HOM) in non-spinning CBC searches, to which side work made in the context of this thesis has contributed. Also, [133],[134], [135] have proposed several ways in which HOM can be hybridized. We will describes their main particularities later. We describe an slightly modified method for hybridizing HOM and proceed to the study of the main sources of PN and NR results for HOM and the influence on the final waveform. The aim of this chapter is to give a detailed procedure that can be followed for coherently constructing hybrid waveforms including higher order modes. Such a procedure does not only provide a standard framework but allows for the detection of errors or inconsistencies that might be present in either the NR or PN results that will automatically stand out. Furthermore, one of the main outcomes are obtention of several figures during the procedure that will yield new error sources and motivate the definition of new figures of merit that will allow to test the influence of several parameters that go into the calculation of both PN and NR waveforms. This will serve for testing not only the accuracy of the final hybrid waveform, but that of the PN and NR waveforms themselves.

The rest of this chapter is organized as follows. Sec. 4.2 will describe the basic definitions regarding waveforms and their possible ambiguities. This will be needed for "putting into agreement" both the NR and PN sides. Section 4.3, will be devoted to discuss the general principles of the construction of hybrid waveforms. In particular, we will discuss the existence of three degrees of freedom required to align PN and NR waveforms. Section 4.4 will provide a brief review regarding the construction of single-mode hybrid waveforms and the corresponding sources of error will be identified and discussed. In

In Section 4.5 a method for coherently constructing our hybrids with higher modes will be described. Let us anticipate that the next chapter will be devoted to the study of residual disagreements between PN and NR in the hybridization region after alignment and identify their origin for afterwards evaluating the influence of NR extraction radius (and extrapolation) on the hybrid in terms of waveform matches.

The numerical waveforms that will be used in this chapter and the next one have been taken from the publicly available SXS catalogue [115] (computed by the SpEC code [97, 101, 102, 104–106, 136–141]),and from a set of waveforms that have recently been constructed with the BAM code [107, 108]. The illustrative examples will focus on mass ratios 8 and 18, where contributions from HM are significantly stronger than for roughly equal masses, but where it is computationally much more expensive to extend NR calculations to low frequencies, where PN is reliable. The results presented in this chapter and Chapter 5 are the basis of [1], which was done in collaboration with the LIGO groups in UIB and Cardiff University, who kindly provided the BAM $q = 8$ and $q = 18$ simulations.

4.2   Waveform definitions and ambiguities

The main goal here is to construct a hybrid waveform from two independently computed pieces, or more generally to compare any two waveforms, such as the results of two numerical relativity calculations. Consequently we then need to understand the different conventions and possible ambiguities that went into the definition of both pieces. We have already described general expressions for CBC waveforms in Chapter 3. However we will here give a brief review and make emphasis in the possible ambiguities that might appear in such a description. Since in particular we will deal with NR waveforms, we will start defining them in terms of the Newman-Penrose scalar Ψ_4, which is the waveform quantity directly computed in many NR codes, and afterwards focus on the strain h, which is the quantity directly relevant to the data analysis of current ground-based gravitational wave detectors. Ψ_4 is computed by contracting the Weyl tensor $C_{\alpha\mu\beta\nu}$ with the appropriate elements of a suitable null tetrad ℓ^μ, m^μ, $\bar{m}^\mu$, n^μ (see [96] for a detailed description of the formalism). As an example, the BAM code uses the definition

$$\Psi_4 = -C_{\alpha\mu\beta\nu}n^\mu n^\nu \bar{m}^\alpha \bar{m}^\beta, \tag{4.1}$$

where ℓ and n are ingoing and outgoing null vectors and $-\ell \cdot n = 1 = m \cdot \bar{m}$. The precise choices made in this code can be found in Sec. III of [107]).

The definition of Ψ_4 carries with it several ambiguities, starting with the overall sign convention for the Riemann and Weyl tensors (including metric signature). As examples, in the BAM code [107] the conventions from Misner, Thorne and Wheeler [71] are used, and the opposite sign is used in the SpEC code (see e.g. the comment above Eq. (2.100) of [142]). In addition, the overall sign in (4.1) is a convention that may change between different authors.

Furthermore, there is freedom in the choice of the tetrad. While ℓ^μ, n^μ will coincide between different codes in the limit $r \to \infty$, there is no canonical choice [2] for the complex null vector m^μ which can be rotated by some angle σ ($m^\mu \to e^{i\sigma} m^\mu$), leading to a redefinition $\Psi_4 \to e^{-2i\sigma} \Psi_4$. The different choices in the definition of Ψ_4 thus amount to an ambiguity $\Psi_4 \to e^{i\psi_0} \Psi_4$, which in physical terms is simply the freedom in defining the two gravitational wave polarizations.

The two real polarizations h_+ and $h_\times$ of a gravitational wave can be conveniently represented as a complex strain

$$h(t, \theta, \varphi; \Xi) = h_+(t, \theta, \varphi; \Xi) - ih_\times(t, \theta, \varphi; \Xi) , \tag{4.2}$$

where t is an inertial coordinate at null infinity, θ is chosen as the angle between the line-of-sight from the detector to the source and the total angular momentum of the binary (which we choose as our z-axis), φ is an azimuth angle in the source frame, and the intrinsic parameters of the source are collectively denoted as Ξ. This quantity can be obtained from Ψ_4 by applying a double time integration (see [100] for a discussion of the issues arising in this procedure), or directly from projecting the metric perturbation onto some orthonormal polarization triad as is usually done in the PN context. Different choices of triad will again lead to a redefinition of the type $h \to e^{i\psi_0} h$ (see for instance Eq. (2.6) of [144]).

It is convenient to decompose the strain into spin -2 weighted spherical harmonic modes $h_{\ell,m}$ as

$$h(t, \theta, \varphi; \Xi) = \sum_{\ell=2}^{\infty} \sum_{m=-\ell}^{\ell} Y_{\ell,m}^{-2}(\theta, \varphi) h_{\ell,m}(t, \Xi), \tag{4.3}$$

where $Y_{\ell,m}^{-2}(\theta, \varphi)$ are the spin -2 weighted spherical harmonic basis functions.

We restrict to the non-precessing case, here the intrinsic parameters are thus the total mass, the mass ratio and the two (dimensionless) spin projections onto the angular momentum of the system, $\Xi = \{M, q, \chi_1, \chi_2\}$. In this case the geometry is symmetric with respect to the orbital plane, which is preserved in time. This equatorial symmetry

---

[2]See e.g. the discussion below Eq. (29) [143]).

implies

$$h(t, \theta, \varphi; \Xi) = h^*(t, \pi - \theta, \varphi; \Xi) \tag{4.4}$$

(where a * denotes complex conjugation) provided that the polarizations are defined using some appropriate choice for the projection triad/tetrad, which is usually the case in the literature. For the individual modes this translates into

$$h_{\ell,m}(t, \Xi) = (-1)^\ell h^*_{\ell,-m}(t, \Xi). \tag{4.5}$$

Therefore, we just need to focus on the $m \geq 0$ modes, except when reconstructing the whole waveforms. Finally, it is convenient to decompose each mode into a real amplitude and phase as

$$h_{\ell,m}(t, \Xi) = A_{\ell,m}(t, \Xi) e^{-i\phi_{\ell,m}(t,\Xi)}. \tag{4.6}$$

In the following we will omit the dependence on Ξ in order to simplify notation and write $h(t, \theta, \varphi)$.

Note that during inspiral the phase of the (ℓ, m) mode approximately follows the rule $\phi_{\ell,m}(t) \approx m\phi_{\mathrm{orb}}(t)$, where ϕ_{orb} is the orbital phase, however this approximate relation has to break down eventually during the merger, as it is violated during the ringdown, as one can check by comparing the quasi-normal frequencies of the different modes. We will return to this issue in the next chapter 5.2.

The strain h^D seen by a detector located in the direction (θ, φ) of the source sky also depends on the luminosity distance d_L to the source, and the orientation of the detector with respect to the source, which we parametrize using three angles $(\bar{\theta}, \bar{\varphi}, \psi)$. Here $(\bar{\theta}, \bar{\varphi})$ are the spherical coordinates of the source in the detector sky, and ψ is a polarization angle. This dependence is encoded in the antenna patterns F_+ and $F_\times$ of the detector as

$$h^D = \frac{F_+(\bar{\theta}, \bar{\varphi}, \psi) h_+(t, \theta, \varphi) + F_\times(\bar{\theta}, \bar{\varphi}, \psi) h_\times(t, \theta, \varphi)}{d_L}. \tag{4.7}$$

where

$$F_+ = \frac{1 + \cos^2 \bar{\theta}}{2} \cos 2\bar{\varphi} \cos 2\psi - \cos \bar{\theta} \sin 2\bar{\varphi} \sin 2\psi,$$

$$F_\times = \frac{1 + \cos^2 \bar{\theta}}{2} \cos 2\bar{\varphi} \sin 2\psi + \cos \bar{\theta} \sin 2\bar{\varphi} \cos 2\psi.$$

It is well known that this can be rewritten as

$$h^D = \frac{F(\bar{\theta}, \bar{\varphi}, \psi)}{d_L} \left[\cos \kappa \, h_+(t, \theta, \varphi) + \sin \kappa \, h_\times(t, \theta, \varphi) \right], \tag{4.8}$$

where κ acts as an effective polarization angle and F/d_L is a simple overall amplitude factor.

We can now list the possible ambiguities in the definition of the waveform and its spherical harmonic modes for two waveforms A and B, computed with different methods and conventions. We use the superscripts A and B to refer to quantities derived from these waveforms. For aligned-spin binaries we assume that computations A and B preserve the manifest equatorial symmetry of the problem, in particular that the z-axis of the coordinate system we use to define our spherical harmonic mode decomposition is parallel to the angular momentum of the system. The remaining conventions to choose are the origin of the azimuthal angle φ of the spherical coordinates, a polarization angle ψ_0, and the origin of the time coordinate. The degree of freedom represented by φ has been largely described in current literature, such as [135] or [132]. However, the angle ψ_0 is described in [134] [text below eq. (76)] and constrained to have a value of $n\pi/2$, n being an integer, in the context of comparing EOB and NR results. Neglecting for the moment issues related to the accuracy of computations A and B, the strains h^A and h^B computed by implementations A and B are related by

$$h^A(t, \theta, \varphi) = e^{i\psi_0} h^B(t + \tau, \theta, \varphi + \varphi_0), \tag{4.9}$$

where ψ_0 and φ_0 are two angles that encode the different choices in conventions. Of course, the same relation applies to Ψ_4. As a result, the h_{lm} modes are related by

$$h_{\ell,m}^A(t) = e^{i(\psi_0 + m\varphi_0)} h_{\ell,m}^B(t + \tau) \tag{4.10}$$

Usually, conventions are chosen such that (4.5) holds for the individual modes. This implies that $\psi_0 \in \{0, \pi\}$ and thus

$$h_{\ell,m}^A(t) = (-1)^{\kappa_0} e^{im\varphi_0} h_{\ell,m}^B(t + \tau) \tag{4.11}$$

with $\kappa_0 \in \{0, 1\}$. In the case where one only considers the dominant $(2,2)$ mode, equations (4.10) and (4.11) can be rewritten as $h_{22}^A(t) = e^{i\varphi_0'} h_{22}^B(t + \tau)$ i.e. the whole angular freedom amounts to a global phase shift. In the multi-mode case, comparing waveforms without ensuring a consistent choice of ψ_0 will lead to incorrect results.

In order to compare or hybridize two waveforms, we thus need to align them to resolve the above ambiguities, i.e. either keep track of the differences in conventions or infer these from the waveforms themselves via comparing the PN and NR pieces. We describe in detail our procedure to do so in Sec.4.5. This requires to define some notion of distance between the two waveforms and minimizing it over the parameters $(\psi_0, \varphi_0, \tau)$. Note that ψ_0 only depends on the difference in the definition of the polarizations between methods A and B and therefore needs to be determined only once whereas τ and φ_0 will differ for each pair of waveforms. Inaccuracies in the waveforms will in general lead to residual

discontinuities between the spherical harmonic modes even after alignment and these are studied in detail in the next chapter.

4.3   NR and PN input waveforms

Let us give a brief reminder of the different properties of PN and NR waveforms that we will use. For more detailed description, please go back to Chapter 2.

Post Newtonian expansions

PN expansions compute an approximate solution of Einstein's equations up to a certain order in the expansion parameter. Since only a finite (small) number of expansion terms are known, it is not possible to perform a strict convergence test to estimate the truncation error. In addition, the approximation breaks down at merger or shortly before. Even at a given PN order for the energy and the flux, different treatments in the derivation of the orbital phase from the balance equation give rise to a variety of "PN approximants", such as the Taylor approximants [79, 145], which are commonly used in gravitational wave data analysis.

The main consequence of the PN truncation error is a phase evolution which progressively deviates from the correct one as the binary evolves. This secular trend translates into the key source of error for the estimation of the time-shift τ between PN and NR, as shown in Fig.4.2, where the secular trend is also shown in comparison with oscillations originating in residual eccentricity of the NR data. Since secular phasing errors in PN grow with frequency, it is desirable to hybridize at low frequencies, or equivalently with very long NR waveforms, to minimize such errors. Longer NR waveforms are however significantly more expensive computationally.

In this chapter and the next one we use the Taylor T1 and T4 approximants including (unless said explictly) 3.5 PN non-spinning [72] and spin-orbit [73] and 2PN spin-spin [75] phase corrections, which we will just denote as T1 and T4 for brevity. We use 3PN non-spinning amplitude corrections for the higher modes [85] and 3.5PN for the 22 mode [146]. The spin corrections to the amplitudes are known up to 2PN [86].

Numerical Relativity

In NR, the expansion parameter of the PN approximation is essentially replaced by an expansion in the resolution of the numerical grid, and at least in principle it is possible to

provide error estimates through a convergence test. Unless the GW signal is calculated at null infinity, e.g. employing the Cauchy characteristic method [100, 147], convergence needs to be checked not only with respect to grid resolution but also extraction radius. It is then possible to either extrapolate to infinity from a series of finite radii using a given order N polynomials (e.g. for the SpEC simulations [97, 99, 101–103]), or to directly use results from a single finite radius. Furthermore, systematic errors arise due to imperfections of the initial data and initial orbital parameters, in particular residual eccentricity, which generates oscillations in amplitude and phase (see e.g. the discussion in [111]). Unphysical radiation content of the initial data manifests itself in a small GW burst at early times, which is usually referred to as "junk radiation".

For mass ratio $q = 18$, new NR simulations have been performed with the BAM code [107, 108], and are summarized in Sec. III. A of [2]. GW strain is computed from Ψ_4 using the fixed-frequency-integration algorithm described in [100]. For a recent comparative discussion of current numerical relativity codes for black hole binaries, including SpEC and BAM see [148, 149]. Fig. 4.1 shows the amplitude of the most important modes for the highest resolution BAM $q = 18$ waveform.
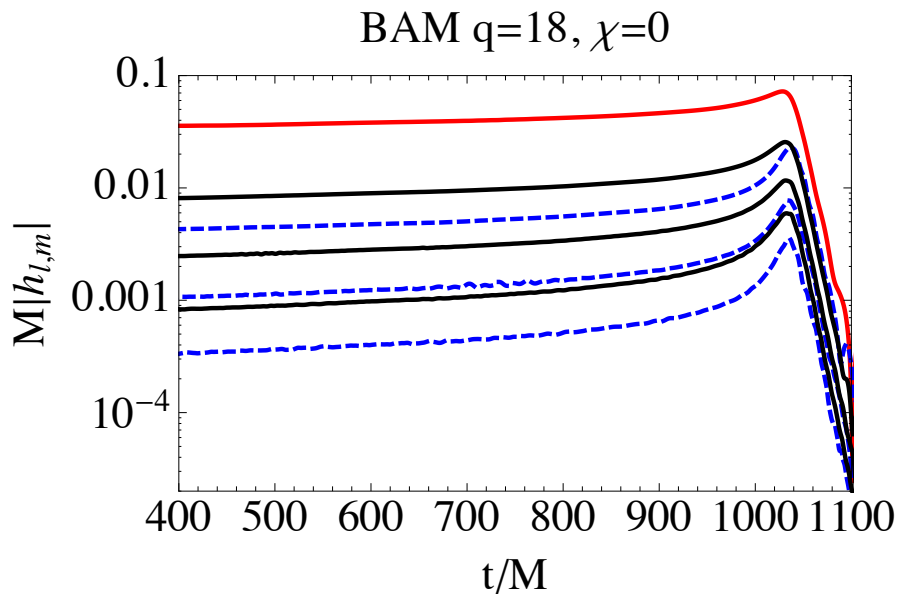
FIGURE 4.1: Logarithmic plot of the mode amplitudes for the non-spinning $q = 18$ configuration. The modes with $(\ell, m = \ell)$ (in black, with $\ell = 3, 4, 5$ from top to bottom) and $(\ell, m = \ell - 1)$ (in dashed blue, with $\ell = 2, 3, 4$ from top to bottom) all have a peak amplitude smaller than that of the $(2,2)$ mode (on top) by a factor between ~ 3 and 20. We show the clean part of the waveform after initial transients due to junk radiation.

4.4 Single mode hybrids

Idealized case

In order to illustrate some key points of the hybrid construction, we first consider a single mode and assume that we have at our disposal two *infinitely accurate* general-relativity computations of some spherical harmonic mode of the strain, $h^A(t)$ and $h^B(t)$, that overlap over some portion of the evolution of the binary, i.e. that there is an interval where they satisfy (4.10). Let us define for convenience the amplitude $A(t)$ and the phase $\phi(t)$ of waveform X (with X= A or B) as $h^X(t) = A^X(t)e^{i\phi^X(t)}$ which we assume to be defined over some interval $[0, t_f^X]$, as well as the frequency $\omega^X(t) = d\phi^X/dt$ which is a monotonic function of t in the case of binaries on circular orbits (we will discuss below the problems introduced by the oscillations due to some residual eccentricity in the NR waveform; however, provided that the eccentricity is small enough, this remains true). We can therefore define the inverse function $t^X(\omega)$, which satisfies $t^X(\omega^X(t)) = t$.

Our idealized infinitely accurate waveforms will satisfy

$$h^B(t) = e^{i\varphi_0} h^A(t + \tau) \tag{4.12}$$

for some τ and φ_0, and t in the interval $[t^A(\omega^B(0)), t_f^A]$, which implies $\omega^B(t) = \omega^A(t+\tau)$. Determining τ and φ_0 is then trivial: one chooses any frequency ω_0 inside the range $[\omega^B(0), \omega^A(t_f^A)]$ and obtains

$$\tau = t^A(\omega_0) - t^B(\omega_0), \quad e^{i\varphi_0} = \frac{h^B(t^B(\omega_0))}{h^A(t^A(\omega_0))}. \tag{4.13}$$

In this idealized case the time alignment and angle φ_0 do not actually depend on the frequency ω_0 and no blending is required, both functions perfectly overlapping before and after the matching point.

Realistic case

In practice both computations are affected by errors, and (4.12) is never exactly satisfied over any interval. One rather has to find the best parameters τ and φ_0 so that (4.12) is the closest to being satisfied in *some* sense and over *some* matching window. We thus now have to make some particular choices in our hybrid construction. We parameterize our window by the initial time t_0 or initial frequency ω_0 (defined as $\omega^{PN}(t_0) = \omega_0$) and the length of the window in the time domain Δt, i.e. our window is $[t_0, t_0 + \Delta t]$. In order to avoid the influence of amplitude errors, we only take into account phase information

when aligning the waveforms in time. We adopt the quantity

$$\Delta(\tau; t_0, \Delta t) = \int_{t_0}^{t_0 + \Delta t} \left(\omega^{PN}(t) - \omega^{NR}(t - \tau) \right)^2 dt, \qquad (4.14)$$

which has the advantage of not depending on φ_0. Other authors have replaced ω by ϕ or h [111] in the integrand (which then depends on φ_0) and tested that their hybrid was not affected much by this choice.

The appropriate time shift τ for a given choice of window $[t_0, t_0 + \Delta t]$ is then obtained by minimizing $\Delta(\tau; t_0, \Delta t)$. Once this is done, the optimal phase shift φ_0 has to be determined. Simple choices are to align the phases at a fixed time, e.g. the beginning of the window, $\varphi_0 = \phi^{NR}(t_0 - \tau) - \phi^{PN}(t_0)$, or to pick the phase shift that minimizes $\int_{t_0}^{t_0 + \Delta t} \left(\phi^{NR}(t - \tau) - \phi^{PN}(t) + \varphi_0 \right)^2 dt$. We have checked that the resulting hybrid depends very weakly on this particular choice. This is due to the fact that the phase has one additional integration with respect to the frequency, so it contains less oscillations.

Once τ and φ_0 have been determined, both waveforms are combined into a piecewise definition

$$h(t) = \begin{cases} e^{i\varphi_0} h^{PN}(t + \tau) & \text{if } t < t_0 - \tau \\ w^-(t) e^{i\varphi_0} h^{PN}(t + \tau) + w^+(t) h^{NR}(t) & \text{if } t_0 - \tau < t < t_0 - \tau + \Delta t \\ h^{NR}(t) & \text{if } t_0 - \tau + \Delta t < t \end{cases} \qquad (4.15)$$

where, with the notation $w^{\pm}_{[t_1, t_2]}(t)$ for blending functions that monotonically go from 0 to 1 (or from 1 to 0) in the interval $[t_1, t_2]$, we have defined $w^{\pm}(t) = w^{\pm}_{[t_0 - \tau, t_0 - \tau + \Delta t]}(t)$, i.e. we perform the blending over the same interval we used to determine τ and φ_0. Here again, different authors have made different choices for the exact shape of these functions. For instance, [111] considers cosine functions, while we here use linear ones.

Note that multiplying the PN part by $e^{i\varphi_0}$ is a redefinition of the conventions for the PN waveform (change of the orbital phase): now the early part of the hybrid does not exactly reduce to the original PN waveform. In the single mode case this is trivial (and multiplying the NR part by $e^{-i\varphi_0}$ would have been equivalent). As single mode matches are always optimized over coalescence phase, this redefinition of conventions will never have any practical consequence. As we will see, in the multimode case, things get more involved.

In order to quantify the error in the time alignment of the waveforms, it is instructive to look at the time shift τ as a function of matching frequency ω_0 and window size Δt (note that the absolute value of τ for some ω_0 is meaningless, what matters is its variation). Fig.4.2 illustrates how our best choice for τ varies with our choices of window length Δt, and how the secular trend depends on the choice of PN approximant. In the present
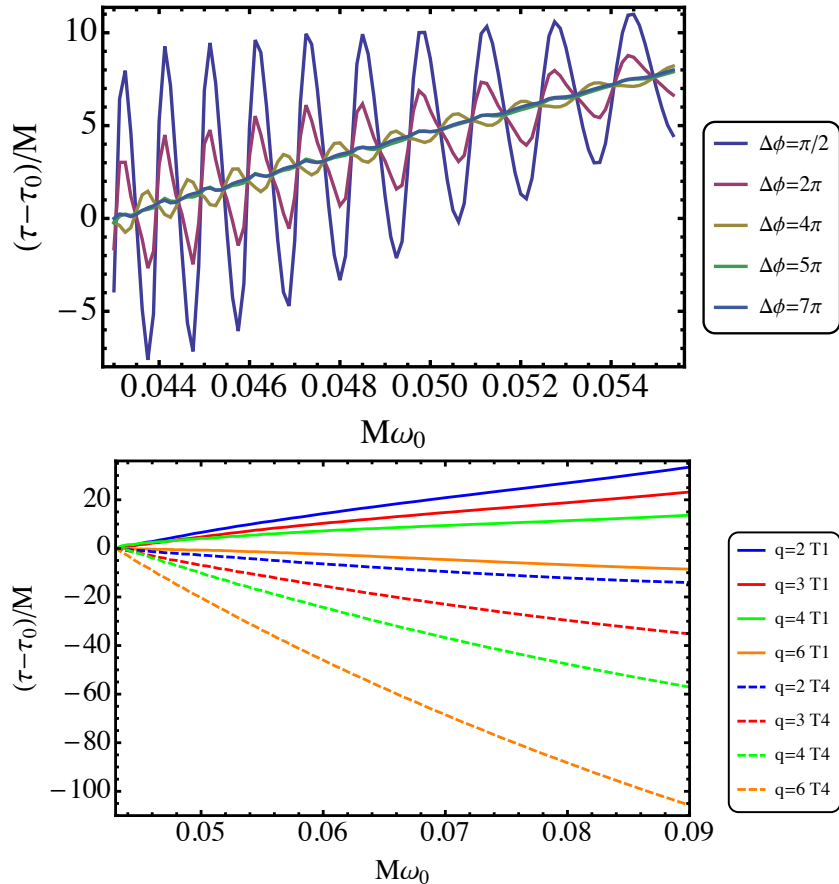
FIGURE 4.2: Top: relative time shift $(\tau - \tau_0)/M$ as a function of $M\omega_0$ for $q = 3$ non-spinning SXS NR data hybridized to T1 for various lengths $\Delta\phi$ of the matching window. The reference time shift τ_0 is the one obtained for $\Delta\phi = 7\pi$ and $M\omega_0 = 0.043$. Note how for larger $\Delta\phi$ the oscillations in the estimation of τ/M are smaller. Bottom: same for several SXS data sets hybridized to T1 and T4 using $\Delta\phi = 7\pi$ (smaller values of q on top) and τ_0 as above.

case, oscillations in the NR waveform are caused in particular by residual eccentricity, which manifests itself at frequencies of the order of the orbital frequency (close to half the frequency of the $(2,2)$ mode). Indeed, for Δt significantly larger than the orbital period, we see that most of the oscillations in the NR data average out, and for a Δt corresponding to at least $\Delta\phi = \phi^{PN}(t_0 + \Delta t) - \phi^{PN}(t_0) \sim 5\pi$ oscillations are smaller than the secular trend due to the phase evolution not being accurate. Unless specified otherwise, we therefore choose Δt such that $\Delta\phi = 7\pi$, i.e. 3.5 GW cycles. Another possibility, proposed in [50] is to force the window extremities to lie at some maximum of the modulation to ensure the cancellation of the effects due to the modulation over the window.

In order to minimize alignment errors due to the secular dephasing between PN and NR, the interval over which one aligns the waveforms should be chosen as early as possible since the accuracy of the PN perturbative treatment degrades as the frequency increases,

but not as early as to be affected by junk radiation or other early-time transient errors. In addition, a comparison of PN approximants as in Fig.4.2 can be used to choose a PN waveform with smaller error in the matching region.
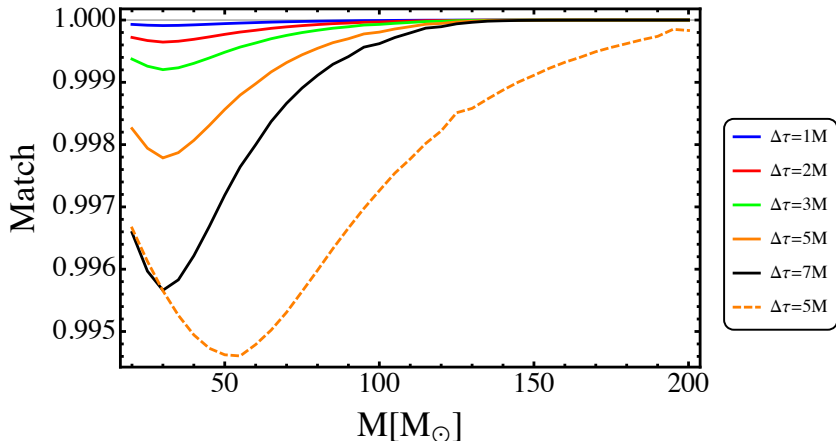
FIGURE 4.3: Effect of $\Delta\tau$ on the final hybrid $(2, 2)$ mode. We show the match $\mathcal{M}[h_{\tau_0}, h_{\Delta\tau}]$ optimized over time and phase between hybrids built from SXS $q = 3$ non-spinning data hybridized to T1 at $M\omega_0 = 0.043$ (solid) and 0.073 (dashed). An artificial time-shift $\tau_0 + \Delta\tau$ is applied when constructing $h_{\Delta\tau}$, while h_{τ_0} has been built using the optimal time-shift τ_0 between PN and NR. See main text for details.

Now we address the question of how much this impacts the waveform in terms of quantities useful for data-analysis. Fig. 4.3 shows the match between $q = 3$ non-spinning hybrid waveforms constructed using artificial time shifts $\tau = \tau_0 + \Delta\tau$ with a reference waveform for which $\tau = \tau_0$. We use the Zero-Detuned High Power noise curve of Advanced LIGO [33] with a lower frequency cutoff of 10Hz in order to facilitate comparison with [111]. Regardless of the intrinsic parameters of the system and the hybridization frequency, the mismatch increases with $\Delta\tau$. When the hybridization region is in band, the match decays by a few 10^{-3} for a value of $\Delta\tau$ of a few M, which is consistent with the results obtained by [111]. Note that $\Delta\tau$ has a larger effect will have on the match for larger frequency ω_0, as expected from the fact that $\Delta\tau$ is then a larger fraction of the period.

4.5 Multi-mode hybrids

In this section, we describe our procedure to construct hybrid waveforms with higher modes and define quantities that will be used in the error analysis of Sec.5. Higher modes become increasingly relevant for binaries with large mass ratio, for this reason we illustrate our procedure using a waveform produced recently with the BAM code for a non-spinning binary with $q = 18$, which we have presented in Sec. 4.3.

Step 1: Determination of τ, ψ_0, φ_0

As discussed in Section 4.2, in the presence of higher modes one needs three parameters $(\tau, \psi_0, \varphi_0)$ to describe the possible differences in conventions between the PN and the NR waveforms. The best choice of such parameters will depend on the matching time or frequency, but it appears fruitful to not make different choices for different directions in the source sky (it seems conceivable but not practical to do this). Several strategies to infer these parameters from the waveforms can be explored. One important ingredient is how to weight the contribution of different modes in determining $(\tau, \psi_0, \varphi_0)$. One natural choice, pursued in [2], is to define a single set of $(\tau, \psi_0, \varphi_0)$ by minimizing the quantity

$$\int dt \sum_{\ell,m} |h_{\ell,m}^{NR}(t-\tau)e^{i(\psi_0+m\varphi_0)} - h_{\ell,m}^{PN}(t)|, \tag{4.16}$$

where the integral is performed over some window corresponding to the hybridization region, and the contribution of each mode is naturally weighted with its amplitude. However, this method does not restrict ψ_0 to belong to the set $\{0, \pi\}$, and the resulting modes do not in general follow the usual relation (4.5). Also, [133] proposed to apply individual time-shifts to each of the modes. We agree with [134] and think that applying individual offsets is quite unnatural since one of our goals is that the resulting NR and PN of the hybrid waveform coincide with the original PN and NR results.

In this thesis, we take a different approach. We will try to constrain the 3 degrees of freedom as much as possible using only the dominant (2,2) mode. The (2,2) mode of hybrids constructed this way will thus coincide with hybrids constructed only for the (2,2) mode, and two hybrids constructed with different sets of higher modes will exactly coincide on their common modes, which facilitates comparisons and studies of the contribution of some specific mode. In practice, our procedure is the following. As in the single mode case, we parametrize how early (or late) in the evolution we perform our hybridization using a "hybridization frequency" ω_0, which defines the "hybridization time" t_0 through

$$\frac{d\phi_{2,2}^{PN}}{dt}(t_0) = \omega_0, \tag{4.17}$$

and the length of the time-window over which the waveforms are aligned in time as Δt. Considerations on how to choose these two parameters have been described in the previous section. The determination of τ can be then carried out by minimizing the same quantity as in the single mode case,

$$\Delta(\tau; t_0, \Delta t) = \int_{t_0}^{t_0+\Delta t} \left(\omega_{2,2}^{PN}(t) - \omega_{2,2}^{NR}(t-\tau)\right)^2 dt, \tag{4.18}$$

since only the frequencies enter in $\Delta(\tau; t_0, \Delta t)$. This makes the determination of τ decouple from that of the phase offsets (ψ_0, φ_0). Before moving on to the determination of (ψ_0, φ_0), let us recall that given a code to generate PN waveforms and an NR code, φ_0 will depend on choices made to generate each individual waveform whereas ψ_0 could in principle be computed once and for all by comparing all the convention choices in both codes. Since for all the PN and NR data we have used (4.5) holds, we assume that ψ_0 can only take the values 0 or π as discussed in Sec. 4.2. Let us define

$$\Delta\phi_{\ell,m} = \phi_{\ell,m}^{NR}(t_0 - \tau) - \phi_{\ell,m}^{PN}(t_0). \tag{4.19}$$

Then ideally (i.e. assuming that (4.10) holds), we have $\psi_0 + 2\varphi_0 + \Delta\phi_{2,2} \equiv 0 \mod 2\pi$ i.e.

$$\varphi_0 \equiv -\frac{\Delta\phi_{2,2} + \psi_0}{2} \mod \pi, \tag{4.20}$$

which gives 2 solutions for φ_0 in the interval $[0, 2\pi[$ if ψ_0 is previously known and 4 solutions if ψ_0 is unknown but restricted to $\psi_0 \in \{0, \pi\}$:

$$(\psi_0, \varphi_0) = \left(\kappa\pi, -\frac{\Delta\phi_{2,2}}{2} + \left(\kappa' - \frac{\kappa}{2}\right)\pi \mod 2\pi \right) \tag{4.21}$$

with $\kappa \in \{0, 1\}$ and $\kappa' \in \{0, 1\}$. To lift this degeneracy, we need information from at least one of the higher modes, say (ℓ_*, m_*), and we use the one with the largest amplitude, typically the (3,3) mode unless it is zero for symmetry reasons. If again both waveforms were infinitely accurate, (4.10) would imply

$$\psi_0 + m_*\varphi_0 + \Delta\phi_{\ell_* m_*} \equiv 0 \mod 2\pi, \tag{4.22}$$

but in the presence of waveform errors this will not hold for any of our four solutions. However, we can choose the solution that is the closest to satisfying this equation, which is uniquely determined only in the case where m_* is odd. Note that in the case where only even m modes are available, φ_0 needs in fact only to be determined modulo π since only the combination $m\varphi_0$ appears in the hybrid construction and the two solutions can be discriminated using any even higher mode. We find that there is a relative ψ_0 shift of π between the BAM and SXS waveforms, and also between BAM and the conventions used in the PN context by Arun et al [144] and Blanchet [72].

Fig 4.4, shows the solutions found using this procedure on the $q = 18$ case hybridized with three different PN approximants as a function of the hybridization frequency. As one would expect, the result corresponds to the lower plot of Fig. 4.2, which shows the dependence of the hybridization time shift on frequency and PN approximant. In Fig 4.4
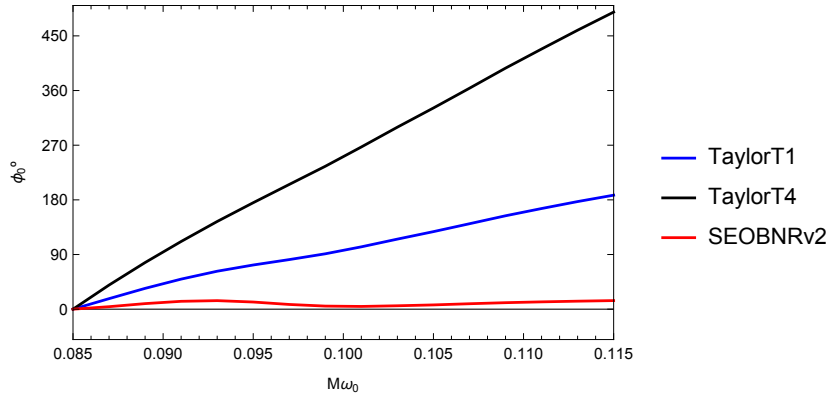
FIGURE 4.4: Estimations for φ_0 as a function of $M\omega_0$ for the case of $q = 18$ non-spinning BAM NR data hybridized to PN T4, T1 and SEOBNRv2 (from top to bottom). For T1, the estimation of φ_0 changes by $\sim \pi$ over the frequency range shown here (corresponding to ~ 7 cycles in $h_{2,2}$).

we see that both the standard T1 and T4 approximants exhibit large secular trends, indicating a large difference in the orbital phase (or more precisely the phase of the $(2,2)$ modes) between the PN waveforms and the NR result over the frequency range shown here. In comparison, the SEOBNRv2 waveform [51] shows almost no secular trend. Evaluating the secular trend of the PN approximant as compared to the NR waveform is an important part of the hybridization procedure. Exactly as in the single mode case, this secular trend translates into some "hybridization error" (for instance, the phase of the (2,2) mode for two hybrids built using T1 but with $M\omega_0 = 0.085$ or $M\omega_0 = 0.115$ and aligned in the early inspiral will differ at the peak by almost one gravitational wave cycle) but this error has nothing to do with the higher modes themselves and controlling it is not our main focus here. Instead, we will try to identify additional figures of merit for the hybrid that directly quantify the additional error due to the higher modes.

As a final remark, and regarding our assumption that $\psi_0 \in \{0, \pi\}$, note that if (4.5) did not hold for either the PN and/or NR inputs, one could simply solve the system

$$\Delta\phi_{2,2} = 2\varphi_0 + \psi_0$$
$$\Delta\phi_{\ell,m} = m\varphi_0 + \psi_0$$

$$(4.23)$$

without imposing any restriction on ψ_0. Whenever we have done this, we have chosen $(\ell, m) = (3, 3)$, as this is the most dominant HOM.

We can now provide a summary of the different methods proposed in the literature for constructing hybrid HOM and the properties they do/do not satisfy.

Both [135] and [132] consider phase shifts $\Delta\phi_{\ell,m} = m\phi_0$ (neglecting ψ_0) for the (ℓ, m) mode and apply an unique time-shift t_0 obtained from the gluing of the dominant $(2, 2)$

mode. In contrast, [133] proposes to apply individual time-shifts $t_0^{\ell,m}$ to each mode, which breaks the alignment in time of the original modes. In [134] and [2], the angle ψ_0 is described and computed in different ways. On the one hand [2] obtains the parameters (ϕ_0, ψ_0, t_0) by considering all the modes at the time and without any restriction on ψ_0 (see (4.16)). Again, (4.16) makes that if the original mode sets satisfy (4.5), the resulting modes will not do it in general. On the other hand, [134] follows an approach quite similar to ours: (t_0, ϕ_0) are obtained by gluing the $(2, 2)$ mode while ψ_0 is constrained to have a value of $n\pi/2$. We refine this a bit: if (4.5) is satisfied by both sets of modes, then we restrict $\psi_0 \in \{0, \pi\}$m making the resulting modes satisfy also (4.5). If this is not the case, ψ_0 can be obtained using two modes applying (4.23).

Step 2: evaluate residual disagreement between PN and NR at the matching point

We now investigate the residual phase and amplitude disagreements between PN and NR at the matching point and define appropriate quantities to describe this disagreement, while we postpone the analysis of the main source of this disagreement to Sec. 5.

In the idealized case, correcting for the differences in conventions using (φ_0, ψ_0) is enough to guarantee that the phase of every mode is continuous between the PN and NR waveforms at the matching point. In other words, the quantities

$$\epsilon_{\ell,m} = \Delta\phi_{\ell,m} + \psi_0 + m\varphi_0, \tag{4.24}$$

which are functions of the hybridization frequency ω_0 are all zero. In practice, this is not the case and we will use these quantities as measures of the residual phase disagreements. The values for the example $q = 18$ case are shown for the most important modes in Fig. 4.5 (left). These are typically of a few degrees for $m = \ell$ modes and $10 - 15$ degrees for $m = \ell - 1$ modes. Apart from the values themselves, one important feature is the fact that unlike for φ_0, these remain roughly constant over the range of hybridization frequencies explored here. This is a consequence of the fact that we are essentially measuring phase differences between the higher modes *after aligning the (2,2) modes at* ω_0 via the term $m\varphi_0$ in Eq. (4.24), which effectively absorbs the secular dephasing shown in Fig. 4.4. In other words, the $\epsilon_{\ell,m}$ really quantify the residual differences between PN and NR in the dephasings between the higher modes and the (2,2) mode, factoring out the error in tracking the orbital phase (or equivalently that of the (2,2) mode) of the system. In order to account for discrepancies in the amplitude, we define the quantity

$$r_{\ell m} = \frac{|h_{\ell m}^{\mathrm{NR}}(t_0 - \tau)|}{|h_{\ell m}^{\mathrm{PN}}(t_0)|}. \tag{4.25}$$

This is plotted in Fig. 4.5 (right). Note that higher frequency modes (i.e., larger m) show larger amplitude disagreements. We will perform a detailed analysis of the phase and amplitude errors in Sec. 5.
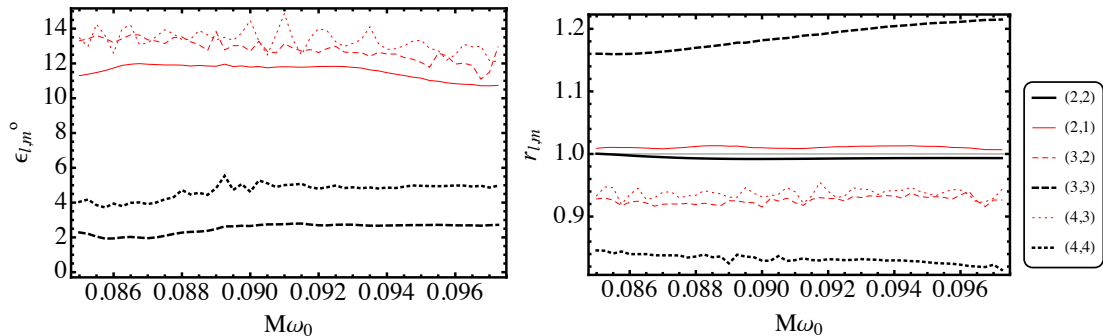
FIGURE 4.5: Top: Phasing errors $\epsilon_{\ell,m}$ (in degrees) for the $q = 18$ non-spinning BAM data hybridized with T1 as a function of $M\omega_0$. Note the lower values for $\ell = m$ modes (black) as compared to $\ell \neq m$ (red). Bottom: Amplitude ratios $r_{\ell,m}$ for the same hybrid construction. Note how modes with larger m, i.e. with larger frequencies, tend to show larger amplitude disagreements.

Step 3: hybrid construction

We can finally proceed to construct the higher hybrid modes as piecewise functions in a similar way as in Eq. (4.15). However, since the early part of higher NR modes might be noisier that that of the quadrupole one, we let the blending windows span over different time intervals. Defining $[t_0^{\ell,m} - \tau, t_0^{\ell,m} - \tau + \Delta t^{\ell,m}]$ to be the blending window used for each mode and $w_{\ell,m}^{\pm}(t) \equiv w_{[t_0^{\ell,m}-\tau,t_0^{\ell,m}-\tau+\Delta t^{\ell,m}]}^{\pm}(t)$ the associated blending functions, we now define

$$h_{\ell,m}(t) = \begin{cases} e^{i(m\varphi_0+\psi_0)}h^{PN}(t+\tau) & t < t_0^{\ell,m} - \tau \\ w_{\ell,m}^{-}(t)e^{i(m\varphi_0+\psi_0)}h^{PN}(t+\tau) + w_{\ell,m}^{+}(t)h^{NR}(t) & t_0^{\ell,m} - \tau < t < t_0^{\ell,m} - \tau + \Delta t^{\ell,m} \\ h^{NR}(t) & t_0^{\ell,m} - \tau + \Delta t^{\ell,m} < t \end{cases} \quad (4.26)$$

with $t_0 \in (t_0^{\ell,m}, t_0^{\ell,m} + \Delta t)$. Fig. 4.6 shows some of the resulting hybrid modes. The three modes shown are three examples of modes for which PN and NR agree well in both amplitude and phase $(2,2)$, only amplitude $(2,1)$ and only phase $(3,3)$. As we will see in detail in Chapter 4, PN truncation errors are the main source for the amplitude disagreements whereas the finitude of the extraction radius of the NR waveform dominates those regarding the phase. The vertical lines in the plots denote the limits of the blending windows. As mentioned some lines above, note the usage of different windows for the $(2,2)$ mode and the other two. Fig. 4.7 shows the real part of several $q = 8$

non-spinning hybrid modes built out of extrapolated $N = 2$ SXS NR data and T1. The length of the SXS simulations allows to perform the hybridization at lower frequencies than that of the hybrids in Fig. 4.6. In particular, here $M\omega_0 = 0.043$, where we are still far away from the junk radiation present at the beginning of the simulation. Although we will focus on this later, it is noticeable how the accuracy of the amplitude of the PN (blue) data decreases for increasing m. In particular, if one compares the $(2,1)$ and $(4,4)$ modes, one can see how the blue PN data deviates strongly from the NR one from $t/M \sim 3000$ for the $(4,4)$ mode while the $(2,1)$ follows it well up to almost the merger.
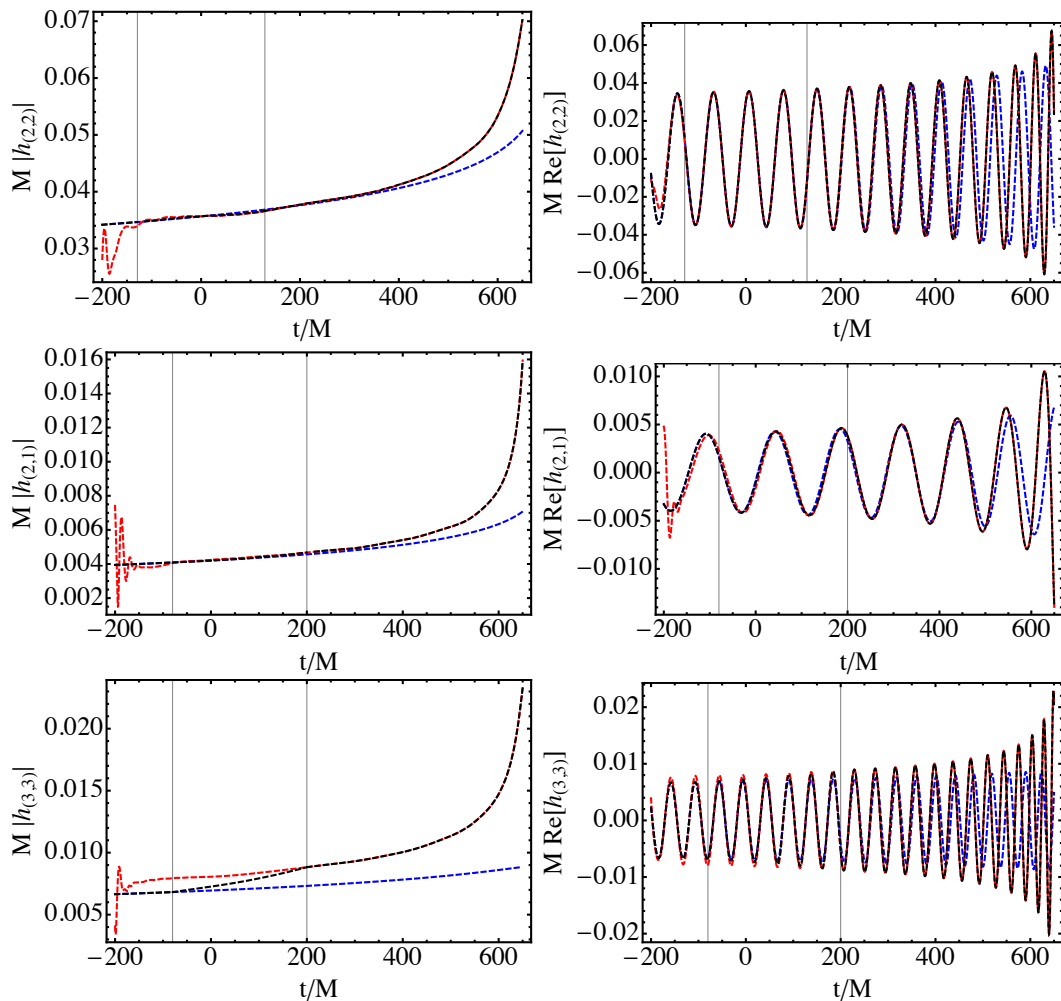
FIGURE 4.6: Amplitude (left) and real part (right) of non-spinning BAM $q = 18$ $(2,2)$, $(2,1)$ and $(3,3)$ modes hybridized with T1, from top to bottom. We show PN (blue), NR (red) and hybrid (black) modes and focus on the hybridization region. The $(2,1)$ mode is a typical example of good amplitude agreement and large $\epsilon_{\ell,m}$, while the $(3,3)$ mode is a typical example of small $\epsilon_{\ell,m}$ and poor amplitude agreement. Note the usage of different blending windows from the one used for the $(2,2)$ mode.
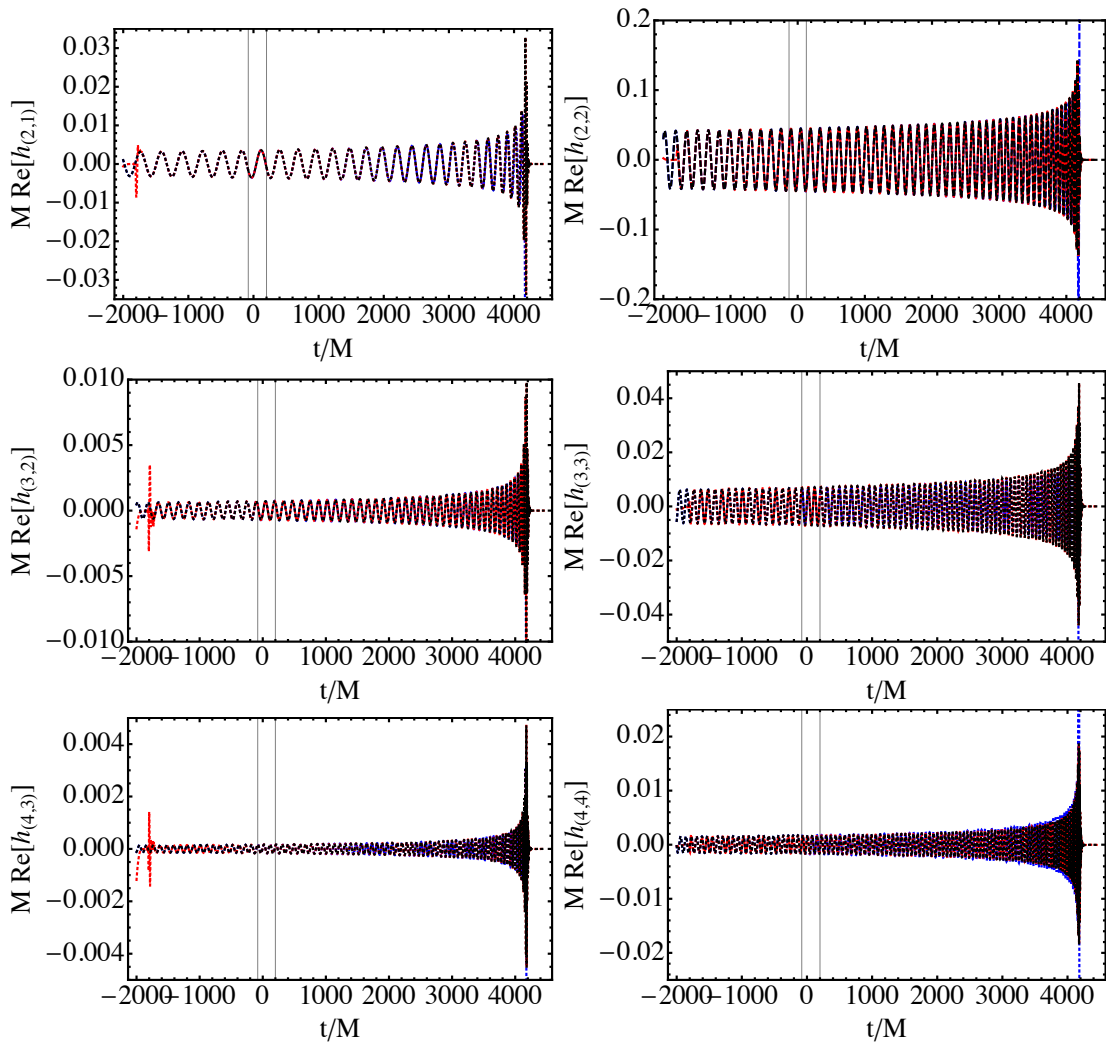
FIGURE 4.7: Real part of non-spinning SXS $q = 8$ modes extrapolated to null infinity to order $N = 2$ hybridized with T1. The plots show PN (blue), NR (red) and hybrid (black) and the vertical lines correspond to the hibridization region.

Chapter 5

Analysis of the accuracy of post-Newtonian and Numerical Relativity higher order modes

In the previous Chapter, we introduced figures of merit that quantify the residual disagreements between the PN and NR higher modes both for the phase (see Eq. (4.24)) and for the amplitude (see Eq. (4.25)), after correcting for the differences in conventions by aligning the (2,2) modes. This Chapter is now devoted to the identification of the main sources of these disagreements among the errors affecting both computations and described in Sec. 4.3. In particular, we will see that the phasing errors $\epsilon_{\ell m}$ have their main source in the finite extraction radius of the NR simulations. Regarding the amplitude errors $r_{\ell m}$, we will see that extraction radius in NR simulations plays an important role (dominant for some modes), but that PN truncation errors are the main source for some other ones. For a detailed analysis of errors in higher modes for a simulation of non-spinning $q = 4$ system, see [103]. One of the main conclusions obtained there is that extrapolation of gravitational waveforms to infinite extraction radius is particularly important for subdominant multipoles with $\ell \neq |m|$, as we will confirm here for a large variety of cases.

In this study, we pay attention to several physical systems (mass ratios, spins), and focus on those ones for which NR simulations performed with several codes are available. The latter provides information about the influence of the different numerical setups, gauge conditions and initial data that are chosen by each code. A particularly interesting system is the the case of a $q = 8$ non-spinning binary simulated using the BAM code [107, 108], and also available in the public SXS catalogue [115]. This physical configuration shows strong higher mode contributions due to the large mass ratio

and for which waveforms are available at different resolutions for both codes, as well as several extraction radii. Furthermore, SXS data sets are also extrapolated to null infinity at several polynomial orders (see [97] for a discussion of different methods, and [99] for a comparison with characteristic extraction results) and this will allow us test its influence. Note that the SXS waveform is significantly longer than the BAM one. This allowed us to hybridize at a frequency $M\omega_0 = 0.043$, while the BAM waveform requires $M\omega_0 > 0.080$. This means hybridizing 40 and 9.2 gravitational wave cycles (in the 22 mode) before merger respectively.

5.1 Errors in the modes amplitude

The effect of the NR extraction radius

In the previous Chapter we defined in the amplitude ratios $r_{\ell,m}$ (Eq. (4.25)). These measure the disagreement between the NR and the PN calculations at their matching point. We will start by investigating the effect of finite radius extraction on these quantities. Fig. 5.1 shows the $r_{\ell,m}$ for several modes as a function of the hybridization frequency ω_0, and for different extraction radii for both the BAM and SXS codes, including the SXS waveform extrapolated to null infinity with a polynomial of order $N = 4$. Note that although curves are amplitude comparisons between NR and PN, by taking the ratio of two curves, one obtains a direct comparison between two NR results. Note that the amplitude of the waveforms extracted at finite radius commonly differs from that of the extrapolated waveform by around $\sim 1\%$ for the highest radii available. However, much larger errors arise when waves are extracted closer to the source. Note also that the ratio between the amplitudes computed at the innermost radius and the extrapolated one is lower the larger m is (for same $M\omega_0$), i.e., the larger the frequency of the mode is. This behavior is kept when looking at a single mode, i.e., the further in the evolution the more similar the extrapolated and finite radius amplitudes are. This is however an expected behavior. In order to perform an accurate extraction of the GW data, the corresponding grid needs to be placed at the so called wavezone, defined by $r \gg \lambda$. Thus, the larger the frequency of the GW (the lower its wavelength λ) the closer to the source the extraction can be carried out. The quantitative values are quite different for data sets computed with different codes. With the exception of the $(3, 2)$-mode, e.g. $r = 100$ BAM data are significantly closer to the extrapolated result than the corresponding SXS $r = 100$ curve [1]. This is not surprising: finite radius errors depend on gauge conditions chosen for each code, and the lapse and shift chosen for each code is indeed different. Currently, no explanation has been obtained for justifying why the BAM $(3, 2)$-mode

---

[1]Note that the BAM results are plotted in a shorter range since the simulation is shorter.

shows anomalous behavior as compared to the other modes. However, as we shall see later, part of this errors could plausibly be due to an effective mode mixing due to the finitude of the radius of the surface in which ψ_4 is computed and decomposed into modes. This might affect different modes in a different way.
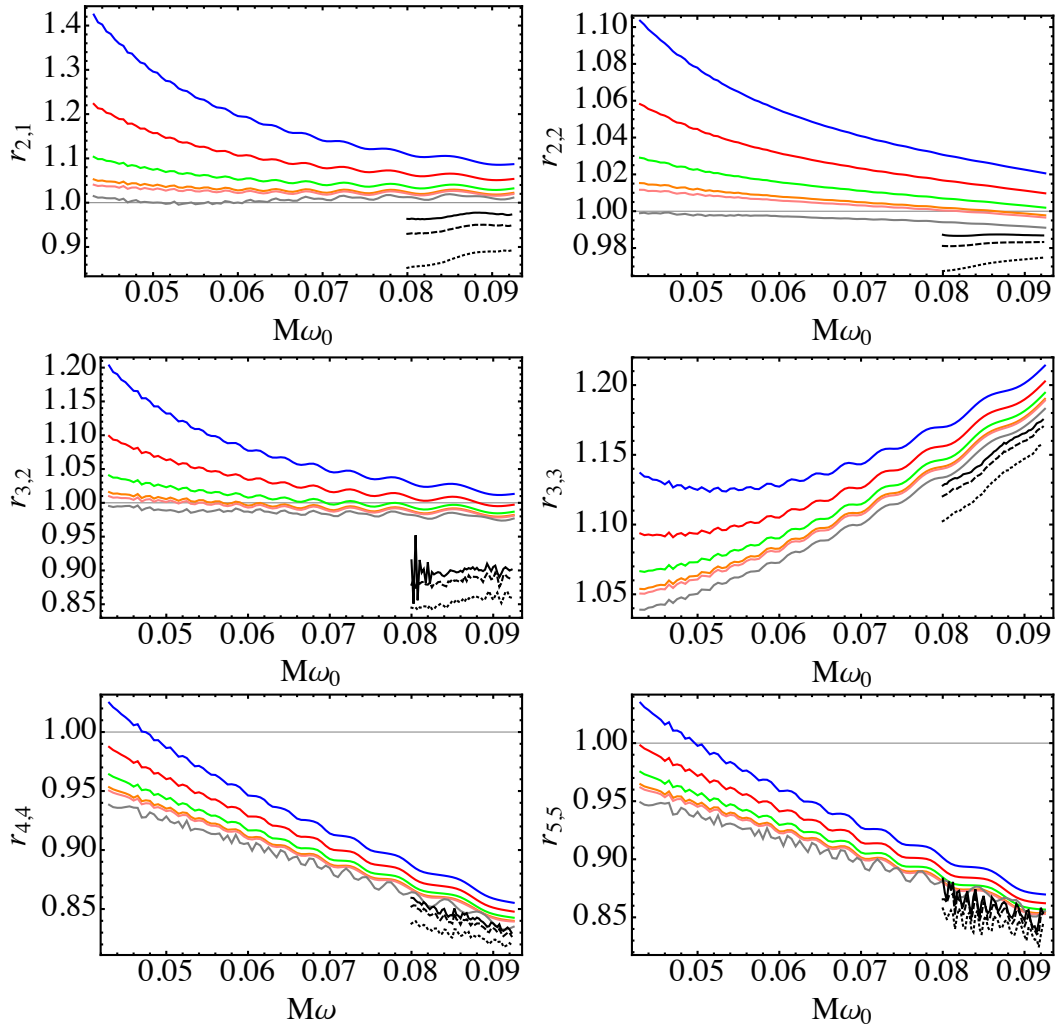
FIGURE 5.1: Ratio of the NR/PN amplitudes as a function of matching frequency $M\omega_0$ for a $q = 8$ non-spinning binary for several NR waveforms matched to T1. The simulations correspond to $r = (100, 133, 190, 266, 307)M$ and extrapolated SXS data (in color and downwards) and BAM $r = (60, 80, 100)M$ (black and upwards).

The effect of PN truncation

Once that we have checked the impact of extraction radius on the NR amplitude, let us now address the direct comparison between NR and PN results. Since we have shown that NR results converge as the extraction radius increases, we will now restrict our attention to the extrapolated SXS amplitude and consider it to be the best possible NR result. For the $(2, 1)$, $(2, 2)$ and $(3, 2)$ modes shown in Fig. 5.1, the ratio $r_{\ell,m}$ remains almost constant and differs from 1 by less than 2 percent over the whole range
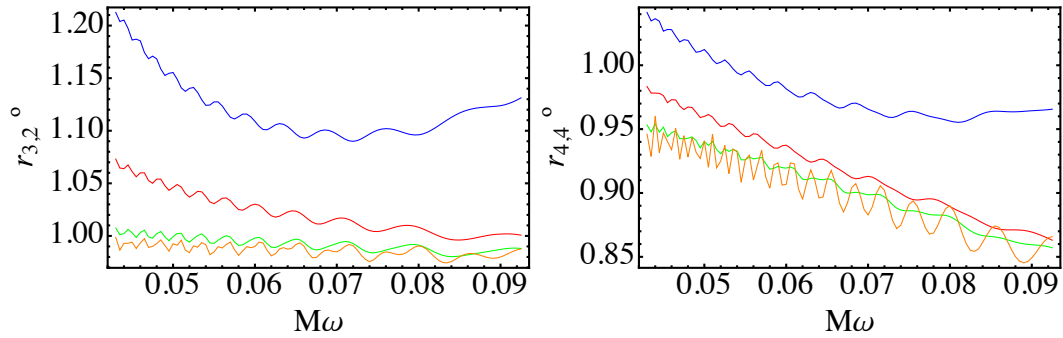
FIGURE 5.2: Ratio of the NR/PN amplitudes as a function of matching frequency $M\omega_0$ for a $q = 4$ non-spinning binary for several NR waveforms matched to T1. The simulations correspond to $r_{q=4} = (100, 154, 380)M$ downwards and extrapolated SXS data in orange.
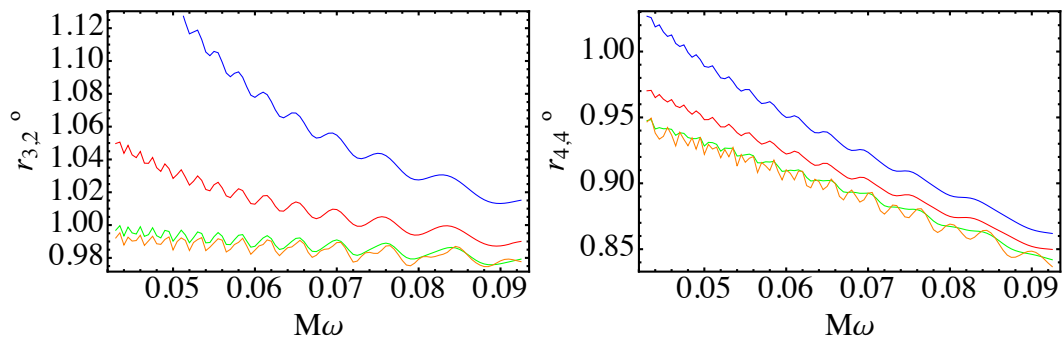
FIGURE 5.3: Ratio of the NR/PN amplitudes as a function of matching frequency $M\omega_0$ for a $q = 6$ non-spinning binary for several NR waveforms matched to T1. The simulations correspond to $r_{q=6} = (100, 174, 550)M$ downwards and extrapolated SXS data in orange.

of frequencies considered. Instead, the ratio for the $(3, 3)$, $(4, 4)$ and $(5, 5)$ modes shows a strong secular trend, which largely deviates from 1 at high frequencies by a few 10%. Some smaller (but still of the order of several percent) disagreements are visible at low frequencies. In orther to check the generality of this behavior, we performed this same study for the $q = \{2, 3, 4, 6\}$ non-spinning cases, for which SXS simulations are available. We observed the same behavior. The corresponding plots for the $(3, 2)$ and $(4, 4)$ modes are shown in Fig. 5.2 and 5.3 for the $q = 4$ and $q = 6$ cases respectively. The agreement between the different NR curves (extrapolated SXS and the outermost extraction radius for BAM), to at least a much higher degree than the disagreement between PN and NR, and the fact that this discrepancy grows with the frequency suggests that the main source of error here is that caused by the PN truncation, which is enhanced by the fact that the disagreement is stronger at high frequencies, when PN is expected to be innaccurate precisely due to the lack of higher PN corrections. In order to analyze this in more detail, it is illustrative to study how the variation of the amplitude ratio $r_{\ell,m}$ (gray curves) changes when different PN orders are used to compute the GW modes. Fig. 5.4 shows the ratio $r_{\ell m}$ for the $(2, 2)$, the $(3, 3)$ and the $(4, 4)$ modes (which exhibited

different behaviors in Fig. 5.1). The NR data used is SXS extrapolated and the PN includes different PN corrections. When looking at this plots, the reader should bear in
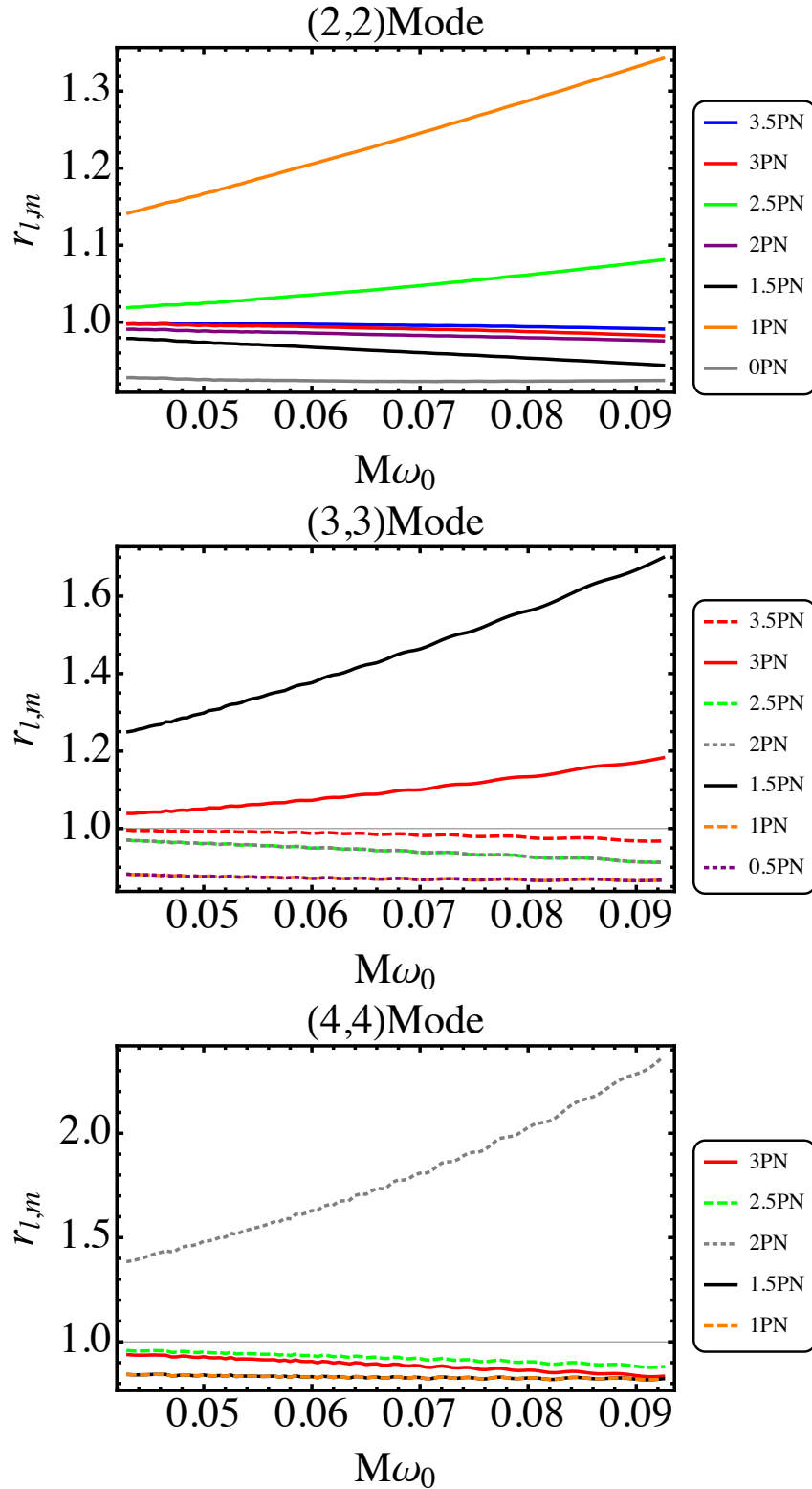
FIGURE 5.4: Ratio of NR and PN amplitudes of $q = 8$ non-spinning SXS NR data extrapolated at $N = 4$ matched to T1 including different PN amplitude corrections as a function of $M\omega_0$. We show the $(2, 2)$ (left) and $(3, 3)$ (right) modes.

mind that the $(2, 2)$ mode amplitude is known up to 3.5 PN while all the other modes are known up to 3PN except that of the $(3, 3)$ mode, which is known up to 3.5PN (Note that however, unless explicitly said, we will use only 3PN for the $(3, 3)$ mode, and again plots in Fig.5.1 use only 3PN). As usual, studying the PN truncation error is more involved than studying for instance the convergence with extraction radius since one does not know a priori how the PN series converges and therefore extrapolating is not possible. In particular, the convergence is not necessarily monotonic and consecutive corrections can have very different magnitudes (note that they originate from or mix several physical effects).

Due to this, the fact that adding a given correction barely changes the result does not guarantee that the next one will be also negligible. In order to see this, look (for instance) at the curves corresponding to (1,1.5,2) PN orders for the $(4, 4)$ mode in Fig.5.4: the first two are superimposed but the 2PN corrections changes the result completely. Furthermore, assuming that extrapolated NR data gives the best result, it is also not guaranteed that the larger the PN order one uses the better result will be achieved, as is clear again from the $(4, 4)$ plot in Fig.5.4. In summary, one cannot estimate the truncation error by comparing the result at n PN and the one at $(n + 1/2)$ PN. Despite these caveats, the spread between several consecutive curves gives a sense of how much PN truncation affects the result and the comparison between different modes suggests that this error is larger for larger m. Note that while all higher modes are shown up to absolute 3PN order (with the convention that the leading order of the $(2, 2)$ amplitude is Newtonian), their leading order is $(\ell - 2)/2$ PN for even values of $\ell + m$ and $(\ell - 1)/2$ PN for odd values of $\ell + m$ so the number of relative corrections actually known for each mode of course varies. However, we highlight that the differences that we observe are not a consequence of a relative higher order knowledge for some modes: if we consider 3PN corrections, both the $(2, 1)$ and the $(3, 3)$ modes for instance are computed with 2.5 PN relative precision and show a very different behavior. The lack of apparent error systematics regarding PN orders or modes is not untypical for PN results, where contributions at different orders often come from very different physical effects, thus their magnitude is hard to anticipate.

Highlighting the effect of a PN correction: the 3.5 PN correction for the $(3, 3)$ mode.

As mentioned above, the $(3, 3)$ mode amplitude has been recently computed up to 3.5PN order but we have only considered corrections up to 3PN order. Its contributions will not be considered for waveforms used in thesis since all the qualitative behaviors obtained will not change. However, it can be very illustrating to study the effects of such a

further correction. The central plot in Fig.5.4 shows in dashed-red the result when such correction for the $(3,3)$ mode is considered. It is noticeable that the PN result agrees now to a much larger accuracy that when 3PN corrections were used. Also, Fig.5.5 shows the $r_{\ell,m}$ values shown in Fig.5.1 when using both 3PN (left) and 3.5PN corrections. It is very noticeable that not only PN agrees better with NR when using 3.5PN but also that this improvement is much larger the larger the frequency is: at low frequencies the improvement is from 4% to $< 1\%$ but at high frequencies it improves from $> 20\%$ to $\sim 2\%$. We recall that that since PN series are not monotonically convergent, the fact that 3.5PN amplitude gives better result than 3PN is not guaranteed before "checking'.' The conclusion is that it would be useful to include 3.5PN corrections when $(3,3)$ modes are considered. for, for instance, building a phenomenological model including HOM.
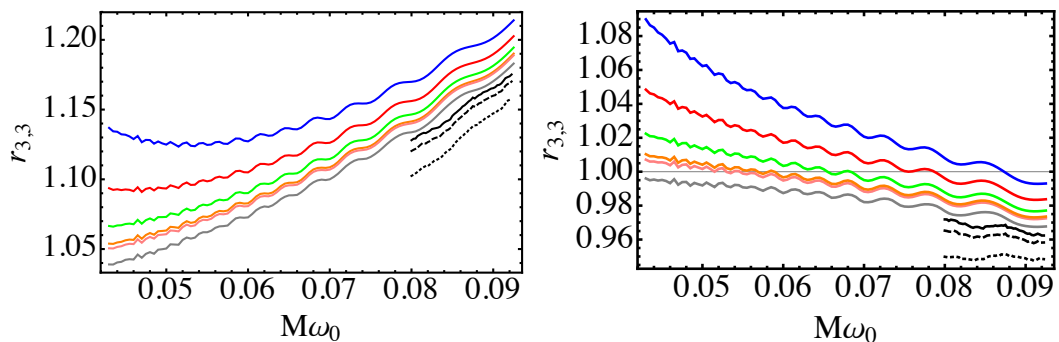
FIGURE 5.5: Same as in Fig.5.1 but only for the $(3,3)$ mode. The left plot shows the result when the PN mode is computed with 3PN corrections while in the right one it has been computed using 3.5PN corrections.

5.2 Comparison of PN and NR phases: analysis of the $\epsilon_{\ell,m}$ values

We will now investigate the sources of the residual phasing errors $\epsilon_{\ell m}$ defined in Eq. (4.24). As discussed in Sec. 4.5, these quantify the discrepancies between PN and NR in the phase difference between the (ℓ,m) mode and the $(2,2)$ mode, i.e. dephasing errors in addition to the difference in tracking the orbital phase of the system. Eq. (4.24) can be rewritten using Eq. (4.21) in order to obtain

$$\epsilon_{\ell,m}(\omega_0) = \left(\phi_{\ell m}^{\mathrm{NR}} - \frac{m}{2}\phi_{22}^{\mathrm{NR}}\right) - \left(\phi_{\ell m}^{\mathrm{PN}} - \frac{m}{2}\phi_{22}^{\mathrm{PN}}\right) \tag{5.1}$$

where the phases have to be taken at the matching point corresponding to the hybridization frequency ω_0. Note that in principle the rhs of Eq. (5.1) should also contain an additional term $(2\kappa' m + (2 - m)\kappa)\pi/2)$ originating from convention differences. In order

to simplify the analysis, we will consider that these have been reabsorbed in the definition of one of the two waveforms. In other words, we adjust the conventions (but only by integer factors of $\pi/2$ for φ_0 and of π for ψ_0) of say the PN waveform so that the $\epsilon_{\ell m}$ vanish in the limit where both the NR and the PN waveform would be infinitely accurate. The $\epsilon_{\ell,m}$ values are more intricate to study than the $r_{\ell m}$ since they not only involve PN and NR but also two different modes. As a first step, it is useful to focus on the simpler quantities

$$\Lambda_{\ell,m}^X(t) = \phi_{\ell,m}^X(t) - \frac{m}{2}\phi_{2,2}^X(t), \tag{5.2}$$

where X is NR or PN, which only involve either the NR or PN waveform. Note that this quantities were already defined in (2.18) as the contributions to the total phase of the mode from the complex part of the mode amplitudes. Note also that $\Lambda_{\ell,m}^X$ is insensitive to a redefinition of the angle ϕ, i.e. to a change in φ_0. However, a redefinition $\psi_0 \to \psi_0 + \delta\psi_0$ affects (5.2) as $\Lambda_{\ell,m}^X \to \Lambda_{\ell,m}^X + \delta\psi_0(1 - m/2)$. In particular, these quantities are defined bearing in mind that during the inspiral they should vanish as the frequency decreases, which implies some particular convention for ψ_0. In the rest of this Chapter, in order to simplify the discussion, we assume that all the waveforms adopt this convention. Note that the conventions adopted in Arun et al [144] and Blanchet [72] differ from this by a shift of π in ψ_0.

In the PN side, one finds that the $\Lambda_{\ell,m}^{\mathrm{PN}}$ are small but non-zero during the inspiral, and vanish in the limit of infinite separation. As a consequence, the PN phase of the (ℓ, m) mode approximately follows the rule $\phi_{\ell,m}^{PN}(t) \approx m\phi_{\mathrm{orb}}(t)$ where ϕ_{orb} is the orbital phase of the system, as was described in Chapter 2. More precisely, in the non-precessing case, the deviations to this expression are due to imaginary coefficients in the mode amplitudes which only appear at high PN orders for the modes we consider (see Eq. (327) of [72] for the non-spinning mode amplitudes; note that the spin corrections to the mode amplitudes that are currently known, i.e. up to 2PN, contain no such complex correction).

Thus, a plausible first assumption could be that the $\epsilon_{\ell,m}$ have their source on PN not providing an accurate estimation of $\Lambda_{\ell,m}$ due to the lack of higher PN corrections. However, an excellent agreement is found between extrapolated NR and PN results regarding the $\Lambda_{\ell,m}$, i.e. in the NR data one finds consistently small but non-zero values of $\Lambda_{\ell,m}^{\mathrm{NR}}$. However, errors arising from finite extraction radius can be large and in what follows we will discuss the dependence of the quantities $\Lambda_{\ell,m}^{\mathrm{NR}}$ on it. Note that these quantities are functions of time. Due to this, we first need to align in time waveforms extracted at different radii. To facilitate the comparison with PN, we pick a reference frequency ω_0 early in the waveform and align all the $(2, 2)$ modes with the one with the largest extraction radius using the same procedure as described in Sec. 4.4. Fig. 5.6
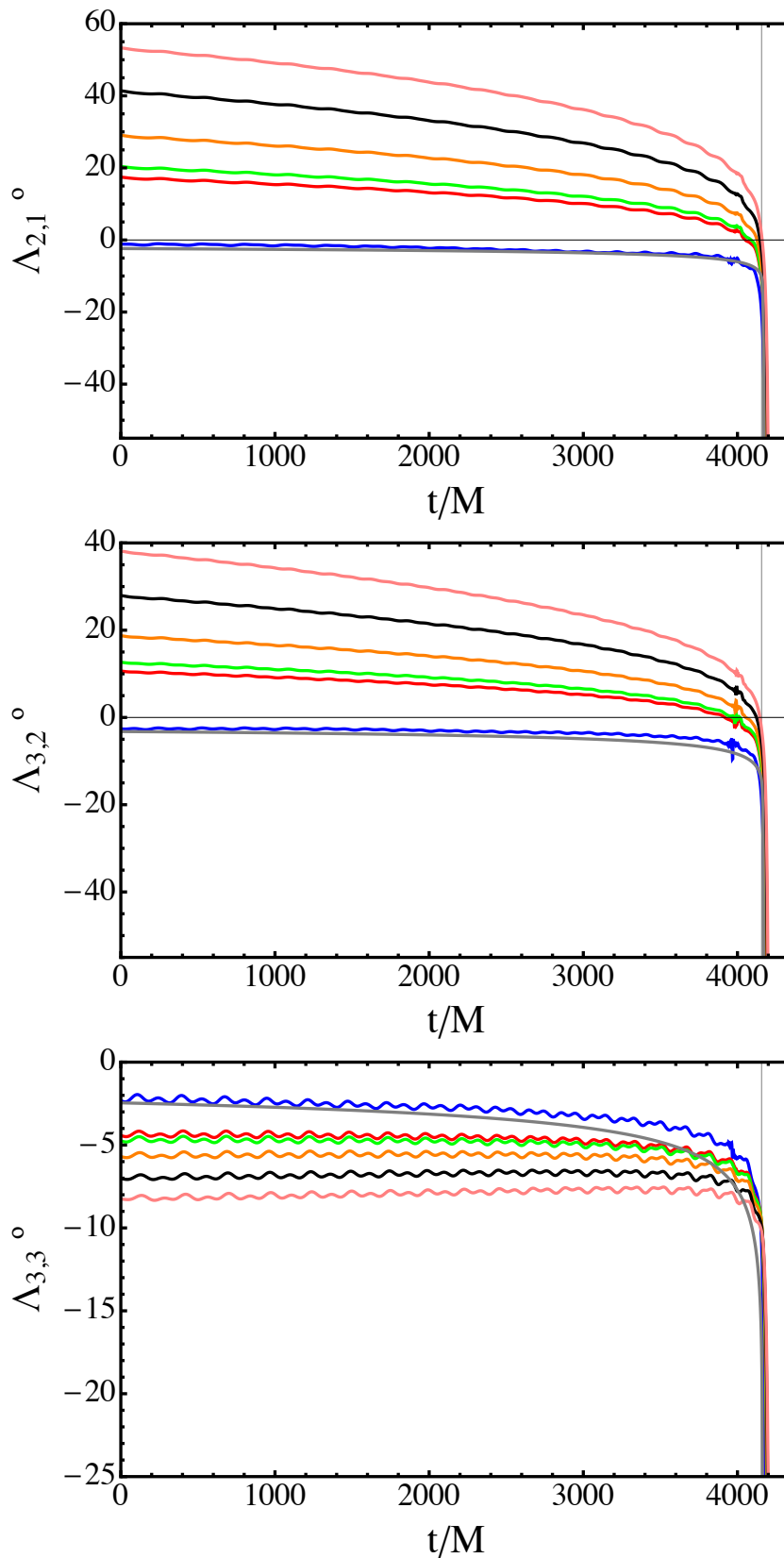
FIGURE 5.6: Value of $\Lambda_{\ell,m}^{\mathrm{NR}}$ for different extraction radii $(100, 133, 190, 266, 307)M$ (from pink to red) for SXS $q = 8$ non-spinning data and PN T1. We show here the $(2, 1)$, $(3, 2)$ and $(3, 3)$ modes. The vertical line denotes the location of the merger. The gray and blue curves correspond to PN and extrapolated $N = 4$ data respectively.

shows the (aligned in time) $\Lambda_{\ell,m}$ for the $(3,3)$, $(3,2)$ and $(2,1)$ modes for the $q = 8$ non-spinning waveform from the SXS catalog for different extraction radii as well as for the $N = 4$ extrapolated numerical waveform and the PN T1 waveform. The alignment has been performed at $M\omega_0 = 0.043$, and the time coordinate used for the plot has been shifted so that $t = 0$ corresponds to $M\omega_0 = 0.043$ for the extrapolated waveform. For the $(2,1)$ mode, the difference with the extrapolated waveform remains of the order of $15 - 20$ degrees even for the outermost available radii, and the same behavior is observed for all the $(\ell, \ell - 1)$ modes. On the contrary, for the $(3,3)$ mode (and the other (ℓ, ℓ) modes), the larger finite radii curves only differ from the extrapolated one by of the order of ~ 2 degrees. More important for our analysis, in both cases, the extrapolated waveform agrees to very high accuracy with the PN one, with a typical difference of only one degree. This illustrates that the main source of disagreement in the $\Lambda_{\ell m}$ is the finite radius extraction. Note also the oscillations present in the late part of the $(3,2)$ mode. These are common for several modes and extrapolated data. In particular Fig.5.7 shows the same quantities for the $(4,3)$ mode, for which these artifacts are of a larger size.
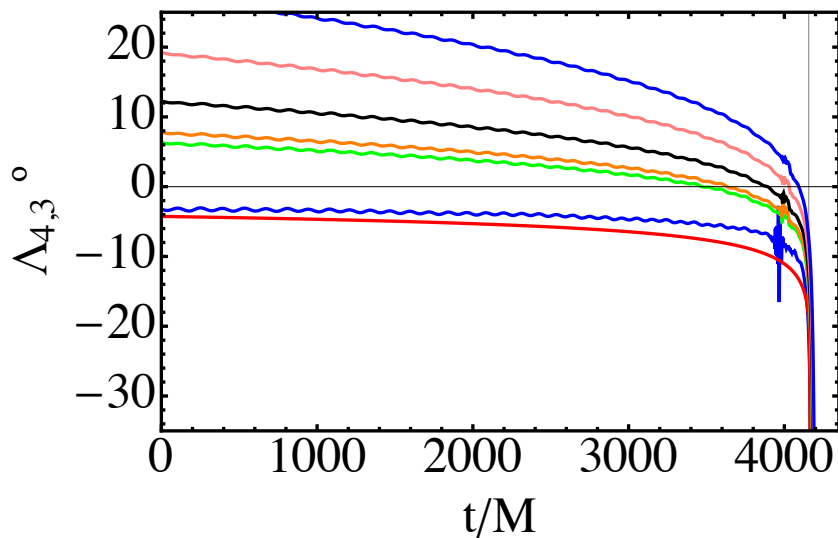
FIGURE 5.7: Same as in 5.6 for the (4,3) mode. Note the larger oscillations for the case of the extrapolated data in the bottom blue curve, which are of the order of 10 degrees.

In order to quantify further the effect of the extraction radius, we focus now on the asymptotic behavior of $\Delta\Lambda_{\ell m} = |\Lambda_{\ell m}^{NR} - \Lambda_{\ell m}^{PN}|$ (averaged in time over the interval $[1000M, 2000M]$ to average out oscillations) as a function of the extraction radius by fitting it to the power law $1°(r/r_0)^n$. The best fit values for n and r_0 are shown in Table 5.1 and suggest an $1/r$ dependence.

Fig. 5.8 shows the corresponding values of the $\epsilon_{\ell,m}$ as a function of frequency. As expected from the analysis of the $\Lambda_{\ell m}$, the errors are again dominated by the finite wave extraction radius. The largest radii differ again significantly from the extrapolated

(ℓ, m)	$(2, 1)$	$(3, 2)$	$(3, 3)$	$(4, 3)$	$(4, 4)$
n	-0.967	-1.015	-0.941	-1.038	-0.947
r_0	3199	4215	293	4182	598

TABLE 5.1: Results for (r_0, n) for the fits $\Delta\Lambda_{\ell m} = 1°(r/r_0)^n$ for the case $q = 8$ non-spinning SXS NR data matched to T1. The values suggest an asymptotic $1/r$-falloff in the inspiral region, where we hybridize.

waveforms, for which the agreement between NR and PN is of the order of only $1°$. Again, the behavior of the $(2, 1)$ mode is typical for the $(\ell, \ell - 1)$ modes, while the (ℓ, ℓ) modes behave similar to the $(3, 3)$ mode shown here. We note that the finite radius errors are strongly dependent on the gauge conditions used in the numerical relativity code. Once again, while the BAM modes show lower $\epsilon_{\ell,m}$ values those from SXS for the $(2, 1)$ and $(3, 3)$ modes, this behavior is broken for the case of the $(3, 2)$ mode (same happened for the amplitude) and the $(4, 3)$ mode added here.
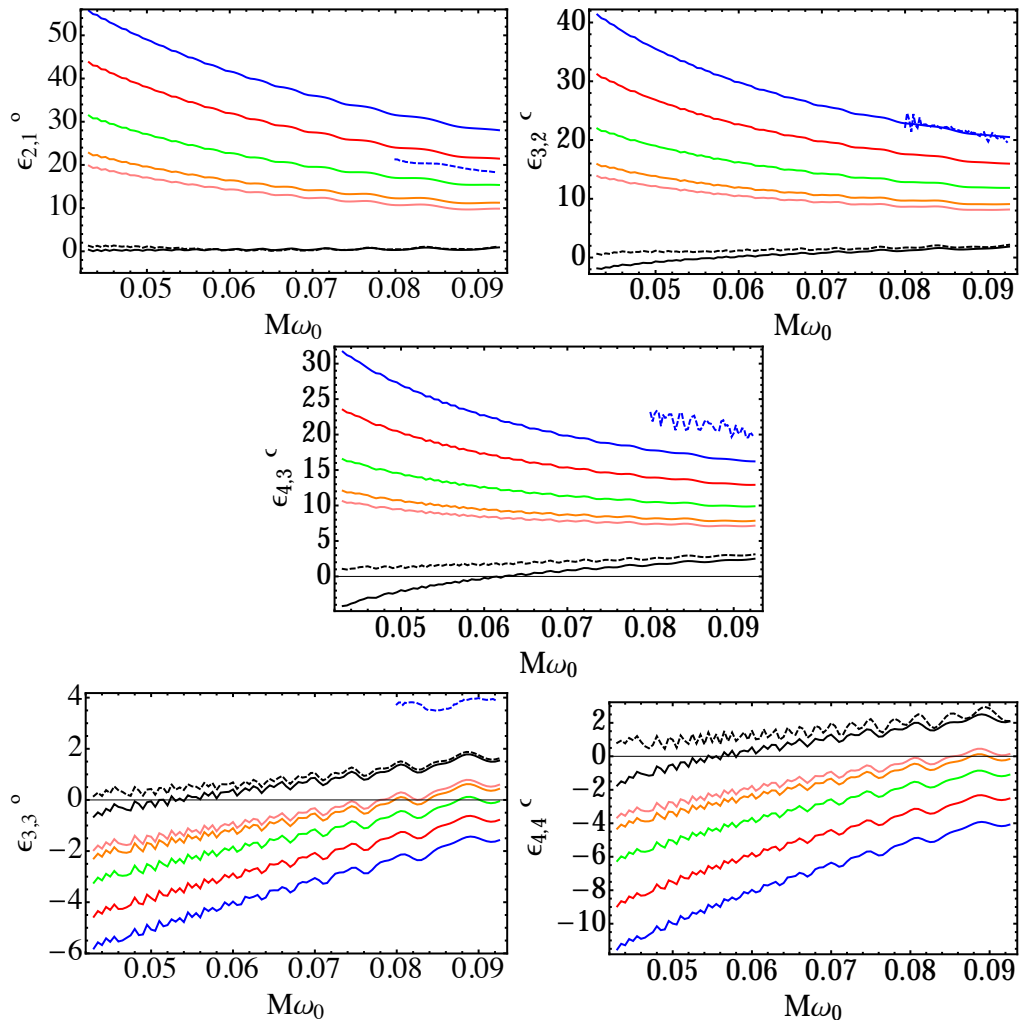
FIGURE 5.8: $\epsilon_{\ell,m}$ values for a the $q = 8$ non-spinning system from the SXS catalog for extraction radii $r = (100, 133, 190, 266, 307)M$ (in color from top to bottom) and extrapolated $N = 2, 4$ (black, respectively solid and dashed) and T1. We also show the BAM $r = 100$ case in dashed blue.

Once is clear that this effect has its source on the extraction radius of the NR simulation, it is natural to ask how will it affect different systems. To this end, we have also analyzed the non-spinning $q = (3, 4, 6)$ and the aligned-spin ($q = 3, \chi = \pm 0.5$) cases. We find that for systems with different mass ratios and spins the quantities $(r_{\ell,m}, \Lambda_{\ell,m}, \epsilon_{\ell,m})$ behave qualitatively the same as function of extraction radius. Furthermore, in Fig.5.9 it is remarkable that the values of $\epsilon_{\ell,m}$ for all the mentioned cases are almost the same for equal extraction radius along all the studied frequency range. This suggests that the influence on the $\epsilon_{\ell,m}$ of the extraction radius r of NR waveforms barely depends on the specific parameters of the simulated systems and that this effect is determined by some systematic "error" affecting simulation setup. A plausible cause is an effective
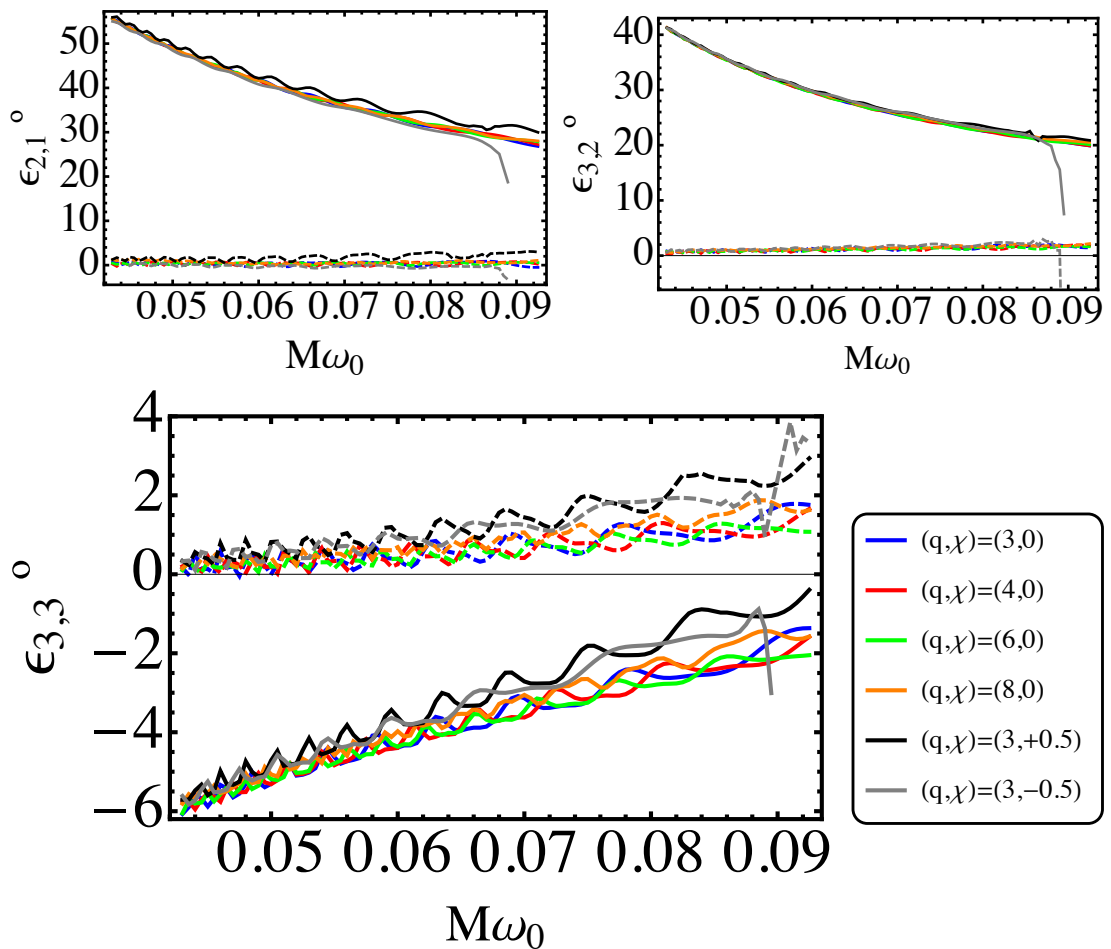
FIGURE 5.9: $\epsilon_{\ell,m}$ values for several SXS catalog systems for $r = 100M$ and extrapolated $N = 4$ data (solid and dashed respectively). Non-spinning systems are shown in color while we use black and grey for positive and negative spins respectively. Note that the values of $\epsilon_{\ell,m}$ are almost equal for all the systems, specially among the non spinning ones.

mode-mixing generated when the ℓ, m modes are obtained from the ψ_4 scalar. As we mentioned in Chapter 2, the individual modes are obtained by taking advantage of the

orthogonality of the $Y_{\ell,m}(\theta,\phi)$ over a sphere via

$$\psi_4^{\ell,m} = \int [\psi_4^+ - i\psi_4^\times] Y_{\ell,m}^{-2*}(\theta,\phi) \sin\theta d\theta d\phi. \tag{5.3}$$

However, the finitude of the extraction radius can make that the actual surface at which on ψ_4 is computed is not an actual sphere but something else: probably a "round" metric sphere, but deformed due to both the curvature of the spacetime and coordinate effects. It is then possible that the posterior decomposition of ψ_4 into its modes $\psi_4^{\ell,m}$ (as if it was extracted on a sphere) leads to slightly wrong modes and generates an effective "mode mixing".

5.3 Effect of NR extraction radius and extrapolation on the match

In the previous sections, we have investigated the disagreement between PN and NR in the region where we align and attach them. The discrepancies we observed illustrate inaccuracies in both waveforms at the typical frequencies where we perform the hybridization which will contribute to the global error budget of the hybrid. However, the accuracy of the full hybrid is of course also affected by the details of how these discrepancies are smoothed in the hybridization window and most importantly by the intrinsic error of the PN and the NR portions before and after the hybridization region. There, the $r_{\ell m}$ and $\epsilon_{\ell m}$ do not inform us about the accuracy. For instance, it could be that the spurious relative dephasings between the NR modes that we have observed may have disappeared around the merger where the higher modes are most important for matches. It is therefore not possible to directly translate the values we observed for the residual phase and amplitude disagreements into an overall error of the final hybrid.

In this section, we take a first step towards quantifying the error budget of the full hybrid in terms of quantities useful for data analysis applications. As usual, we will replace the unanswerable question of how much the hybrid differs from the true signal by a study of the typical mismatch that one obtains when one varies the different ingredients in the procedure. A systematic study, which properly addresses the different requirements for the detection and parameter estimation problems across a significant portion of the black hole parameter space, is beyond the scope of this thesis. Instead, we restrict the scope of this study to understanding the effect of the extraction radius of the NR waves (and their extrapolation) on the match. In doing this, we do not claim that this is the main source of inaccuracy for the hybrid: using for instance a PN approximant that predicts a phase evolution very different from the NR one (see e.g. T4 in Fig. 4.4) will certainly

lead to larger mismatches. Rather, motivated by the observations of the previous section that suggest that extraction radius can have a strong effect on the agreement between PN and NR in the late inspiral, we illustrate here how much of an effect it makes on the match between full hybrids. Comparing the results to other studies in the literature can give a first impression of the relative contribution of different imprecisions for data analysis applications and guide more systematic future investigations.

We illustrate our results with the $q = 8$ non-spinning case from the SXS catalog and use the 2015 early Advanced LIGO noise curve [34]. We hybridize with T1 (the PN approximant that gives the smallest secular trend between the PN and the NR $(2,2)$ mode frequencies for this case) hybridized at $\omega_0 = 0.073$. With this choice, and given the length of our blending windows, the NR $(2,2)$ mode covers the entire instrumental band (say starting from 20 Hz) for total masses larger than $\sim 120 M_\odot$. Here we have chosen to hybridize at a relatively large frequency to facilitate comparisons with shorter NR simulations. We focus for now on the highest resolution available (namely `Lev. 5`) and on the waves extracted at $r = 100$M (innermost radius available) and 307M (outermost one) as well as those extrapolated to null infinity using $N = 2$ and $N = 4$ polynomial orders. We denote these waveforms h_{100}, h_{307}, $h_{N=2}$ and $h_{N=4}$ respectively.

Our hybridization procedure applied to each of these NR waveforms yields a hybrid $h_X(\theta, \varphi, \kappa)$ (with the notation of Eq. (4.8)) whose modes are defined in Eq. (4.26) and slightly different values for the shift φ_0 needed to adjust conventions [2] between PN and NR. This is of course a mere consequence of the fact that our procedure to infer the differences in conventions is affected by the inaccuracies in the original waveforms (here we know that the conventions are the same for all the NR waveforms that we consider). Since in the presence of higher modes, the dependence on φ is non trivial, one has to be careful to compare waveforms at the same physical sky orientation (or optimize over it depending on the application). In the general case, if two hybrids are built out of different PN pieces and different NR pieces, comparing at the *same* angle φ makes no sense in principle since the definitions of the origin of the azimuthal angle are a priori independent. In the present case however, φ has the same meaning for all the numerical waveforms that we consider (and therefore, with our choice of applying the φ_0 rotation to the PN part in Eq. (4.26), for the hybrids) and it makes sense to compute

$$\max_{t_0} \mathcal{O}\left[h_1(\pi/2, 0, 0), h_2(\pi/2, 0, 0)\right], \tag{5.4}$$

i.e. the overlap optimized over time-shifts only of the two waveforms at the same (source) sky location ($\theta = \pi/2, \varphi = 0$) chosen so that the higher modes contribute significantly to

---

[2] We find $\varphi_0^X - \varphi_0^{N=4} = .04°, 7.19°, 21.87°$ for $X = (N = 2)$, 307, 100 respectively. We find the same ψ_0 for all these cases.

the full waveform and at the arbitrary effective polarization $\kappa = 0$. This is the quantity plotted in plain green in Fig. 5.10. Note however that the early inspiral portions of our hybrids now differ by a shift in φ, i.e. despite the fact that we are using the same PN input in all our hybrids, the quantity defined in Eq. (5.4) will not go exactly to 1 in the limit of small masses where only the PN tail is in band[3]. Often in data-analysis applications, it is also interesting to optimize this match over φ, reason why we also plot in dashed-green the quantity

$$\max_{t_0,\varphi} \mathcal{O}\left[h_1(\pi/2,0,0), h_2(\pi/2,\varphi,0)\right] \tag{5.5}$$

in the figures below.
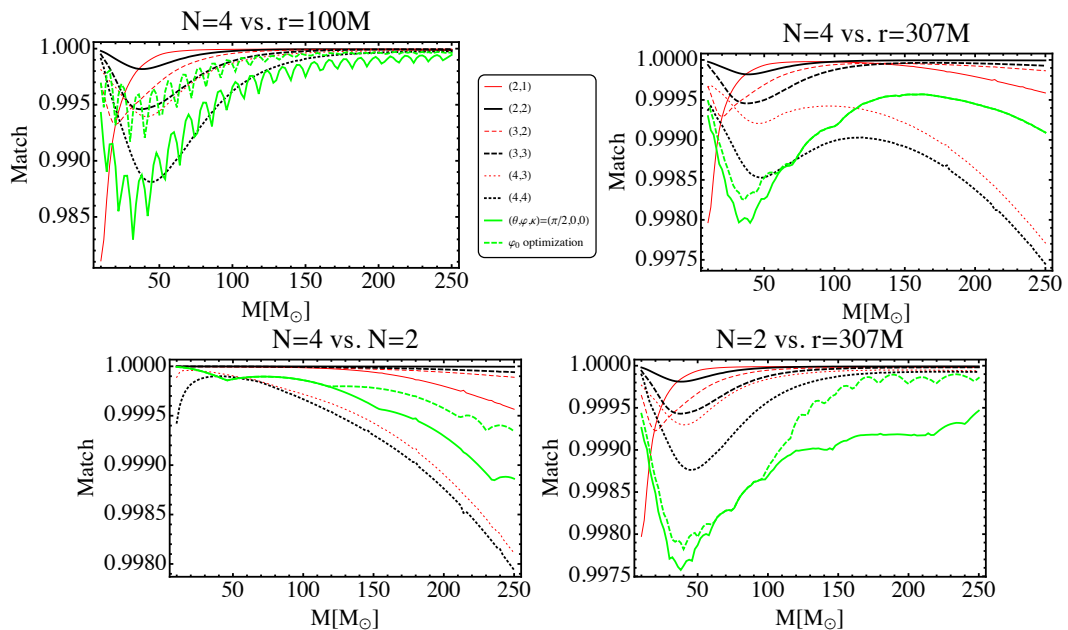
FIGURE 5.10: Match of individual modes (optimized over phase and time) and full waveforms at $(\theta, \varphi, \psi) = (\pi/2, 0, 0)$ optimized only over time (in solid green) and time and phase (dashed green) for $q = 8$ non-spinning hybrid waveforms built out of T1 and SXS NR waveforms produced during a single simulation but either extracted at finite radius $r = 100M$ and $r = 307M$ or extrapolated with polynomial orders $N = 2$ and $N = 4$.

Fig. 5.10 (beware of the different scale for the top left panel) displays the result of this study for various couples of waveforms. In each panel, we additionally show the overlap between the individual modes (in black and red) optimized over time and phase to check to what extent the modes of both hybrids agree if we allow ourselves to align them one by one independently. We first focus on the top plots. In order to interpret these,

---

[3]An equally valid point of view would be to modify Eq. (4.26) by applying the φ_0 shift to the NR portion, i.e. redefining the conventions of the NR waveforms to reproduce those of the PN (as always up to errors in the determination of this convention shift). Then, when computed using the waveforms evaluated at the same φ, the match goes to 1 for small enough masses since we are comparing the original waveform against itself but differs from the match between the pure NR waveforms at masses large enough that the hybridization region is out of band.

one should keep in mind that for large masses, the hybridization window is pushed to lower frequencies than those accessible to the instrument and this becomes a pure NR comparison. In this region, the typical mismatch between $h_{N=4}$ and h_{100} is of a few 0.1% and goes below 0.1% for h_{307}. As we move to smaller masses and the hybridization region enters the instrumental band, the match degrades and reaches a minimum around $40 M_\odot$: while the mismatch there is above 1% in the $R = 100$ vs $N = 4$ case (this gets reduced by a factor ~ 2 after φ-optimization), it remains as low as 0.2% when using $R = 307$. At even lower masses, the comparison becomes dominated by the PN tail (and particularly by the $(2, 2)$ mode) which is identical for both waveforms up to the φ shift discussed above and the match grows again (the optimized one going to 1 exactly in the low mass limit).

From this comparison, where the $N = 4$ waveforms has been used as a reference, one can argue that for the NR data set studied here, extracting the waves in the SpEC code at radii of $\mathcal{O}(300\,M)$ (as typically available in the SXS catalog) is sufficient to control the error to the $\sim 0.1\%$ level in terms of mismatch.

To check the effect of extrapolation orders on this study, in the lower right panel we reproduce the upper right one but use $N = 2$ instead of $N = 4$. While the general behavior and scale remains essentially unchanged, we note that the $(4, 4)$ and $(4, 3)$ modes which were significantly disagreeing at high frequencies and dominating the total mismatch between $N = 4$ and $R = 307$ now give much higher matches at high masses (note also that after optimization over φ the matches between the hybrid become very close to 1). This is consistent with the Ref. [97], where it is also observed that different orders may show varying performance during the evolution, and higher orders may in particular be problematic during merger-ringdown. Except for these discrepancies at high mass which come from the presence of unphysical features in these two $N = 4$ modes and which remain on the order of $\sim 0.1\%$, the order of extrapolation therefore does not seem to affect our previous conclusion, as also illustrated by the lower left panel in which we directly compare the hybrids built with $N = 4$ and $N = 2$.

Finally, we perform a similar study to compare the effect of numerical resolution on the match to the effect from different extraction radii. In Fig. 5.11 we plot matches as in Fig. 5.10, but using hybrids constructed from numerical waveforms produced at different numerical resolutions instead of extraction radii. For the faster than polynomial convergence exhibited by spectral codes such as SpEC one typically quotes the difference between the highest and next-highest resolution as an error estimate, see e.g. [149] for a comparative discussion of the error analysis performed in spectral and finite-difference numerical relativity codes. Here we conservatively use the highest available resolution level (5) and a resolution two levels coarser (3), and we find mismatches smaller or at

comparable level that the mismatches shown in Fig. 5.10 resulting from finite extraction radius. In both cases, the mismatches are certainly not larger than what can be expected in waveform models such as [36, 48, 51, 56]. In addition, any actual signal searches or parameter estimation calculations will be based on discrete or continuous waveform families and matches will effectively be optimized over all physical parameters.
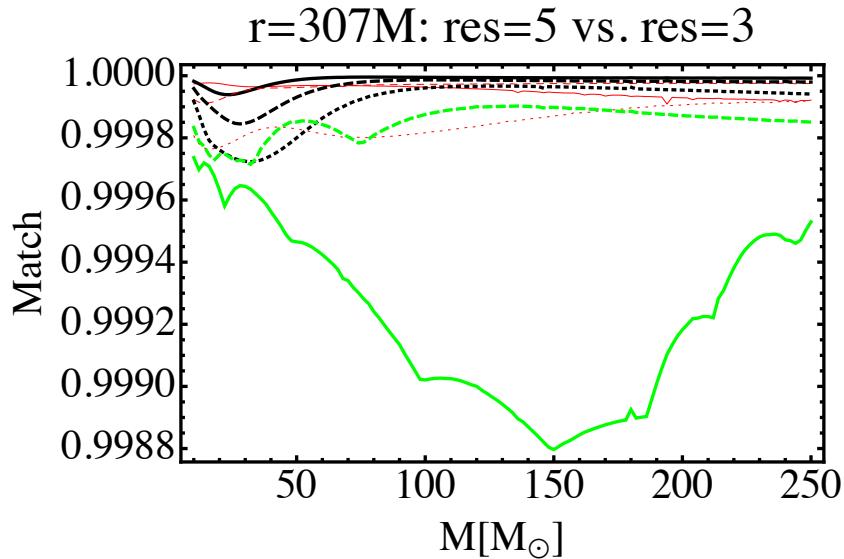
FIGURE 5.11: Match as in Fig. 5.10, but between hybrids constructed from numerical waveforms produced at different numerical resolutions instead of extraction radii. We use the highest available resolution level (5) and a lower resolution level (3) for $R = 307M$.

Complementary analysis: rotating NR

In the analysis performed above, the PN tails of the different hybrid waveforms disagreed due to the different φ_0 rotations applied when hybridizing them to NR. Since the PN approximant used is always the same, these effect can in principle have two sources: either different NR simulations show different frequency evolutions or they show, in some effective way, different conventions for the φ_0 angle. We in principle discard the latter since all SXS simulations are supposed be performed using the same conventions. In any case, if this effect was dominant we can get rid of it by rotating the NR modes when constructing the hybrid waveform and investigate the effect of the other one. Fig. 5.12 shows the same results as 5.10 and 5.11 (except for the optimization in φ_0, which is not important for our purposes) when the modes are constructed by rotating the NR modes. Since we know that the PN tail of all waveforms is now exactly the same, we cannot argue that there might be φ_0 shifts between the NR tails unless that was originally the case (i.e., that different NR simulations performed at different extraction radii have different conventions), which we have discarded. Keep in mind however, that for these waveforms one finds different $\epsilon_{\ell,m}$ values that, in particular, need to be
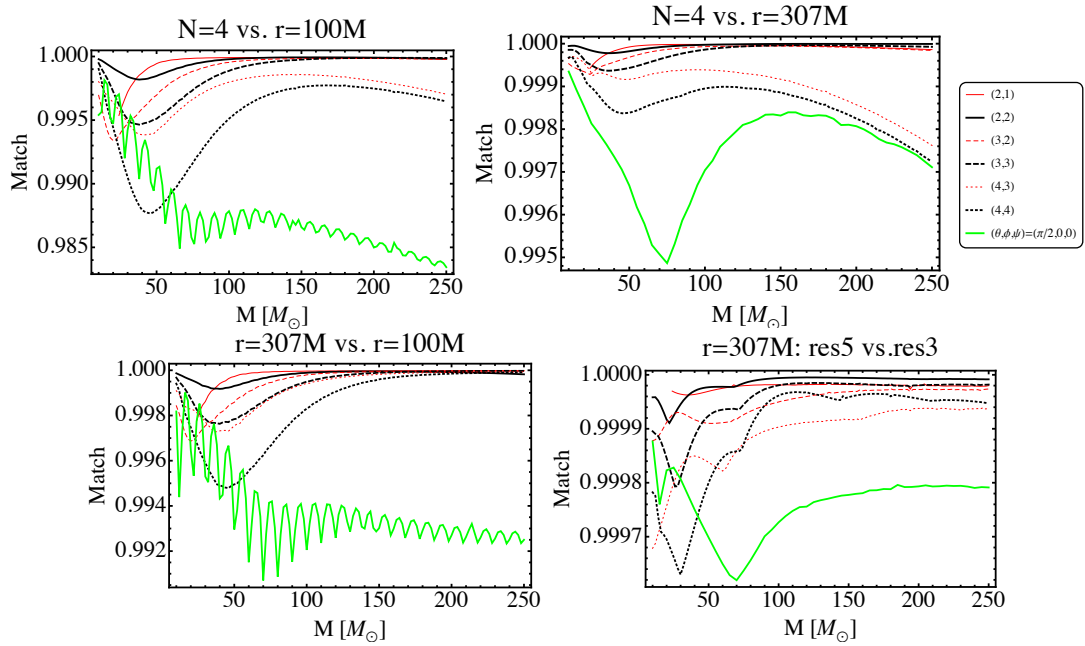
FIGURE 5.12: Match of individual modes (optimized over phase and time) and full waveforms at $(\theta, \varphi, \psi) = (\pi/2, 0, 0)$ optimized only over time (in solid green) and time and phase (dashed green) for $q = 8$ non-spinning hybrid waveforms built out of T1 and SXS NR waveforms produced during a single simulation but either extracted at finite radius $r = 100M$ and $r = 307M$ or extrapolated with polynomial orders $N = 2$ and $N = 4$. Here the $m\varphi_0 + \psi_0$ rotation has been applied to the NR side.

smoothed over the hybridization region.

The $\epsilon_{\ell,m}$ measure the difference between the rotation that should be applied for making NR and PN conventions agree and the one needed for making two particular modes to agree: so they imply that different modes are being represented at different values of φ for the same simulation. Due to this, all plots show the following qualitative behavior: at low masses matches are now high and would go to exactly 1 at very low ones due to the PN tails being exactly the same. When the mass grows and the hybridization region gets in band, the match decays due to two reasons. On the one hand each waveform presents different $\epsilon_{\ell,m}$ values which will introduce different artificial frequencies when smoothed. On the other, the NR modes themselves might be slightly different. In order to estimate how much the latter dominates, we again compute the match of the individual modes optimized over φ_0. The mismatch between the individual modes is comparable to the total one in the case of the top right plot, where the $N = 4$ and $r = 307M$ waves are compared. In particular, and again, the mismatch at high masses is dominated by mismatches of the $(4, 4)$ and $(4, 3)$ modes. Note also that these two hybrids present the two lowest (and more similar) $\epsilon_{\ell,m}$ values (see Fig. 5.8). However, for the top left plot, where we compare $N = 4$ with $r = 100$ the match decays more in the hybridization region and is not dominated anymore by the individual modes in the high mass region, but rather by the fact that the several modes are describing the

GW radiation at different effective φ_0 angles. Exactly the same behavior can be noted in the lower left panel. Finally, In the lower right plot, we compare again the two $r = 307$ simulations computed with different resolutions. The $\epsilon_{\ell,m}$ values of these two NR simulations agree to a $\sim 0.1\%$. Note that both the individual and total mismatches are comparable and much larger that for the other cases. Since we initially discarded that different NR simulations extracted at different extraction radius have different φ_0 conventions and the secular trend does not play a crucial role (individual matches are large), what remains is the possibility of an effective mode mixing as a result of the finite radius extraction: larger the lower r is.

Altogether, the finitude of the extraction radius clearly dominates the error budget of both the individual modes and the total waveform, having it a larger impact when waveforms are to be described at edge-on locations and for high mass. The close relation $r \leftrightarrow \epsilon_{\ell,m}$ and the one $\epsilon_{\ell,m} \leftrightarrow \mathcal{O}$, makes the $\epsilon_{\ell,m}$ (which arise for free during the hybridization process) provide a good diagnostic of the impact of r. Extrapolation can also introduce secondary errors due to artifacts present at high frequency.

5.4 Discussion

The aim of this Chapter has been to evaluate the accuracy of both the PN and NR results for the higher order modes and the study of their sources as well as the impact they have on the final waveform.

Regarding NR amplitude errors, we find a strong dependence on the numerical code used, which we attribute to the difference in coordinate gauge conditions. With the exception of the $(3,2)$-mode, e.g. $r = 100$ BAM data are significantly closer to the extrapolated result than the corresponding SXS $r = 100$ curve. On the other hand, it also shows larger oscillations. We also note that, for any given finite extraction radius, the error becomes larger at lower frequencies. This is the expected consequence of the fact that as the frequency increases (or equivalently as their wavelength decreases), the wave zone (defined by $r \gg \lambda$) extends to smaller radii. We find good agreement between post-Newtonian amplitude and those extrapolated to infinity from several extraction radii in a numerical relativity calculation for the $(2,1)$, $(2,2)$ and $(3,2)$ modes, but significantly larger errors of up to a few 10% for the modes $(3,3)$, $(4,3)$, $(4,4)$ and $(5,5)$, and we find that these deviations are consistent with the spread between PN results at different orders. Also, we have seen that the inclusion of the latest 3.5PN correction to the amplitude of the $(3,3)$ mode enormously increases its accuracy.

Regarding the phase differences $\epsilon_{\ell,m}$, we have found an excellent agreement on the order of $1°$ of PN results with numerical relativity waveforms extrapolated to null infinity, while deviations at finite radius can be as large as tens of degrees for $(\ell, \ell-1)$ modes. On the contrary, for the (ℓ, ℓ) modes, the larger finite radii curves only differ from the extrapolated one by of the order of 2 degrees. In particular, we find that the influence on the $\epsilon_{\ell,m}$ values of the extraction radius r of NR waveforms depends on the specific parameters of the simulated systems only rather weakly. The results shown imply that during the inspiral, the complex part of the standard PN waveform amplitudes can be taken as the correct value for practical purposes. This yields in particular a convenient test for finite radius errors in numerical relativity (since a practically exact result is known), and may serve to determine favorable coordinate gauge conditions for wave extraction.

A systematic study of the effect of the phase and amplitude errors which we discuss on gravitational wave data analysis, both regarding the detection problem and parameter estimation is beyond the scope of this work. Instead we have performed simple match calculations with the initial and design sensitivity advanced LIGO noise curve, evaluating the match between waveforms resulting from different extraction radii or numerical resolutions. This simplistic study can serve for comparisons due to mismatches resulting from other effects, such as the choice of PN approximant, or waveform modelling errors, and thus give a first impression of the relative importance of different types of waveform imprecisions, and help guide more detailed investigations. This part of the Chapter overlaps with other investigations such as [97–99] regarding the errors in finite radius and extrapolated waveforms. Our results appear consistent with previous work, but add the aspect of considering full hybrids and investigating how the match varies when the hybridization region is in band and puts the focus on errors in higher modes. The close relation between the mismatch found and the value of the $\epsilon_{\ell,m}$ coefficients, makes the latter a good diagnose of the quality of the higher order modes and the mismatch that will be generated.

In particular, we have seen that the extraction radius can lead to significant phase and amplitude errors. Corresponding mismatches as discussed in Sec. 5.3 are roughly at the level of 0.1% for the cases we have considered. Mismatches at this level appear at least negligible for GW searches. However, in principle this might affect parameter estimation at very high SNR for high mass edge-on systems which in turn are the ones generating the lowest SNR.

The larger importance of higher order modes for the case of precessing systems may motivate the systematic application of this kind of analysis for precessing waveforms. Also, the recent extrapolation to infinity method based on a $1/r$ expansion of the finite

radius results presented in [110] will provide new sets of NR waveforms with which our results should be checked.

Chapter 6

Impact of higher order modes in aligned-spin searches for Binary Black Holes

6.1 Goals and previous studies

Current GW searches for CBCs implement template banks whose waveforms do only contain the quadrupolar $(\ell, |m|) = (2, 2)$ modes of the GW emission, known as quadrupolar waveforms, neglecting the HOM content of the incoming signal. This is justified by the fact that, in the non-precessing case, most of the power emitted by the source is carried by these two modes, as we discussed in Chapter 2 (see Figs.2.4, 2.5 and 2.6). Also, as shown in Chapter 3, the usage of quadrupolar waveforms allows for an analytical optimization of the SNR over the extrinsic parameters of the waveform, which is much faster than the numerical optimization that would be needed if HOM were included.

The goal of this chapter is to study the consequences of this neglection in current and future searches, both in terms of loss of detection rates and biases caused in the estimation of the parameters of the source. We will focus on the case of non spinning BBH within the mass range $50 M_\odot < M < 220 M_\odot$ and will add four spinning cases: a $q = 3$ system with equal $\chi = \pm 0.5$ dimensionless spins and a $q = 1$ system with equal $\chi = \pm 0.2$. We will consider the case of a template bank including a single effective spin parameter χ for the case of two Advanced LIGO noise curves: the early version (eaLIGO) with a lower frequency cutoff $f_0 = 30$Hz and the design Zero-Detuned-High-Energy-Power version (AdvLIGO) with $f_0 = 10$Hz. Since no detections were made in initial LIGO (iLIGO) data, for which searches have been performed using a non-spinning template bank, we

will also pay attention to this case for which we will consider non-spinning targets, a non spinning template bank and $f_0 = 30$Hz.

The case of non-spinning targets and a non-spinning template bank for the case of AdvLIGO has been widely studied. Pekowsky et al. [150] explored the mass range $M > 100M_\odot$ noted that the match between BBH NR waveforms including HOM and the corresponding ones including only quadrupolar modes is < 0.97 for most of the orientations of the binary. They also noticed that however, these orientations coincide with those for which the SNR is the lowest, mitigating the effect of HOM when average over orientations is considered. More recently, Brown et.al., [151] and Capano et. al., [125] studied respectively the *fitting factor* FF of a non-spinning quadrupolar template bank towards non-spinning waveforms including HOM for the total mass range $m_1, m_2 \leq 25M_\odot$ and $m_1, m_2 \leq 200M_\odot$. The result is that for total masses $M < 50_\odot$ and mass ratios $q < 4$ one does not expect event losses larger than 10%, which is within the commonly accepted limit in GW searches. Furthermore, [125] also computed the χ^2 and ρ_{new} of the target signals towards their bank, simulating the effect of HOM in a full search neglecting HOM and estimated the false alarm rate (FAR) of a search including them. This allowed them to compare the sensitivity of both searches to signals including HOM. They concluded that inclusion of HOM in current template banks would only be advantageous for certain regions of the parameter space for which the FF of the bank towards their target signals were particularly low. In particular for $q \geq 4$ and $M > 100M_\odot$. These event loss results widely agree with those presented by Varma et al., [2], to which work in the context of this thesis contributed. They also studied the systematic parameter bias caused by the neglection of HOM and compared it with the statistical uncertainty due to the presence of Gaussian noise in the data stream. They concluded that the former dominate the latter for mass ratio $q \geq 4$ and total masses $M > 150M_\odot$ for a SNR $\rho \sim 8$. This study was based on the Fisher information matrix formalism, which allowed them to study a large number of points in the parameter space. In contrast [152] studied the presence of systematic biases in the estimated parameters of the CBC but compared them against the expected statistical errors using Markov-Chain Monte-Carlo (MCMC) techniques. However, the large computational cost of this study restricted it to a few points of the parameter space. They obtained that, for binaries such that $1 \leq q \leq 6$ and $M < 60M_\odot$ and fixing inclination angle to $\theta = \pi/3$, systematic errors introduced by the neglection of HOM are smaller than the expected statistical errors at SNR ~ 12. However, for larger masses ($M = 120M_\odot$, $q = 6$), systematic biases will dominate statistical errors at SNR ~ 12.

As said above, we will extend the study performed in [2] to the case of a template bank including a single effective spin χ and equal spin target signals and add the cases of the

eaLIGO and iLIGO noise curves. This is motivated by the fact that it is expected that at least single effective spin template banks will be used in the shortcoming searches and it might happen that for the case of non-spinning targets, the presence of spin in the template bank mitigates the effect of HOM in detection. We also want to understand how neglection of HOM will affect spinning targets. Finally, the higher frequency cutoff of the upcoming eaLIGO (30Hz) compared to the widely studied AdvLIGO (10Hz) could in principle cause larger event losses and parameter biases, as elucidated in Chapter 3 and by [153].

The rest of this chapter is organized as follows. In Section 6.2 we will give an overview of the situations in which HOM may be important/dominate the mode content of a GW signal. In Section 6.3 we will describe the target and bank waveforms used and how the relevant quantities for this study have been computed. The next two Sections 6.4 and 6.5 will show results regarding detection losses and systematic parameter biases due to neglection of HOM and compare the latter to the statistical uncertainty due to the presence of Gaussian noise in the detector data. In the next section, take advantage of the hybrid modes used in this chapter and discuss the contribution of each "pair" of them to the kick of the final black hole. Finally, in Section 6.7 will discuss the results found along the chapter.

6.2 The role of higher order modes

Several factors determine the HOM content of the incoming GW signal. These can be divided in three main groups: the nature of the source, the position of the detector on the sky of the source (or orientation of the binary) and the actual sensitivity curve of the detector.

The nature of the source: intrinsic parameters

The ratio between the amplitude of HOM and the quadrupolar $(2,2)$ mode, $\mathcal{A}_{\ell,m}(\Xi;t) = \frac{|h_{\ell,m}|}{h_{2,2}}$ depends on the intrinsic parameters (q,χ) of the source. During the inspiral, this behavior can be directly observed from the value of the post-Newtonian amplitudes [72], which we showed in Chapter 2, Figs.2.5 and 2.6. Note how in the frequency range shown in these plots, the amplitude of the $(2,2)$ mode is about 2 orders of magnitude larger than that of the next most dominant mode (typically the $(3,3)$, when present) for all the sources shown. However, Fig.2.4 shows that during the late inspiral and merger this ratio can get up to ~ 0.3 for the case of a $q = 8$ non-spinning system. As a general trend,

the larger q is, the larger the contribution from HOM will be (see Fig.2.5). This will translate into larger event losses due to neglection of HOM for larger q. The dependance on the spin is more intricate. Fig. 2.6 shows that different modes have different behaviors for a given mass ratio. It can be noted how all the modes shown contribute more for the case of positive spin except for the $(3,3)$ mode, which is however the most dominant HOM. This makes difficult to predict how losses due to neglection of HOM will depend on the spin χ.

Geometrical facts: the orientation of the binary

The previous point dealt with the values of the $h_{\ell,m}$ modes themselves. However, when constructing the full signal h

$$h(\theta, \varphi; t) = h_+ - i h_\times = \sum_{\ell \geq 2} \sum_{m=-\ell}^{m=\ell} Y_{\ell,m}^{-2}(\theta, \varphi) h_{\ell,m}(t). \tag{6.1}$$

The modes $h_{\ell,m}$ are weighted by the $Y_{\ell,m}$ factors. This determines how much each mode contributes at a given sky location (θ, ϕ) (or orientation of the binary). Fig. 2.7, in Chapter 2, shows the values of the amplitudes of several spherical harmonics as a function of θ. Note that $|Y_{2,2}|$ has its maximum at the pole $\theta = 0$ and its minimum at the equatorial plane located at $\theta = \pi/2$, while most of the $m \neq 2$ modes behave in the opposite way. This means that a waveform including only the $(2,2)$ mode should be a good representation of the total signal if the system is face-on (detector located at $\theta = \{0, \pi\}$), getting its accuracy reduced as the system is closer to be edge-on ($\theta = \pi/2$). This was checked by [150], which also noted that the for the latter case the optimal SNR of the signal is the lowest. Consequently, when event losses are averaged over all sky-locations (all orientations), the net effect of the neglection of HOM gets mitigated by the fact that the loudest signals are well recovered by quadrupole templates.

The detector noise curve

Finally, as noted in [153], there is a combined effect of the detector sensitivity curve and the total mass M of the CBC. The frequency of each mode roughly scales with the orbital frequency as $\omega_{\ell,m}(t) = \frac{d\phi_{\ell,m}}{dt} \simeq m \times \omega_{orb}(t)$. Also, as the total mass M of the source increases, $\omega_{orb}(t)$ falls off as $1/M$. When M is such that the $(2,2)$ is below the detector band, larger m modes will dominate the incoming signal, which will not be well filtered by quadrupolar templates. This can be noticed in Fig.6.1. Also, the specific features of the curves will produce different effects. In the $200 M_\odot$ case, the HOM dominate the signal content at the most sensitive point or sweet-spot for the three noise

curves shown. Note however, that the AdvLIGO curve is much flatter than the other two. Consequently, its sensitivity at frequencies for which the $(2, 2)$ mode dominates the signal is not much lower than at its sweet-spot, which makes that piece of the waveform (which can be well filtered by quadrupolar waveforms) weight almost as much as the one at the sweet-spot. This is clearly not the case for the other two curves, which will make the quadrupolar template bank to have a lower FF towards the full signal, translating this into larger event losses for the case of eaLIGO and iLIGO.

6.3 Analysis set up

Target signals & bank waveforms

The target signals employed in this study correspond to the hybrid waveforms containing HOM described in Chapters 4 and 5, using SXS NR data extrapolated to infinity. Since we want to pay special attention to the high frequency content of the signals (where HOM dominate) we want to have as clean high-m modes as possible. Consequently, the extrapolation order was chosen to be $N = 2$ since as shown in Chapter 5, it shows lower oscillations at high frequencies in the $(4, 3)$ and $(4, 4)$ modes. The PN pieces of the target signals are Taylor T1 waveforms with 3.5PN non-spinning and 2.5PN spin corrections to the phase. The non-spinning amplitude corrections are 3PN for all modes. Spin-orbit and spin-spin corrections have been included up to 2PN order. The corrections employed here are in contrast with those used in Chapter 5. This is due to the fact that some of the latest corrections were not implemented in the PN code employed when this work was done. However, as HOM are not important until the late inspiral and merger of the coalescence (where SXS NR waveforms do always extend to) this is not in principle a caveat. Equal mass cases included the $\{(2 \pm 2), (3 \pm 2), (4 \pm 2), (4, \pm 4)\}$ modes while $q \neq 1$ targets include the $\{(2 \pm 1), (2 \pm 2), (3 \pm 2), (3 \pm 3), (4 \pm 3), (4, \pm 4)\}$ ones.

For each NR simulation with parameters (q_i, χ_i) Table 6.1 we constructed the corresponding full hybrid waveform $h_{i,j} \equiv h(\Xi_i, \Lambda_j)$ for all the values of Λ and M described in Table 6.2. Note that with the described grid in angles, we only cover the upper sphere of the source of the sky and half of the polarizations. This however suffices to obtain results for all the possible angles since it holds

$$
\begin{aligned}
h(\pi - \theta, \varphi, \psi) &= h(\theta, \varphi, \pi - \psi) \\
h(\theta, \varphi, \pi + \psi) &= -h(\theta, \varphi, \psi).
\end{aligned}
\tag{6.2}
$$
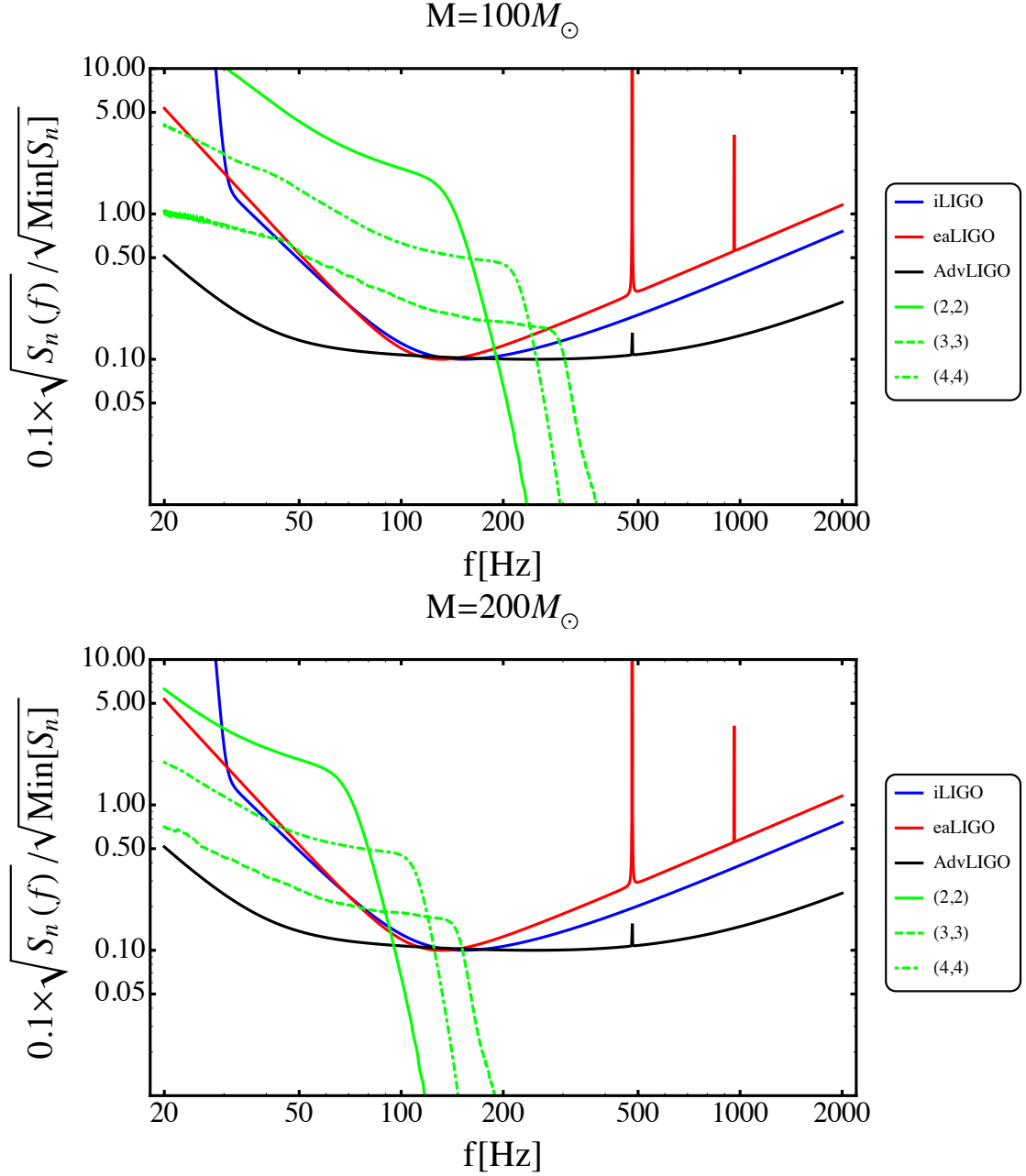
FIGURE 6.1: The plots show the ratio $0.1 \times \frac{\sqrt{S_n(f)}}{\sqrt{\min S_n}}$ for the three noise curves considered in this thesis. The amplitude of the Fourier transform of the $(2,2)$, $(3,3)$ and $(4,4)$ modes are shown in different styles of green and scaled by an appropriate factor. The chosen source is a $q = 8$ non-spinning BBH. The panel above shows the modes for the case of $M = 100 M_\odot$ and the one below for the case of $M = 200 M_\odot$. Note how as we increase the total mass, the $(2,2)$ mode, which is clearly dominant at low frequencies, gets out of band while, the region where the different modes have comparable amplitudes becomes more important. This effect is less dramatic for the case of AdvLIGO due to the larger flatness of its noise curve and its lower frequency cutoff. This makes the $(2,2)$ to be kept in band for larger total masses than for the other two noise curves.

The bank waveforms $h^{\mathcal{B}}$ belong to the SEOBNRv1-ROM family [118], which do only include the $(2,2)$ mode and which use a single effective spin parameter χ. These

SIM ID	q	χ	PN	$M\omega_0^{(2,2)}$
SXS:BBH:0168	3	0	T1	0.043
SXS:BBH:0167	4	0	T1	0.045
SXS:BBH:0166	6	0	T1	0.045
SXS:BBH:0063	8	0	T1	0.043
SXS:BBH:0150	1	+0.2	T1	0.035
SXS:BBH:0149	1	-0.2	T1	0.043
SXS:BBH:0046	3	+0.5	T1	0.038
SXS:BBH:0047	3	-0.5	T1	0.043

TABLE 6.1: Summary of hybrid waveforms used for testing the effects of HOM

Magnitude	M	$cos\theta$	ϕ	ψ
Range	$[50,218]M_\odot$	$[0,1]$	$[0,2\pi)$	$[0,\pi)$
Step	$12M_\odot$	0.05	$\pi/20$	$\pi/6$

TABLE 6.2: Grid in Mass and angles Λ used for our studies.

cover the domain $q \in [1,80]$ $\chi \in [-1,+0.6]$ and $Mf \in (0.001,0.14)$. Note that the $(q,\chi) = (3,+0.5)$ case is near the limit of the range of validity of the SEOBNRv1-ROM model, which could in principle cause it to have lower FF or larger parameter biases due to an intrinsic mis-modeling of its $(2,2)$ mode by the SEOBNRv1-ROM mode. Although no effect was found in terms of fitting factors, it was observed that this system showed the largest parameter biases when only the $(2,2)$ mode was included, as will be highlighted afterwards. This was however one of the most interesting cases to study, as it is the only NR simulation present in the SXS catalogue with reasonably large positive spin and mass ratio.

Calculation of the fitting factor

For each full waveform $h_{i,j}$ one can compute the fitting factor $\mathcal{F}_{i,j} \equiv \mathcal{F}_\mathcal{B} h_{i,j}$ (see (3.34)) and the corresponding optimal SNR of the signal $\rho_{i,j}$ together with the intrinsic parameters $\Xi_{i,j}^\mathcal{B}$ of the best matching waveform $h_{i,j}^\mathcal{B}$. The speed at which ROM waveforms can be generated allowed for the usage of such a dense grid (~ 2400 combinations of (θ,φ,ψ) per each combination of (q,M,χ)), which would have been too computationally demanding using the original SEOBNRv1 model.

Maximization of the fitting factor over time shifts t_0 between target and template over relative time-shifts t_0 and extrinsic parameters Λ of the template was performed analytically using (3.43), discussed in Chapter 3. As also mentioned in Chapter 3, maximization of the overlap over the extrinsic parameters $\Xi = (q,M,\chi)$ of the bank templates

needed to be performed numerically. This was done using a Nelder-Mead simplex algorithm as implemented in [154]. Provided some initial region of the parameter space, the Nelder-Mead aims to find the maximums of a function $f(\vec{x})$ by successively evaluating it at several points $\vec{x}$. The algorithm considers to have found a maximum in a region $(\vec{x}_{i-n}, \vec{x}_{i+n})$ if the quantity $\delta f = f(\vec{x_j}) - f(\vec{x_k})$ is lower than a certain limit for all pairs $(j, k) \in (i - n, i + n)$. Also, one can set a maximum number of evaluations N_{max}. Running the Nelder-Mead algorithm several times from several starting points $\vec{x}_0$ proved to be an effective method for finding the global maximum of our fitting factor. As can be guessed, there is a certain probability that the Nelder-Mead will settle down in a local maximum, depending on the initial evaluation region used and N_{max}. In order to prevent this, every fitting factor was computed running a minimum of 4 Nelder-Mead algorithms from different initial points $\vec{x}_0 = (q_0, M_0, \chi_0)$ of the parameter space and choosing the maximum of the returned fitting factors as the "real fitting factor". In fact, for some cases, up to 18 Nelder-Meads were run. Also, since for a given (q_i, M_i, χ_i) system, the fitting factors $\mathcal{F}_{i,j}$ were successively computed for smoothly varying extrinsic parameters Λ_j, it was convenient to force one of the Nelder-Meads to always start around the best parameters found for the Λ_{j-1} case.

Computing event rate losses

The distance at which a signal described by $h_{i,j}$ can be detected is directly proportional to the SNR $\rho_{i,j}$ that it produces when it is filtered. If $h_{i,j}$ is filtered with a template $h_{i,j}^{\mathcal{B}}$ that matches it with match $\mathcal{F}_{i,j}$ this distance will decay to a fraction $\mathcal{F}_{i,j}$ of the optimal one. Bearing this in mind one can then compute the ratio of the optimal volume $V_{i,j}$ in which a signal could be observed if higher modes were included in the bank $V_{i,j}$ and the suboptimal volume $V_{i,j}^{\mathcal{B}}$ in which it can be observed when higher order modes are not included as

$$R_{i,j} = \frac{V_{i,j}^{\mathcal{B}}}{V_{i,j}} = \left(\frac{\rho_{i,j} \mathcal{F}_{i,j}}{\rho_{i,j}} \right)^3 = \mathcal{F}_{i,j}^3. \tag{6.3}$$

For each system with parameters Ξ_i we can then compute the averaged volume loss over all the possible extrinsic parameters Λ_j as

$$R_i = \sum_j \left(\frac{\rho_{i,j} \mathcal{F}_{i,j}}{\rho_{i,j}} \right)^3. \tag{6.4}$$

Systematic and statistical parameter bias

Similarly, the averaged parameter recovery over the accessible volume can be computed as

$$\Xi_i^{\mathcal{B}} = \sum_j \Xi_{i,j}^{\mathcal{B}} \left(\frac{\rho_{i,j} \mathcal{F}_{i,j}}{\rho_{i,j}} \right)^3 \tag{6.5}$$

and thus the averaged systematic bias will be given by

$$\Delta \Xi_i = \Xi_i - \Xi_i^{\mathcal{B}} \tag{6.6}$$

Note that even in the case that the signal does not include HOM, the parameters recovered by the SEOBNRv1-ROM model will not in general match the ones of the signal described by the hybrid waveform model. We denote the parameters recovered in this case as $\Xi_{i,0}^{\mathcal{B}}$ and thus consider the parameter bias generated by the presence of HOM to be

$$\Delta \Xi_i = \Xi_{i,0} - \Xi_i^{\mathcal{B}}. \tag{6.7}$$

This represents the systematic parameter bias averaged over Λ_j due to the presence of HOM in the signal. In order to asses the significance of these biases, we compared them to the corresponding statistical uncertainty that searches are affected by due to the presence of Gaussian noise in the data. In order to evaluate this, we employ the indistinguishability criterion for two waveforms with mismatch $\epsilon = 1 - \mathcal{O}$ given by [131] and used in [111]. Two waveforms are indistinguishable at a given SNR ρ if $\epsilon < 1/2\rho^2$. We will thus consider that parameter estimation[1] is not compromised due to the presence of HOM in the target if the best matching template $h^{\mathcal{B}}(\Xi_i^{\mathcal{B}})$ and the one best matching the injection with no HOM $h^{\mathcal{B}}(\Xi_{i,0})$ are insdistinguishable.

All the waveforms playing a role in this process are geometrically represented in Fig. 6.2. The target template $h(\Xi)$ is recovered by the bank template $h^{\mathcal{B}}(\Xi^{\mathcal{B}})$ when it includes HOM with a match of $\mathcal{F}$. Since the waveform model describing the $(2,2)$ modes of the target and template bank waveforms may differ, $h(\Xi)$ is in general recovered by $h^{\mathcal{B}}(\Xi_0^{\mathcal{B}})$ when it does not include HOM, and not by $h^{\mathcal{B}}(\Xi)$. The two recovering waveforms have a mismatch of ϵ. The systematic bias due to the presence of HOM is then $\Delta \Xi_i = \Xi_0^{\mathcal{B}} - \Xi^{\mathcal{B}}$. If $\epsilon = 1 - \mathcal{O}(h^{\mathcal{B}}(\Xi^{\mathcal{B}})|h^{\mathcal{B}}(\Xi_0^{\mathcal{B}}))$ is lower than $1/2\rho^2$ there is a reasonably high probability that $h^{\mathcal{B}}(\Xi_0^{\mathcal{B}}) + n$ is best filtered by $h^{\mathcal{B}}(\Xi^{\mathcal{B}})$ due to the presence of noise n in the data stream. We will say then that these two waveforms are indistinguishable and that statistical errors overcome systematic biases. Although this method does not provide a complete parameter estimation study as the usage of Bayesian MCMC methods [152] would do, it does provide a reasonable fast first estimation of the effect of higher modes for PE purposes.

---

[1]Or measurement following the notation in [131].
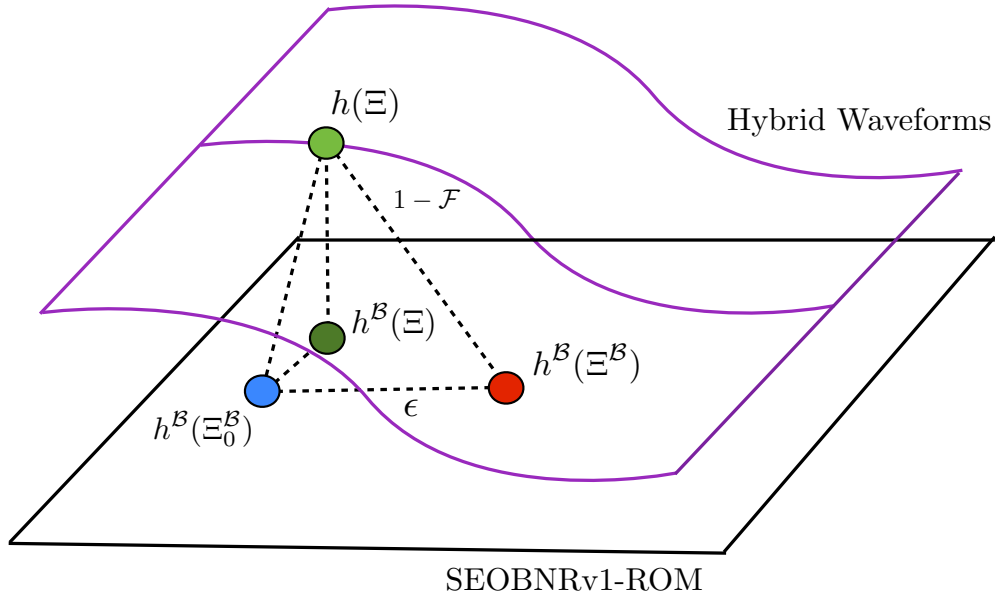
FIGURE 6.2: Representation of the waveform manifolds containing the target hybrid waveforms and the SEOBNRv1 model.

6.4 Effect on detection

Fitting factor and signal-to-noise ratio

The effect of HOM in detection depends on both the optimal SNR that the target signal $h_{i,j}$ produces and the fitting factor of our template bank to that particular signal. The left column of Fig. 6.3 shows the fitting factor of our quadrupole-only template bank towards hybrid waveforms corresponding to a non-spinning $q = 8$, $M = 218 M_{\odot}$ system as a function of the sky location of the detector (θ, φ) averaged over the polarization angle ψ. Each plot corresponds to a different detector. As shown by [2] and [150] the fitting factor is close to 1 when $\theta = 0$ (face-on system) and it decays as θ increases. As elucidated in Sec.6.2, this effect is due to the $(2, 2)$ spherical harmonic $Y_{2,2}^{-2}(\theta, \varphi)$ having its minimum at $\theta = \pi/2$ where most HOM are close to their maximums (see Fig.ex:fig:harmonicsprofile). As a consequence, the corresponding signal has larger contributions from HOM and can not be well filtered with quadrupole templates. However,

as also noted by [2] and [150] the θ angles for which the fitting factor is lower correspond to those for which the SNR is also the lower, as can be noticed in the right column of Fig. 6.3.

This mitigates the net effect of HOM in detection, which we compute by averaging the fitting factor over all possible (θ, ϕ, ψ).
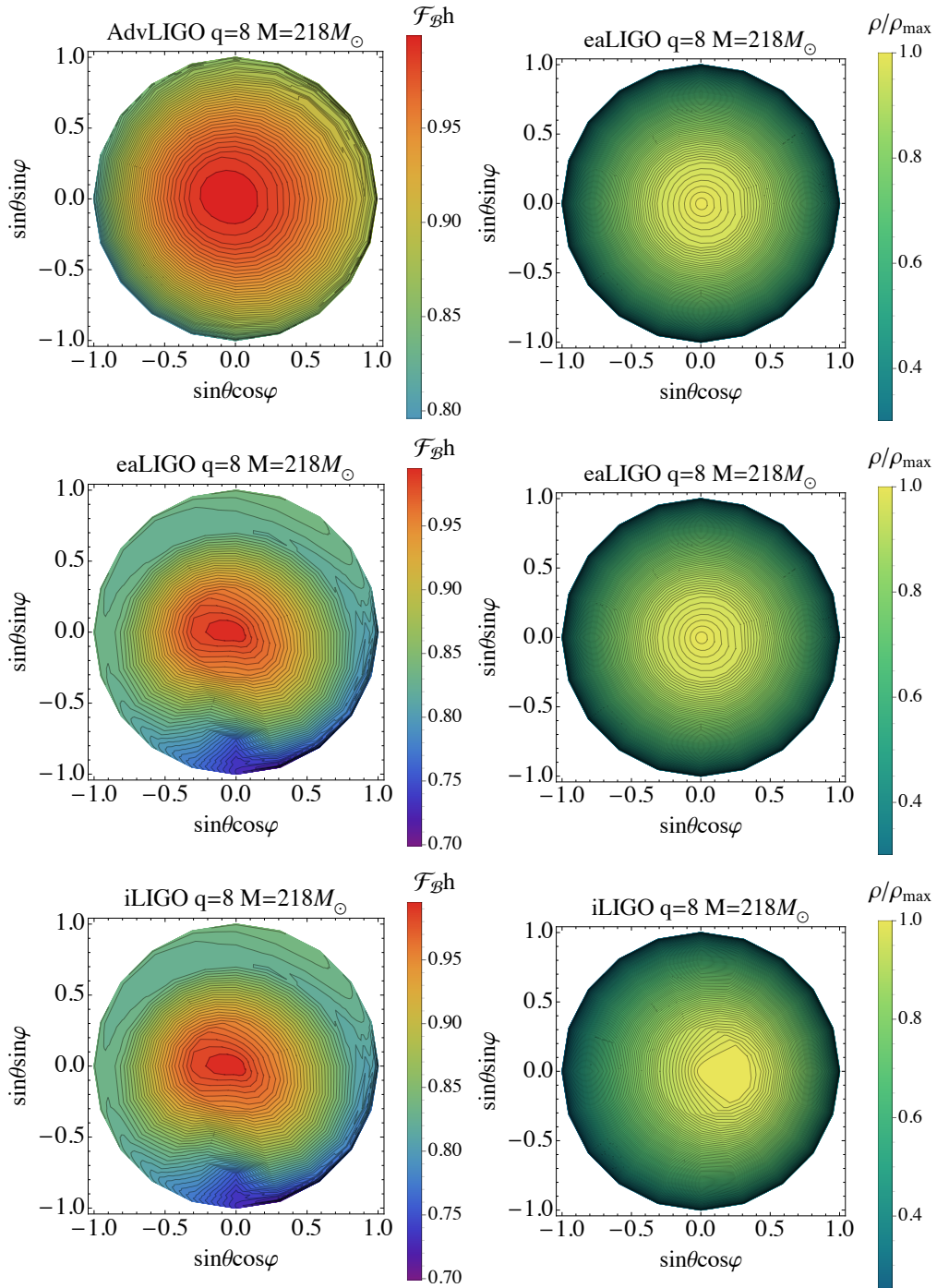
FIGURE 6.3: Fitting factor (Left) and SNR (Right) for a $(q, M) = (8, 218 M_\odot)$ system as as a function of (θ, φ) for the 3 studied detectors. The factor ρ_{max} corresponds to the maximum SNR obtained along the sphere.

The effect of the noise curve

We have started showing results for the most extreme target used (in terms of mass ratio and mass) because is where the main differences depending on the detector we use are the clearest. Let us summarize them:

- The main difference between AdvLIGO and eaLIGO is their different frequency cutoff, which is respectively located at 10Hz and 30Hz. This allows AdvLIGO to be sensitive to a much longer PN inspiral, in which HOM are negligible, and allows for a better filtering of the full signal with quadrupole templates. Mainly due to this, the fitting factor obtained with AdvLIGO is always equal or larger than the one for eaLIGO. Note that for instance, in Fig. 6.3, the fitting factor for eaLIGO decays down to ~ 0.70 while for AdvLIGO the minimum value is ~ 0.80. This behavior has been observed for every source.

- Both eaLIGO and iLIGO use the same lower frequency cutoff. However for eaLIGO we considered single-aligned spin bank waveforms while the ones for iLIGO were non-spinning. This gives an extra degree of freedom than can be exploited by quadrupolar templates for compensating the neglection of HOM non-spinning signals to the cost of a wrong estimation of the spin. In fact we large spin biases are obtained for the case eaLIGO, as we will discuss later. Consequently, fitting factors for iLIGO are in general lower to those obtained for eaLIGO.

- Since quadrupolar modes dominate the emitted radiation and the corresponding spherical harmonics have their maximums at face-on orientations, one would expect the maximum SNR to be always obtained when the source is face on. However, for very massive systems, HOM can be as dominating as the quadrupole mode in the detector band, This causes the maximum SNR to be obtained for a location other than $\theta = 0$, where the quadrupole mode and the HOM interact constructively. For this reason, the peak of the SNR for the case shown for iLIGO case in Fig. 6.3 is displaced from $\theta = 0$.

The effect of the total mass and the mass ratio

Let us now focus on the dependance of the fitting factor on the mass ratio q and total mass M of a given system. Fig.6.4 shows the value of the fitting factor for the $(q, M) = (8, 218 M_\odot)$ system and for a $(q, M) = (4, 50 M_\odot)$ system. Notice the scale of the fitting factors in each plot. It is clear that for every detector, fitting factors are always lower the larger M and q are. Again, this is due to HOM being weaker for low q, as we shown in Fig.2.5 and due to the $(2, 2)$ mode being dominating in the band of the detector

for low M. Notice also how in the left panel of each column (which have lower M and q) the fitting factors are almost axisymmetric, while for the lower case they are highly non axisymmetric (except for the case of AdvLIGO). The reason behind this is the different interaction between modes as a function of φ, which is only dominant when HOM dominate the full signal. Consequently, this behavior is not observed for AdvLIGO.
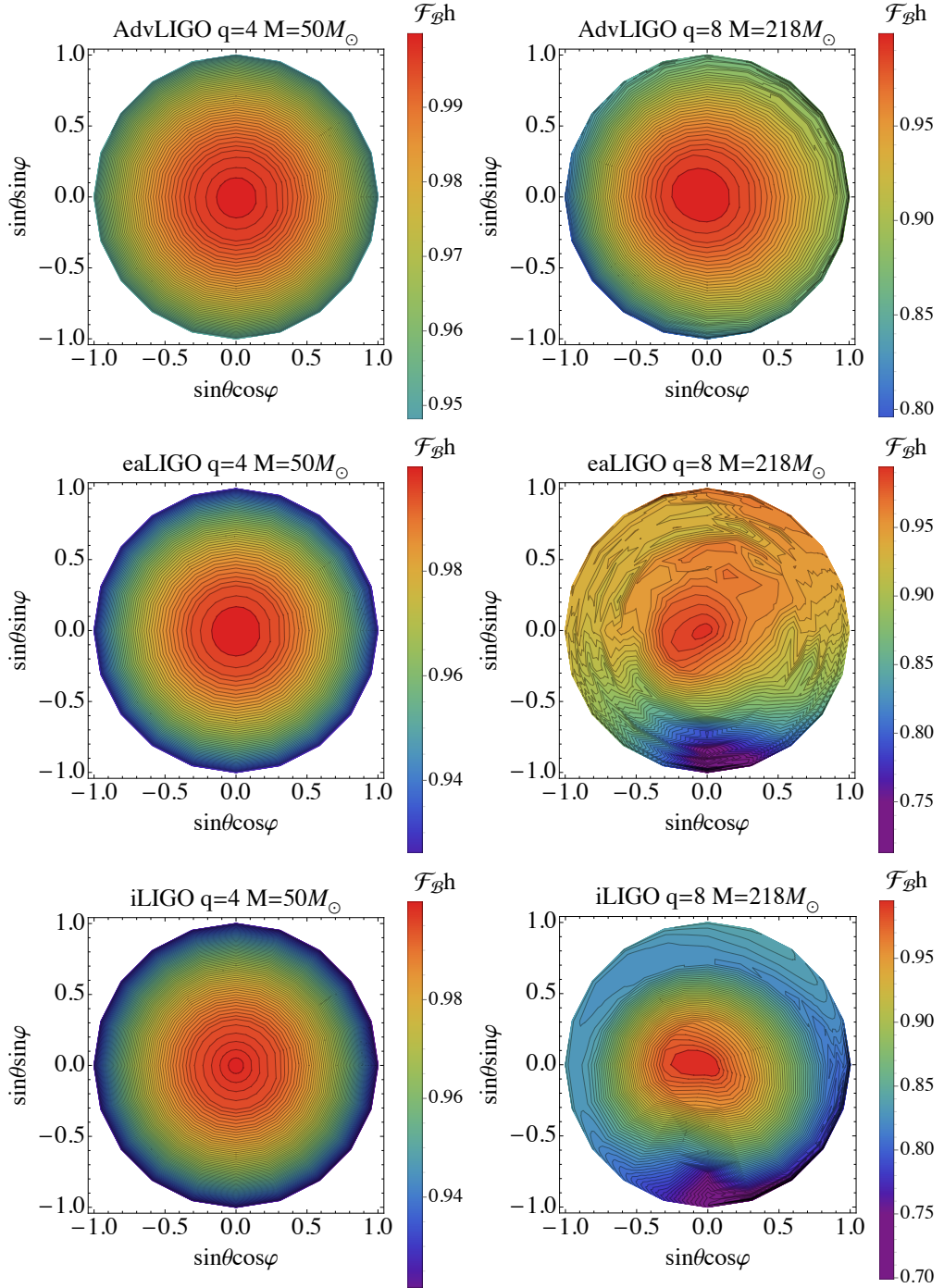

FIGURE 6.4: Fitting factor for $(q, M) = (4, 50 M_\odot)$ and $(q, M) = (8, 218 M_\odot)$ systems as a function of (θ, φ) for the 3 studied detectors.

Event losses due to neglection of higher order modes

Let us now compute the event loss due to negelction of HOM. For this we will compute the averaged fitting factors over all (θ, φ) using (6.3) and (6.4). The corresponding results are shown in Fig.6.5 for the several systems we have studied. Again, as q and M increase, the larger contribution from HOM to the total signal makes $\mathcal{F}^{eff}$ decay consequently. For the case of AdvLIGO losses never reach 20% for any of the studied cases while 10% losses happen for $q \geq 6$, $M \geq 100 M_\odot$ systems. However, losses notably increase for the case of iLIGO and more importantly, the upcoming eaLIGO. Note how the higher frequency cutoff of eaLIGO (and iLIGO) generates losses that reach values of 26% (36%) for the largest (q, M) studied. In the case of eaLIGO, losses of 10% happen already for $q \geq 4$. Also, losses of 20% happen for most of the studied (non-spinning) cases for iLIGO.

 The fact that the lower frequency cutoff is the main reason behind the different behavior of eaLIGO and AdvLIGO is clear noticing that both curves have similar values up to masses of $M \sim 110 M_\odot$. Up to this point, the $(2,2)$ mode of the target waveform dominates the full signal content in the band of the detector and can be well filtered by a bank that only contains quadrupolar modes. However, at such masses, the $(2,2)$ mode starts to be below the sensitive band of eaLIGO ($f_0 = 30$Hz) while it remains in band for AdvLIGO. The different behavior at initial masses is justified by the fact of the AdvLIGO curve being flatter, which makes the PN piece of the waveform (where the contribution of HOM is lower) to have a larger weight in the observed signal in the case of AdvLIGO making the incoming signal be better filtered by quadrupolar waveforms. The losses obtained for AdvLIGO are (as expected) a bit below those obtained by [2] due to the inclusion of the effective spin parameter χ in our template waveforms, which provides an extra degree of freedom that can be exploited by quadrupolar waveforms to imitate signals containing HOM. This is also the main reason for the different results obtained for iLIGO and eaLIGO, which have the same frequency cutoff.

Regarding the effect of spin, none of the $q = 1$ spinning cases reached losses even close to 2% and is for this reason that they are not included in Fig.6.5. However, for the $(q, \chi) = (3, \pm 0.5)$ case, losses are very similar those obtained for corresponding non-spinning case (see lower panel of 6.5). Note that for the two studied cases, losses are larger for the aligned-spin case than for the anti-aligned one for low mass. Looking at Fig.2.6 it is hard to check whether this behavior is to be expected. Note that as the spin gets more positive, the contribution of HOM to the signal grows in all cases except for the $(3,3)$ mode, which is however the most dominant HOM, as shown in Fig.2.4. For high mass, PN results are not expected to be accurate and Fig.6.5 shows that contributions from HOM become equally important in terms of fitting factors. Of course,
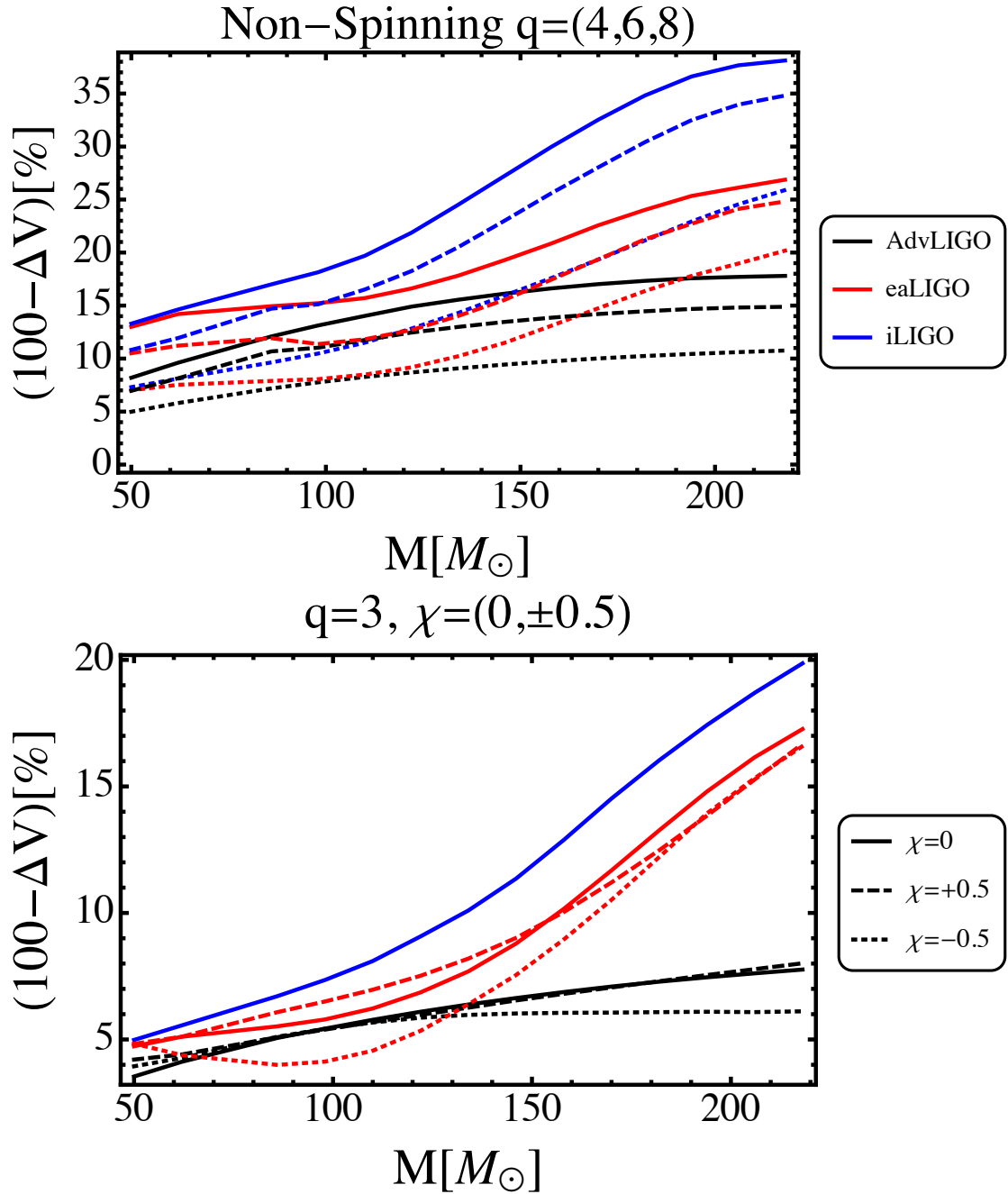
FIGURE 6.5: Top: Fractional volume loss in % for non-spinning $q = (4, 6, 8)$ systems in (dotted, dashed, solid). Bottom: same for $(q, \chi) = (3; 0, \pm 0.5)$ with the style code indicated in the corresponding caption. Note that since we used a non-spinning template bank for iLIGO, we did not consider spinning targets.

the study of only two spinning systems does not allow to obtain general conclusions about the importance of HM for general spinning systems. We have however considered the non-precessing cases present in the SXS catalogue that were HOM are plausibly most dominating. These particular result seems to indicate that for high masses the effect of HOM is rather dominated by the mass ratio q (and the total mass), so that results obtained for non-spinning systems are a good clue of what will be obtained for equal spin

ones. At low masses, this behavior is more complex but it seems that the losses obtained for the non-spinning system are a good clue regarding the maximum ones obtained for the corresponding equal spins ones. It would be very interesting to check that larger losses are always obtained for the aligned-spin case, as suggested by 6.5.

6.5   Parameter Bias

We now move to the systematic parameter biases produced by the non inclusion of HOM in the bank waveforms. Since at low masses the signal is dominated by the quadrupolar mods, which explicitly depend on the chirp mass (defined by $\mathcal{M}_c = M\eta^{3/5}$, where $\eta = q/(q+1)^2$, we will express results not for (q, M) but for the chirp mass and the total mass M. As mentioned before, these systematic biases will be a combination of those of the SEOBNRv1-ROM model towards our hybrid $(2, 2)$ modes ($\Xi_{i,0}$ in (6.7)) and those produced by the presence of higher modes in our hybrid target signals. It is important to note that the former, except for the $(q, \chi) = (3, +0.5)$ case (which is in the limits of the validity range of the SEOBNRv1-ROM model) were never larger than $(|\Delta M|, |\Delta\mathcal{M}_c|, |\Delta\chi|) = (2\%, 2\%, 0.04)$. For the $(q, \chi) = (3, +0.5)$ case, these reached maximum values of $(4\%, 6\%, 0.05)$.

Fig. 6.6 shows the fractional bias in % in the recovery of the total mass M for several systems in the context of the eaLIGO and AdvLIGO detectors. As expected, when the $(2, 2)$ mode dominates the signal at $\theta = 0$, the bias is very close to 0. As we move to equatorial locations, the bias starts to grow to both negative and positive values. This qualitative behavior coincides with that observed in [2]. Note that systematic parameter biases can get as large as -30% for the $(q, M) = (8, 218M_\odot)$ case for AdvLIGO, while for eaLIGO such a bias is already obtained for $(q, M) = (8, 98M_\odot)$ due to its higher frequency cutoff. This difference in the magnitude of systematic parameter biases between both detectors is also observed for the case of the spin and chirp mass parameters. In particular, Fig.6.7 shows the corresponding spin χ biases for the same systems and detectors as before. Note how the estimation of the spin of a non-spinning system can be as low as $\chi = -0.8$ for the two cases highlighted before (bottom row of Fig.6.7). Furthermore, for the $M \geq 150M_\odot$ cases for eaLIGO, values of $\chi = -0.99$ are commonly recovered at edge-on locations. For low q and low M cases HOMs are intrinsically weaker and the $(2, 2)$ mode is well in band, systematic biases are tiny and comparable for both detectors as can be noticed in top row of Figs. 6.7 and 6.6.
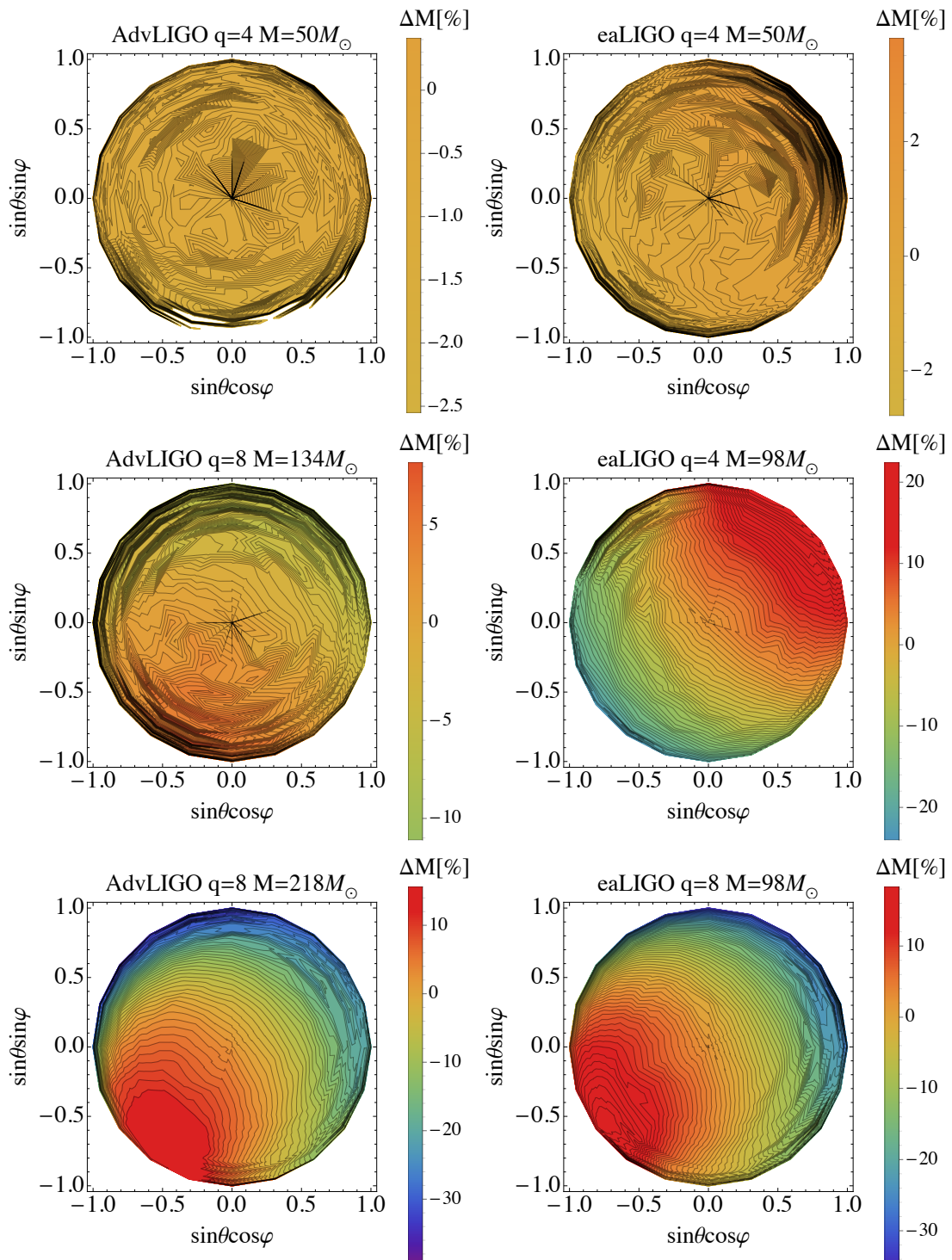
FIGURE 6.6: Fractional mass bias ΔM in % for several systems as a function of (θ, φ) for the case of AdvLIGO (Left) and eaLIGO (Right).

Averaged systematic biases and statistical errors

Fig.6.8 shows the averaged parameter bias over the observable volume for the studied systems. As a general trend, neglection of HOM causes biases towards lower $(\chi, M, \mathcal{M}_c)$
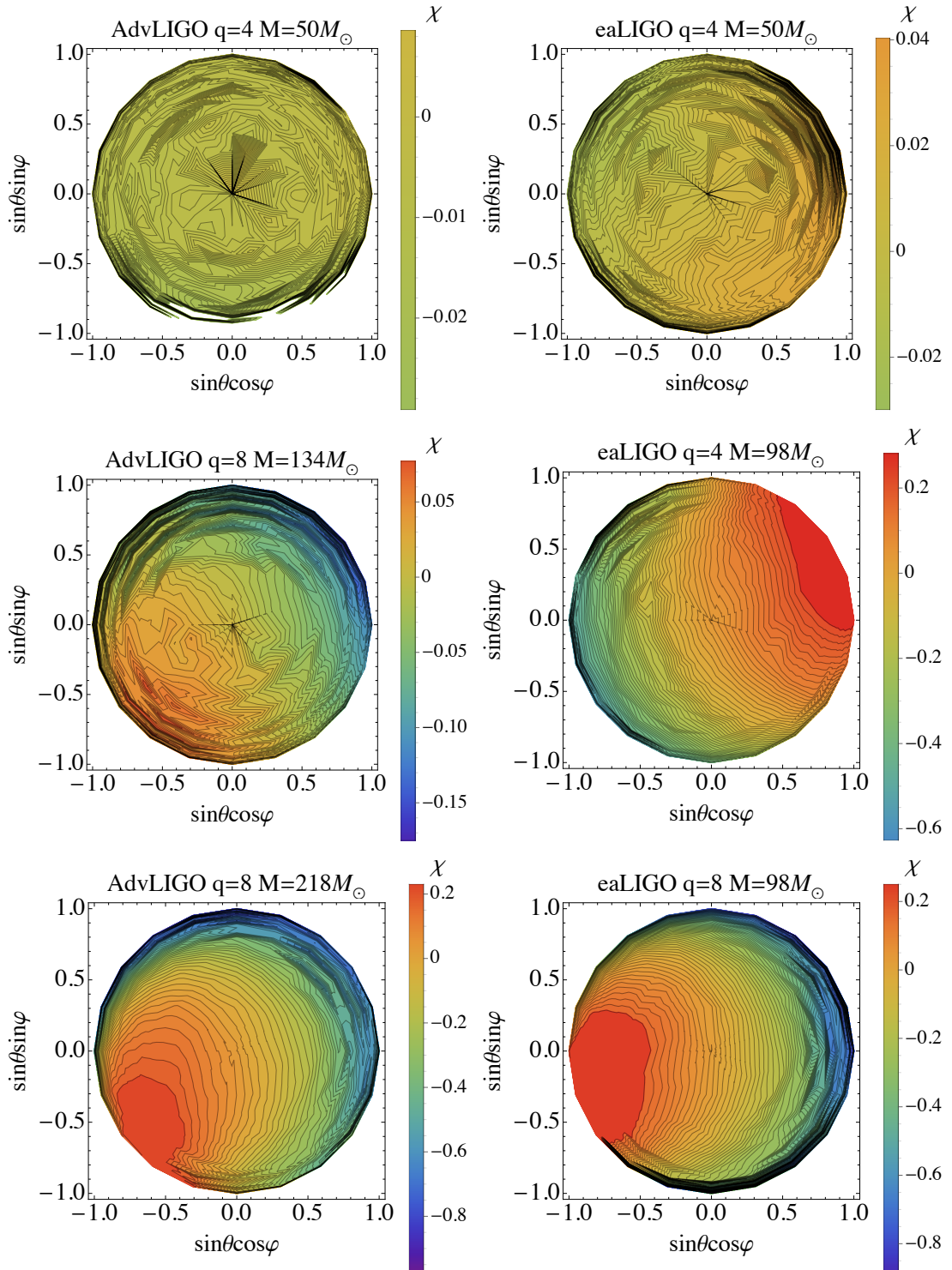
FIGURE 6.7: Recovered spin χ for several systems as a function of (θ, φ) for the case of AdvLIGO (Left) and eaLIGO (Right).

(thus, to higher q) which increase as M and q do. As expected, biases are much larger for iLIGO and eaLIGO than for AdvLIGO. In particular, note that the lower seismic wall of AdvLIGO allows for an excellent recovery of $\mathcal{M}_c$ for most of the mass range. Regarding spinning cases, larger systematic biases were obtained for anti-aligned spin cases than
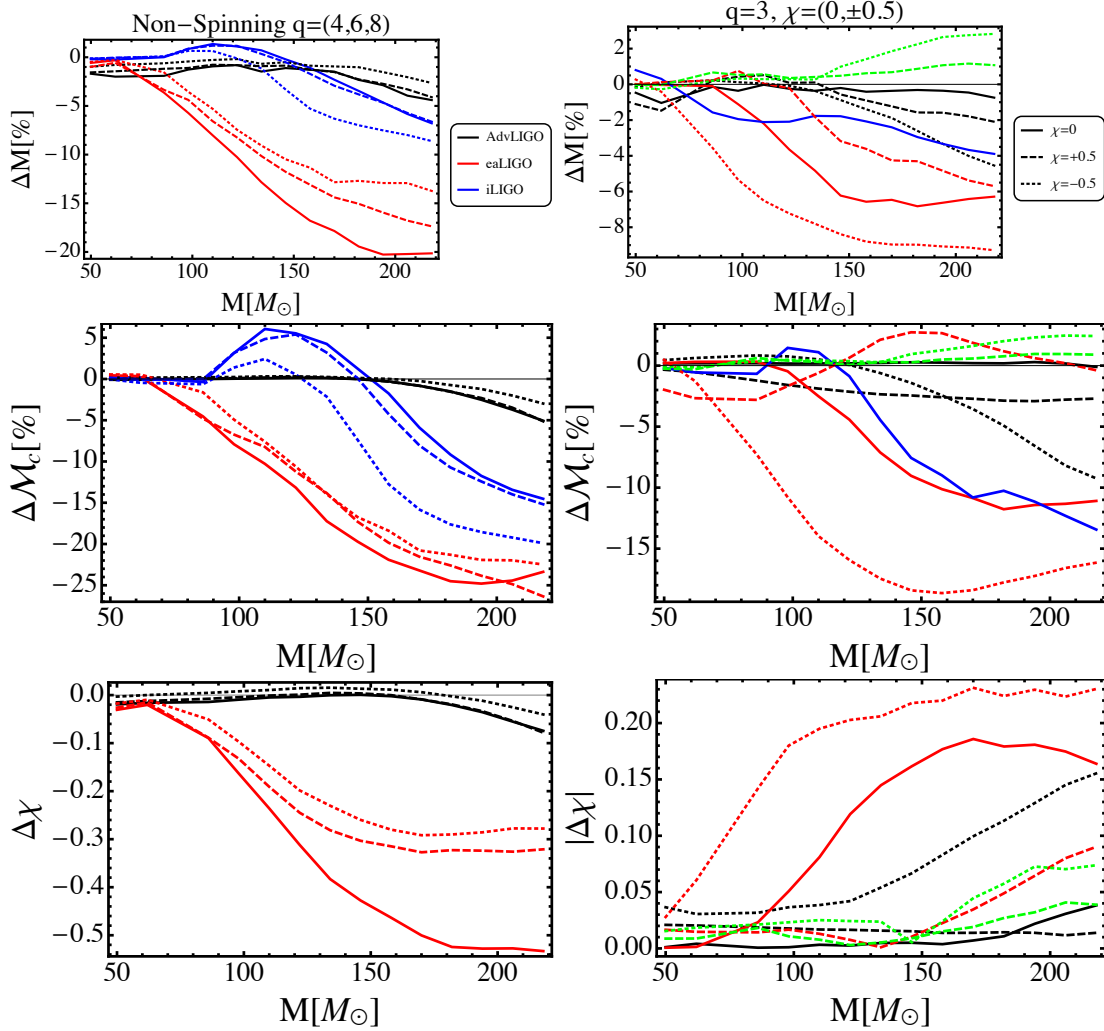
FIGURE 6.8: Top: M, $\mathcal{M}_c$, and χ systematic bias for the $q = (3, 4, 6, 8)$ (from solid to dot-dashed) nS cases. We use the same color-detector code as in Fig.2. Bottom: Same for the $(q; \chi) = (3; 0, \pm 0.5)$. We use dashed (dotted) for - (+) spin and add $(q, \chi) = (1, -0.2)$ case in solid green for eaLIGO.

for aligned spin ones. For $q = 1$, only the eaLIGO cases are shown, which were the only ones having systematic biases comparable to those of the other systems. Last, we want to note that biases typically reach values of $\Delta(M, \mathcal{M}_c, \chi) = (-40\%, -20\%, -0.9)$ for $q \geq 4$ high mass edge-on cases for eaLIGO and $(-30\%, -20\%, -0.5)$ for AdvLIGO. Since these orientations the SNR is the lowest, they are the ones contributing the less to the averaged biases. Recall this behavior was also observed for the case of event losses.

We now move to the comparison the sky-averaged systematic biases to the statistical uncertainty we expect for each detector via computing the SNR ρ_0 at which the former dominate the latter. However, unlike the volume loss R_i, note that $\rho_0 = \sqrt{1/2\epsilon}$ is extremely sensitive to tiny variations in the parameters recovered by the Nelder-Mead algorithm, which has always a certain risk of settling in a local maximum. In particular,

for an error $\Delta\epsilon$ in the estimation of ϵ, using (3.4.2) we obtain $\Delta\rho_0 \sim \epsilon^{-3/2}\Delta\epsilon$. Consequently, this will especially affect regions of the parameter space where systematic biases are lower and regions where the parameter space is denser i.e., regions for which tiny variations $\Delta\Xi_i$ in the parameters Ξ_i cause large mismatches $\epsilon = 1 - \mathcal{O}(h(\Xi_i)|h(\Xi_i + \Delta\Xi_i))$.[2] Due to this, although some of the Nelder-Meads were run up to 18 times, Fig. 6.9 shows several peaks that do only allow us to give a rough estimate of ρ_0. Results suggest that at an SNR of $\rho \sim 8$, HOM would only be required for PE at $M \geq 180M_\odot$ and for the largest q for the case of AdvLIGO, which is consistent with [2]. However, for the case of eaLIGO, HOM affect PE at $M \leq 80M_\odot$ for roughly the same cases due to the larger systematic biases. Regarding spin, we note that systematic biases are more (less) likely to affect PE in the anti-aligned (aligned) spin case, for which again, systematic biases are larger (lower).

The results suggest that, in average, systematic biases due neglection of HOM dominate those due to statistical uncertainty at SNR $\rho \sim 8$ for total masses larger than $(80, 170)M_\odot$ for eaLIGO and AdvLIGO respectively. The latter is consistent with the results found by [2] in the case of a non-spinning search. Again, the ultimate reason behind the different results for the different two detectors is the fact that the lower frequency cutoff of AdvLIGO makes it sensitive to a much longer PN tail of the incoming signal totally dominated by the quadrupolar modes. This generates lower systematic biases which do not dominate those due to statistical uncertainty.
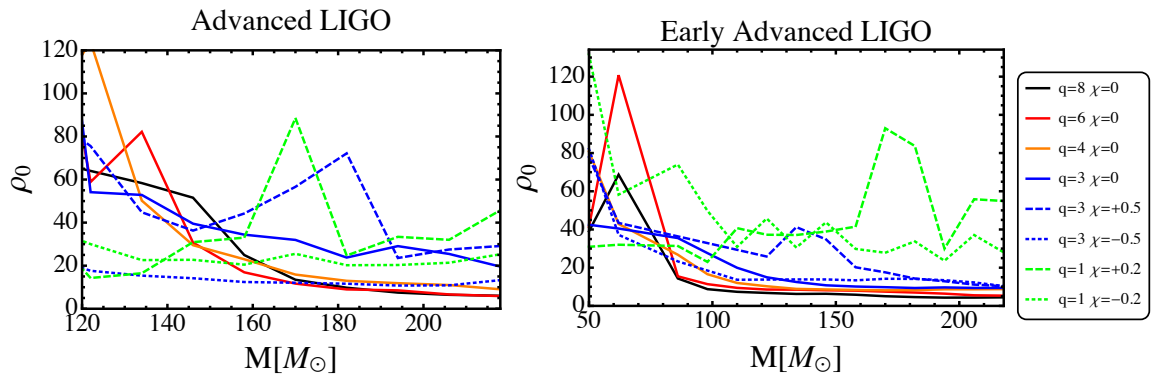
FIGURE 6.9: Comparison between (θ, φ, ψ)-averaged systematic errors and statistical uncertainties. We show the minimum SNR ρ_0 at which systematic biases due to the neglection of HOM dominate those due to statistical uncertainties for the studied sources. Note that for particular cases, like edge-on-high mass ones, the value of ρ_0 would be much lower and systematic biases would be more dominant.

---

[2]Low mass cases and AdvLIGO due to the tiny parameter bias expected and to the large density of the parameter space. Also, for the latter reason, large mass ratio and positive spin cases should also be affected.

6.6 Higher order modes and binary black hole kicks

At the end of a coalescence, after both BH merge, it is known that the resulting perturbed Kerr BH acquires a characteristic velocity $\vec{v_K}$, known also as recoil velocity or BH kick. Several studies [155–157] have computed this characteristic velocity to be of the order of $\sim 10 - 100km/s$ for non-spinning binaries and $\sim 1000km/s$ for highly spinning ones. In particular, [155] shows that a maximum kick happens for $q \sim 3$ in the case of non-spinning systems. Also, [158] studied which modes dominate the resulting kick for equal mass binaries with opposite spins. In this section we will extend this last study to the case of the binaries used in the previous part of this chapter. In the non-precessing case, the reason behind the BH kick is the non-axisymmetry of the GW radiation, due to the different interaction of the GW modes at different angles φ. The corresponding momentum $\vec{P}$ can be computed as a function of the ψ_4 scalar as

$$\frac{dP_i}{dt} = \lim_{r \to \infty} \left[\frac{r^2}{16\pi} \int_\Omega l_i \left(\int_{-\infty}^t \psi_4 d\bar{t} \right)^2 d\Omega \right], \tag{6.8}$$

where $\vec{l} = (\sin\theta\cos\varphi, \sin\theta\sin\varphi, \cos\theta)$. Note, as we will show later, that this velocity would be exactly zero if one considers only the quadrupolar $(\ell, |m|) = (2, 2)$ modes of the GW radiation. Also, the symmetry with respect of the equatorial plane imposed in the non-precessing case by (4.4) makes P_z to be zero. Hence, the kick of the resultant BH will keep it within the original orbital plane. In this section we will investigate which modes of the GW radiation dominate the value of the kick $\vec{v_K}$.

Mode hierarchy in black hole kicks

Equation (6.8) can be expressed as a sum over products of modes as

$$v_K^i = \lim_{r \to \infty} \left[\frac{r^2}{16\pi M} \sum_{\ell', m'} \sum_{\ell, m} \int_\Omega l_i Y_{\ell, m}(\theta, \varphi) Y_{\ell', m'}^*(\theta, \varphi) d\Omega \times \left(\int_{-\infty}^t \left(\frac{dh_{\ell, m}}{d\bar{t}} \right) \left(\frac{dh_{\ell, m}}{d\bar{t}} \right)^* d\bar{t} \right) \right], \tag{6.9}$$

which we might re-express as

$$v_K^i = \lim_{r \to \infty} \left[\frac{r^2}{16\pi M} \sum_{\ell', m'} \sum_{\ell, m} \Psi_{\ell, m, \ell', m'}^i \right]. \tag{6.10}$$

The previous quantity can be regarded as the final velocity that the BH acquires when only the (ℓ, m) and (ℓ', m') modes are considered. Due to the symmetry of the system, all $m = m'$ terms give a zero contribution to the final kick. This should not be surprising since given that the radiation described by these doublets of modes is axisymmetric, thus

no net final momentum should be obtained. Because of the symmetry relation between positive and negative modes given by (4.5), the relation between positive and negative m harmonics and their orthogonality (2.15), one gets

$$
\begin{aligned}
\Psi^i_{\ell,m,\ell',m'} &= \Psi^i_{\ell',m',\ell,m} \\
\Psi^i_{\ell,m,\ell',m'} &= \Psi^i_{\ell',-m',\ell,-m} \\
\Psi^i_{\ell,m,\ell',m'} &= 0, \qquad\qquad m \neq m' \pm 1
\end{aligned}
\tag{6.11}
$$

Hence, we can further simplify the expression of the final black hole kick to

$$
v^i_K = \lim_{r\to\infty}\left[\frac{r^2}{16\pi M}\sum_{\ell,m>0,\ell'}\hat{\Psi}^i_{\ell,m,\ell',m+1}\right],
\tag{6.12}
$$

where, for instance

$$
\hat{\Psi}^i_{2,2,3,3} = \Psi^i_{2,2,3,3} + \Psi^i_{3,3,2,2} + \Psi^i_{2,-2,3,-3} + \Psi^i_{3,-3,2,-2}.
\tag{6.13}
$$

Computing the individual $\Psi^i_{\ell,m,\ell',m'}$ terms allows for determining which couples of modes dominate the value of the BH kick. Table 6.3 shows the ratio

$$
R_{\ell,m,\ell',m'} = \frac{\sqrt{(\hat{\Psi}^x_{\ell,m,\ell',m'})^2 + (\hat{\Psi}^y_{\ell,m,\ell',m'})^2}}{\sqrt{(\hat{\Psi}^x_{2,2,3,3})^2 + (\hat{\Psi}^y_{2,2,3,3})^2}}.
\tag{6.14}
$$

for two of the systems and the corresponding modes included in the fitting factor study, where the lower limit of integration has been chosen to be $t_i = 500M$ before the end of the waveforms. From the ratios shown in the table, it is clear that the BH kick is dominated by the interaction of the $(2,2)$ and $(3,3)$ modest, the $(2,2)$ and the $(2,1)$ and $(3,3)$ and $(4,4)$. This hierarchy should not be surprising since, as we discussed in Chapter 2, these are the most dominant modes in the net GW emission (see.2.4). In [158] it was obtained that the kick is largely dominated (by ~ 2 orders of magnitude) by the interaction between the $(2,2)$ and $(2,1)$ modes. However, since they consider equal mass binaries, the symmetries of the problem highly suppress the rest of the modes, in particular the $(3,3)$. For completeness, 6.3 also shows the value of the final kick $|\vec{v}_K|$ obtained for the final BH and that obtained when all the modes are included, i.e., when one includes the full ψ_4 in (6.8), quoted from [115]. Note we have only included in our calculation the most dominant HOM. Since the velocity of the center of mass of the binary oscillates around zero during inspiral, there choice for t_i will introduce a certain error. Ref.[155] estimated this error to be of a 3% of the measured kick. Note also that the artifacts observed in Chapter 5 for large m modes due to extrapolation, which are not likely to affect the fitting factor studies due to the presence of a detector noise curve

that alleviates them, may be another source of error for this calculation. These sources of error are however not likely to affect the statement that the kick dominated by the interference of $(2, 2)$ and $(2, 1)$ modes followed by that of the $(2, 2)$ and $(3, 3)$ modes and the one corresponding to the $(3, 3)$ and $(4, 4)$ modes. This qualitative behavior was observed for all the systems studied in this chapter although the exact values depended on their particular parameters. In order to get a clear image of the contribution of each

(ℓ, m)	(ℓ', m')	$(q, \chi) = (8, 0)$	$(3, +0.5)$
$(2, 1)$	$(2, 2)$	1	1
$(2, 2)$	$(3, 3)$	0.4611	0.5536
$(3, 3)$	$(4, 4)$	0.1961	0.2163
$(3, 2)$	$(3, 3)$	0.0904	0.0473
$(2, 1)$	$(3, 2)$	0.0169	0.0404
$(2, 2)$	$(4, 3)$	0.0066	0.0126
$(3, 2)$	$(4, 3)$	0.0126	0.0126
$(4, 4)$	$(4, 3)$	0.0158	0.0065
Total Kick		90.69	84.06
Total Kick (SXS) [km/s]		88.10	80.01

TABLE 6.3: Hierarchy of the different modes regarding their contribution to the final black hole kick. The upper rows show the value of $R_{\ell, m, \ell', m'}$ two of the studied systems. In the lower ones, "Total Kick" denotes the value obtained for the kick using our finite set of modes and "Total Kick (SXS)" is the value obtained in the original NR simulations, which consider all possible modes.

couple of modes, Fig.6.10 shows the components of the partial kicks generated by each mode-doublet and the total kick for a non-spinning $q = 8$ binary black hole. In the left panel the dominancy of the $(2, 1, 2, 2)$, $(2, 2, 3, 3)$ and $(3, 3, 4, 4)$ modes is clear while the right one shows in detail the contribution of the subdominant ones.
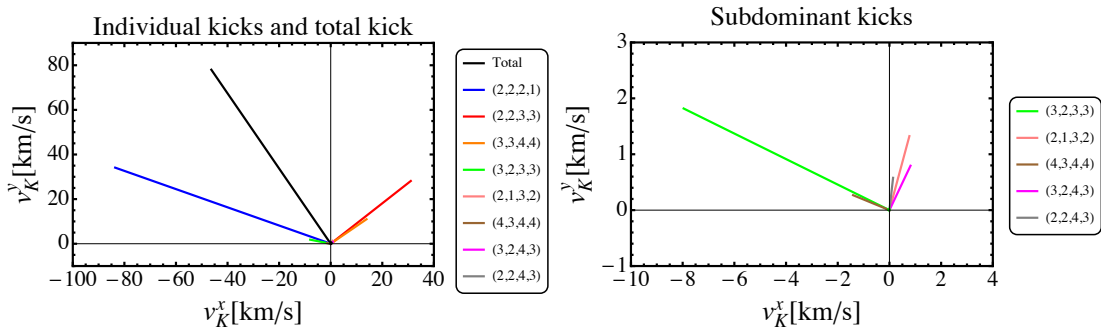
FIGURE 6.10: Left: Components in km/s of the partial kicks due to each couple of modes (in color) and total kick (in black) for a non-spinning $q = 8$ binary black hole. Right: Detail of the contribution of the subdominant doublets.

Finally, it is worth to note the close relation between the individual kicks of the modes which dominate the radiation as seen by the detector and the dipolar structure of the parameter bias plots in Figs. 6.7, 6.6 and 6.11. For masses such that the $(3, 3)$ and $(4, 4)$ contribute enough to the signal, this structure appears to get aligned with the

kicks due to the interaction of the $(2,2)$ and $(3,3)$ modes and that of the $(3,3)$ and $(4,4)$. In particular, biases to large masses and positive spins happen for the direction opposite to these two kicks. Note that since the $(2,1)$ mode is largely dominated by the $(2,2)$ when it is in band, it has a negligible effect both in terms of event losses and parameter bias and no structure appears at low masses. The evolution of the mentioned pattern with the total mass is visible looking at the $q=8$ plots in the figures mentioned and clear in the plot series of Fig.6.11. Note that since the effect of HOM in AdvLIGO gets shifted to larger masses due to its lower frequency cutoff, the dipolar structure appears at larger masses than in the case of eaLIGO, for which this structure starts to appear at $M \sim 100 M_\odot$. This is precisely the region where the event loss curves of eaLIGO in Fig.6.5 start to separate from those corresponding to AdvLIGO, thus where the contribution of HOM (mainly the $(3,3)$ mode) starts to be important.
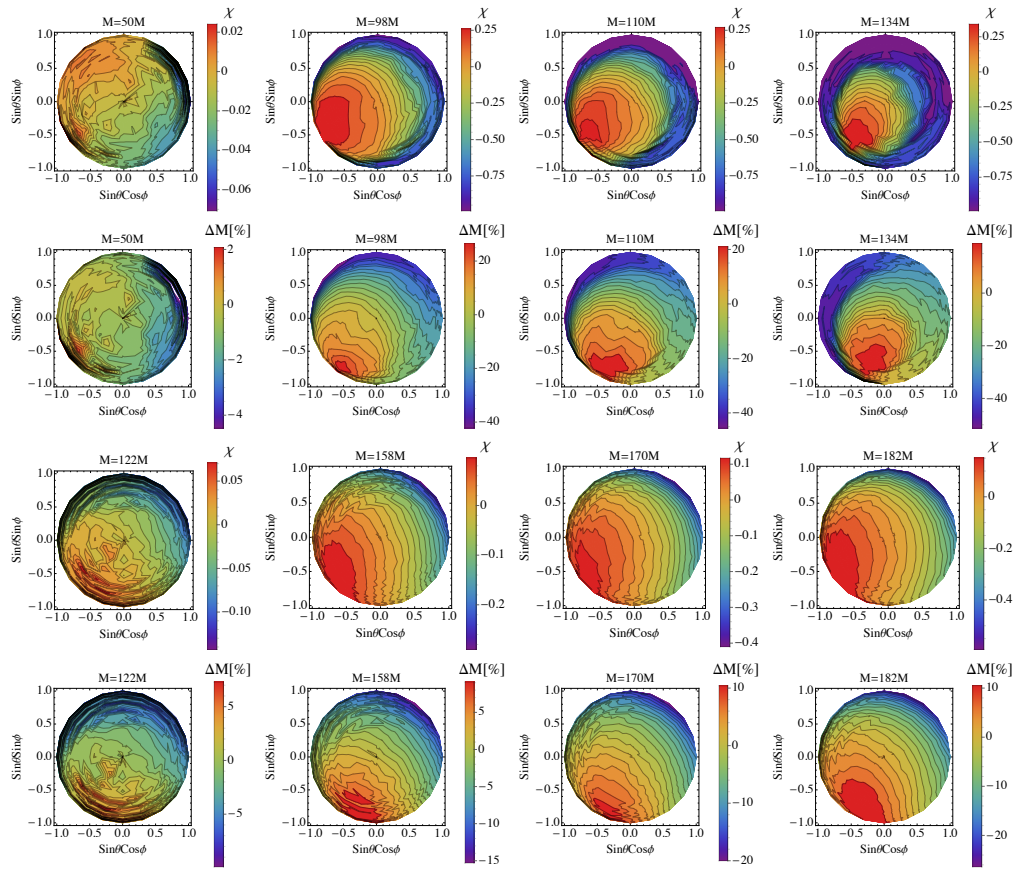
FIGURE 6.11: Evolution of the dipolar pattern observed in the parameter bias for χ and M as a function of the total mass M of a non-spinning $q=8$ binary. The two upper rows show results for eaLIGO while the two lower ones show results for AdvLIGO. Note how the dipolar pattern forms at larger masses for the case of the AdvLIGO.

6.7   Discussion

In this chapter we have studied the impact of the neglection of HOM in current searches for CBC both in terms of event losses and parameter bias. The study performed for the case of AdvLIGO (for the case of a single aligned-spin search) predicts losses $> 10\%$ for the $(q \geq 6, M \geq 100 M_\odot)$ region of the explored parameter space. This is in good agreement with the results shown in [2] for the case of a non-spinning search, which is in turn consistent with the results presented in [125]. However, we have shown that these losses not only happen for a larger portion of the parameter space $q \geq 4$ for the case of eaLIGO and iLIGO but also reach values of 26% and 36% respectively for the largest mass and mass ratio. In [125], they also estimated the increment of the FAR of a search including HOM as well as the effect of signal based vetoes. They estimated that the threshold SNR for such a search would need to be raised from 8 to 8.3 (so, by a 10%). Note that this implies that if we want to compute the event loss due to the neglection of HOM in terms of search sensitivity, we would have to reduce the values in 6.5 by roughly a 10%. Ref. [125] concluded that a search including HOM would only be more sensitive than a one not including HOM for the region of the parameter space $(q \geq 4, M > 100 M_\odot)$, for which fitting factors of quadrupole templates towards full target signals are particularly low. However, since we have found lower fitting factors for the case of eaLIGO than for AdvLIGO for the same target parameters, the region of the parameter space where a search including HOM would be advantageous should certainly be larger for eaLIGO, which may motivate some effort towards the development of such a search. Notice also that we have not considered the effect of signal based vetoes used in real GW searches [38] such as the χ^2 [126], which would further punish signals with low FF and should increase the event losses when HOM are not considered.

Regarding parameter bias due to the neglection of HOM, for the eaLIGO case, averaged systematic biases affecting parameter estimation are normally above $(\Delta M, \Delta \chi, \Delta \mathcal{M}_c) = (-5\%, -10\%, -0.1)$ for the most part of the explored parameter space and reach values of $(-15\%, -25\%, -0.5)$ for the largest (q, M) cases. As expected, systematic biases are lower for the case of AdvLIGO due to its lower frequency cutoff. We compared these systematic biases to the corresponding statistical uncertainties due to the presence of gaussian noise in the data. Results for eaLIGO suggest that measurements with SNR$\simeq 8$ would be affected by the presence of HOM at $M \geq 80 M_\odot$ for the largest q considered. In the case of AdvLIGO, we estimate that PE is likely to be affected at $\rho \sim 8$ for $M \geq 180 M_\odot$ for the largest q studied, which is consistent with [2]. Finally, it is worth pointing that an interesting extension of this work would be to consider the case of precessing targets, for which the contribution of HOM is much stronger. Finally, taking advantage of the hybrid waveforms used for this chapter, we have shown that for unequal

mass ratio binaries the kick of the final black hole is largely dominated by the non-axisymmetric interaction between the $(2,2)$, $(2,1)$ modes, and that of the $(2,2)$ and $(3,3)$ modes.

Chapter 7

Conclusions

In this thesis we have studied the effect of the neglection of higher order modes in gravitational wave searches in terms of reduction of observed events due to mis-modeling and in terms of biases in the parameters estimated for the corresponding source. To this end, we have first dealt with the construction of hybrid PN/NR waveforms containing HM in Chapters 4 and 5. In Chapter 6 we have used these hybrid waveforms as models of the true gravitational wave signal and filtered them with waveforms that do only consider the quadrupolar modes [118] in order to obtain a first estimation of the performance of a real search. Also, results obtained regarding the process of constructing hybrid waveforms allowed us to perform studies of the accuracy and error sources of both PN and NR calculations in Chapter 5. In particular, we payed special attention to the effect of truncation in the PN results and to the effect of finite extraction radius and extrapolation order in the NR results. The global results and conclusions of this thesis are the following.

- In Chapter 4, we have described a method for the construction of hybrid waveforms for non-precessing CBC including higher order modes. We have found that in general, three sources of ambiguity in the description of both pieces of the hybrid waveform must be fixed: a relative time-shift t_0 and orbital phase-shift φ_0 and a "polarization" shift ψ_0. The global phase shift applied to the (ℓ, m) mode is then $\Delta\phi_{\ell,m} = \psi_0 + m\varphi_0$. The t_0 and φ_0 factors coincide with those described by [135] and [132]. The need to correct for ψ_0 was already noted by [134], who however restricted $\psi_0 \in \{0, \pi/2, \pi, 3\pi/2\}$. We note that in general $\psi_0 \in [0, 2\pi)$. However, if as usual, the two independent sets of modes satisfy (4.5), then $\psi_0 \in \{0, \pi\}$ in order for the resultant hybrid modes to satisfy the same equation. We have provided a general method for finding the right t_0, φ_0, ψ_0 choice.

- In an ideal case, after having corrected for (t_0, ϕ_0, ψ_0), one should expect to obtain continuous phases for all modes at a given matching point. However, as shown in the last part of Chapter 4, this is not the case. We have shown the existence of phase offsets $\epsilon_{\ell,m}$ between different modes $h_{\ell,m}$ which need to be smoothed along a matching window together with amplitude disagreements $r_{\ell,m}$ between PN and NR. This smoothing introduces artificial frequencies in the final waveform.

- In Chapter 5, we have studied the sources of both $r_{\ell,m}$ and $\epsilon_{\ell,m}$. Regarding the former, we have found that its main error source is the truncation of the PN series at a given PN order. The magnitude of the error incurred is highly-mode dependent: different PN corrections have different consequences depending on the mode studied. In general, a new PN correction does not imply a more accurate result. We have however shown how the recently computed 3.5PN correction to the amplitude of the $(3,3)$ mode greatly improves the agreement between PN and NR results.

- Regarding the $\epsilon_{\ell,m}$ values, we have demonstrated that their main source is the magnitude of the extraction radius r in NR simulations. We have found that values of several tens of degrees are typical for the weaker modes for finite extraction radius while a few degrees are found for the stronger $\ell = m$ ones. We have shown that these converge with the extraction radius as $1/r$. I fact, for the case of extrapolated data, $\epsilon_{\ell,m}$ are never larger than a couple of degrees. Remarkably, we have also demonstrated that the quantitative values of $\epsilon_{\ell,m}$ do almost not depend on the simulated system. We have shown this for non-spinning $q \in \{3,4,6,8\}$ systems and $(q,\chi) = (3, \pm 5)$ ones. The study of the $\epsilon_{\ell,m}$ values has lead us to demonstrate that current PN results compute with great accuracy the contributions to the total phase $\phi_{\ell,m}$ from the argument of the PN complex amplitudes $\Lambda_{\ell,m}$ even at only few cycles before the merger.

- At the end of Chapter 5, we tested the effect of the finitude of extraction radius, extrapolation order and numerical resolution in terms of matches of the resulting hybrid waveforms. Qualitatively we found that high extrapolation order is likely to generate artifacts in the high m modes at large frequencies, making this dominate the mismatch for total masses such that the $(2,2)$ mode is out of band. More importantly, we have shown that the lower the extraction radius, the higher the mismatch with the corresponding hybrid built using extrapolated data is. This mismatch appears in the hybridization region of the hybrid waveform due to the large $\epsilon_{\ell,m}$ values that need to be smoothed in the case of finite radius NR data. In the late part of the waveform, the different $\epsilon_{\ell,m}$ values of each waveform introduce further mismatch. We computed these mismatches for the worst (edge-on) case and

found matches always larger than 0.97 for the early Advanced LIGO noise curve, which suggest that detection should not be affected by this kind of errors. However, parameter estimation at large SNR could require the usage of only extrapolated NR data. Resolution of NR shown to introduce negligible mismatches. Last, the close relation between the $\epsilon_{\ell,m}$ values and the corresponding mismatches makes the former a good test of the quality of the final waveform and can be used for diagnosing it.

- As the main result of Chapter 6, it has been shown that neglection of HM in CBC searches can generate important detection rate losses and parameter biases whose size strongly depends on the source and detector considered. We extended previous studies by considering non-precessing BBH with total mass $50M_\odot < M < 220M_\odot$ and an aligned spin template bank for the cases of AdvLIGO and eaLIGO. We added the case of a non-spinning template bank and targets for iLIGO. For the case of AdvLIGO, 10% event losses happen for $q \geq 6$ and $M \geq 100M_\odot$ and 20% is never achieved for the studied cases. However for the upcoming eaLIGO the situation is notably worse: maximum losses of 10% happen for already $q \geq 4$ and maximum losses of 26% are observed. Regarding parameter estimation, large parameter biases can be generated for high-mass, edge-on systems that can reach values of $(\Delta M, \Delta \chi, \Delta \mathcal{M}_c) = (-40\%, -20\%, -0.9)$. These get lowered when one considers the orientantion-averaged values. When comparing these systematic biases with the statistical uncertainty, we found that the latter dominates for total mass $M < (80, 170)M_\odot$ for an SNR of 8, for eaLIGO and AdvLIGO respectively. This suggests that HOM could be needed for PE for cases with total mass $M > (80, 170)M_\odot$ for eaLIGO and AdvLIGO respectively at an SNR of 8. The results obtained for AdvLIGO are consistent with those obtained in [2] for the case of a non-spinning search. A limitation of this study is the lack of proper parameter estimation using, for instance, bayesian MCMC techniques. Also, we have not compared the actual sensitivity of an aligned-spin search including only quadrupole modes and one including higher order modes. However, results obtained by [125] suggest that the corresponding gain/loss of events would in principle be a 10% lower than what computed in Fig.6.5.

- At the end of Chapter 6, we have studied the phenomenon of black hole kicks as an effect of the non-axisymmetric interaction between different modes. In particular, we have shown that its value is by far dominated by the interaction between the $(2, 1)$, $(2, 2)$ and $(3, 3)$ modes for the studied cases. We have also shown a close relation between the parameter biases observed due to neglection of higher modes as a function of the sky-location of the detector and the direction in which the modes in the band of the detector contribute to the kick.

- The results shown in Chapter 6, together with the description of higher modes given in Chapter 2, suggest that in order to improve current waveform models via the inclusion of higher modes, one should focus on the $(3,3)$ mode due to its intrinsic magnitude and its importance for edge-on systems and the $(3,2)$. The latter, although not being as dominating as the $(3,3)$, can have important contributions to the optimum SNR (mainly when the source is face-on) due to its lower frequency content. Note that EOB models do not include this last mode.

- Finally, BBH searches are especially affected by the presence of sine-Gaussian glitches in the detector data stream. These are poorly identified by current signal-based vetoes. However, the results shown in Fig.3.3 suggest that they should be discriminated from real GW signals if they were considered as possible signal models and a complete parameter estimation study (as for example MCMC) was performed.

Current work, in collaboration with AEI Hannover, is dealing with the injection of the hybrid waveforms developed in this thesis in simulated detector data, similar to what was done in the context of the NINJA-2 project [34]. Based on the results presented in Chapter 6, we want to measure the real efficiency of current detection pipelines towards signals containing higher harmonics, like the ones we expect from nature. This will account for further effects not investigated in this thesis such as the chi-square χ^2 veto [126]. This should further punish the mis-modeling of real signals by quadrupole waveforms.

Bibliography

[1] Juan Calderón Bustillo, Alejandro Bohé, Sascha Husa, Alicia M. Sintes, Mark Hannam, et al. Comparison of subdominant gravitational wave harmonics between post-Newtonian and numerical relativity calculations and construction of multi-mode hybrids. *arXiv:1501.00918*, 2015.

[2] Vijay Varma, Parameswaran Ajith, Sascha Husa, Juan Calderon Bustillo, Mark Hannam, et al. Gravitational-wave observations of binary black holes: Effect of nonquadrupole modes. *Phys.Rev.*, D90(12):124004, 2014. doi: 10.1103/PhysRevD.90.124004.

[3] Albert Einstein. The foundation of the general theory of relativity. *Annalen Phys.*, *49:769–822*, 1916.

[4] Sascha Husa. Michele Maggiore: Gravitational waves. Volume 1: Theory and experiments. *Gen.Rel.Grav.*, 41:1667–1669, 2009. doi: 10.1007/s10714-009-0762-5.

[5] R.A. Hulse and J.H. Taylor. Discovery of a pulsar in a binary system. *Astrophys.J.*, *195:L51–L53*, Astrophys.J., 1975.

[6] J.M. Weisberg, J.H. Taylor, and L.A. Fowler. Gravitational waves from an orbiting pulsar. *Sci.Am.*, 245:66–74, 1981. doi: 10.1038/scientificamerican1081-74.

[7] A.G. Lyne, Marta Burgay, M. Kramer, A. Possenti, R.N. Manchester, et al. A Double - pulsar system - A Rare laboratory for relativistic gravity and plasma physics. *Science*, 303:1153–1157, 2004. doi: 10.1126/science.1094645.

[8] M. Kramer, Ingrid H. Stairs, R.N. Manchester, M.A. McLaughlin, A.G. Lyne, et al. Tests of general relativity from timing the double pulsar. *Science*, 314: 97–102, 2006. doi: 10.1126/science.1132305.

[9] Rene P. Breton, Victoria M. Kaspi, 2 Kramer, Michael, Maura A. McLaughlin, Maxim Lyutikov, et al. Relativistic Spin Precession in the Double Pulsar. *Science*, 321:104–107, 2008. doi: 10.1126/science.1159295.

[10] Joel M. Weisberg and Joseph H. Taylor. Relativistic binary pulsar B1913+16: Thirty years of observations and analysis. *ASP Conf.Ser.*, 328:25, 2005.

[11] S.W. Hawking. Black hole explosions. *Nature*, 248:30–31, 1974. doi: 10.1038/ 248030a0.

[12] C.E. Fichtel, D.L. Bertsch, B.L. Dingus, J.A. Esposito, R.C. Hartman, et al. Search of the Energetic Gamma-Ray Experiment Telescope (EGRET) data for high-energy gamma-ray microsecond bursts. *Astrophys.J.*, 434:557–559, 1994. doi: 10.1086/174758.

[13] Arno A. Penzias and Robert Woodrow Wilson. A Measurement of excess antenna temperature at 4080-Mc/s. *Astrophys.J.*, 142:419–421, 1965. doi: 10.1086/148307.

[14] J. Aasi et al. Improved Upper Limits on the Stochastic Gravitational-Wave Background from 2009–2010 LIGO and Virgo Data. *Phys.Rev.Lett.*, 113(23):231101, 2014. doi: 10.1103/PhysRevLett.113.231101.

[15] B.P. Abbott et al. An Upper Limit on the Stochastic Gravitational-Wave Background of Cosmological Origin. *Nature*, 460:990, 2009. doi: 10.1038/nature08278.

[16] J. Aasi et al. Constraints on cosmic strings from the LIGO-Virgo gravitational-wave detectors. *Phys.Rev.Lett.*, 112:131101, 2014. doi: 10.1103/PhysRevLett.112. 131101.

[17] J. Abadie et al. Search for Gravitational Waves from Low Mass Compact Binary Coalescence in LIGO's Sixth Science Run and Virgo's Science Runs 2 and 3. *Phys.Rev.*, D85:082002, 2012. doi: 10.1103/PhysRevD.85.082002.

[18] G. M. Harry and LIGO Scientific Collaboration. Advanced LIGO: the next generation of gravitational wave detectors. *Classical and Quantum Gravity*, 27(8): 084006, April 2010. doi: 10.1088/0264-9381/27/8/084006.

[19] D. Shoemaker and the Advanced LIGO Team. Advanced ligo reference design. *LIGO-M060056*, 2009.

[20] T. Accadia et al. Status of the Virgo project. *Classical and Quantum Gravity*, 28 (11):114002, June 2011. doi: 10.1088/0264-9381/28/11/114002.

[21] The Virgo Collaboration. Advanced virgo baseline design. *Virgo technical report VIR-0027A-09*, 2009.

[22] Kentaro Somiya. Detector configuration of KAGRA: The Japanese cryogenic gravitational-wave detector. *Class.Quant.Grav.*, 29:124007, 2012. doi: 10.1088/ 0264-9381/29/12/124007.

[23] Matthew Pitkin, Stuart Reid, Sheila Rowan, and Jim Hough. Gravitational Wave Detection by Interferometry (Ground and Space). *Living Rev.Rel.*, 14:5, 2011. doi: 10.12942/lrr-2011-5.

[24] Pau Amaro-Seoane, Sofiane Aoudia, Stanislav Babak, Pierre Binetruy, Emanuele Berti, et al. eLISA/NGO: Astrophysics and cosmology in the gravitational-wave millihertz regime. *GW Notes*, 6:4–110, 2013.

[25] Pau Amaro-Seoane, Sofiane Aoudia, Stanislav Babak, Pierre Binetruy, Emanuele Berti, et al. Low-frequency gravitational-wave science with eLISA/NGO. *Class.Quant.Grav.*, 29:124016, 2012. doi: 10.1088/0264-9381/29/12/124016.

[26] Alberto Sesana. Pulsar timing arrays and the challenge of massive black hole binary astrophysics. *Astrophys.Space Sci.Proc.*, 40:147–165, 2015. doi: 10.1007/978-3-319-10488-1_13.

[27] Alan H. Guth. The Inflationary Universe: A Possible Solution to the Horizon and Flatness Problems. *Phys.Rev.*, D23:347–356, 1981. doi: 10.1103/PhysRevD.23.347.

[28] Daniel Baumann. TASI Lectures on Inflation. 2009.

[29] P.A.R. Ade et al. Detection of B-Mode Polarization at Degree Angular Scales by BICEP2. *Phys.Rev.Lett.*, 112(24):241101, 2014. doi: 10.1103/PhysRevLett.112.241101.

[30] R. Adam et al. Planck intermediate results. XXX. The angular power spectrum of polarized dust emission at intermediate and high Galactic latitudes. 2014.

[31] http://www.cosmos.esa.int/web/planck/publications.

[32] J. Abadie et al. Sensitivity Achieved by the LIGO and Virgo Gravitational Wave Detectors during LIGO's Sixth and Virgo's Second and Third Science Runs. 2012.

[33] D. Shoemaker et al. Advanced ligo anticipated sensitivity curves. *LIGO-T0900288, https://dcc.ligo.org/cgi-bin/DocDB/ShowDocument?docid=2974*, 2010.

[34] J. Aasi et al. The NINJA-2 project: Detecting and characterizing gravitational waveforms modelled using numerical binary black hole simulations. *Class.Quant.Grav.*, 31:115004, 2014. doi: 10.1088/0264-9381/31/11/115004.

[35] J. Abadie et al. A Gravitational wave observatory operating beyond the quantum shot-noise limit: Squeezed light in application. *Nature Phys.*, 7:962–965, 2011. doi: 10.1038/nphys2083.

[36] L. Santamaria, F. Ohme, P. Ajith, B. Bruegmann, N. Dorband, et al. Matching post-Newtonian and numerical relativity waveforms: systematic errors and a new phenomenological model for non-precessing black hole binaries. *Phys.Rev.*, D82: 064016, 2010. doi: 10.1103/PhysRevD.82.064016.

[37] Patrick J. Sutton, Gareth Jones, Shourov Chatterji, Peter Michael Kalmus, Isabel Leonor, et al. X-Pipeline: An Analysis package for autonomous gravitational-wave burst searches. *New J.Phys.*, 12:053034, 2010. doi: 10.1088/1367-2630/12/5/053034.

[38] S. Babak, R. Biswas, P.R. Brady, D.A. Brown, K. Cannon, et al. Searching for gravitational waves from binary coalescence. *Phys.Rev.*, D87(2):024033, 2013. doi: 10.1103/PhysRevD.87.024033.

[39] Kipp Cannon, Romain Cariou, Adrian Chapman, Mireia Crispin-Ortuzar, Nickolas Fotopoulos, et al. Toward Early-Warning Detection of Gravitational Waves from Compact Binary Coalescence. *Astrophys.J.*, 748:136, 2012. doi: 10.1088/0004-637X/748/2/136.

[40] S. Bonazzola and E. Gourgoulhon. Gravitational waves from neutron stars. *CERN Lectures, cds.cern.ch/record/304315/files/9605187.pdf*.

[41] C. Palomba. Searches for continuous gravitational wave signals and stochastic backgrounds in LIGO and Virgo data. pages 27–34, 2012.

[42] J. Aasi et al. Directed search for continuous gravitational waves from the Galactic center. *Phys.Rev.*, D88(10):102002, 2013. doi: 10.1103/PhysRevD.88.102002.

[43] Reinhard Prix and Badri Krishnan. Targeted search for continuous gravitational waves: Bayesian versus maximum-likelihood statistics. *Class.Quant.Grav.*, 26: 204013, 2009. doi: 10.1088/0264-9381/26/20/204013.

[44] J. Aasi et al. First all-sky search for continuous gravitational waves from unknown sources in binary systems. *Phys.Rev.*, D90(6):062010, 2014. doi: 10.1103/PhysRevD.90.062010.

[45] J. Abadie et al. Search for gravitational waves from binary black hole inspiral, merger and ringdown. *Phys.Rev.*, D83:122005, 2011. doi: 10.1103/PhysRevD.86.069903,10.1103/PhysRevD.85.089904,10.1103/PhysRevD.83.122005.

[46] Thilina Dayanga. Searching for Gravitational-Waves from Compact Binary Coalescences while Dealing With Challenges of Real Data and Simulated Waveforms.

[47] L.A. Wainstein and V.D. Zubakov. Extraction of signals from noise. *Prentice-Hall, Englewood Cliffs*, 1962.

[48] A. Buonanno and T. Damour. Effective one-body approach to general relativistic two-body dynamics. *Phys.Rev.*, D59:084006, 1999. doi: 10.1103/PhysRevD.59. 084006.

[49] Alessandra Buonanno and Thibault Damour. Transition from inspiral to plunge in binary black hole coalescences. *Phys.Rev.*, D62:064015, 2000. doi: 10.1103/ PhysRevD.62.064015.

[50] Andrea Taracchini, Yi Pan, Alessandra Buonanno, Enrico Barausse, Michael Boyle, et al. Prototype effective-one-body model for nonprecessing spinning inspiral-merger-ringdown waveforms. *Phys.Rev.*, D86:024011, 2012. doi: 10.1103/ PhysRevD.86.024011.

[51] Andrea Taracchini, Alessandra Buonanno, Yi Pan, Tanja Hinderer, Michael Boyle, et al. Effective-one-body model for black-hole binaries with generic mass ratios and spins. *Phys.Rev.*, D89(6):061502, 2014. doi: 10.1103/PhysRevD.89.061502.

[52] Jorg Frauendiener. Miguel Alcubierre: Introduction to 3 + 1 numerical relativity. *Gen.Rel.Grav.*, 43:2931–2933, 2011. doi: 10.1007/s10714-011-1195-5.

[53] Luis Lehner. Numerical relativity: A Review. *Class.Quant.Grav.*, 18:R25–R86, 2001. doi: 10.1088/0264-9381/18/17/202.

[54] Ulrich Sperhake. The numerical relativity breakthrough for binary black holes. 2014.

[55] Frank Loffler, Joshua Faber, Eloisa Bentivegna, Tanja Bode, Peter Diener, et al. The Einstein Toolkit: A Community Computational Infrastructure for Relativistic Astrophysics. *Class.Quant.Grav.*, 29:115001, 2012. doi: 10.1088/0264-9381/29/ 11/115001.

[56] Parameswaran Ajith, S. Babak, Y. Chen, M. Hewitson, B. Krishnan, et al. Phenomenological template family for black-hole coalescence waveforms. *Class.Quant.Grav.*, 24:S689–S700, 2007. doi: 10.1088/0264-9381/24/19/S31.

[57] Mark Hannam, Patricia Schmidt, Alejandro Bohé, Leila Haegel, Sascha Husa, et al. A simple model of complete precessing black-hole-binary gravitational waveforms. *Phys.Rev.Lett.*, 113:151101, 2014. doi: 10.1103/PhysRevLett.113.151101.

[58] Carlos Palenzuela, Enrico Barausse, Marcelo Ponce, and Luis Lehner. Dynamical scalarization of neutron stars in scalar-tensor gravity theories. *Phys.Rev.*, D89(4): 044024, 2014. doi: 10.1103/PhysRevD.89.044024.

[59] Laura Sampson, Nicolás Yunes, Neil Cornish, Marcelo Ponce, Enrico Barausse, et al. Projected Constraints on Scalarization with Gravitational Waves from Neutron Star Binaries. *Phys.Rev.*, D90(12):124091, 2014. doi: 10.1103/PhysRevD.90. 124091.

[60] Luc Blanchet. Gravitational radiation from post-Newtonian sources and inspiralling compact binaries. *Living Rev.Rel.*, 9:4, 2006.

[61] Kostas D. Kokkotas and Bernd G. Schmidt. Quasinormal modes of stars and black holes. *Living Rev.Rel.*, 2:2, 1999.

[62] Carlos O. Lousto. Gravitational waves from binary black holes in the extreme mass ratio regime: Self-force calculations. *Class.Quant.Grav.*, 22:S369–374, 2005. doi: 10.1088/0264-9381/22/10/031.

[63] Lior M. Burko. Orbital evolution for extreme mass-ratio binaries: Conservative self forces. *AIP Conf.Proc.*, 873:269–273, 2006. doi: 10.1063/1.2405054.

[64] Leor Barack. Gravitational self force in extreme mass-ratio inspirals. *Class.Quant.Grav.*, 26:213001, 2009. doi: 10.1088/0264-9381/26/21/213001.

[65] Frans Pretorius. Evolution of binary black hole spacetimes. *Phys.Rev.Lett.*, 95: 121101, 2005. doi: 10.1103/PhysRevLett.95.121101.

[66] Frans Pretorius. Numerical relativity using a generalized harmonic decomposition. *Class.Quant.Grav.*, 22:425–452, 2005. doi: 10.1088/0264-9381/22/2/014.

[67] Kipp Cannon, Chad Hanna, and Drew Keppel. Method to estimate the significance of coincident gravitational-wave observations from compact binary coalescence. *Phys.Rev.*, D88(2):024025, 2013. doi: 10.1103/PhysRevD.88.024025.

[68] Kipp Cannon, Chad Hanna, and Drew Keppel. Efficiently enclosing the compact binary parameter space by singular-value decomposition. *Phys.Rev.*, D84:084003, 2011. doi: 10.1103/PhysRevD.84.084003.

[69] Tito Dal Canton, Alexander H. Nitz, Andrew P. Lundgren, Alex B. Nielsen, Duncan A. Brown, et al. Implementing a search for aligned-spin neutron star-black hole systems with advanced ground based gravitational wave detectors. *Phys.Rev.*, D90(8):082004, 2014. doi: 10.1103/PhysRevD.90.082004.

[70] Tanja Bode, Pablo Laguna, and Richard Matzner. Super-Extremal Spinning Black Holes via Accretion. *Phys.Rev.*, D84:064044, 2011. doi: 10.1103/PhysRevD.84. 064044.

[71] Charles W. Misner, K.S. Thorne, and J.A. Wheeler. Gravitation. 1974.

[72] Luc Blanchet. Gravitational Radiation from Post-Newtonian Sources and Inspiralling Compact Binaries. *Living Rev.Rel.*, 17:2, 2014. doi: 10.12942/lrr-2014-2.

[73] Alejandro Bohe, Sylvain Marsat, and Luc Blanchet. Next-to-next-to-leading order spin-orbit effects in the gravitational wave flux and orbital phasing of compact binaries. *Class.Quant.Grav.*, 30:135009, 2013. doi: 10.1088/0264-9381/30/13/135009.

[74] Alejandro Bohé, Guillaume Faye, Sylvain Marsat, and Edward K Porter. Quadratic-in-spin effects in the orbital dynamics and gravitational-wave energy flux of compact binaries at the 3PN order. 2015.

[75] Balazs Mikoczi, Matyas Vasuth, and Laszlo A. Gergely. Self-interaction spin effects in inspiralling compact binaries. *Phys.Rev.*, D71:124043, 2005. doi: 10.1103/PhysRevD.71.124043.

[76] Clifford M. Will and Alan G. Wiseman. Gravitational radiation from compact binary systems: Gravitational wave forms and energy loss to second postNewtonian order. *Phys.Rev.*, D54:4813–4848, 1996. doi: 10.1103/PhysRevD.54.4813.

[77] Luc Blanchet, Thibault Damour, Bala R. Iyer, Clifford M. Will, and Alan.G. Wiseman. Gravitational radiation damping of compact binary systems to second postNewtonian order. *Phys.Rev.Lett.*, 74:3515–3518, 1995. doi: 10.1103/PhysRevLett.74.3515.

[78] Luc Blanchet, Thibault Damour, and Bala R. Iyer. Gravitational waves from inspiralling compact binaries: Energy loss and wave form to second postNewtonian order. *Phys.Rev.*, D51:5360, 1995. doi: 10.1103/PhysRevD.51.5360,10.1103/PhysRevD.54.1860,10.1103/PhysRevD.51.536010.1103/PhysRevD.54.1860.

[79] Thibault Damour, Bala R. Iyer, and B.S. Sathyaprakash. A Comparison of search templates for gravitational waves from binary inspiral. *Phys.Rev.*, D63:044023, 2001. doi: 10.1103/PhysRevD.63.044023,10.1103/PhysRevD.72.029902,10.1103/PhysRevD.63.04402310.1103/PhysRevD.72.029902.

[80] Luc Blanchet and Bala R. Iyer. Hadamard regularization of the third postNewtonian gravitational wave generation of two point masses. *Phys.Rev.*, D71:024004, 2005. doi: 10.1103/PhysRevD.71.024004.

[81] Luc Blanchet, Thibault Damour, Gilles Esposito-Farese, and Bala R. Iyer. Gravitational radiation from inspiralling compact binaries completed at the third postNewtonian order. *Phys.Rev.Lett.*, 93:091101, 2004. doi: 10.1103/PhysRevLett.93.091101.

[82] Thibault Damour, Bala R. Iyer, and B.S. Sathyaprakash. A Comparison of search templates for gravitational waves from binary inspiral - 3.5PN update. *Phys.Rev.*, D66:027502, 2002. doi: 10.1103/PhysRevD.66.027502.

[83] Alessandra Buonanno, Yan-bei Chen, and Michele Vallisneri. Detecting gravitational waves from precessing binaries of spinning compact objects: Adiabatic limit. *Phys.Rev.*, D67:104025, 2003. doi: 10.1103/PhysRevD.67.104025,10.1103/PhysRevD.67.10402510.1103/PhysRevD. 74.029904,10.1103/PhysRevD.74.029904.

[84] G.F. Torres del Castillo. Spin-weighted spherical harmonics and their applications. *Revista Mexicana de Física*, 53(eS2):pp. 125–134, febrero 2007.

[85] Luc Blanchet, Guillaume Faye, Bala R. Iyer, and Siddhartha Sinha. The Third post-Newtonian gravitational wave polarisations and associated spherical harmonic modes for inspiralling compact binaries in quasi-circular orbits. *Class.Quant.Grav.*, 25:165003, 2008. doi: 10.1088/0264-9381/25/16/165003.

[86] Alessandra Buonanno, Guillaume Faye, and Tanja Hinderer. Spin effects on gravitational waves from inspiraling compact binaries at second post-Newtonian order. *Phys.Rev.*, D87(4):044009, 2013. doi: 10.1103/PhysRevD.87.044009.

[87] Guillaume Faye, Luc Blanchet, and Bala R. Iyer. Non-linear multipole interactions and gravitational-wave octupole modes for inspiralling compact binaries to third-and-a-half post-Newtonian order. *Class.Quant.Grav.*, 32:045016, 2015. doi: 10. 1088/0264-9381/32/4/045016.

[88] Alexander H. Nitz, Andrew Lundgren, Duncan A. Brown, Evan Ochsner, Drew Keppel, et al. Accuracy of gravitational waveform models for observing neutron-star–black-hole binaries in Advanced LIGO. *Phys.Rev.*, D88(12):124039, 2013. doi: 10.1103/PhysRevD.88.124039.

[89] Richard L. Arnowitt, Stanley Deser, and Charles W. Misner. Dynamical Structure and Definition of Energy in General Relativity. *Phys.Rev.*, 116:1322–1330, 1959. doi: 10.1103/PhysRev.116.1322.

[90] Masaru Shibata and Takashi Nakamura. Evolution of three-dimensional gravitational waves: Harmonic slicing case. *Phys.Rev.*, D52:5428–5444, 1995. doi: 10.1103/PhysRevD.52.5428.

[91] Thomas W. Baumgarte and Stuart L. Shapiro. On the numerical integration of Einstein's field equations. *Phys.Rev.*, D59:024007, 1999. doi: 10.1103/PhysRevD. 59.024007.

[92] J. David Brown. BSSN in spherical symmetry. *Class.Quant.Grav.*, 25:205004, 2008. doi: 10.1088/0264-9381/25/20/205004.

[93] C. Bona, T. Ledvinka, C. Palenzuela, and M. Zacek. General covariant evolution formalism for numerical relativity. *Phys.Rev.*, D67:104005, 2003. doi: 10.1103/ PhysRevD.67.104005.

[94] Daniela Alic, Carles Bona-Casas, Carles Bona, Luciano Rezzolla, and Carlos Palenzuela. Conformal and covariant formulation of the Z4 system with constraint-violation damping. *Phys.Rev.*, D85:064040, 2012. doi: 10.1103/PhysRevD.85. 064040.

[95] Nicolas Sanchis-Gual, Pedro J. Montero, Jose A. Font, Ewald Müller, and Thomas W. Baumgarte. Fully covariant and conformal formulation of the Z4 system in a reference-metric approach: comparison with the BSSN formulation in spherical symmetry. *Phys.Rev.*, D89(10):104033, 2014. doi: 10.1103/PhysRevD. 89.104033.

[96] Ezra Newman and Roger Penrose. An Approach to gravitational radiation by a method of spin coefficients. *J.Math.Phys.*, 3:566–578, 1962. doi: 10.1063/1. 1724257.

[97] Michael Boyle and Abdul H. Mroue. Extrapolating gravitational-wave data from numerical simulations. *Phys.Rev.*, D80:124045, 2009. doi: 10.1103/PhysRevD.80. 124045.

[98] Denis Pollney, Christian Reisswig, Erik Schnetter, Nils Dorband, and Peter Diener. High accuracy binary black hole simulations with an extended wave zone. *Phys.Rev.*, D83:044045, 2011. doi: 10.1103/PhysRevD.83.044045.

[99] Nicholas W. Taylor, Michael Boyle, Christian Reisswig, Mark A. Scheel, Tony Chu, et al. Comparing Gravitational Waveform Extrapolation to Cauchy-Characteristic Extraction in Binary Black Hole Simulations. *Phys.Rev.*, D88(12):124010, 2013. doi: 10.1103/PhysRevD.88.124010.

[100] Christian Reisswig and Denis Pollney. Notes on the integration of numerical relativity waveforms. *Class.Quant.Grav.*, 28:195015, 2011. doi: 10.1088/0264-9381/ 28/19/195015.

[101] Bela Szilagyi, Lee Lindblom, and Mark A. Scheel. Simulations of Binary Black Hole Mergers Using Spectral Methods. *Phys.Rev.*, D80:124010, 2009. doi: 10. 1103/PhysRevD.80.124010.

[102] Mark A. Scheel, Michael Boyle, Tony Chu, Lawrence E. Kidder, Keith D. Matthews, et al. High-accuracy waveforms for binary black hole inspiral, merger, and ringdown. *Phys.Rev.*, D79:024003, 2009. doi: 10.1103/PhysRevD.79.024003.

[103] Ulrich Sperhake, Bernd Bruegmann, Doreen Mueller, and Carlos F. Sopuerta. Black-hole binaries go to eleven orbits. 2010.

[104] Lee Lindblom, Mark A. Scheel, Lawrence E. Kidder, Robert Owen, and Oliver Rinne. A New generalized harmonic evolution system. *Class.Quant.Grav.*, 23: S447–S462, 2006. doi: 10.1088/0264-9381/23/16/S09.

[105] Daniel A. Hemberger, Mark A. Scheel, Lawrence E. Kidder, Bela Szilagyi, Geoffrey Lovelace, et al. Dynamical Excision Boundaries in Spectral Evolutions of Binary Black Hole Spacetimes. *Class.Quant.Grav.*, 30:115001, 2013. doi: 10.1088/0264-9381/30/11/115001.

[106] Harald P. Pfeiffer, Lawrence E. Kidder, Mark A. Scheel, and Saul A. Teukolsky. A Multidomain spectral method for solving elliptic equations. *Comput.Phys.Commun.*, 152:253–273, 2003. doi: 10.1016/S0010-4655(02)00847-0.

[107] Bernd Bruegmann, Jose A. Gonzalez, Mark Hannam, Sascha Husa, Ulrich Sperhake, et al. Calibration of Moving Puncture Simulations. *Phys.Rev.*, D77:024027, 2008. doi: 10.1103/PhysRevD.77.024027.

[108] Sascha Husa, Jose A. Gonzalez, Mark Hannam, Bernd Bruegmann, and Ulrich Sperhake. Reducing phase error in long numerical binary black hole evolutions with sixth order finite differencing. *Class.Quant.Grav.*, 25:105006, 2008. doi: 10.1088/0264-9381/25/10/105006.

[109] Manuela Campanelli, C.O. Lousto, P. Marronetti, and Y. Zlochower. Accurate evolutions of orbiting black-hole binaries without excision. *Phys.Rev.Lett.*, 96: 111101, 2006. doi: 10.1103/PhysRevLett.96.111101.

[110] H. Nakano, J. Healy, C.O. Lousto, and Y. Zlochower. Perturbative extraction of gravitational waveforms generated with Numerical Relativity. 2015.

[111] Ilana MacDonald, Samaya Nissanke, Harald P. Pfeiffer, and Harald P. Pfeiffer. Suitability of post-Newtonian/numerical-relativity hybrid waveforms for gravitational wave detectors. *Class.Quant.Grav.*, 28:134002, 2011. doi: 10.1088/ 0264-9381/28/13/134002.

[112] Alex Vañó-Viñuales, Sascha Husa, and David Hilditch. Spherical symmetry as a test case for unconstrained hyperboloidal evolution. 2014.

[113] Alex Vaňó-Viñuales and Sascha Husa. Unconstrained hyperboloidal evolution of black holes in spherical symmetry with GBSSN and Z4c. 2014.

[114] Mark Hannam, Sascha Husa, Ulrich Sperhake, Bernd Bruegmann, and Jose A. Gonzalez. Where post-Newtonian and numerical-relativity waveforms meet. *Phys.Rev.*, D77:044020, 2008. doi: 10.1103/PhysRevD.77.044020.

[115] The SXS Collaboration. www.black-holes.org. *www.black-holes.org.*

[116] Mark Hannam, Sascha Husa, Frank Ohme, Doreen Muller, and Bernd Bruegmann. Simulations of black-hole binaries with unequal masses or nonprecessing spins: Accuracy, physical properties, and comparison with post-Newtonian results. *Phys.Rev.*, D82:124008, 2010. doi: 10.1103/PhysRevD.82.124008.

[117] Bela Szilagyi, Jonathan Blackman, Alessandra Buonanno, Andrea Taracchini, Harald P. Pfeiffer, et al. Numerical relativity reaching into post-Newtonian territory: a compact-object binary simulation spanning 350 gravitational-wave cycles. 2015.

[118] Michael Pürrer. Frequency domain reduced order models for gravitational waves from aligned-spin compact binaries. *Class.Quant.Grav.*, 31(19):195010, 2014. doi: 10.1088/0264-9381/31/19/195010.

[119] Piotr Jaranowski, Andrzej Krolak, and Bernard F. Schutz. Data analysis of gravitational - wave signals from spinning neutron stars. 1. The Signal and its detection. *Phys.Rev.*, D58:063001, 1998. doi: 10.1103/PhysRevD.58.063001.

[120] Peter D. Welch. The use of fast fourier transform for the estimation of power spectra: A method based on time aver. aging over short, modified periodograms. *IEEE Transactions on audio and electroacoustics , VOL. AU-15, NO. 2, June*, 1967.

[121] Chad Hanna. Searching for gravitational waves from binary systems in non-stationary data. *Ph.D Thesis*, 2008.

[122] Serge Droz, Daniel J. Knapp, Eric Poisson, and Benjamin J. Owen. Gravitational waves from inspiraling compact binaries: Validity of the stationary phase approximation to the Fourier transform. *Phys.Rev.*, D59:124016, 1999. doi: 10.1103/PhysRevD.59.124016.

[123] Miquel Trias Cornellana. Gravitational wave observation of compact binaries. *PhD. Thesis, Universitat de les Illes Balears*, 2010.

[124] Philip Bevington and D. Keith Robinson. Data reduction and error analysis for the physical sciences.

[125] Collin Capano, Yi Pan, and Alessandra Buonanno. Impact of Higher Harmonics in Searching for Gravitational Waves from Non-Spinning Binary Black Holes. *Phys.Rev.*, D89:102003, 2014. doi: 10.1103/PhysRevD.89.102003.

[126] Bruce Allen. A chi**2 time-frequency discriminator for gravitational wave detection. *Phys.Rev.*, D71:062001, 2005. doi: 10.1103/PhysRevD.71.062001.

[127] T. Dal Canton, S. Bhagwat, S.V. Dhurandhar, and A. Lundgren. Effect of sine-Gaussian glitches on searches for binary coalescence. *Class.Quant.Grav.*, 31: 015016, 2014. doi: 10.1088/0264-9381/31/1/015016.

[128] Emily Baird, Stephen Fairhurst, Mark Hannam, and Patricia Murphy. Degeneracy between mass and spin in black-hole-binary waveforms. *Phys.Rev.*, D87(2):024035, 2013. doi: 10.1103/PhysRevD.87.024035.

[129] Carl L. Rodriguez, Benjamin Farr, Will M. Farr, and Ilya Mandel. Inadequacies of the Fisher Information Matrix in gravitational-wave parameter estimation. *Phys.Rev.*, D88(8):084013, 2013. doi: 10.1103/PhysRevD.88.084013.

[130] Michele Vallisneri. Use and abuse of the Fisher information matrix in the assessment of gravitational-wave parameter-estimation prospects. *Phys.Rev.*, D77: 042001, 2008. doi: 10.1103/PhysRevD.77.042001.

[131] Lee Lindblom, Benjamin J. Owen, and Duncan A. Brown. Model Waveform Accuracy Standards for Gravitational Wave Data Analysis. *Phys.Rev.*, D78:124020, 2008. doi: 10.1103/PhysRevD.78.124020.

[132] Frank Ohme. Bridging the gap between post - newtonian theory and numerical relativity in gravitational wave data analysis. *Ph.D Thesis*, 2012.

[133] Yi Pan, Alessandra Buonanno, Michael Boyle, Luisa T. Buchman, Lawrence E. Kidder, et al. Inspiral-merger-ringdown multipolar waveforms of nonspinning black-hole binaries using the effective-one-body formalism. *Phys.Rev.*, D84:124052, 2011. doi: 10.1103/PhysRevD.84.124052.

[134] Thibault Damour, Alessandro Nagar, and Sebastiano Bernuzzi. Improved effective-one-body description of coalescing nonspinning black-hole binaries and its numerical-relativity completion. *Phys.Rev.*, D87(8):084035, 2013. doi: 10. 1103/PhysRevD.87.084035.

[135] Michael Boyle. Uncertainty in hybrid gravitational waveforms: Optimizing initial orbital frequencies for binary black-hole simulations. *Phys.Rev.*, D84:064013, 2011. doi: 10.1103/PhysRevD.84.064013.

[136] Serguei Ossokine, Lawrence E. Kidder, and Harald P. Pfeiffer. Precession-tracking coordinates for simulations of compact-object-binaries. *Phys.Rev.*, D88:084031, 2013. doi: 10.1103/PhysRevD.88.084031.

[137] Michael Boyle, Duncan A. Brown, Lawrence E. Kidder, Abdul H. Mroue, Harald P. Pfeiffer, et al. High-accuracy comparison of numerical relativity simulations with post-Newtonian expansions. *Phys.Rev.*, D76:124038, 2007. doi: 10.1103/PhysRevD.76.124038.

[138] Mark A. Scheel, Harald P. Pfeiffer, Lee Lindblom, Lawrence E. Kidder, Oliver Rinne, et al. Solving Einstein's equations with dual coordinate frames. *Phys.Rev.*, D74:104006, 2006. doi: 10.1103/PhysRevD.74.104006.

[139] Abdul H. Mroue and Harald P. Pfeiffer. Precessing Binary Black Holes Simulations: Quasicircular Initial Data. 2012.

[140] Abdul H. Mroue, Mark A. Scheel, Bela Szilagyi, Harald P. Pfeiffer, Michael Boyle, et al. A catalog of 174 binary black-hole simulations for gravitational-wave astronomy. *Phys.Rev.Lett.*, 111:241104, 2013. doi: 10.1103/PhysRevLett.111.241104.

[141] Luisa T. Buchman, Harald P. Pfeiffer, Mark A. Scheel, and Bela Szilagyi. Simulations of non-equal mass black hole binaries with spectral methods. *Phys.Rev.*, D86:084033, 2012. doi: 10.1103/PhysRevD.86.084033.

[142] Tony Chu. Numerical simulations of black-hole spacetimes. *INSPIRE-1118187*.

[143] Harald P. Pfeiffer, Duncan A. Brown, Lawrence E. Kidder, Lee Lindblom, Geoffrey Lovelace, et al. Reducing orbital eccentricity in binary black hole simulations. *Class.Quant.Grav.*, 24:S59–S82, 2007. doi: 10.1088/0264-9381/24/12/S06.

[144] K.G. Arun, Luc Blanchet, Bala R. Iyer, and Siddhartha Sinha. Third post-Newtonian angular momentum flux and the secular evolution of orbital elements for inspiralling compact binaries in quasi-elliptical orbits. *Phys.Rev.*, D80:124018, 2009. doi: 10.1103/PhysRevD.80.124018.

[145] Alessandra Buonanno, Bala Iyer, Evan Ochsner, Yi Pan, and B.S. Sathyaprakash. Comparison of post-Newtonian templates for compact binary inspiral signals in gravitational-wave detectors. *Phys.Rev.*, D80:084043, 2009. doi: 10.1103/PhysRevD.80.084043.

[146] Guillaume Faye, Sylvain Marsat, Luc Blanchet, and Bala R. Iyer. The third and a half post-Newtonian gravitational wave quadrupole mode for quasi-circular inspiralling compact binaries. *Class.Quant.Grav.*, 29:175004, 2012. doi: 10.1088/0264-9381/29/17/175004.

[147] Denis Pollney and Christian Reisswig. Gravitational memory in binary black hole mergers. *Astrophys.J.*, 732:L13, 2011. doi: 10.1088/2041-8205/732/1/L13.

[148] P. Ajith, Michael Boyle, Duncan A. Brown, Bernd Brügmann, Luisa T. Buchman, et al. The NINJA-2 catalog of hybrid post-Newtonian/numerical-relativity waveforms for non-precessing black-hole binaries. *Class.Quant.Grav.*, 29:124001, 2012. doi: 10.1088/0264-9381/30/19/199401,10.1088/0264-9381/29/12/124001.

[149] Ian Hinder, Alessandra Buonanno, Michael Boyle, Zachariah B. Etienne, James Healy, et al. Error-analysis and comparison to analytical models of numerical waveforms produced by the NRAR Collaboration. *Class.Quant.Grav.*, 31:025012, 2014. doi: 10.1088/0264-9381/31/2/025012.

[150] Larne Pekowsky, James Healy, Deirdre Shoemaker, and Pablo Laguna. Impact of Higher-order Modes on the Detection of Binary Black Hole Coalescences. *Phys.Rev.*, D87:084008, 2013. doi: 10.1103/PhysRevD.87.084008.

[151] Duncan A. Brown, Prayush Kumar, and Alexander H. Nitz. Template banks to search for low-mass binary black holes in advanced gravitational-wave detectors. *Phys.Rev.*, D87:082004, 2013. doi: 10.1103/PhysRevD.87.082004.

[152] Tyson B. Littenberg, John G. Baker, Alessandra Buonanno, and Bernard J. Kelly. Systematic biases in parameter estimation of binary black-hole mergers. *Phys.Rev.*, D87(10):104003, 2013. doi: 10.1103/PhysRevD.87.104003.

[153] Chris Van Den Broeck and Anand S. Sengupta. Phenomenology of amplitude-corrected post-Newtonian gravitational waveforms for compact binary inspiral. I. Signal-to-noise ratios. *Class.Quant.Grav.*, 24:155–176, 2007. doi: 10.1088/0264-9381/24/1/009.

[154] Inc. Wolfram Research. *Mathematica Edition: Version 9.0, 10.0.*

[155] Jose A. Gonzalez, Ulrich Sperhake, Bernd Bruegmann, Mark Hannam, and Sascha Husa. Total recoil: The Maximum kick from nonspinning black-hole binary inspiral. *Phys.Rev.Lett.*, 98:091101, 2007. doi: 10.1103/PhysRevLett.98.091101.

[156] John G. Baker, Joan Centrella, Dae-Il Choi, Michael Koppitz, James R. van Meter, et al. Getting a kick out of numerical relativity. *Astrophys.J.*, 653:L93–L96, 2006. doi: 10.1086/510448.

[157] Michael Koppitz, Denis Pollney, Christian Reisswig, Luciano Rezzolla, Jonathan Thornburg, et al. Recoil Velocities from Equal-Mass Binary-Black-Hole Mergers. *Phys.Rev.Lett.*, 99:041102, 2007. doi: 10.1103/PhysRevLett.99.041102.

[158] Frank Herrmann, Ian Hinder, Deirdre Shoemaker, Pablo Laguna, and Richard A. Matzner. Gravitational recoil from spinning binary black hole mergers. *Astrophys.J.*, 661:430–436, 2007. doi: 10.1086/513603.